Spin-orbit interactions for steering Bloch surface waves with the optical magnetic field and for locally controlling light polarization by swirling surface plasmons

Mengjia Wang

To cite this version:

Mengjia Wang. Spin-orbit interactions for steering Bloch surface waves with the optical magnetic field and for locally controlling light polarization by swirling surface plasmons. Optics / Photonic. Université Bourgogne Franche-Comté, 2019. English. NNT : 2019UBFCD013 . tel-02313634

HAL Id: tel-02313634
https://theses.hal.science/tel-02313634

Submitted on 11 Oct 2019

HAL is a multi-disciplinary open access archive for the deposit and dissemination of scientific research documents, whether they are published or not. The documents may come from teaching and research institutions in France or abroad, or from public or private research centers.

L'archive ouverte pluridisciplinaire **HAL**, est destinée au dépôt et à la diffusion de documents scientifiques de niveau recherche, publiés ou non, émanant des établissements d'enseignement et de recherche français ou étrangers, des laboratoires publics ou privés.

UBFC
UNIVERSITÉ
BOURGOGNE FRANCHE-COMTÉ

UFC
UNIVERSITÉ
DE FRANCHE-COMTÉ

THÈSE DE DOCTORAT DE L'ÉTABLISSEMENT UNIVERSITÉ BOURGOGNE FRANCHE-COMTÉ

PRÉPARÉE À L'UNIVERSITÉ DE FRANCHE-COMTÉ

École doctorale n°37
Sciences Pour l'Ingénieur et Microtechniques

Doctorat d'Optique et Photonique

par

MENGJIA WANG

Spin-orbit interactions for steering Bloch surface waves with the optical magnetic field and for locally controlling light polarization by swirling surface plasmons

Thèse présentée et soutenue à Besançon, le 13 Feburary 2019

Composition du Jury :

BERNAL-ARTAJONA MARIA-PILAR	Directeur de Recherche CNRS, UBFC, FEMTO-ST	Président
DESCROVI EMILIANO	Professeur à Politecnico di Torino	Rapporteur
BANZER PETER	Professeur à Max Planck Institute for the Science of Light	Rapporteur
GENEVET PATRICE	Chargé de Recherche CNRS, CRHEA, à l'Université Côte d'Azur	Examinateur
GROSJEAN THIERRY	Chargé de Recherche CNRS, UBFC, FEMTO-ST	Directeur de thèse
MARTIN NICOLAS	Professeur à ENSMM	Codirecteur de thèse
SALUT ROLAND	Ingénieur à UBFC, FEMTO-ST	Invité
SUAREZ MIGUEL	Ingénieur à UBFC, FEMTO-ST	Invité

N° | X | X | X |

école doctorale **sciences pour l'ingénieur et microtechniques**

Title: Spin-orbit interactions for steering Bloch surface waves with the optical magnetic field and for locally controlling light polarization by swirling surface plasmons

Keywords: Spin-orbit interaction magnetic field of light; circular polarization Bloch surface waves; traveling-wave helical optical antenna polarization control tunability

Abstract:

My thesis is devoted to novel nano-optical phenomena and devices based on spin-orbit interaction (SOI) of light. First, magnetic spin-locking, i.e., an SOI solely driven by the magnetic field of light, is demonstrated with Bloch surface waves. It provides a new manifestation of the magnetic light field. Then, we propose and demonstrate the concept of traveling-wave helical plasmonic antenna (TW-HPA), consisting of a narrow helical gold-coated wire non-radiatively fed with a dipolar nano-antenna. By swirling surface plasmons, the TW-HPA combines subwavelength illumination and polarization transformation. The TW-HPA is demonstrated to radiate on the subwavelength scale almost perfectly circularly polarized optical waves upon illumination with linearly polarized light. With this subwavelength plasmonic antenna, we developed strongly integrated arrays of point-light emissions of opposite handedness and tunable intensities. Finally, by coupling two couples of TW-HPAs of opposite handedness, we obtained new polarization properties so far unattainable.

Titre : Spin-orbit interactions for steering Bloch surface waves with the optical magnetic field and for locally controlling light polarization by swirling surface plasmons

Mots-clés : Interaction spin-orbite; polarisation circulaire; moments orbitaux et de spin de la lumière ; ondes de surface de Bloch; champ magnétique optique ; nano-antenne optique hélicoïdale à ondes progressives; contrôle de la polarisation; accordabilité; nouveaux degrés de liberté

Résumé :

Ma thèse est consacrée aux nouveaux phénomènes nano-optiques et aux dispositifs basés sur l'interaction spin-orbite de la lumière (SOI). Tout d'abord, il a été démontré un SOI uniquement piloté par le champ magnétique de la lumière permettant de diriger avec précision les ondes de surface de Bloch, offrant ainsi une nouvelle manifestation du champ magnétique optique. Ensuite, nous avons proposé et démontré le concept de nano-antenne plasmonique hélicoïdale à ondes progressives (TW-HPA), c'est-à-dire un fil hélicoïdal en or étroit alimenté optiquement par une nano-antenne dipolaire dans une configuration « end-firing ». Une telle nano-antenne a été démontrée comme la première optique de polarisation sublongueur d'onde. L'agencement de TW-HPAs à l'échelle de quelques microns a permis de convertir « à la carte » un faisceau polarisé linéairement en une distribution de faisceaux directifs présentant des polarisations différentes définies de façon déterministe par la géométrie et les dimensions des nano-antennes. Par le biais d'un couplage en champ proche de quatre nano-antennes à hélicités opposées, nous avons obtenus une optique sublongueur d'onde permettant un degré de liberté dans le contrôle de la polarisation qui est interdit avec les composants et méthodes classiques basées sur l'exploitation de matériaux biréfringents ou dichroïques, ou de métamatériaux imitant ces propriétés.

Université Bourgogne Franche-Comté
32, avenue de l'Observatoire
25000 Besançon, France

ACKNOWLEGEMENT

First and foremost, I would like to express my sincere gratitude to my supervisor Dr. Thierry Grosjean, for his getting me enrolled in such an appalling topic and for his continuous support for my PhD study. He is enthusiastic, open-minded and full of scientific thoughts and ideas. Discussion with him is always inspiring and agreeable, which is a lifelong treasure for me. Under his help, I have learnt a lot, not only to propose and solve scientific problems but also to quest and enjoy the beauty of science. I also would like to acknowledge my co-supervisor Prof. Nicolas Martin. He has been giving me a lot of warm encouragement and concrete help with the sample fabrication and manuscript preparation. He is also approachable by simply knocking the door of his office, with great patience and helpful scientific discussions.

Besides, I would like to thank the reviewers of my thesis: Prof. Emiliano Descrovi and Prof. Peter Banzer. Many thanks to them for carefully reading my manuscript and providing constructive comments, which help improve the quality of my thesis. I would like to thank all the jury members for their approval and recommendation of my work. Their warm words will continuously encourage me to develop further my academic career. I also feel grateful for the inspiring questions raised by the jury members, which deepen my understandings and add new scientific perspectives to my research. Special thanks to Prof. Maria-Pilar Bernal-Artajona for preparing the report of my defense and Dr. Patrice Genevet for giving me valuable suggestions.

Many thanks to Dr. Roland Salut. His excellent job on FIB fabrication offers me a much easier access to high-quality samples, which have greatly facilitated my PhD study. Same thanks to Dr. Miguel Suarez for his kind help with programming and experimental benches, as well as many instructive discussions. I would like to thank Prof. Lu HuiHui for helping me with the experimental characterizations. In addition, I would like to acknowledge Dr. Tatiana Kovalevich and our collaborators in EPFL (Prof. Hans-Peter Herzig and Dr. Myun-Sik Kim) for preparing the photonic crystal samples.

My colleagues and friends in FEMTO-ST and Besançon are also acknowledged. How lucky am I to have the chance to work and live with you! I am especially grateful to Dr. Zhihua Xie and Dr. Wentao Xie, who helped me a lot upon my first arrival in France. I would like to thank Prof. Chen Xie and Prof. Guoping Lin for their useful advices. Also many thanks to Yannick, Tatiana, Quentin, Tingting, Xueyan, Hongyi, Fanchao, Qingxiang, Yanfeng, Xavier, Tintu, Bogdan, Venancio, Alexis, Tahseen, Yinjuan, Xumin, Pengbai, Danjing, Zhihao, Jifei, Ke, Wanying, Shiyi, Runlian, Shan, Nana and so on for their help in my life. Thank Jun for her timely cheering me up during the difficult period of my PhD research. Special thanks to my former supervisor Prof. Yu and my friends in China: Ting, Minzhe, Yi, Lei, Jinshuang, Xinhong, Guoqiang, ShuiYan, Furong, Qiuqun and Wuxia.

Finally, I would like to express my deepest gratitude to my family: my grandparents, my parents, my wife, my brothers and sisters. It is your love that invigorates me to keep on moving whatever happens. Special thanks to my wife Chen, who has been spending plenty of time in taking care of my daily life and helping me correct the typos in my manuscript. Thank you so much for accompanying and helping me, your smiles of love will always be the best reward for my endeavor! Same thanks to my mother land: China, wish you long and prosper!

At the end, I would like to acknowledge the French Ministry of Higher Education, Research and Innovation (MESRI) for the financial support of my work.

CONTENTS

1 Research background 3

1.1 Angular momenta of light 4

1.1.1 Classical electromagnetic descriptions of the optical AMs 4

1.1.2 Spin angular momentum and polarization structure of light 7

1.1.3 Orbital angular momentum and phase structure of light 13

1.1.4 Extrinsic orbital angular momentum and light trajectories 14

1.2 Spin-orbit interaction of light (SOI) 15

1.2.1 General rules underlying SOI 15

1.2.1.1 Angular momentum conservation 15

1.2.1.2 Geometric phase 16

1.2.2 Various SOI phenomena 18

1.2.2.1 Spin-orbit interaction induced by geometric phases 18

1.2.2.2 Spin-orbit interaction with evanescent waves 21

1.3 Conclusions 25

2 Magnetic spin-orbit interaction steers Bloch surface waves 27

2.1 Transverse spin in the magnetic field of TE-polarized Bloch surface waves . 29

2.2 Unidirectional excitation of Bloch surface waves by electric and magnetic dipoles 32

2.3 Experimental demonstration of the magnetic spin-orbit interaction 35

2.3.1 Experimental setup 35

2.3.2 Analytical model of the experimental setup 37

2.3.3 Numerical simulation of the experimental setup 41

2.3.4 Results and discussions 43

2.4 Conclusions 45

3 Traveling-wave helical plasmonic antenna: concept and design 47

3.1 Basics and state of the art for optical antennas 48

3.2 The concept of helical antenna for light 51

3.2.1 Helical antennas in low-frequency regime 51

- 3.2.1.1 Description of the helical antennas 51
- 3.2.1.2 Operation modes of low-frequency helical antennas 52
- 3.2.1.3 Different mechanisms underpinning the normal and axial modes 54
- 3.2.2 Helical antennas in optical regime 56
  - 3.2.2.1 Helices in metamaterials 56
  - 3.2.2.2 Traveling-wave helical plasmonic antenna 57
- 3.2.3 Traveling-wave HPA (TW-HPA): generating CP light via spin-orbit interaction 61
- 3.3 Design of TW-HPAs as subwavelength circular polarizer 63
  - 3.3.1 Design of the helix 63
    - 3.3.1.1 Effect of the helix vertical pitch 65
    - 3.3.1.2 Effect of the wire thickness 66
    - 3.3.1.3 Effect of the helix radius 68
    - 3.3.1.4 Effect of the number of turn 68
    - 3.3.1.5 Effect of the helix handedness 69
    - 3.3.1.6 Conclusions 70
  - 3.3.2 Near-field feed element 70
    - 3.3.2.1 Helix fed with a rectangular nanoaperture 72
- 3.4 Conclusions 75

4 Traveling-wave helical plasmonic antenna: fabrication and experimental demonstration 77

- 4.1 Overview of the fabrication techniques 77
- 4.2 Fabrication of the TW-HPA 80
  - 4.2.1 GLAD-based fabrication 80
  - 4.2.2 FIBID-based fabrication 82
    - 4.2.2.1 Carbon helix 83
    - 4.2.2.2 Metal coating 84
    - 4.2.2.3 Feed elements 86
- 4.3 Experimental demonstration of TW-HPA 87
  - 4.3.1 Experimental set-up 87
  - 4.3.2 Optical response of the feed element 89
  - 4.3.3 Polarization properties of the TW-HPA 89
  - 4.3.4 Demonstration of the plasmon swirling effect in circular polarization generation 92

4.3.4.1 Demonstration of the end-fire excitation process of the plasmonic helix 93
4.3.4.2 Demonstration of a higher AR when the helix turn number increases 94
4.4 Conclusions 94

5 TW-HPA-based platform for detecting and controlling light polarization 97
5.1 Traveling-wave helical plasmonic antenna and circular dichroism 97
5.1.1 Concept and simulation 97
5.1.2 Experimental demonstration 99
5.2 Closely packed subwavelength light sources with opposite helicity 101
5.2.1 Concept and analytical model 101
5.2.2 Experimental demonstration 102
5.3 Subwavelength-scale wave-plate by coupling four TW-HPAs 103
5.3.1 Concept and analytical model 104
5.3.2 Experimental demonstration 106
5.4 Conclusions 109

6 Summary and perspectives 111

GENERAL INTRODUCTION

Tackling optics near or beyond the diffraction limit of light, nano-optics has been offering us a host of fascinating applications in both fundamental and applied science [1]. Near-field probing[1, 2, 3, 4, 5, 6, 7, 8, 9, 10], enhanced Raman scattering [11, 12, 13, 14, 15], surface plasmons (SPs) [1, 16, 17, 18] [19, 20, 21, 22, 23, 24, 25, 26] and optical antennas [1, 27, 28, 29, 30, 31, 32] and metamaterials [33, 34, 35, 36, 37, 38, 39, 40, 41, 42, 43, 44] are elegant paradigms of those kinds. With the help of most-advanced nano-fabrication tools, a wide spectra of nano-optical components have been developed to confine, guide or collect light on the nanoscale, which boosted the development of nano-optics [1, 10]. It is noted that, such nano-optical elements in general has poor flexibility: once a nano structure is fabricated, its optical properties are fixed and thus cannot be modified. Therefore, it is of practical significance to add tunability to nano-optics, for opening up new functionalities on the nanoscale. Quantum computing and information may benefit from a flexible subwavelength control of light on the subwavelength scale.

Recently, it has been shown that optical metamaterials [41, 42, 43, 44], which are formed by arrays of nano building blocks, can be used to gain flexibility in controlling light polarization [45], intensity [46] and trajectory [47]. These nano building blocks normally play in a resonant way and work collectively to attain these functionalities [41, 45, 48]. Given such a principle, one will lose targeted properties and performance with a single cell that is picked out from metamaterials. Besides, though the constituent cells are on the subwavelength scale and are arranged with a subwavelength periodicity, the resulting optical metamaterials as a whole extend much larger than the wavelength range. Therefore, it seems unlikely for metamaterials to operate well at a subwavelength overall component size.

Optical antennas, which are translated from low-frequency wireless telecommunication antennas through size downscaling, are frequently used to efficiently link propagating light and localized optical energy [1, 28, 31]. As most optical antennas are intrinsically subwavelength in size, they enable the control of light-matter interaction on the true nanometer scale[1, 28]. For example, optical antennas have demonstrated full control over the direction, polarization and emission rate from point-like quantum emitters [1, 49, 50, 51, 52]. However, like other nanooptical elements, present optical antennas also suffer from lack of tunability.

Recent researches show that optical tunability can be gained by taking advantage of the angular momenta (AMs) of light. Light carries AMs in the form of spin and orbital angular momenta [53, 54, 55, 56, 57]. Remarkably, these two types of angular momenta are not independent: spin angular momentum (SAM) can be converted into orbital angular momentum (OAM), and vice versa, a phenomenon called spin-orbit interaction of light (SOI) [55]. SOI has recently drawn much interest for applications involving tunable light manipulation at small scale [55], which include small particle manipulation [58, 59], light beam shaping [60, 61, 62, 63], subwavelength optical probing [56, 64, 65, 66, 67] and the spin-locked unidirectional waveguiding [68, 69, 70, 71, 72, 73, 74], etc.

My thesis refers to two specific SOIs: 1) Magnetic spin-orbit interaction of light, ie., an SOI solely driven by the magnetic field of light. We show that the helicity of optical magnetic field mediates the directional propagation of TE-polarized Bloch surface waves (BSWs) on top of a 1D photonic crystal, revealing a magnetic SOI for light. 2) Extrinsic-OAM-to-SAM transfer in a traveling-wave helical plasmonic antenna (TW-HPA). TW-HPA is a new concept of plasmonic antenna, which develops the ability of swirling surface plasmons. In the course of propagation, the swirling subdiffraction surface plasmons are released in free space under the form of a circularly polarized confined light, owing to optical SOI. This offers a complete subwavelength approach for controlling light polarization.

This manuscript consists of six chapters. The first chapter will be a background part. We will start from basic electromagnetic descriptions of light waves. We will introduce the spin angular momentum and orbital angular momentum of light, as well as their link with the polarization, phase and trajectory. Then, we will review existing studies on various SOIs of light.

In Chapter 2, we will show the magnetic spin-orbit interaction of light. We will show that the optical magnetic field can tunably steer Bloch surface waves. We first numerically study the unidirectional excitation of Bloch surface waves with a spinning magnetic dipole. Then, we experimentally demonstrate that the helicity of optical magnetic field defines a directional excitation phenomenon.

In Chapter 3, we will introduce the concept of TW-HPA, as well as the underlying SOI process of this antenna. We will also detail the design process of such an antenna. At last, we will show an optimum design that generates almost perfect circular polarization at optical telecommunication wavelengths.

Chapter 4 will deal with the fabrication and characterization of TW-HPA. Our fabrication method combines two existing technologies, namely focused ion beam induced deposition and glancing angle deposition. We will show the circular polarization property of the fabricated TW-HPA at optical telecommunication wavelengths. We will also show experimental proofs that support the SOI working mechanism of such an antenna.

In Chapter 5, we will mainly explore the application of the developed TW-HPA in controlling the polarization state of light. We will show strongly integrated arrays of point-light emissions of opposite handedness and tunable intensities, as well as a 3D device of subwavelength volume that enables polarization manipulation unreachable with conventional materials. Circular dichroism properties of the TW-HPA will also be shown in this chapter.

My thesis will end with a short summary and perspective chapter.

1

RESEARCH BACKGROUND

The unchanging law of the universe is that everything changes, in a way of time and space. Luckily, in most common cases, we can understand and describe those 4-dimensional movements with basic physical quantities such as energy and momentum. The inherent translation invariance of time and space imposes on such quantities a universal law of conservation, framing any physical dynamic processes [75].

Momenta are physical quantities directly attached to moving objects. According to the specific form of movement, say translational movement and rotational movement, we discriminate linear momentum and angular momentum (AM), respectively. For an object undergoing rotational movement, we have the following relation between its linear and angular momenta[75, 76]:

$$\boldsymbol{L} = \boldsymbol{r} \times \boldsymbol{P}, \tag{1.1}$$

where $\boldsymbol{r}$ is the position vector, $\boldsymbol{L}$ and $\boldsymbol{P}$ are the angular and linear momenta, respectively. From Eq. 1.1, we can see that the angular momentum is transverse to the instantaneous linear momentum associated with the rotational movement.

There exist two types of angular momenta, namely the spin angular momentum (SAM) and orbital angular momentum (OAM). In the classical picture, SAM is associated with the rotating motion of an object around its body axis while OAM refers to the orbiting motion of an object regarding an external reference. We have the following expression for the total angular momentum:

$$\boldsymbol{J} = \boldsymbol{L} + \boldsymbol{S}, \tag{1.2}$$

where $\boldsymbol{J}$, $\boldsymbol{L}$ and $\boldsymbol{S}$ denote the total AM, SAM and OAM, respectively. In nature, the two kinds of angular momenta coexist in many systems. Examples span from huge celestial bodies to invisible electrons. Interestingly, the two kinds of angular momenta can be transferred to each other, coining the term "spin-orbit interaction". Spin-orbit interactions give rise to observable effects in both macroscopic and microscopic regimes. For example, a flying football with spin normally has a curved trajectory due to the lateral force induced by spin-orbit interaction (Magnus effect). As to atoms, it is the spin-orbit interaction of electrons that leads to the fine structure in emission and absorption spectra. With the constraint of angular momentum conservation, we have the selection rule and Zeeman effect for atomic transitions.

Light also carries linear, spin and orbital angular momenta [77]. Poynting first noticed that circularly polarized light carries spin angular momentum. He envisaged an experiment where circularly polarized light pass successively a series of suspending polarizers. He anticipated that, in the course of propagation, light would transfer angular momentum to these polarizers and thus cause a toque to drive them to rotate, which was later demonstrated by Beth in 1936. The orbital angular momentum of light was found by Allen and coworkers in 1992 [78]. They first demonstrated that light with a helical phase structure carries orbital angular momentum, which is integer times of $\hbar$ per photon. They observed the mechanical effect of OAM-carrying light by using cylindrical lens to transform ordinary Hermite-Gaussian mode to OAM-carrying LG mode [77].

Unlike these with macroscopic objects, the optical OAM and SAM correspond to different properties of light[53, 77]. Specifically, the SAM of light is associated with the polarization state, whereas the OAMs are associated with the trajectories and phase structures [55, 77]. The two kinds of optical AMs manifest the polarization and spatial degrees of freedom of light, respectively [55]. Interestingly, the two kinds of optical angular momenta are not independent, they can transfer to each other. This phenomenon is called optical spin-orbit interaction (SOI). Optical SOI has demonstrated a wide spectrum of striking phenomena and appealing applications including optical sensing, information, waveguiding and manipulation [55, 56, 79].

In this chapter, we will first separately introduce the SAM and OAM of the light. We will refer to their formulated expressions and manifestations. Then, we will review the state-of-the-art of optical SOIs as well as their applications.

1.1/ ANGULAR MOMENTA OF LIGHT

Due to the wave-particle duality of light, we can describe optical AMs in both electromagnetic wave and photon pictures. In the former picture, light is treated as time-spatial electromagnetic oscillation over a certain wavelength range. Classical field languages, such as gradient, divergence and curl, are used to describe the generation, propagation of light and its interaction with materials [80]. The energy, linear and angular momenta density (per unit volume) of light can thus be derived by treating those electromagnetic fields. In the latter picture, light is an assembly of energy quanta (photons) and quantum operator language are used to describe light behavior. Energy, linear and angular momenta are the direct outcomes of the corresponding operators, which create a physical view analogous to the description of moving particles [77].

Herein, we will start with the wave picture of light and give a general electromagnetic description of optical angular momenta. Then, we will refer to the polarization and phase structure of several specific light waves and show their links to the spin and orbital angular momenta of light. In these discussions, we will also incorporate the quantum view of light and show its consistency with the classical description.

1.1.1/ CLASSICAL ELECTROMAGNETIC DESCRIPTIONS OF THE OPTICAL AMS

In the context of nano-optics, it is usually sufficient to adopt the wave picture to describe most light behaviors. In this frame, one can use the classical Maxwell's equations to describe optical electromagnetic fields, which take the following differential form in SI units [1]:

$$\begin{aligned}
\nabla \times \boldsymbol{E}(\boldsymbol{r}, t) &= -\frac{\partial \boldsymbol{B}(\boldsymbol{r}, t)}{\partial t} && (1.3)\\
\nabla \times \boldsymbol{H}(\boldsymbol{r}, t) &= \frac{\partial \boldsymbol{D}(\boldsymbol{r}, t)}{\partial t} + \boldsymbol{j}_f(\boldsymbol{r}, t) && (1.4)\\
\nabla \cdot \boldsymbol{D}(\boldsymbol{r}, \boldsymbol{t}) &= \rho(\boldsymbol{r}, t) && (1.5)\\
\nabla \cdot \boldsymbol{B}(\boldsymbol{r}, \boldsymbol{t}) &= 0 && (1.6)
\end{aligned}$$

where the vectors $\boldsymbol{E}$, $\boldsymbol{H}$, $\boldsymbol{D}$, $\boldsymbol{B}$, $\boldsymbol{j}_f$ denote the electric field, the magnetic field, the electric displacement, the magnetic induction and the free current density, respectively. Scalar ρ denotes the free charge density. They are all functions of space coordinate ($\boldsymbol{r}$) and time (t).

In my thesis, all materials considered are linear, isotropic, homogeneous and source free, which obeys the following constituent conditions [1]:

$$\begin{aligned}
\boldsymbol{D} &= \epsilon_r \epsilon_0 \boldsymbol{E} && (1.7)\\
\boldsymbol{B} &= \mu_r \mu_0 \boldsymbol{H} && (1.8)\\
\boldsymbol{j}_c &= \sigma_e \boldsymbol{E} && (1.9)
\end{aligned}$$

Here, ϵ_0 and ϵ is the vacuum and relative permittivities, μ_0 and μ are the vacuum and relative permeabilities, respectively. $\boldsymbol{j}_c$ denotes the inductive current density, σ_e is the conductivity. ϵ, μ and σ_e together describe the response of materials to electromagnetic fields. In the following, we only consider the vacuum case to simplify the illustration of the optical energy and angular momenta.

Poynting first quantified the momentum and energy flux carried with an electromagnetic field. The energy stored in electromagnetic fields per unit volume can be expressed as follows[80]:

$$w = \frac{1}{2}(\boldsymbol{D} \cdot \boldsymbol{E} + \boldsymbol{B} \cdot \boldsymbol{H}) = \frac{1}{2}(\epsilon_0 |\boldsymbol{E}|^2 + \mu_0 |\boldsymbol{H}|^2) \qquad (1.10)$$

Poynting vector, which represents the energy flux density, takes the following form [80]:

$$\mathfrak{S} = \boldsymbol{E} \times \boldsymbol{H} \qquad (1.11)$$

The linear momentum per unit volume associated with an electromagnetic wave can be expressed as follows [77]:

$$\boldsymbol{p} = \epsilon_0 \boldsymbol{E} \times \boldsymbol{B} = \epsilon_0 \mu_0 \mathfrak{S} \qquad (1.12)$$

As shown in Eq. 1.12, the linear momentum per unit volume is proportional to the Poynting vector. Naturally, by substituting Eq. 1.12 into Eq. 1.1, we obtain the angular momentum per unit volume [77]:

$$\boldsymbol{j} = \epsilon_0 \mu_0 [\boldsymbol{r} \times (\boldsymbol{E} \times \boldsymbol{H})] \qquad (1.13)$$

To calculate the total energy, linear and angular momenta, we need to take the volume integral of the quantities given in Eqs. 1.10, 1.12 and 1.13, respectively. We have [77]:

$$
\begin{aligned}
W &= \frac{1}{2}\int(\epsilon_0|\boldsymbol{E}|^2+\mu_0|\boldsymbol{H}|^2)dV &\quad (1.14)\\
\boldsymbol{P} &= \epsilon_0\mu_0\int(\boldsymbol{E}\times\boldsymbol{H})dV &\quad (1.15)\\
\boldsymbol{J} &= \epsilon_0\mu_0\int[\boldsymbol{r}\times(\boldsymbol{E}\times\boldsymbol{H})]dV &\quad (1.16)
\end{aligned}
$$

Monochromatic electromagnetic wave of angular frequency ω can be described by the following time-harmonic functions:

$$
\begin{aligned}
\boldsymbol{E}(\boldsymbol{r},t) &= \Re\mathfrak{e}[\boldsymbol{E}(\boldsymbol{r})e^{-j\omega t}] &\quad (1.17)\\
\boldsymbol{H}(\boldsymbol{r},t) &= \Re\mathfrak{e}[\boldsymbol{H}(\boldsymbol{r})e^{-j\omega t}] &\quad (1.18)\\
& &\quad (1.19)
\end{aligned}
$$

Owing to Maxwell's Equations in vacuum (Eq. 1.5 and 1.6), we have:

$$
\begin{aligned}
\boldsymbol{H}(\boldsymbol{r}) &= \frac{1}{j\mu_0\omega}\nabla\times\boldsymbol{E}(\boldsymbol{r}) &\quad (1.20)\\
\boldsymbol{E}(\boldsymbol{r}) &= \frac{j}{\epsilon_0\omega}\nabla\times\boldsymbol{H}(\boldsymbol{r}) &\quad (1.21)\\
& &\quad (1.22)
\end{aligned}
$$

We can thus rewrite Eq. 1.16 as follows [81]:

$$
\boldsymbol{J} = \frac{\epsilon_0}{2j\omega}\int\left(\sum_{i=x,y,z}E_i\boldsymbol{r}\times\nabla E_i^*\right)dV + \frac{\epsilon_0}{2j\omega}\int(\boldsymbol{E}\times\boldsymbol{E}^*)\,dV = \boldsymbol{L}+\boldsymbol{S} \quad (1.23)
$$

where the first and second items in Eq. 1.23 have been identified as the OAM and SAM of the electromagnetic field, denoted as $\boldsymbol{L}$ and $\boldsymbol{S}$, respectively.

For time-harmonic waves, we usually average these quantities within one oscillation cycle, which read [77, 81]:

$$
\begin{aligned}
\bar{w} &= \frac{1}{4}\left(\epsilon_0|\boldsymbol{E}|^2+\mu_0|\boldsymbol{H}|^2\right) &\quad (1.24)\\
\bar{\boldsymbol{p}} &= \frac{\epsilon_0\mu_0}{2}(\boldsymbol{E}\times\boldsymbol{H}^*) &\quad (1.25)\\
\bar{\boldsymbol{l}} &= -\frac{\epsilon_0}{2\omega}\Im\mathfrak{m}\left(\sum_{i=x,y,z}E_i^*\boldsymbol{r}\times\nabla E_i\right) &\quad (1.26)\\
\bar{\boldsymbol{s}} &= -\frac{\epsilon_0}{2\omega}\Im\mathfrak{m}(\boldsymbol{E}^*\times\boldsymbol{E}) &\quad (1.27)\\
\bar{\boldsymbol{j}} &= \bar{\boldsymbol{l}}+\bar{\boldsymbol{s}} &\quad (1.28)
\end{aligned}
$$

1.1.2/ SPIN ANGULAR MOMENTUM AND POLARIZATION STRUCTURE OF LIGHT

Longitudinal SAM of light The most simple optical wave is the plane wave, whose electric and magnetic fields can be expressed as:

$$\begin{aligned} \boldsymbol{E}(\boldsymbol{r}, t) &= \boldsymbol{E_0} e^{j(\boldsymbol{kr}-\omega t)} \; (\boldsymbol{k} \cdot \boldsymbol{E} = 0) \quad (1.29) \\ \boldsymbol{H}(\boldsymbol{r}, t) &= \boldsymbol{H_0} e^{j(\boldsymbol{kr}-\omega t)} \; (\boldsymbol{k} \cdot \boldsymbol{H} = 0) \quad (1.30) \\ \boldsymbol{H}_0 &= \frac{1}{\mu_0 \omega} \boldsymbol{k} \times \boldsymbol{E}_0 \quad (1.31) \end{aligned}$$

where $\boldsymbol{k}$ is the wave vector, $\boldsymbol{E_0}$ and $\boldsymbol{H_0}$ are constant vectors, which define the polarization structure of light, respectively. For simplicity, let us consider that the plane wave propagates along $+z$ direction, we can thus define $\boldsymbol{E_0}$ as follows:

$$\boldsymbol{E_0} = E_x \hat{\boldsymbol{x}} + E_y \hat{\boldsymbol{y}}, \quad (1.32)$$

E_x and E_y denote the complex amplitude of the electric components along the x and y axis, respectively. To consider the SAM, it is convenient to express the polarization vector $\boldsymbol{E_0}$ in the form of Jones vector [82], which reads:

$$\boldsymbol{E_0} = |\boldsymbol{E_0}| e^{j\phi_x} |\Psi\rangle \quad (1.33)$$

where

$$|\Psi\rangle = \begin{bmatrix} \cos\theta \\ e^{j\Delta\phi} \sin\theta \end{bmatrix} \quad (1.34)$$

is the Jones vector. It gives a normalized expression of the polarization state, with:

$$\begin{aligned} \Delta\phi &= \phi_y - \phi_x \quad (1.35) \\ \tan\theta &= |E_y|/|E_x|, \quad (1.36) \end{aligned}$$

where ϕ_x (ϕ_y) and $|E_x|$ ($|E_y|$) are the phase and amplitude of E_x (E_y), respectively. Let $\theta = \pi/4$ and $\Delta\phi = \sigma\pi/2$ ($\sigma = \pm 1$), we have the two circular polarization (CP) states. Denote the left and right CP (LCP and RCP) states with $|\Psi_L\rangle$ and $|\Psi_R\rangle$, we have:

$$\begin{aligned} |\Psi_R\rangle &= \frac{1}{\sqrt{2}} \begin{bmatrix} 1 \\ +j \end{bmatrix} \quad (1.37) \\ |\Psi_L\rangle &= \frac{1}{\sqrt{2}} \begin{bmatrix} 1 \\ -j \end{bmatrix} \quad (1.38) \end{aligned}$$

For circularly polarized lights, the corresponding spin densities read:

$$\bar{\boldsymbol{s}} = \sigma \frac{\epsilon_0}{2\omega} |\boldsymbol{E_0}|^2 \hat{\boldsymbol{k}} \quad (1.39)$$

The time-averaged energy density can be written as:

$$\bar{w} = \frac{\epsilon_0}{2}|\boldsymbol{E_0}|^2 \tag{1.40}$$

Taking a ratio of Eq. 1.39 to Eq. 1.40, we have:

$$\frac{\bar{\boldsymbol{s}}}{\bar{w}} = \frac{\sigma}{\omega} = \sigma\frac{\hbar\hat{\boldsymbol{k}}}{\hbar\omega} \tag{1.41}$$

Thus, it is clear that circularly polarized light carries an intrinsic SAM of $\hbar$ per photon, which is parallel or anti-parallel to the wave propagation depending on its helicity σ. This is consistent with the quantum description of the SAM of photons.

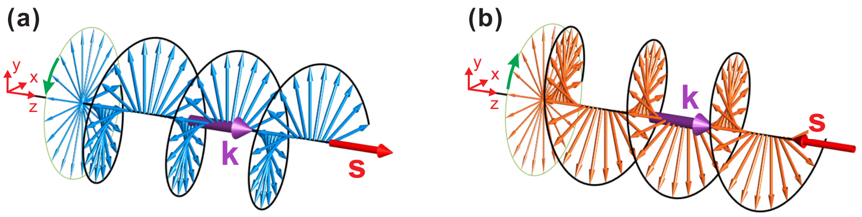

RCP (σ=+1) **LCP (σ=-1)**

Figure 1.1: Schematics of the electric fields of circularly polarized light with: (a) right and (b) left handedness, respectively. The green curved arrows indicate the rotation sense of the electric field in a single transverse plane. σ denotes the helicity of SAM ($\boldsymbol{s}$), which is parallel or anti-parallel to the wave vector $\boldsymbol{k}$.

Figures 1.1 (a) and (b) schematically show the electric fields and SAMs corresponding to the LCP and RCP states, respectively. The direction of the SAM is associated with the rotation sense of the electric field. In a general case, the polarization state of light can be seen as the linear supposition of the two CP states [81]:

$$|\Psi\rangle = \sum_{i=L,\ R} \alpha_i\, |\Psi_i\rangle \tag{1.42}$$

where

$$\alpha_i = \langle\Psi_i|\Psi\rangle \tag{1.43}$$

are the linear coefficients of the two CP components. The according SAM per photon can be calculated as:

$$\frac{\bar{\boldsymbol{s}}}{\bar{w}} = (|\alpha_R|^2 - |\alpha_L|^2)\frac{\hbar\hat{\boldsymbol{k}}}{\hbar\omega} = \bar{\sigma}\frac{\hbar\hat{\boldsymbol{k}}}{\hbar\omega} \tag{1.44}$$

Therefore, we can see that in a general case, the SAM of light is $\bar{\sigma}\hbar$ per photon, where $\bar{\sigma} \in [-1, 1]$ is associated with the proportions of the LCP and RCP components. It is noted that the absolute value of $\bar{\sigma}$ has a direct link to the degree of circular polarization (DOCP), which is defined as follows [46]:

$$DOCP \equiv \frac{|I_{LCP} - I_{RCP}|}{I_{LCP} + I_{RCP}} = \bar{\sigma} \tag{1.45}$$

where I_{LCP} and I_{RCP} are the intensity of the LCP and RCP components, respectively.

Geometric representation of light polarization The polarization state of light can also be presented geometrically with the polarization ellipse and Poincaré sphere.

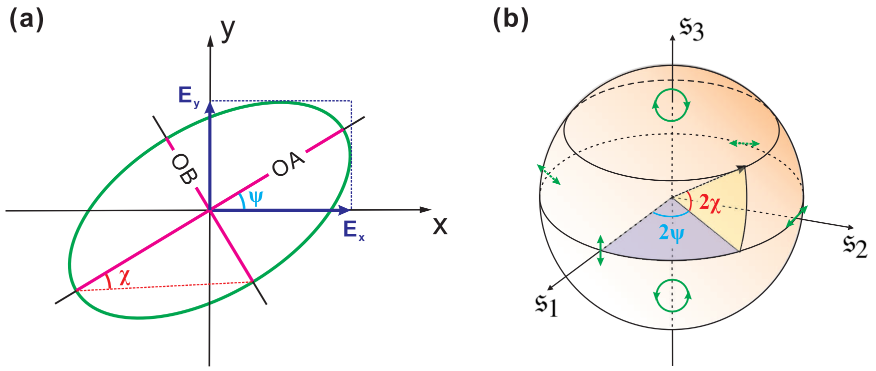

Figure 1.2: Schematic diagrams of (a) polarization ellipse and (b) Poincaré sphere. Note the north and south poles of the Poincaré sphere stand for RCP and LCP, respectively. On the equator of the Poincaré sphere, the corresponding polarization states are linear with the orientation varying with the azimuthal position.

In general, the polarization vector defined by Eqs. 1.32~1.36 describes, by its tip, a tilted ellipse in the plane perpendicular to light propagation (see Fig. 1.2(a)). The major and minor axes of such an ellipse take respectively the following forms [83]:

$$OA = \frac{1}{\sqrt{2}}\left[|E_x|^2 + |E_y|^2 + \sqrt{|E_x|^4 + |E_y|^4 + 2|E_x|^2|E_y|^2\cos(2\Delta\phi)}\right]^{\frac{1}{2}}, \tag{1.46}$$

$$OB = \frac{1}{\sqrt{2}}\left[|E_x|^2 + |E_y|^2 - \sqrt{|E_x|^4 + |E_y|^4 + 2|E_x|^2|E_y|^2\cos(2\Delta\phi)}\right]^{\frac{1}{2}}, \tag{1.47}$$

Axial ratio (AR), which is frequently used to evaluate the ellipticity of the polarization ellipse, reads:

$$AR = \frac{OB}{OA} \tag{1.48}$$

Following simple procedures, we find the following relation between AR and $DOCP$:

$$DOCP = \frac{2AR}{1 + AR^2} \tag{1.49}$$

Poincaré sphere can also be used to represent the polarization state of light, which is a unitary sphere with its Cartesian coordinates $(\mathfrak{s}_1, \mathfrak{s}_2, \mathfrak{s}_3)$ equals to the normalized Stokes parameters[82] (see Fig. 1.2(b)):

$$\mathfrak{s} = \begin{bmatrix} \mathfrak{s}_1 \\ \mathfrak{s}_2 \\ \mathfrak{s}_3 \end{bmatrix} = \frac{1}{\mathcal{S}_0} \begin{bmatrix} \mathcal{S}_1 \\ \mathcal{S}_2 \\ \mathcal{S}_3 \end{bmatrix} \tag{1.50}$$

where $\mathcal{S}_0$, $\mathcal{S}_1$, $\mathcal{S}_2$ and $\mathcal{S}_3$ have the following expressions:

$$\begin{cases} \mathcal{S}_0 = |E_x|^2 + |E_y|^2 \\ \mathcal{S}_1 = |E_x|^2 - |E_y|^2 \\ \mathcal{S}_2 = 2|E_x||E_y| \cos \Delta\phi \\ \mathcal{S}_3 = 2|E_x||E_y| \sin \Delta\phi \end{cases} \tag{1.51}$$

The spherical coordinates $(2\chi, 2\psi)$ of the Poincaré sphere, can be expressed as follows:

$$\begin{cases} 2\chi = \mathrm{atan}(\mathcal{S}_2/\mathcal{S}_1) \\ 2\psi = \mathrm{asin}(\mathcal{S}_3/\mathcal{S}_0) \end{cases} \tag{1.52}$$

where the sign and absolute value of χ defines the handedness and ellipticity of the polarization ellipse. ψ represents the tilt angle of the polarization ellipse, counted from the x axis.

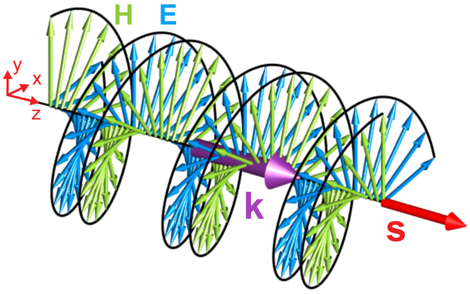

Figure 1.3: Schematic diagram depicting the rotating electric and magnetic fields of a circularly polarized light.

The role of magnetic field and SAM In the above description of the optical SAM, we only consider the electric component field of light. However, for circularly polarized light, both its electric and magnetic fields are spinning (see Fig. 1.3). As suggested, we should also take the magnetic part to consider the total spin density of the light [66]:

$$\boldsymbol{s} = \frac{1}{4\omega} \Im\mathfrak{m} \left[\mu_0 \boldsymbol{H}^* \times \boldsymbol{H} + \epsilon_0 \boldsymbol{E}^* \times \boldsymbol{E} \right] \equiv \boldsymbol{s}_H + \boldsymbol{s}_E \tag{1.53}$$

where the first item $\boldsymbol{s}_H$ and second item $\boldsymbol{s}_E$ denote the magnetic and electric contributions to the spin density of light, respectively.

Transverse SAM of light The SAM of a freely propagating light is aligned with its wave vector, which is thus called "longitudinal SAM". In fact, there also exists another kind of

SAM, which is called "transverse SAM" as it is perpendicular to the wave vector. Transverse SAM is universal in evanescent fields, which dampens spatially along certain directions. Many optical modes contain evanescent fields, such as surface plasmons and various waveguiding modes [55].

Figure 1.4 schematically shows an evanescent field propagating along $+z$ direction, which decays exponentially along the x-axis. The wave vector of such a field can be written as:

$$\boldsymbol{k} = \hat{z}k_z + j\kappa\hat{\boldsymbol{x}} \tag{1.54}$$

where the imaginary item κ describes the field damping along the x-axis. Supposing a transverse magnetic (TM) polarization of the evanescent field, we have the following expressions for its magnetic and electric fields:

$$\boldsymbol{H_0} = \hat{\boldsymbol{y}}H_y \tag{1.55}$$

$$\boldsymbol{E_0} = -\frac{jH_y}{\epsilon_0\omega}(\hat{\boldsymbol{z}}\kappa + \hat{\boldsymbol{x}}jk_z) \tag{1.56}$$

As shown in Eq. 1.56, the electric field contains two components along x and z, which are phase-shifted by $\pi/2$. That means the electric and magnetic fields of a TM-polarized evanescent wave is elliptically and linearly polarized, respectively. Fig. 1.4 (b) schematically shows such a polarization structure. We can see that the electric field rotates in the $x0z$ plane, signifying a SAM along the y axis, perpendicular to the wave propagation.

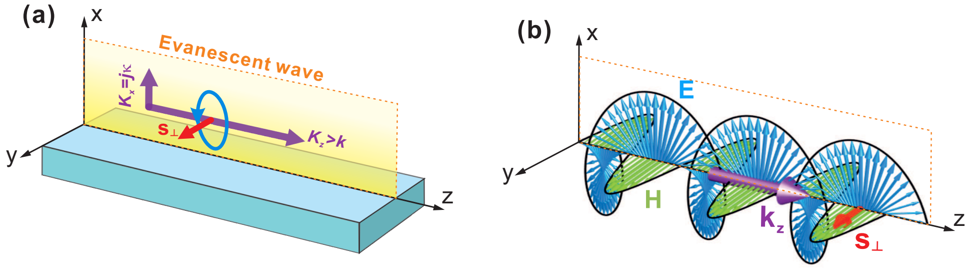

Figure 1.4: Transverse spin angular momentum and optical evanescent fields. (a) Schematic showing the field damping and the corresponding spin angular momentum ($s_\perp$). k_x and k_z are the wave vector projections along the x and z axis, respectively. (b) Polarization structure of a TM-polarized evanescent wave.

For a transverse electric (TE) evanescent mode, it is not trivial to obtain:

$$\boldsymbol{E_0} = \hat{\boldsymbol{y}}E_y \tag{1.57}$$

$$\boldsymbol{H_0} = -\frac{jE_y}{\mu_0\omega}(\hat{\boldsymbol{z}}\kappa + \hat{\boldsymbol{x}}jk_z) \tag{1.58}$$

where we can see that the electric field is linearly polarized whereas the magnetic field becomes elliptically polarized. By further comparing Eqs. 1.58 and 1.56, we can see the x-components have the same ratio of $j\kappa/k$ to the z-components, which signifies an identical spin density independent of the TE or TM polarizations. This point, as suggested by Bliokh, originates from the universal transversality of evanescent fields:

$$\begin{aligned} \boldsymbol{k} \cdot \boldsymbol{E} &= 0\,(TE) && (1.59) \\ \boldsymbol{k} \cdot \boldsymbol{H} &= 0\,(TM) && (1.60) \end{aligned}$$

For the above two evanescent fields, the corresponding transverse SAM has the following universal form [55]:

$$\boldsymbol{S}_{\perp} = \frac{\Re\mathfrak{e}(\boldsymbol{k}) \times \Im\mathfrak{m}(\boldsymbol{k})}{\Re\mathfrak{e}(\boldsymbol{k})^2} \tag{1.61}$$

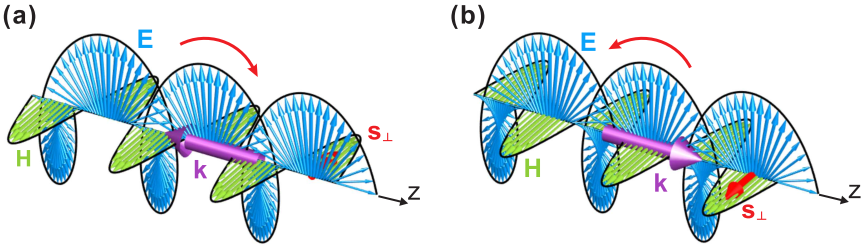

Figure 1.5: Coupling between the helicity of transverse SAM to the propagation direction of evanescent waves: (a) and (b) schematically show TM-polarized evanescent waves propagating to the left (a) and right (b), respectively. This spin-locking phenomenon is akin to that with a rolling wheel, which thus gives optical transverse SAM the name "photonic wheel" [56].

A characteristic of transverse SAM is that its helicity is locked to the propagation direction. As shown in Fig. 1.5, the SAMs conveyed by two anti-propagating evanescent waves point to opposite directions. This can also be evidenced by flipping the sign of k_z in Eq. 1.54:

$$\boldsymbol{k} = -\hat{z}k_z + j\kappa\hat{\boldsymbol{x}} \tag{1.62}$$

Substituting Eq. 1.54 and Eq. 1.62 into Eq. 1.61 leads to SAMs with the opposite signs. Sometimes, the helicity of transverse SAM also depends on the spatial position where the evanescent field resides. For example, on the two sides of a gold slab, evanescent fields decay along the opposite directions. This changes the sign of κ in Eq. 1.54 and thus inverses the sign of transverse SAM.

It is worthy of noting that, transverse spins are not limited to evanescent waves. They also exist elsewhere, even in free space. Transverse SMAs have been found in structured lights like azimuthally polarized Bessel beam [84], two interfering plane waves [85] and focused linearly polarized light [56]. More detailed discussion about these types of transverse spins can be found in literature [86, 87, 88, 89, 90].

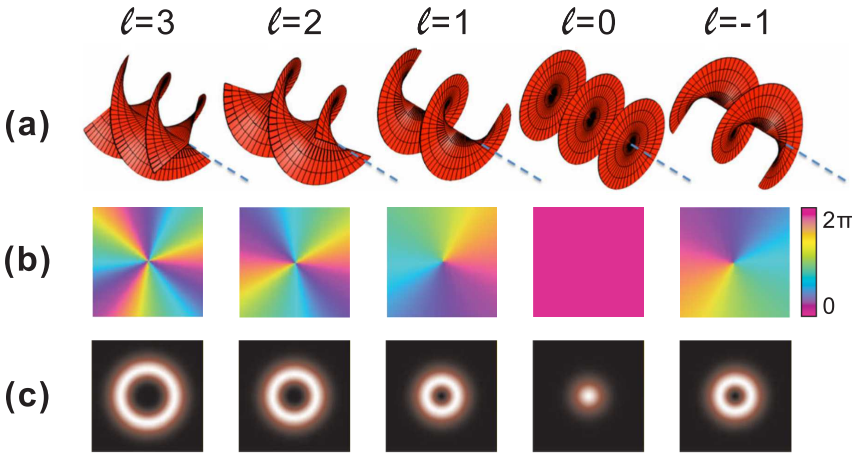

Figure 1.6: Phase and intensity properties of light beams with a vortex charge number $\ell = -1, 0, 1, 2, 3$ (from right to left): (a) Schematic snapshots of the instantaneous phase. Helical phase fronts occurs when $\ell \neq 0$. The blue dash lines indicate the wave propagation. (b) Phase profiles in a transverse plane [91]. (c) Intensity distributions in a transverse plane. Annual intensity patterns can be seen when $\ell \neq 0$.

1.1.3/ ORBITAL ANGULAR MOMENTUM AND PHASE STRUCTURE OF LIGHT

Paraxial beams with an azimuthal phase item $e^{j\ell\phi}$, for example collimated ℓ-th order Laguerre-Gaussian (LG) beams, carry well-defined OAM $\ell\hbar$ per photon[92]. Following Allen and Padget [77, 93], below we will give a brief deduction of OAM from the phase structure of the paraxial beam.

Paraxial wave equation can be written in the following form:

$$j\frac{\partial u}{\partial z} = -\frac{1}{2k}\left(\frac{\partial x^2}{\partial x^2} + \frac{\partial y^2}{\partial y^2}\right)u \tag{1.63}$$

Considering a vector potential $\boldsymbol{A}$ linearly polarized along the x axis, we have:

$$\boldsymbol{A} = u(x, y, z)e^{jkz}\hat{\boldsymbol{x}} \tag{1.64}$$

The corresponding electric and magnetic fields and cycle-averaged linear angular momentum, read:

$$\boldsymbol{E} = \left[u\hat{\boldsymbol{x}} + \frac{j}{k}\frac{\partial u}{\partial y}\hat{\boldsymbol{z}}\right]e^{jkz} \tag{1.65}$$

$$\boldsymbol{H} = \frac{1}{\mu_0}\left[u\hat{\boldsymbol{y}} + \frac{j}{k}\frac{\partial u}{\partial y}\hat{\boldsymbol{z}}\right]e^{jkz} \tag{1.66}$$

$$\bar{\boldsymbol{p}} = \frac{j\omega\epsilon_0}{2}\left(u\nabla u^* - u^*\nabla u\right) + \omega k\epsilon_0|u|^2\hat{\boldsymbol{z}} \tag{1.67}$$

From Eqs. 1.65 and 1.66, we can identify a longitudinal field component, which is critical for acquiring OAMs. Let us assume that $u(x, y, z)$ in Eq. 1.64 takes the following form in cylindrical coordinate frame:

$$u(r,\phi,z) = u_0(r,z)e^{j\ell\phi} \tag{1.68}$$

Taking the product of the position coordinate r and the azimuthal component contained in Eq. 1.67, we have the following expression for the longitudinal AM density ($\bar{j}_z$):

$$\bar{j}_z = \ell\epsilon_0\omega|u|^2 \tag{1.69}$$

The corresponding energy density reads:

$$\bar{w} = \epsilon_0\omega|u|^2 \tag{1.70}$$

Integrating $\bar{j}_z$ and $\bar{w}$ over the xy plane and taking the ratio between the two, we obtain:

$$\frac{\bar{J}_z}{\bar{W}} = \frac{\int\int rdrd\phi\bar{j}_z}{\int\int rdrd\phi\bar{w}} = \frac{\ell\hbar}{\hbar\omega} \tag{1.71}$$

Now we can see that the azimuthal phase item $e^{j\ell\phi}$ describes a quantized OAM $\ell\hbar$ per photon to the paraxial beam, regardless of its linear polarization state.

Figure 1.6 shows the phase structure and intensity property of lights carrying OAM of various ℓ values. When $\ell \neq 0$, the azimuthal phase item $e^{j\ell\phi}$ and the common propagation phase item e^{jk_z}, together, define an intertwined helical phase structure for OAM-carrying light (Fig. 1.6(a)). The topological number of this twist equals to $|\ell|$ while the twist handedness is defined by the sign of ℓ. Due to its vortex-like feature, OAM-carrying light is well-known as "optical vortex". Figure 1.6(b) shows the corresponding phase distributions in the transverse plane. We can see a phase dislocation or phase singularity at the center of the beams when $\ell \neq 0$. Such a phase singularity impart these beams an annular intensity profile as shown in Fig. 1.6(c). The effective radii of these bright rings, are also quantized, proportional to ℓ. [92]

The azimuthal phase item that defines the OAM is linked to the spatial variation of the light intensity and is independent of the polarization structure. Therefore, we can see that the optical SAM and OAM manifest the different degrees of freedom of light.

1.1.4/ EXTRINSIC ORBITAL ANGULAR MOMENTUM AND LIGHT TRAJECTORIES

The aforementioned optical AMs, ie., SAM and OAM, are independent of any external reference. They are only associated with the intrinsic properties of light and thus are called intrinsic optical AMs. In fact, real beams, which are aperture-limited, can also gain an orbital angular momentum when their centroids have a distance with respect to an external reference (see Fig. 1.7). This extrinsic orbital angular momentum (EOAM) of light simply takes the same form as that of a macroscopic object:

$$\boldsymbol{L}^{ext} = \boldsymbol{R} \times \boldsymbol{P} \tag{1.72}$$

Equation 1.72 signifies that the instantaneous EOAM is always transverse to the orbital (canonical) momentum. However, a time-averaged EOAM can sometimes align (longitudinal) to the overall wave propagation. Figure 1.7 (b) shows an example for this situation,

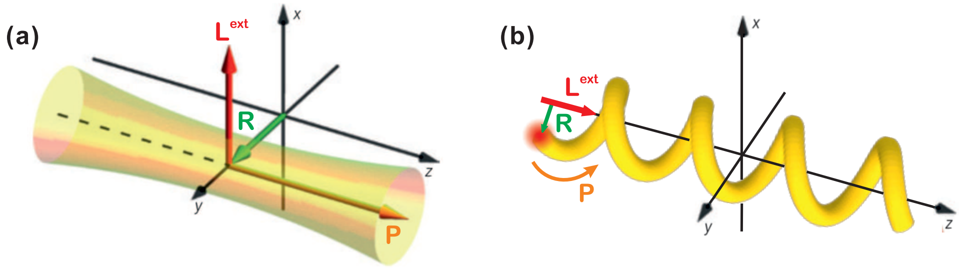

Figure 1.7: Two examples for extrinsic orbital angular momentum (EOAM) of light. (a) Light gains a transverse EOAM when its centroid has a distance with respect to an external reference (z-axis). (b) Light propagates along a helical trajectory, developing an EOAM parallel to z-axis.

where the surface plasmons excited at one end of a gold nanowire swirl along a helical pathway. This case will be discussed in details in later chapters.

1.2/ SPIN-ORBIT INTERACTION OF LIGHT (SOI)

From former discussions, we can see that optical SAM and OAM basically describe different degrees of freedom (DOFs) of light. The former is mainly associated with the polarization state while the latter is linked to the phase structure and trajectory of light. Recent studies reveal that the coupling between the two optical DOFs underpins all basic optical processes, leading to a big family of optical phenomena called spin-orbit interactions (SOIs). SOI is especially striking in the regime of nanooptics, plasmonics and nanophotonics [55]. In these fields, wavelength-scale inhomogeneity generally exists, which greatly enhances the coupling between different optical AMs.

1.2.1/ GENERAL RULES UNDERLYING SOI

1.2.1.1/ ANGULAR MOMENTUM CONSERVATION

In a closed system, total AM ($\boldsymbol{J}^{tot}$) should conserve. For optical processes, contributors of the total AM include the longitudinal and transverse SAMs ($\boldsymbol{S}_{\parallel}$ and $\boldsymbol{S}_{\perp}$), intrinsic and extrinsic OAMs ($\boldsymbol{L}^{int}$ and $\boldsymbol{L}^{ext}$), as well as the AM exchanged between light and matters ($\boldsymbol{J}^{exc}$). We can thus express the total AM as follows:

$$\boldsymbol{J}^{tot} = \boldsymbol{S}_{\parallel} + \boldsymbol{S}_{\perp} + \boldsymbol{L}^{int} + \boldsymbol{L}^{ext} + \boldsymbol{J}^{exc} \tag{1.73}$$

Angular momentum conservation underlies all optical process, laying the most fundamental basis for analyzing optical SOIs [94].

1.2.1.2/ GEOMETRIC PHASE

Geometric phase or Berry phase, found by Micheal Berry, refers to the phase a system acquires while undergoing an adiabatically transformation from one state to another [95, 96]. Geometric phase in optics originates from the coupling between intrinsic angular momentum and the rotation of coordinate frames.

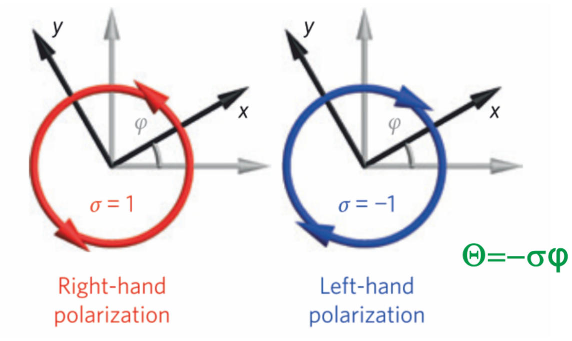

Figure 1.8: Schematic illustrating the geometric phase induced by the rotation of coordinate frames.

Figure 1.8 schematically shows the geometric phase (Θ) induced by rotating coordinate frames. Circular polarization vectors $\boldsymbol{E}_\sigma$ ($\sigma = \pm 1$, $\boldsymbol{E}_{+1} \propto |\Psi_R\rangle$ and $\boldsymbol{E}_{-1} \propto |\Psi_L\rangle$) in the black coordinate frames change to $\boldsymbol{E}'_\sigma$ in the gray ones, which read:

$$\boldsymbol{E}'_\sigma = \begin{bmatrix} \cos\varphi & -\sin\varphi \\ \sin\varphi & \cos\varphi \end{bmatrix} \times \boldsymbol{E}_\sigma = e^{-j\sigma\varphi}\boldsymbol{E}_\sigma, \tag{1.74}$$

where φ is the angle between the two coordinate frames. We can thus identify from Eq. 1.74 an additional phase item:

$$\Theta = -\sigma\varphi \ (\sigma = \pm 1), \tag{1.75}$$

which depends on the helicity of the CP component.

In general, optical geometric phase can be introduced by two approaches: (1) SAM redirection (Rytov-Vladimirskii-Berry phase) and (2) polarization manipulation (Pancharatnam-Berry phase) [97]. Both operations cause an equivalent rotation of the local coordinates frames for CP light components.

Rytov-Vladimirskii-Berry phase relies on the transversality of electromagnetic waves. In free space, light fields are transverse and thus we have:

$$\boldsymbol{k} \cdot \boldsymbol{E}(\boldsymbol{k}) = 0, \tag{1.76}$$

where $\boldsymbol{E}(\boldsymbol{k})$ denotes the polarization vectors of the plane-wave component with a wavevector $\boldsymbol{k}$.

When light is deflected, its wavevector changes, say from $\boldsymbol{k}_1$ to $\boldsymbol{k}_2$. The transversality condition shown in Eq. 1.76 imposes on the polarization vectors of light a parallel transport from $\boldsymbol{E}(\boldsymbol{k}_1)$ to $\boldsymbol{E}(\boldsymbol{k}_2)$ on the $\boldsymbol{k}$-sphere (see Fig. 1.9(a)). In other words, the local coordinate

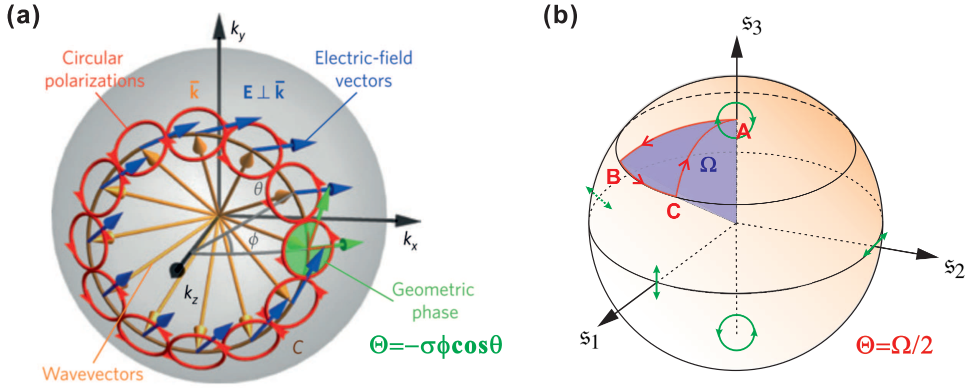

Figure 1.9: Schematics illustrating the optical geometric phases induced by (a) the redirection of wave vectors [55] and (b) the transformation of polarization state on the Poincaré sphere. (a,b) are reproduced from literature [98].

frames attached to the polarization vectors rotates with respect to the global spherical coordinate frame, giving rise to a geometric phase. For example, wavevector variation along a special contour C shown in Fig. 1.9 ($\theta = \theta_0,\ \phi = 0 \rightarrow \phi$) introduces to CP light a helicity-dependent geometric phase, which reads:

$$\Theta = -\sigma\phi\cos\theta_0 = -S_z\phi. \tag{1.77}$$

Here S_z is the SAM projection along the z-axis. Therefore, Eq. 1.75 reveals that the geometric phase caused by wave redirection can be attributed to SAM-rotation coupling.

Pancharatnam-Berry (PB) phase results from the fact that wave plates define the local coordinate frames for light by their anisotropic axes. For example, let us consider a half-wave plate (HWP) whose optical axes have an angle φ with respect the incident polarization vectors E_σ. The transmitted polarization vectors E'_σ can be expressed by [79]:

$$\boldsymbol{E}'_\sigma \propto \boldsymbol{E}_{-\sigma}e^{j2\sigma\varphi}. \tag{1.78}$$

Equation 1.78 shows an additional geometric phase $\Theta = 2\sigma\varphi$, which can be seen as the result of coordinate rotation imposed by the HWP anisotropic axes. Similarly, PB phase can also be introduced by other types of birefringence wave plates[79].

Pancharatnam theorem gives a geometric description of the PB phase induced by polarization transformation. Figure 1.9 (b) shows a cyclic polarization manipulation along the geodesic contour A→B→C on the Poincaré sphere. Pancharatnam theorem says that the geometric phase gained by light, when return to the polarization state A, is equal to half of the solid angle occupied by the geodesic triangle ABC ($\Theta = \Omega/2$) [95].

Geometric phase plays an important role in spin-orbit interactions. Both RVB and PB type geometric phases can lead to observable effects, which accounts for a larger portion of the optical SOI phenomena that have been found.

1.2.2/ VARIOUS SOI PHENOMENA

There are many types of optical SOIs. Insightful and exhaustive reviews on these phenomena can be found in up-to-date literature [53, 54, 56, 55, 57, 79, 88, 99]. Following the framework built by these reviews, we basically sort the optical SOI phenomena into two main categories according to the underlying mechanisms: (1) SOIs that involve geometric phases and (2) SOIs within evanescent waves. The latter, as suggested, are disconnected from the geometric phases [55]. For SOIs of the first kind, we also discriminate these induced by RVB phase (wave redirection) and these by PB phase (space-variant anisotropy) [97]. For each type of SOI, we will show a few representative examples, where we emphasis the role of geometric phases or angular momentum conservation. The related applications will be briefly introduced as well. More specific reviews that are closely related to the topic of my study can be found at the beginning of the following chapters.

1.2.2.1/ SPIN-ORBIT INTERACTION INDUCED BY GEOMETRIC PHASES

SOI in paraxial regime In later 1980s, Chiao and coworkers found that linearly polarized light propagating along a helical pathway, say in a coiled fiber, undergoes a continuous rotation of the polarization orientation [100, 101]. Akin to other well-known polarization-rotation phenomena, such as Faraday effect and optical activity in chiral materials, this rotation actually means that the LCP and RCP light components are dephased during the propagation process. Figure 1.10(a) shows another case where light follows a helical pathway in a glass cylinder [98, 55]. Figure 1.10(b) shows the direct measurement of a splitting effect in the light trajectories between LCP and RCP states. We can see a shift in the beam transverse positions, which accumulates with the turns of the helix. Analogous to the spin-Hall effect of electrons in condensed matters, this effect gains the name “spin-Hall effect (SHE) of light" [55] or historically “optical Magnus effect" [102].

Note here the SHE is induced completely geometrically, which thus provides a direct evidence for Berry phase [55, 100, 101]. Indeed, during the propagation process, the wave vector of light is redirected and follows a close loop in the $\boldsymbol{k}$-space. It thus acquires a helicity-dependent geometric phase. Theoretical analysis of light propagation in index-gradient media indicates that the SAM of light will add a geometric item to wave equation [98, 103]. This item can be seen as a “Lorentz force" induced by the gradient of Berry phase, which leads to the transverse shift of light [55] due to the angular momentum conservation in axis-symmetrical systems. In above examples, light gains an EOAM while following the helical pathway. Therefore, these examples show an interplay between the SAM and EOAM of light.

SHE also manifests itself with a simple optical interface. A specific case is the so-called Imbert-Fedorov effect [54], which refers to the transverse shift of light upon reflection [106, 107] or refraction [104]. Figure 1.10 (c) schematically shows the scenario for the total internal reflection of a RCP light, where we can see that the reflected light has a lateral displacement on the left side of the incidence beam. This phenomenon can also be explained with the geometric phase induced by wavevector redirection [55, 79]. According to angular spectrum theory, real beams can be decomposed into a series of plane waves propagating along different spatial directions [1]. When light beam reflects or refracts at sharp interfaces, these spatial components in general gain different geometric phases, leading to a geometric phase gradient along the transverse direction. As a consequence,

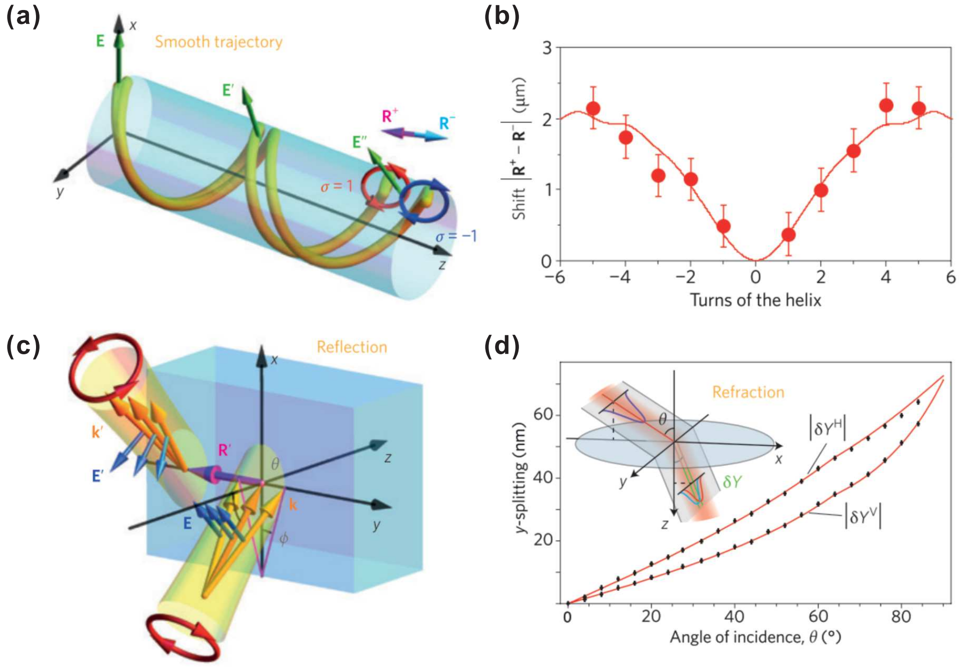

Figure 1.10: Spin-orbit interactions in paraxial regime. Spin-Hall effect occurs when light travels along a helical pathway in a glass cylinder [55, 98]: (a) schematic showing the helicity-dependent trajectories for LCP and RCP lights, and (b) measured transverse splitting of LCP and RCP lights with respect to the propagation distance. Helicity-dependent lateral shift of a paraxial beam occurs while deflecting at optical interfaces [104]: (c) schematic showing the transverse shift attached to a RCP light during reflection. (d) Measured Spin-Hall splitting of the LCP and RCP components when a linearly polarized Gaussian beam refracts at air-glass interface. Angstrom accuracy can be reached with "quantum weak measurement" techniques [104, 105]. (a-d) are grabbed from the literature [55].

the centroid of the emerging light experiences a lateral shift. In the case shown in Fig. 1.10 (c), the relative shift can be quantified as follows [55]:

$$Y' = -\frac{\sigma + \sigma'}{k} \cot\theta \tag{1.79}$$

where σ' and Y' are the helicity and centroid coordinate of the reflected beam. Recently, “quantum weak measurement" has demonstrated its notably high accuracy of a few angstrom, enabling the direct measurement of such a subwavelength shift. Figure 1.10 (d) shows the experimental results corresponding to the scenario shown in Fig. 1.10 (c). We can see that the experimental data have a good match with the curve predicted by SOI theory. This shift, as suggested, is imposed by the angular momentum conservation along the z-axis, again showing an interplay between SAM and EOAM [55]. Similar crosstalk can happen between the intrinsic and extrinsic OAMs that a vortex beam in inhomogeneous medium undergoes a charge number-dependent transverse shift [54]. This kind of SOIs are called "orbit-Hall effect" and "orbit-orbit" interaction of light [55].

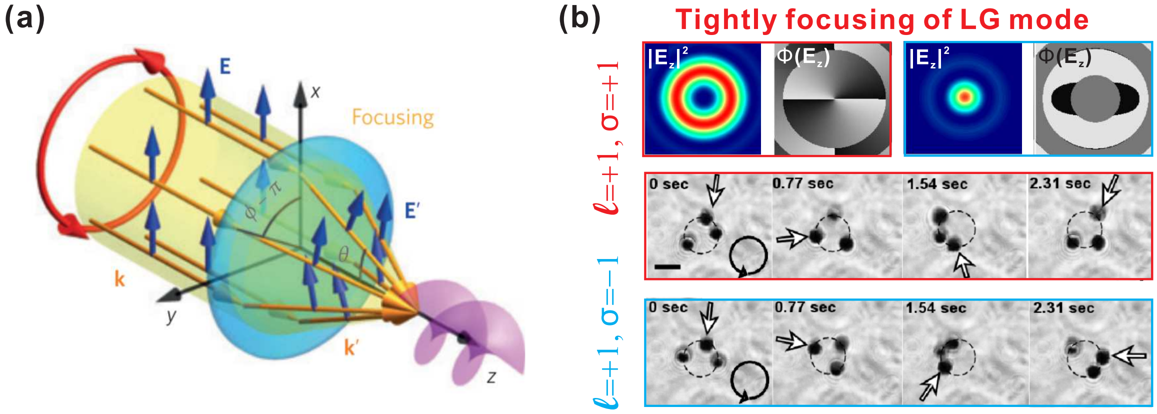

Figure 1.11: Spin-orbit interactions in nonparaxial regime: (a) Schematic showing the optical vortex generated by tightly focusing circularly polarized light [55] (b) Tightly focused LG modes with $\ell = 1$ and $\sigma = \pm 1$. An optical vortex appears in the longitudinal electric component when σ and ℓ have the same sign (top panel), evidenced by a faster orbiting speed of the trapped nanoparticles (middle panel) than that with σ and ℓ of opposite sign (bottom panel) [58].

SOI in nonparaxial regime In the above two cases, it is the redirection of the wave vector that leads to SOI. This suggests that strong SOI effects may appear in nonparaxial fields where light are strongly deflected. Figure 1.11 (a) gives an example of SOI in tight focusing of light with high numerical aperture lens [58, 59]. In 2007, Zhao et al experientially demonstrated this phenomenon by observing the circulating movement of trapped gold nanoparticles, driven by the IOAM of light. They focused helicity-opposite LG_0^1 beams with a $NA/1.3$ objective and found different orbiting speeds in these particles. Specifically, RCP LG_0^1 mode ($\ell = 1,\ \sigma_z = +1$) drives the particles faster than the LCP LG_0^1 mode ($\ell = 1,\ \sigma_z = -1$), as shown in Fig. 1.11 (b). The difference in the orbiting speed of the nanoparticles signifies that the former has a larger IOAM than the latter, which is also caused by SOI: tight focusing converts part of light's SAM into IOAM of the same helicity. By checking the transformation matrix associated with tight focusing, one can see that a helical phase term has been introduced into the longitudinal component during tight focusing. This transferred IOAM, plus the original one carried by the LG_0^1 mode, cause different intensity distributions that depend on the sign of the helicity [58]. Figure 1.11 (b) shows the intensity distributions of the Ez component at focus, the one with ($\ell = 1,\ \sigma_z = -1$) has a null intensity at center while the other ($\ell = 1,\ \sigma_z = +1$) shows a bright spot, as shown in Fig. 1.11 (b).

From the geometric phase perspective, tightly focusing strongly bends the collimated wave in the $\boldsymbol{k}$-space from $\theta \simeq 0$ to $\theta \neq 0$, forming light cones with azimuthal geometric phases. For a circularly polarized light cone with an apex angle θ (see Fig. 1.11 (a)), the SAM and IOAM take the following forms [55]:

$$\boldsymbol{S} = \sigma \cos\theta \hat{z},\ \boldsymbol{L} = [\ell + \sigma(1 - \cos\theta)]\, \hat{z}, \tag{1.80}$$

where we can see a direct AM conversion from SAM to IOAM, fulfilling the total AM conservation $\boldsymbol{L} + \boldsymbol{S} = \sigma + \ell$. A similar case happens when circularly polarized light is scattered by a small particle [108] or reflected by a cone mirror [109]. SOI in nonparallel field may find various potential applications involving particle manipulation and beam shaping [55]. The latter lies in the fact that SOI influences the light intensity distribution of the focal field, which can be controlled by manipulating light polarizations [58].

SOI induced by space-variant media and structures With simple optical interfaces, SHE is generally very weak. It has been demonstrated that this phenomenon can be greatly enhanced with structured surfaces [60, 110]. The underlying mechanism is to engineer the local anisotropy distribution to induce Pancharatnam-Berry phase (PB-phase) gradient [55, 79]. This way, one can introduce a transverse correction to the original wave vector, which suggests a lateral deflection of the wave propagation. On the basis of SOI, periodic x-variant half-wave plate ($\alpha(\boldsymbol{r}_\perp) = \alpha_0 + qx$) can act as a tunable blazed grating whose blazing effect is reversible with the helicity of the incident light (see Fig. 1.12 (a)) [110]. If the space-variation is a function of the azimuthal angle (ϕ), say $\alpha(\boldsymbol{r}_\perp) = \alpha_0 + q\phi$, $q = 0, \pm 1/2, \pm 1...$, we will induce a helical phase in the transmitted light with the topological charge defined as $\ell' = 2\sigma q$. Fig. 1.12 (b) shows the cases with q from $1/2$ to 2, where a RCP light is transformed into optical vortices with ℓ' from 1 to 4, respectively [60]. As a flexible way to generate vortex beam with an arbitrary charge number, the concept of "q-plate" arises from the SOI-enabled manipulation of light. Especially when $q = 1$, we have a AM conservation held between the incident light and the emerging vortex beam: $\sigma = \sigma' + \ell'$. With other q values, however, this simple AM conservation is not valid. That is because the corresponding structures are not axis-symmetrical and thus lead to an AM exchange with matter. [55].

The space-variant anisotropy can be engineered in many ways. In the two examples described above, subwavelength quasi-periodic grooves are used, which behave like a space-variant uniaxial crystal with the optical axes parallel or perpendicular to the subwavelength grooves [60, 110]. Besides, we can use nematic liquid crystal molecules to define the local anisotropy, in forms of 2D pixel array [113] or even a single droplet [61] (see Fig. 1.12 (c)). Similar functions have been realized with metasurface and planar metamaterials, which are formed by orderly arranging plasmonic or dielectric nanostructures of different orientations in a subwavelength lattice (see Fig. 1.12 (d)). Metamaterials offer a great flexibility in defining the geometrical phase and anisotropy by tailoring the constituent elements. With metamaterials, giant helicity-dependent splitting has been observed in free space light [41, 114, 115, 116] and in confined light modes such as surface plasmons [47].

It is also possible to generate PB-phase with structures of reduced complexity. For example, high-order optical vortices have been demonstrated with topological closed-path nano-slits [63] (see Fig. 1.12 (e)) and chains of plasmonic apertures with spatial-variant orientations [62] (see Fig. 1.12 (f)). Recent works from our group demonstrate the unidirectional waveguiding of slot surface plasmon modes [112, 117] (see Fig. 1.12 (a)). Such an operation is realized by using a simple arc-shape nano slot to mediate the SOI between the SAM of the incident light and the EOAM of the emerging guided mode.

1.2.2.2/ SPIN-ORBIT INTERACTION WITH EVANESCENT WAVES

In 2012, Lee et al. first demonstrated that circularly polarized light impinging on a subwavelength groove develops a helicity-dependent unidirectional excitation of surface plasmons [122]. Almost during the same period, Zayats' group separately reported a similar

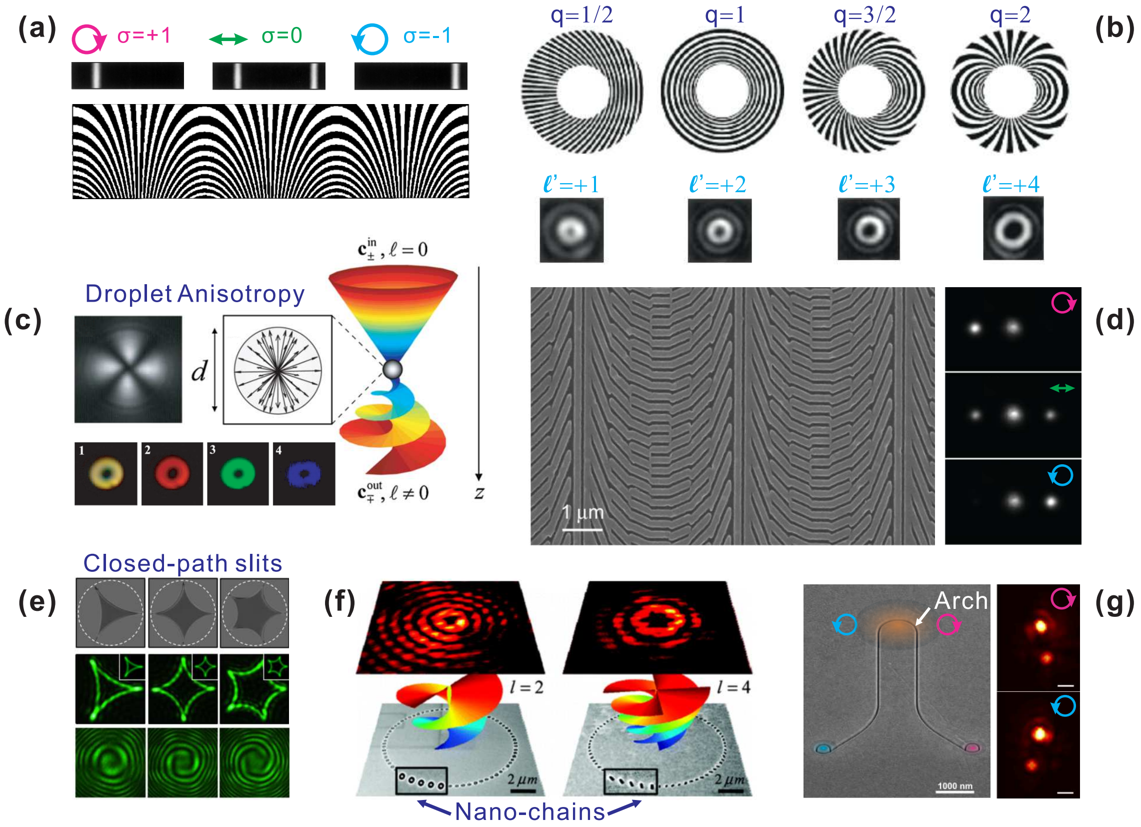

Figure 1.12: Spin-orbit interactions due to Pancharatnam-Berry (PB) phase. Space-variant wave plates induce (a) linear [110] and (b) azimuthal PB phase gradients, leading to a helicity-dependent light splitting and optical vortices with charge numbers $\ell' = 2q$, respectively. (c) Polychromatic optical vortex generation with a single nematic liquid crystal droplet whose anisotropy directs radially in three dimensions. The numbered photos show the intensity profile of the polychromatic vortex and its RGB components, respectively. [61] (d) A 100-nm thick silicon metamaterial splits lights of opposite handedness [111]. (e) Closed-path nano-slits convert CP light into optical vortices, with the charge number defined by the number of slit loops. [63] (f) Chains of plasmonic nano-structures generate vortex beams of various orders [62]. (g) A simple subwavelength arch leads to tunable helicity-controlled directional excitation of nanoscale surface plasmons. The orange, blue and pink halos indicate the positions of incident light and those from the right and left nanoantenna out-couplers, respectively. [112]

phenomenon. Figures 1.13 (a) and (b) show the simulated scenarios of a single spinning electric dipole and its interaction with surface plasmons, respectively [68]. We can see from Fig. 1.13(b) that the emerging surface plasmon mode propagates mostly on the left side with a high directionality. Figure 1.13(c) shows a schematic diagram of the experimental setup they used to demonstrate this phenomenon, where a subwavelength groove under the illumination of circularly polarized light at grazing incidence is utilized to model the spinning electric dipole. The intensities of the SPs excited on the two sides of the groove show a clear dependence on the helicity of the incidence light (see Fig. 1.13(d)).

In these early works, the unidirectional propagation of surface plasmons was explained as a near-field interference effect [68, 122], which later was recognized as a SOI effect [69].

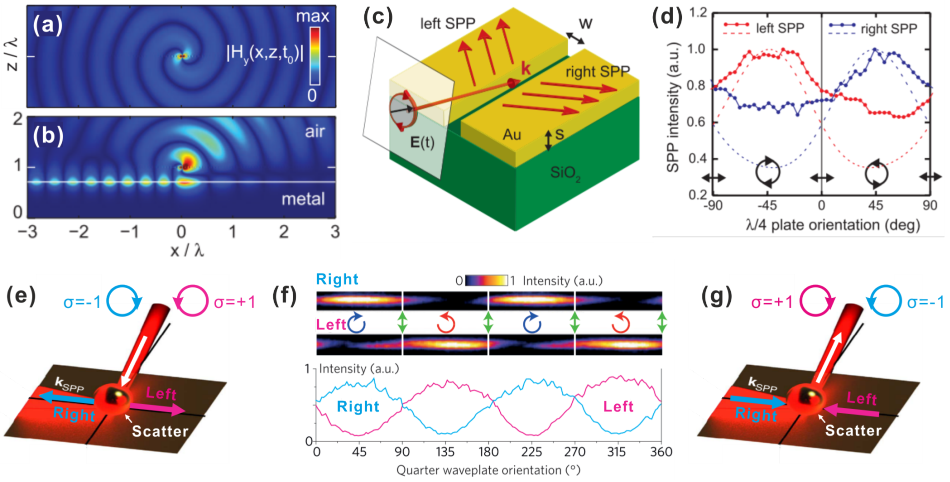

Figure 1.13: Spin-locked unidirectional excitation of surface plasmons (SPs). (a,b) Simulation snapshots of the transverse magnetic component of a spinning electric dipole (a) in air and (b) coupled to surface plasmons [118]. (c,d) Experimental demonstration of the spin-locked directional launching of surface plasmons with a subwavelength groove: (c) schematic of the experimental setup and (d) measured coupling ratios of the left and right SPs (solid lines), in comparison with simulation results (dash lines) [118]. (e-g) Unidirectional light-SP coupling mediated by a gold nanoparticle: (e) schematic for the light-to-SP coupling process, (f) measured left and right SP intensities with respect to the polarization state of the incident light and (g) schematic of the reciprocal SP-to-light coupling process. The scattered light shows a tunable helicity, depending on the direction at which the SP encounters the nanoparticle. [69]

Indeed, during the energy coupling process, the longitudinal spin carried by the incident light field matches the transverse spin of surface plasmons so that a spin-spin coupling can be accomplished [55]. Therefore, the transverse SAM, which is locked to the propagation direction [68], dictates that only one side can be excited with preference with elliptic polarizations. Note this spin-locked directionality is completely intrinsic, different from the case shown previously where certain types of space-variant coupler is necessary. Given the presence of evanescent field, this phenomenon happens universally, regardless of the type of coupler or interface. Moreover, near-unity directionality has been observed in various evanescent-mode systems [69, 72, 119, 120, 121], showing the strong robustness of this phenomenon [55].

By replacing the groove coupler with a gold nanoparticle, a higher directionality has been observed, as shown in Fig. 1.13(f) [69]. The reciprocal process has also been demonstrated (Fig. 1.13(g)) that surface plasmons encountering the scatterer at different angles lead to scattered light of different helicities.

The spin-locking concept soon extended to nano-fibers [70, 120] and photonic crystal waveguides [72, 73]. With dielectric waveguides, the helicity of transverse spin is locked not only to the propagation direction of waveguiding mode but also to the lateral position regarding the waveguide (see Fig. 1.14 (a)). When a point-like light source is placed in close proximity to, or inside the waveguide, both the position and helicity of the emitter will influence the propagation direction of the light coupled into the waveguide, in a predictable way (see Fig. 1.14 (a)). The point-like light source can be a scattering nanoparticle [120],

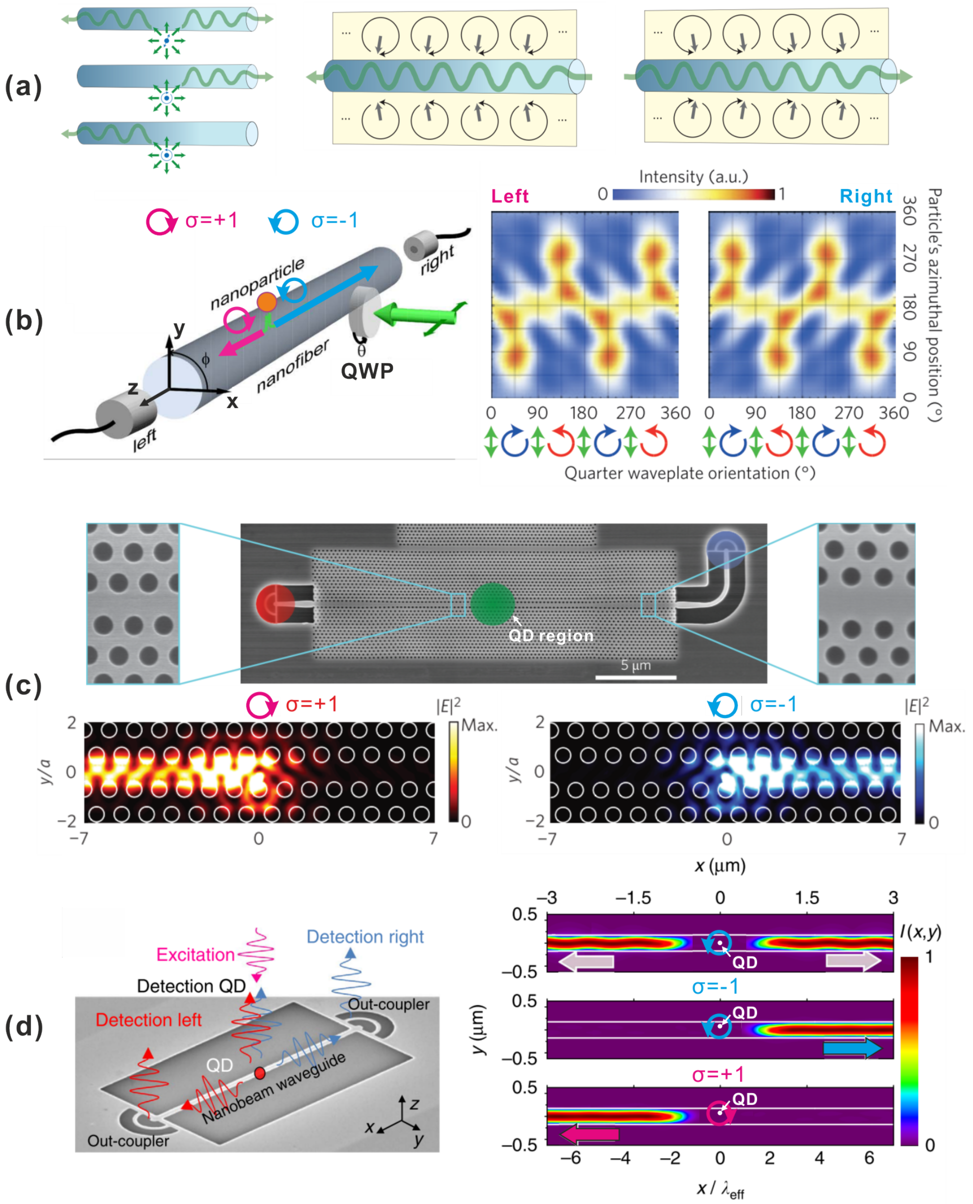
(a)
(b)
σ=+1
σ=-1
nanoparticle
right
y
z
x
ϕ
θ
nanofiber
QWP
left
Left
Intensity (a.u.)
0
1
Right
Particle's azimuthal position (°)
0 90 180 270 360
Quarter waveplate orientation (°)
(c)
QD region
5 μm
|E|^2
Max.
0
y/a
2
0
−2
−7
0
7
x (μm)
(d)
Excitation
Detection right
Detection QD
Detection left
Out-coupler
QD
Nanobeam waveguide
z
x
y
−3 −1.5 0 1.5 3
0.5
−0.5
y (μm)
I(x,y)
1
0
QD
σ=−1
σ=+1
−6 −4 −2 0 2 4 6
x / λ_{eff}

Figure 1.14: (a) Schematics of the helicity-dependent unidirectional light coupling from a local emitter to an optical waveguide (left panel). The right two panels show that the helicity of the transverse spin depends on both the propagation direction of the waveguide mode and the azimuthal position regarding the waveguide. [119] (b) A spin-locking architecture built by attaching a scattering nanoparticle to a nano fiber. Both the polarization state of the illumination (green arrow) and the azimuthal position of the scatterer are controlled separately, which lead to a tuning ratio of energies coupled to the left and right sides of the nanofiber. [120] (c) Quantum dot zone inside a photonic crystal waveguide that is engineered to be asymmetric (glided plane-waveguide), allowing one-way propagation of helicity-opposite photons. [72] (d) QD embedded in a symmetric suspended waveguide, the directionality shows a dependence on the lateral position of the QD in the waveguide. [121]

a quantum dot [72, 121], a near-field probe [73] and extremely individual atoms [70], while the waveguide can be engineered to have a symmetric [70, 73, 121] or asymmetric [72] transmission property. Examples with scattering nanoparticle [120] and quantum dots [56, 72] are shown in Figs. 1.14 (b), (c) and (d), respectively. The purpose here is to sort photons of different spin states [73], which holds the promise for integrated quantum optics [72, 73, 120]. These photon spin states can be created, for example, by locally applying magnetic field to induce the Zeeman splitting [72].

Transverse SAM of light is not limited to waveguiding usage. Recent studies also indicate its perspectives in optical probing and manipulation. It has been demonstrated by Leuchs' group that the interplay between a nanoparticle and the transverse spin density allows us to extract rich information associated from focused waves and evanescent fields [56, 64, 65, 66, 67]. An on-chip silicon micro-disk has been demonstrated to resolve the light handedness of elliptically polarized light [123]. In addition, under the illumination of polarized light, a nanoparticle coupled to waveguide basically develops asymmetric guided modes on its two side, which imposes a lateral force exited on the nanoparticle [89, 124, 125, 126, 127]. This has been proposed to sort chiral particles [128] and to translate nanoparticles by controlling the polarization of incident light [126].

1.3/ CONCLUSIONS

We have shown the different main types of optical angular momenta and their relationship with the polarization, phase and propagation trajectory of light. From a general viewpoint, the SAM and OAM manifest the spatial and polarization degrees of freedom of light, respectively. Under the context of nanooptics and plasmonics, their coupling commonly exists, which gives rise to many new phenomena and applications. Under the framework of geometric phase and angular momentum conservation, we have tried to give a concise but exhaustive review of existing studies on SOI.

My thesis devotes to two new aspects in SOI. The first part (Chapter 2) will be focused on demonstrating the magnetic spin-locking phenomenon in Bloch surface waves. The rest part (Chapters 3-5) shows the new concept of traveling-wave helical plasmonic antenna developed on basis of an inverse SOI process. Our results show that such an antenna helps gain a deterministic and tunable control over light polarizations at the subwavelength scale.

2

MAGNETIC SPIN-ORBIT INTERACTION STEERS BLOCH SURFACE WAVES

The magnetic field of light is often considered as the negligible contributor in light-matter interaction. Recently, with the advent of left-handed metamaterials [129, 130, 131, 132], this hidden role has been revealed in resonant plasmonics and nano-photonics. Those magnetic resonances in nano-structures have been used to achieve negative refractive index [132], to control magnetic transitions in matter [133, 134, 135], to map optical magnetic fields [136, 137, 138, 139, 140, 141] and to study magnetic effects at optical frequencies [142, 143, 144]. In this chapter, we will show a new manifestation of the optical magnetic field. The spin-orbit interaction can control the light coupling into optical waves even without magnetic resonances on nano-structures.

As discussed before, light can carry both spin and orbital angular momenta [78], which are not independent quantities [55]. The two kinds of angular momenta can be coupled when light is confined [55]. Such a spin-orbit interaction (SOI) has recently demonstrated its remarkable property of controlling the propagation direction of optical guided modes, such as surface plasmons, fiber and waveguide modes, leading to the concept of spin-controlled unidirectional waveguiding [47, 68, 71, 73, 112, 114, 117, 122, 123, 145, 146]. Spin-controlled unidirectional waveguiding relies on the transverse SAM arising in evanescent waves [86, 147, 148, 149]. With the help of a subwavelength (dipole) coupler, the longitudinal SAM of the free-space light can be transferred to the transverse SAM of the evanescent tail of guided modes, leading to a spin-directional effect [68, 71, 122]. This effect has a near-100% directionality and works at any interface that supports the evanescent-tail of a guided mode, showing its robustness [55].

In the above studies, evanescent-tail modes, e.g. surface plasmons and the guided mode of a nanofiber, are TM-polarized and thus the corresponding transverse SAMs is defined by the rotating electric field. Therefore, it is the electric component of light that plays as the photon source to originate the transverse spin-direction coupling [68, 147, 148], endowing those SOIs a distinct "electric" characteristic. In fact, the spin density of light is usually defined by both the rotating electric and magnetic optical fields [86, 65, 89]. Therefore, the rotating magnetic field of light should also be capable of contributing to the SAM for SOIs. Here, we call the SOI of this kind as "magnetic spin-orbit interaction (magnetic SOI)" to stress their difference from those via the electric field of light. A recent theoretical work shows that, a spinning magnetic dipole can excite an unidirectional optical mode on magnetic materials that possess a complex permeability (see Fig. 2.1) [150]. This is exactly the magnetic counterpart of the unidirectional excitation of surface plasmons by

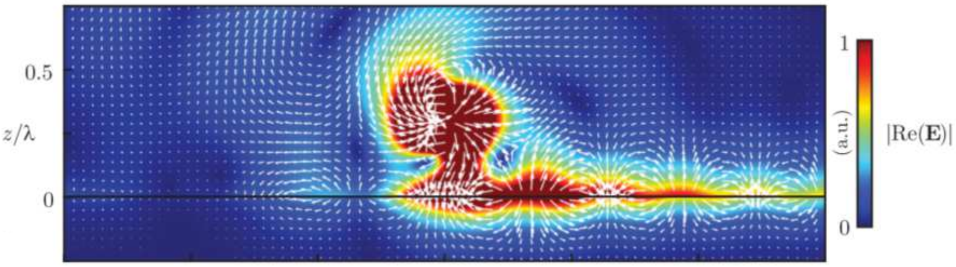

Figure 2.1: Electromagnetic field induced by a circularly polarized magnetic dipole in close proximity to an interface of a material with $\mu = -1.5 + 0.2j$, $(j = \sqrt{-1})$ and $\epsilon = 1$. The color map represents amplitude, and white arrows represent the direction of instantaneous magnetic field. [150]

a spinning electric dipole. It is noted that, however, this μ−negative material dose not exist with bulk materials at optical wavelengths and thus is non-realistic for experimental demonstration. Alternatively, we turn to Bloch surface waves, which enable us to both theoretically and experimentally demonstrate the magnetic SOI.

Bloch surface waves (BSWs) are optical modes propagating at the free surface of one-dimensional photonic crystals (1D PC), which are formed by periodically stacked pairs of dielectric layers with different refractive indices [151, 152, 153, 154]. BSWs benefit from both high field confinement and low propagation losses, holding promise for various applications in integrated optics [155], optical sensing [156], particle trapping and transporting [157, 158]. Importantly, BSWs can be TE- or TM-polarized by tailoring the constitutive materials and layer thicknesses of the 1D PC [159]. Importantly, when the BSW is TE-polarized, its evanescent tail in the surrounding medium is described by a rotating magnetic field. We take advantage of this polarization property of TE-polarized BSWs to introduce the concept of spin-direction locking mediated solely by a rotating magnetic field.

In this chapter, we will at first show the polarization property of a 1D PC that solely supports TE-polarized BSWs at a wavelength of $1.55\ \mu$m. Then, we will numerically show that the tunable unidirectional excitation of the TE-polarized BSWs can be realized using a spinning magnetic dipole source (MD), experimentally demonstrating that the rotating magnetic field of a BSW carries SAM. At last, we will study the light coupling in BSWs by projecting polarized light onto a subwavelength groove, which is used as the light-to-BSW converter. With this configuration, we observe that the directionality of the incoupled light is helicity-dependent. From the intrinsic spin properties of TE-polarized evanescent waves and an analytical model for the coupling. We infer that the resulting spin-controlled directional coupling is mediated by the magnetic optical field, thus revealing a magnetic SOI for light. Despite the electric dipole (ED) nature of the subwavelength groove, this magnetic optical effect is found to be of the same order of magnitude of the electric effects involved in the coupling process. It is noteworthy that such a magnetic SOI is intrinsic to optics; it is not related to a magnetic SOI in matter controlled by a static magnetic field [160].

2.1/ Transverse spin in the magnetic field of TE-polarized Bloch surface waves

It is well known that in a natural crystal, orderly arranged atoms exert periodic potential fields to the motion of electrons, which finally lead to electronic band gaps. Likewise, the periodic arrangement of dissimilar optical materials can form periodic boundary conditions for light and develop photonic band gaps. Bloch surface waves work within the photonic band gaps. In this case, light can not penetrate the 1D Photonic crystal and thus is confined at the free surface.

The 1D PC design work was accomplished by my colleague Tatiana Kovalevich, where she followed the impedance approach [153, 158]. This method treats the electromagnetic properties of optical material with "characteristic impedance", analogue to that used in electronic transmission line theory [159]. Then, this characteristic impedance is used to calculate Fresnel coefficients associated with reflection and transmission. By applying continuity condition of the tangent electromagnetic components at each interface, we can derive the dispersion relation and field profile for the BSW modes. Here, silicon dioxide and silicon nitride are chosen as the constituent materials for the 1D PC. At optical telecom wavelength ($\lambda = 1.55$ μm), their refractive indices are 1.45 and 1.79, respectively. The design goal is to reach, at the free surface of the 1D PC, a purely TE-polarized BSW mode at $\lambda = 1.55$ μm (TM or TM-like modes do not exist). For this purpose, we first optimize the thickness of the two material layers to reach the maximum extinction per layer. Then, we optimize the total number of pairs in the 1D PC to reach the minimum total reflectance. More details about the design and optimization process can be found in literature [158, 159].

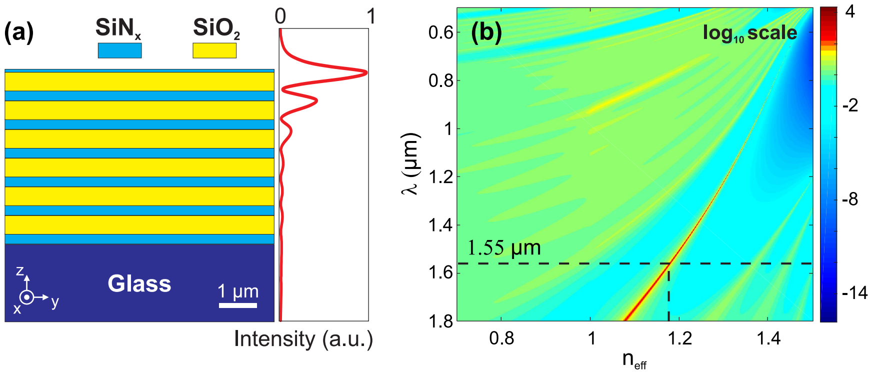

Figure 2.2: Design of the 1D photonic crystal (1D PC). (a) Schematic diagram for the 1D PC structure and corresponding field intensity distribution across the 1D PC (at a wavelength of 1.55 μm). (b) Dispersion diagram of the 1D PC with a log-scale color bar. The structure generates a photonic band gap at the middle of which a BSW dispersion curve is observed.

Figure 2.2(a) shows a schematic diagram of the final design of the 1D PC. As shown, the photonic crystal consists of a stack of 6 pairs of silicon dioxide and silicon nitride layers, whose thicknesses are 492 nm and 263 nm, respectively. The multilayer lies on a glass substrate (refractive index of 1.5) and is covered with a thin 80-nm-thick layer of silicon nitride. The red curve on the right side of Fig. 2.2 (a) shows the intensity profile of the BSW mode. We can see the BSW mode is mainly confined at the free surface of the 1D

PC. There also exists some decaying optical fields within the 1D PC. Figure 2.2 (b) shows the dispersion diagram of the structure. This diagram shows a photonic bandgap, within which we can see the dispersion curve for a BSW mode. Given the above 1D PC design, this surface mode is TE-polarized.

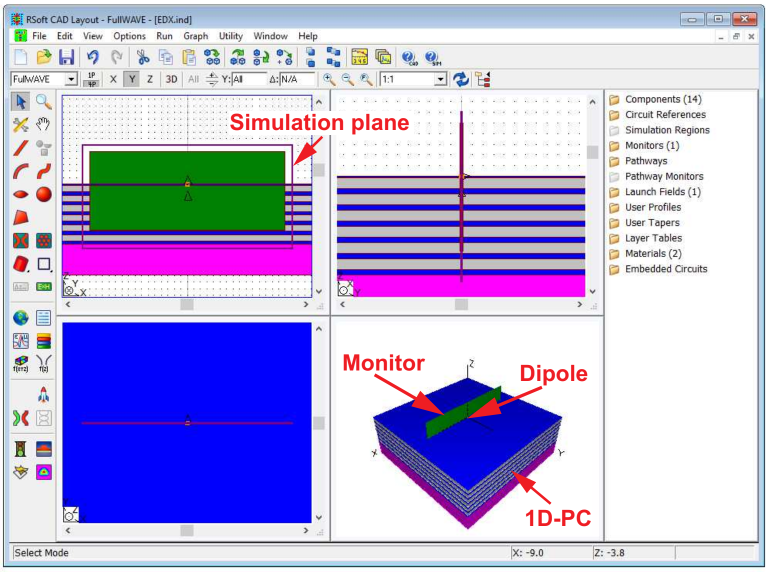
RSoft CAD Layout - FullWAVE - [EDX.ind]
File
Edit
View
Options
Run
Graph
Utility
Window
Help
FullWAVE
1P
4P
X
Y
Z
3D
All
Y: All
Δ: N/A
1:1
Components (14)
Circuit References
Simulation Regions
Monitors (1)
Pathways
Pathway Monitors
Launch Fields (1)
User Profiles
User Tapers
Layer Tables
Materials (2)
Embedded Circuits
Simulation plane
Monitor
Dipole
1D-PC
Select Mode
X: -9.0
Z: -3.8

Figure 2.3: Screen print of the 3D FDTD model built in Rsoft Fullwave for simulating the scenarios of BSW mode excitation with various electric dipole sources. Here, we show the case of an electric dipole oriented along x−axis.

To demonstrate the polarization property of the BSWs, we numerically study the dipole-to-BSW near-field coupling with a rigorous numerical method (Finite Difference Time Domain algorithm [161], FDTD). These simulations are carried out with commercial softwares (Fullwave and Lumerical). Figure 2.3 shows a screen print of the simulation model built with Fullwave, where an x−orientated electric dipole (ED) is positioned 10 nm above the top surface of the 1D PC to excite the BSWs. The ED radiates in continuous regime, at a wavelength of 1.55 μm. As shown in Fig. 2.3, the FDTD model consists of an area about the dipole spanning ± 9 μm along the y direction and ± 5.5 μm along the z direction. The system is invariant along the y direction. The 1D PC design follows what has been described before. All four boundaries for the computation volume are terminated with perfectly matched layers to avoid parasitic unphysical reflections around the structure. The grid resolution is 10 nm. All electromagnetic fields across the structure are recorded with a plane monitor.

The x−orientated ED excites two symmetric BSWs that propagate to the left and right sides of the dipole source. Figures 2.4 (a) and (b) show the snapshots of the real parts of the transverse electric component (E_y) and magnetic component (H_y) of the BSW propagating along the right side. As shown, the former is universally null while the latter has a non-zero distribution.

Figures 2.4 (c) and (d) show the snapshots of the two corresponding in-plane magnetic components of the BSW mode. As shown, they have a comparable amplitude and a relative phase shift of $\pi/2$. That means the magnetic field of the BSW here is elliptically polarized, indicating that the designed 1D PC supports TE-polarized BSW modes. The

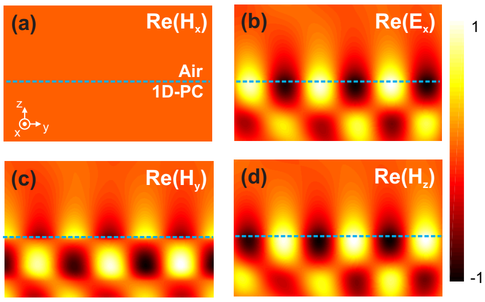

Figure 2.4: Simulation of the electromagnetic field of the BSW mode: (a) and (b) real part of the magnetic and electric field components H_x and E_x, respectively. (c) and (d) real part of the in-plane magnetic field components H_y and H_z, respectively.

magnetic field rotates within the propagation plane (y, z) and thus conveys a transverse SAM along $(0x)$. This transverse SAM originates from the inherent transversality condition of evanescent waves [55]. As a contrast, the electric field is linearly polarized, and thus carry no SAM.

Further, we deduce the expression of the magnetic field of the BSW propagating to the left side ($\boldsymbol{H}^l_{BSW}$) and right side ($\boldsymbol{H}^l_{BSW}$) and find that:

$$\boldsymbol{H}^l_{BSW} \propto (0.53\hat{\boldsymbol{y}} + j\hat{\boldsymbol{z}}) \tag{2.1}$$

$$\boldsymbol{H}^r_{BSW} \propto (0.53\hat{\boldsymbol{y}} - j\hat{\boldsymbol{z}}), \tag{2.2}$$

where $\hat{\boldsymbol{y}}$ and $\hat{\boldsymbol{z}}$ are the unit vectors along y and z axis, respectively. Figures 2.5 (a) and (b) show the schematic diagram of the electromagnetic fields of the TE-polarized BSWs drawn according to Eq. 2.1 and 2.2. As can be seen from Fig. 2.5 (a) and (b), in the local coordinate frames attached to the left- and right BSWs, the magnetic field rotate consistently from the wave vector direction to the surface normal direction. That means in global coordinate frames (x, y, z), the rotation senses of the two magnetic fields are opposite.

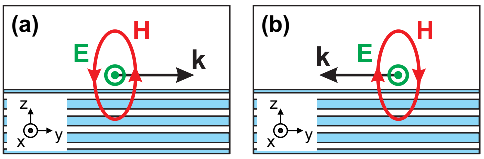

Figure 2.5: Schematic diagram of the polarization of TE-polarized BSWs. (a) and (b) correspond to BSWs propagating toward the right and left directions, respectively.

To conclude, there exists an intrinsic helicity in the magnetic field of TE-polarized BSWs, whose sign depends on the propagation direction of the BSW in global coordinate frame (x, y, z). According to this observation, we expect a differential response between the left and right BSWs to external sources that also possess helicity in the magnetic field. Besides, as the BSW electric field is linearly polarized and shows no helicity, any helicity-dependent phenomenon should solely originate from the magnetic field.

2.2/ UNIDIRECTIONAL EXCITATION OF BLOCH SURFACE WAVES BY ELECTRIC AND MAGNETIC DIPOLES

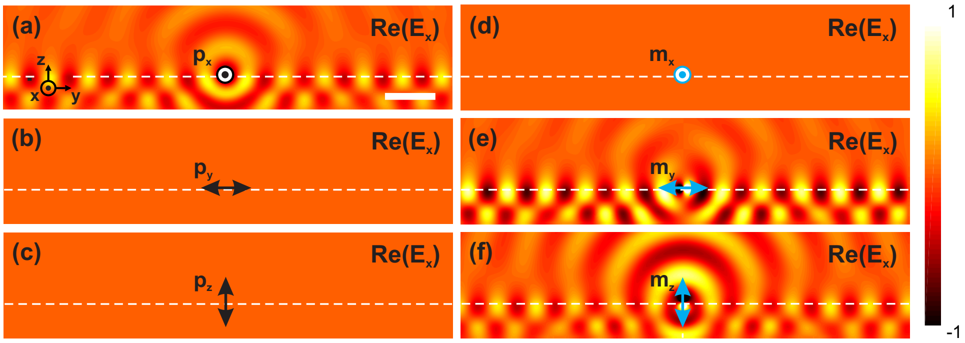

Figure 2.6: Real part of the electric field (Ex) of the TE-polarized Bloch surface wave excited with various dipole sources. (a), (b) and (c) are obtained with an electric dipole oriented along the x, y and z axis, respectively. (d), (e) and (f) are obtained with a magnetic dipole oriented along the x, y and z axis, respectively.

TE-polarized BSWs can be excited by electric and magnetic dipole sources. Figures 2.6 (a~f) show the simulated distribution of BSW electric field (Ex) under the excitation by linear ED and MD sources orientated along x, y and z axis. As shown in 2.6 (a), (e) and (f), BSWs have been successfully excited on both sides of the source, with an ED along x axis and MDs orientated along y and z axis. As a contrast, a MD along x axis, or EDs along y and z axis leads to zero excitation, as shown in Figs. 2.6 (b~d).

As can also be seen from Figs. 2.6 (a), (e) and (f), the BSWs excited on the two sides of the point-like sources show different symmetry behaviors, which are dictated by the parity of the dipole sources. When the dipole source has an even-parity, i.e. the x-oriented ED or z-oriented MD, the BSWs are symmetric as shown in Figs. 2.6 (a) and (f). An anti-symmetric field occurs when the dipole source has an odd-parity, i.e. in the y-oriented MD case, as shown in Fig. 2.6 (e).

Through 2D-FDTD simulations, we further investigate the excitation of BSWs with a spinning MD source. Its dipole moment is defined as follows:

$$\boldsymbol{m} = \frac{1}{\sqrt{1+\tan^2\chi}}(\hat{\boldsymbol{y}} + j\tan\chi\hat{\boldsymbol{z}}) \tag{2.3}$$

where j is the imaginary unit and χ is used to define the ellipticity of the spinning MD (2χ is the polar coordinate of the Poincaré sphere). We can see from Eq. 2.3 that the spinning MD has been normalized to have a unit amplitude. It is constructed from two linear MDs along y- and z-axis, which have a fixed phase difference of $\pm\pi/2$ and a relative amplitude of $\tan\chi$. Then, the BSW field excited with the spinning MD source is constructed by linearly adding the simulation results obtained from the two constitutive MDs. The according linear coefficients are those defined in Eq. 2.3.

Figure 2.7 shows the snapshots of the resulting electric field amplitude along the (yz) plane, for the ED (Fig. 2.7(a)) and spinning MD (Fig. 2.7(b) and (c)) excitations. The MD, whose dipole moment is $\boldsymbol{m} \propto \hat{\boldsymbol{y}} \pm 0.53j\hat{\boldsymbol{z}}$ ($j = \sqrt{-1}$), rotates either anti-clockwise

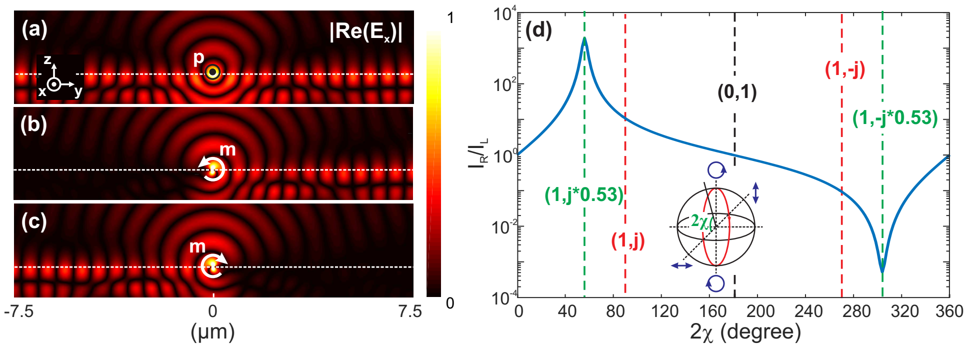

Figure 2.7: TE-polarized Bloch surface waves excited with linear ED and spinning MD. Simulation by FDTD of the coupling of (a) an ED oriented along the x axis, and (b,c), a spinning MD, to a TE-polarized BSW. All three results show, in false colors, the absolute value of the real part of the electric field ($|Re(E_x)|$).The MD rotates either (b) anti-clockwise or (c) clockwise. (d) Directionality factor (ratio of the electric intensities for the left and right BSWs) for various MD polarizations. The MD polarization ellipticity is changed along the path shown in red in the Poincaré sphere (see inset). The MD moment is also expressed at specific values of the ellipticity angle 2χ related to the Poincaré sphere. [74]

(Fig. 2.7(b)) or clockwise (Fig. 2.7(c)). In these figures, the field distributions around the dipoles are saturated to provide a better view of the BSWs. With the ED, the BSW is symmetrically excited on both sides of the point-like source (Fig. 2.7 (a)). No directionality is observed in the optical coupling process. In contrast, the optical coupling process becomes unidirectional with the spinning MDs (Fig. 2.7 (b) and (c)). Depending on the helicity of the spinning magnetic dipole, all incoupled energy is directed to the left and right side, respectively. This helicity-dependent phenomenon validates our concept.

The unidirectional excitation of TE-polarized BSWs can be explained from two following aspects: 1) near-field interference of the BSW fields excited by the two constitutive linear magnetic dipoles (cf Fig. 2.6) and 2) spin-locked unidirectionality.

As from the first aspect, there exists the following three critical differences for the surface waves excited with the $y-$ and $z-$orientated MDs (see Figs. 2.6 (e), (f)): 1) parity difference, which is odd in the former case yet even in the latter case; 2) relative phase difference on the left and right sides, which is $+\pi/2$ and $-\pi/2$, respectively. 3) difference in coupling efficiency, the field amplitude excited by a $y-$oriented MD is as 0.53 times as large as that excited by a $z-$orientated MD. By offsetting the $z-$orientated MD by a factor of $0.53j$, the resulting BSW fields (Fig. 2.8 (b)) on the left/right side become exactly anti-symmetric/symmetric with respect to that obtained with a $y-$orientated MD (Fig. 2.8 (a)). For a spinning MD moment proportional to $\hat{y}+0.53j\hat{z}$, the BSWs generated by the two orthogonal MDs lead to the destructive and constructive interferences on the left and right sides of the MD, respectively (Fig. 2.8 (c)). The opposite interference picture is observed for the MD moment proportional to $\hat{y}-0.53j\hat{z}$(see Fig. 2.8 (d)). Both configurations lead to a single propagation channel for the BSWs (on the right in Fig. 2.8 (c) and on the left in Fig. 2.8 (d)).

As from a SOI point-of-view, the spinning magnetic dipole carries SAM, which is transferred to the transverse SAM of the emerging BSWs. The optimal coupling is then dictated by the projection between the two SAMs, in terms of both handedness and ellipticity. Par-

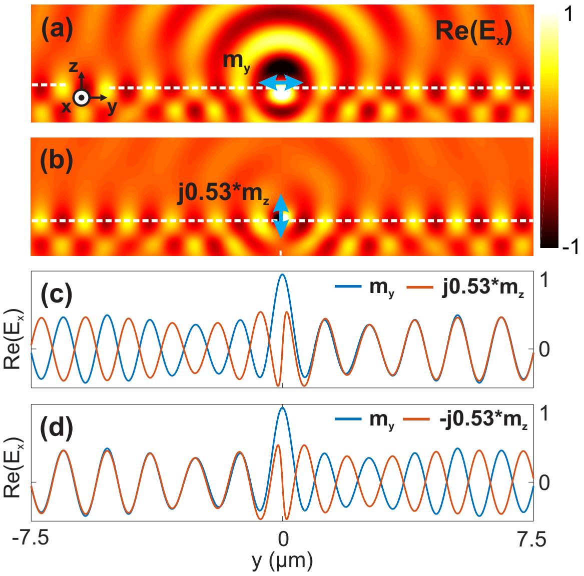

Figure 2.8: (a) and (b) Snapshots (FDTD simulations) of the optical electric field produced in the (yz) plane by two MDs oriented along y and z axis, respectively. In these figures, the field around the dipoles has been saturated in order to provide a better view of the light distributions across the structure. The field distribution in (b) is multiplied by $0.53j$. By adding/subtracting the results of (a) and (b), we achieve the field distributions across the 1D photonic crystal, produced by two spinning MDs of opposite handedness, which are described by dipole moments $\boldsymbol{m}$ proportional to $(\boldsymbol{e}_y \pm 0.53j\boldsymbol{e}_z)$. (c) Electric field profiles $(Re(E_x))$ along the dashed lines of (a) and (b), respectively. Adding these field profiles leads to the total electric field produced by a spinning MD moment proportional to $\boldsymbol{e}_y + 0.53j\boldsymbol{e}_z$ (anti-clockwise rotation). (d) Electric field profiles with a spinning MD moment of $\boldsymbol{e}_y - 0.53j\boldsymbol{e}_z$ (the field plotted in (b) is inverted, leading to a clockwise rotating MD). (c) and (d) show that the BSW coupling process is unidirectional and tunable with the helicity of light.

ticularly, when the two SAMs are orthogonal, the excitation process is blocked. By saying "orthogonal", it means the polarization ellipses corresponding to the two SAMs have: 1) the same shape or ellipticity, 2) the opposite handedness and 3) perpendicular orientations. By recalling Eq. 2.1 and 2.2, we can see the spinning MD source $\boldsymbol{m} = \hat{\boldsymbol{y}} + 0.53j\hat{\boldsymbol{z}}$ has the orthogonal polarization state with respect to that of the BSW magnetic field on the left side, which has been schematically shown in Fig. 2.9 (b). In this case, the excitation of the left BSW is totally blocked and thus the emerging BSW can only propagate to the right direction (Fig. 2.7 (b) and 2.9(b)). By inverting the sign of the input SAM $(\boldsymbol{m} = \hat{\boldsymbol{y}} - 0.53j\hat{\boldsymbol{z}})$, the polarization orthogonality is valid on the right side. As a result, we will observe an unidirectional propagation of BSWs on the left side (see Fig. 2.7 (c)). As the electric component of the BSWs is linearly polarized along x–axis, an x–orientated linear ED source matches the intrinsic polarization of the BSWs on both sides, leading to a symmetric BSW intensity distributions (see Fig. 2.7 (a) and Fig. 2.9 (a)).

We further study the directional excitation of BSWs by spinning MDs of various ellipticities. Figure 2.7 (d) shows the ratio of the electric intensities of the left and right BSWs, for various MD ellipticities. The MD ellipticity is tuned along the path shown in red in the Poincaré sphere (see figure inset). In this case, only the ellipticity angle 2χ for the MD

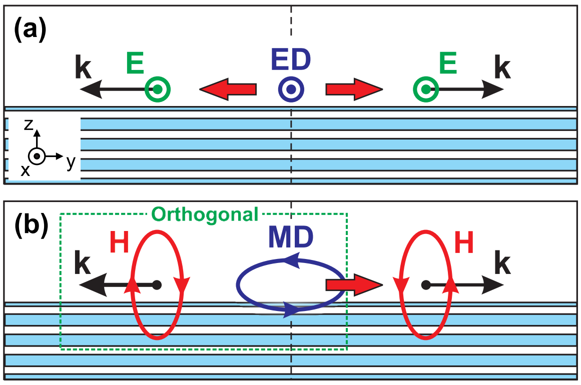

Figure 2.9: Schematic diagrams of the excitation process of the BSW mode with (a) a linear ED and (b) spinning MD source, which corresponds to the scenarios shown in 2.7(a) and (b), respectively. The schematics compare the polarization states of the excitation dipole sources and the corresponding electric or magnetic components of the BSW mode. Large red arrows show the energy flow of the emerging BSW mode. In (a), the ED source(purple) is linearly polarized, which coincides with the polarization state of the BSW electric field. In (b), the MD is elliptically polarized (in purple), which is orthogonal to the polarization state of the BSW electric field on the left side.

moment varies. Our directionality factor (intensity ratio) becomes larger than 10^3 at $2\chi = 55.8°$and smaller than 10^{-3} at $2\chi = 304.2°$. At these two particular angles, the portion of the incoupled power that propagates in one of the two possible directions becomes larger than 99.9% of the total incoupled power. In addition, the variation of the left-to-right intensity ratio with respect to angle 2χ indicates that one can tune the directionality by manipulating the ellipticity of the spinning MD.

To conclude, our simulation results reveal a tunable unidirectional optical coupling controlled by the magnetic field of light. They also confirm that the rotating magnetic field of a TE-polarized BSW carries SAM. From an experimental point-of-view, it is possible to realize a tunable directional coupling for BSW with a spinning MD using a dielectric sphere showing magnetic resonances [134, 162, 163] directly deposited on top of the 1D photonic crystal. Such a bead can be illuminated with a circularly polarized beam at near-grazing incidence, following the electric spin-controlled excitation process of surface plasmons [118]. We choose another type of coupler.

2.3/ EXPERIMENTAL DEMONSTRATION OF THE MAGNETIC SPIN-ORBIT INTERACTION

2.3.1/ EXPERIMENTAL SETUP

Experimentally, the BSW sample has been fabricated via chemical vapor deposition, which is realized at EPFL. In order to couple light to BSWs, we consider a simple groove milled in the top layer of the 1D PC. Figure 2.10 shows the schematics and pictures of our experimental setup. Light at $\lambda_0 = 1.55\ \mu$m emerging from a tunable laser source (Agilent) is coupled to a single mode fiber (SMF-28, Corning). It is collimated by a first lens

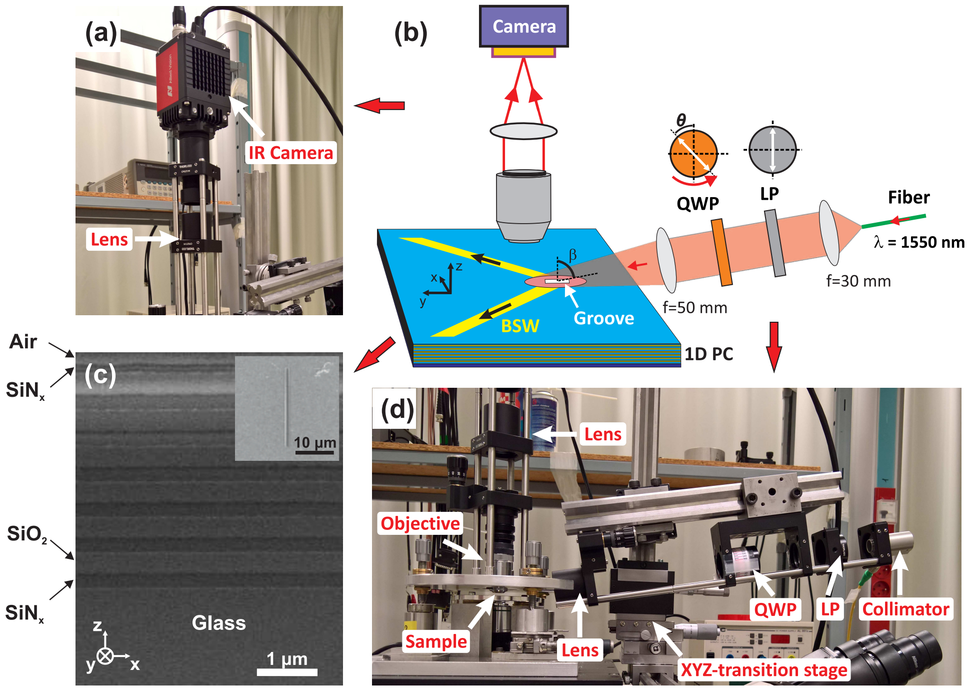

Figure 2.10: A simple all-dielectric platform unveiling the magnetic spin-orbit interaction. (a) Photograph of the collection bench, (b) Schematic diagram of the experimental setup, (c) SEM images of the 1D PC (inset: top view graphs of the subwavelength groove milled in the top layer of the 1D PC), (d) photo of the illumination bench. BSW: Bloch surface wave, PC: photonic crystal, QWP: quarter wave plate, LP: linear polarizer.

($f = 33$ mm, Thorlabs) and focused by the second lens ($f = 50$ mm, Thorlabs). The polarization of the collimated wave is manipulated by using a linear polarizer (LP, Thorlabs LPNIR100-MP) and a quarter-wave plate (QWP, Thorlabs AQWP05M-1600) positioned in between the two lenses. The quarter-wave plate can be rotated at will with respect to the polarizer. Focused waves are projected directly onto the groove at almost grazing incidence (incidence angle $\beta = 80°$, Fig. 2.10 (b)). The groove and its surrounding region are imaged with an objective ($20\times$, $NA = 0.4$) coupled to an infrared camera (GoldEye model G-033, Allied Vision Technologies GmbH). Far-field imaging of the surface waves is rendered possible by the slight surface roughness on the top layer of the 1D photonic crystal, which scatters the surface waves into free space. As the scattering is proportional to the BSW intensity, we measure the intensities of these scattered lights to study the energy distribution into the left and right BSWs.

Figure 2.11 shows images by collecting scattered light from the surface of the 1D PC with incident light at three polarization states: linear (Fig. 2.11 (a)) and two elliptic polarizations with opposite handedness (Fig. 2.11 (b) and (c)). In all those images, we can see a bright elongated spot (along y-axis) surrounded by two narrow rays on both sides. The central bright spot is the cross-section of the excitation beam along the surface. The two narrow rays on both sides of the excitation spot are the traces of the BSWs excited by the subwavelength groove. Notably, there is an angle between the BSW traces and that of the incident light, which is dictated by the phase matching condition (i.e., linear momentum conservation) between the BSW and the incident light.

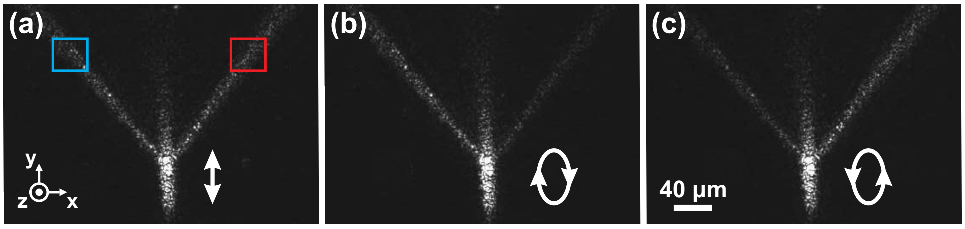

Figure 2.11: Images of the 1D PC surface obtained by illuminating the subwavelength groove with light of various polarization states: (a) linear polarization (b) right elliptic polarization (c) left elliptic polarization.

The phase matching condition requires that the wave vector projections of the incident light and the BSWs should be equal along y-axis. Thus, we have:

$$k_0 \sin\beta = k_{BSW} \cos\gamma \tag{2.4}$$

where k_0 and k_{BSW} are the wave vector of the incident light and the BSWs, respectively. γ represents the angle between the BSW trajectories and the groove. In our case, $n_{eff} = 1.185$ and $\beta = 80°$, we obtain $\gamma = 33.8°$, which matches quite well with the measured γ value ($\gamma \sim 36°$). As our 1D PC contains no magnetic material and the groove does not work under resonance condition, the permeability distribution is homogeneous. As a comparison, the permittivity distribution is discontinuous across the groove and the 1D PC. Such a discontinuity gives to the subwavelength groove a pure electric optical response, which can be described by an electric dipole moment (per unit length).

As shown in Fig. 2.11, the intensities of the BSWs excited on the two sides of the groove are equal when the incident light is linearly polarized. However, when the incident light becomes elliptically polarized, this symmetry is broken. Depending on the helicity of the incident light, BSWs are preferentially excited on the left or right side, indicating a helicity-dependent directional coupling (Fig. 2.11 (b) and (c)).

2.3.2/ ANALYTICAL MODEL OF THE EXPERIMENTAL SETUP

The experimental architecture described above appears to be more complex than the theoretical description of a spinning MD releasing energy to TE-polarized BSW. On the one hand, the subwavelength groove coupler has a pure electric response while the directional excitation of BSWs hints the involvement of the magnetic field. On the other hand, all electromagnetic components of the incident light have non-zero projections with respect to the BSWs, due to the oblique illumination and the tilted BSW trajectory with respect to the groove. Therefore, more careful investigations are mandatory to clarify the origins of this helicity-dependent directionality.

We find that the above issue can be fixed by modulating the polarization state of the incident light. In general, one can either: 1) fix the QWP yet rotate the linear polarizer or 2) fix the LP yet rotate the QWP. Fig. 2.12 (a) and (b) schematically show the polarization ellipses of the emerging light (that is incident onto the 1D photonic crystal) in the two cases, respectively. The two approaches are equivalent in terms of tuning the ellipticity of incident light, which is only dictated by the relative angle (θ) between the LP and the

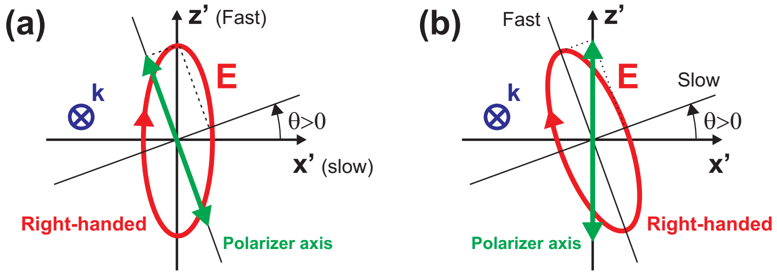

Figure 2.12: Schematic diagrams for the polarization state of the incident light after passing through a LP and a QWP: (a) the QWP is fixed and the LP is rotated. (b) the LP is fixed and the QWP is rotated. The green arrow in (a) and (b) show the immediate linear polarization state after the LP. The red ellipse (with handedness indication) in (a) and (b) show the final polarization state after the QWP.

QWP. However, the two approaches are distinct in terms of the orientation of the output polarization ellipse. In the former case (Fig. 2.12 (a)), the orientation of the polarization ellipse is fixed. As a contrast, it rotates when the QWP is set in rotation (see Fig. 2.12 (b)), which introduces an extra modulation to the incident light.

Now let us focus on the modulation generated by rotating the QWP a full turn with respect to the fixed linear polarizer. When $\theta = k90°$, $k = 0, 1, 2, 3$, the output polarization is linear whereas a circular polarization is realized for $\theta = 45° + k90°$, $k = 0,1,2,3$. For intermediate angles, the polarization is elliptical. Thus, by rotating the QWP a full turn, the helicity of the output light has 2θ periodicity. At the same time, as the polarization ellipse rotates together with the crystalline axes of the quarter-wave plate, electric and magnetic amplitudes of the incident light have, by projection, a 2θ dependence. The energy coupling to the right and left BSWs thus undergoes a 4θ dependence as it is homogeneous to the intensity (this point will be discussed in detail later). Thus, for the incident light, the rotation of the QWP modulates its magnetic field helicity with 2θ dependence and electric field intensity with 4θ dependence. Such a difference is critical for recognizing the magnetic and electric contributions in the coupling process of BSWs.

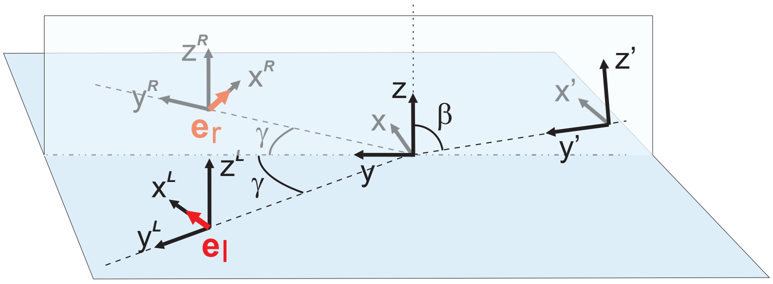

Figure 2.13: Schematic diagram of the electric field projection and corresponding global and local coordinate frames. e_r and e_l (in red) represent the unit vectors parallel to the electric field components of the right and left BSWs.

To fully understand the modulation effect caused by the rotating QWP, we calculate the projection of the incident field with respect to that of the BSWs. For simplicity, we treat the collimated Gaussian beam as a plane wave. Figure 2.13 illustrates the local coordinate frames (x',y',z') of the incident plane wave, and (x^L,y^L,z^L) and (x^R,y^R,z^R) of the BSWs propagating on the left and right sides of the groove, respectively. It also shows the global coordinate frame (x,y,z) linked to the surface of the 1D photonic crystal. β denotes the incidence angle of the plane wave. γ is the angle between the emerging BSWs and the y-axis (ie., the groove axis).

To define the incident electric field $\boldsymbol{E}_{inc}$, we assume that the incident plane wave, initially polarized along z' direction, is phase retarded by a quarter-wavelength along an axis tilted by an angle θ with respect to the polarizer axis (z'-axis) (cf Fig. 2.12(b)). we can express the electric field of the incidence light, in the (x,y,z) coordinate frame as follows:

$$\boldsymbol{E}_{inc} \propto \begin{bmatrix} -(1-j)\sin\theta\cos\theta \\ (\cos^2\theta + j\sin^2\theta)\cos\beta \\ (\cos^2\theta + j\sin^2\theta)\sin\beta \end{bmatrix} \tag{2.5}$$

According to our former discussion, the dielectric groove on top of the 1D photonic crystal has mainly an electric optical response described by an ED moment per unit length. We can thus define, in the first approximation, its interaction with the incoming plane wave and related BSW production by the coupling rates:

$$R_i = \alpha|\boldsymbol{e}_i \cdot \boldsymbol{E}_{inc}(\boldsymbol{r}_0)|^2, \tag{2.6}$$

where the subscription $i = r, l$ denotes the right and left sides of the groove, respectively. α is a constant. $\boldsymbol{E}_{inc}(\boldsymbol{r}_0)$ is the incident electric field at a single point for the coordinate $\boldsymbol{r}_0$ along the subwavelength groove. $\boldsymbol{e}_i$ are unit vectors parallel to the electric field of the right and left BSWs, which are represented with red arrow in Fig. 2.13. The unit vectors $\boldsymbol{e}_i = (1,0,0)$ in the local coordinate frame (x^L, y^L, z^L) and (x^R, y^R, z^R), in the global coordinate frame (x,y,z) take the form:

$$\boldsymbol{e}_r = \begin{bmatrix} \cos\gamma \\ -\sin\gamma \\ 0 \end{bmatrix} \tag{2.7}$$

$$\boldsymbol{e}_l = \begin{bmatrix} \cos\gamma \\ \sin\gamma \\ 0 \end{bmatrix} \tag{2.8}$$

Substituting Eqs. 2.5, 2.7 and 2.8 into Eq. 2.6, we calculate the coupling rates R_r and R_l of the incident wave to the right and left BSWs:

$$R_r = \alpha|(1-j)\sin\theta\cos\theta\cos\gamma + (\cos^2\theta + j\sin^2\theta)\cos\beta\sin\gamma|^2 \tag{2.9}$$

$$R_l = \alpha|(1-j)\sin\theta\cos\theta\cos\gamma - (\cos^2\theta + j\sin^2\theta)\cos\beta\sin\gamma|^2 \tag{2.10}$$

Figure 2.14 (b) shows the plots of R_r and R_l as a function of the angle θ. The blue and red curves represent the coupling rates to the left and right BSWs. These two coefficients, which describe a pure electric coupling in the BSW excitation process, show a 4θ dependence. They are shifted by an angle of about 8°. Moreover, changing the polarization

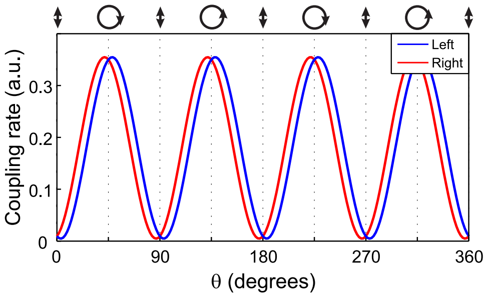

Figure 2.14: Pure electric coupling model for the excitation of BSWs from the oblique illumination of a subwavelength groove. Plot of the coupling rates R_r and R_l of the incident light into the right and left BSWs, calculated from Eqs. 2.9 and 2.10, respectively.

handedness does not interchange the values for the two coefficients, which indicates that pure electric coupling of the incident light to the TE-polarized surface waves is helicity independent. Indeed, the intrinsic electric field of a TE polarized BSW is linearly polarized and thus is described by a zero helicity.

The helicity-dependent phenomenon shown in Figures 2.11 suggests that the magnetic field projections may be responsible for the directional excitation BSWs. According to the Maxwell-Faraday equation, the magnetic field of the incident plane wave can be derived from Eq. 2.5 as:

$$\boldsymbol{H}_{inc} \propto \begin{bmatrix} \cos^2\theta + j\sin^2\theta \\ (1-j)\sin\theta\cos\theta\cos\beta \\ (1-j)\sin\theta\cos\theta\sin\beta \end{bmatrix}. \tag{2.11}$$

We examine the ellipticity of the incident magnetic field in the helicity planes of the BSW. To this end, we make a transformation of $\boldsymbol{H}_{inc}$ from the global coordinate frame (x, y, z) to local ones (x^L, y^L, z^L) and (x^R, y^R, z^R). We define $\boldsymbol{H}_i = M_i \times \boldsymbol{H}_{inc}$, where $i = r, l$. M_r and M_l are the transformation matrices having the following forms for the right and left BSWs:

$$M_r = \begin{pmatrix} \cos\gamma & -\sin\gamma & 0 \\ \sin\gamma & \cos\gamma & 0 \\ 0 & 0 & 1 \end{pmatrix}, \tag{2.12}$$

$$M_l = \begin{pmatrix} \cos\gamma & \sin\gamma & 0 \\ -\sin\gamma & \cos\gamma & 0 \\ 0 & 0 & 1 \end{pmatrix}. \tag{2.13}$$

The ellipticity of the incident magnetic field is defined by the polar angle (2χ) of the Poincaré sphere. Figure 2.15 (b) represents 2χ in the helicity planes (y^L, z^L) and (y^R, z^R) of the left and right BSWs, respectively, as a function of the angle θ between the LP and the QWP. The two curves show an oscillating behavior with a 2θ dependence and an amplitude of $63.7°$. They are in opposition from each other, i.e., shifted by $180°$. Switching polarization handedness changes the sign of the angle 2χ, it is obviously helicity-dependent. Figure 2.15 (a) shows a schematic diagram depicting the helicity of the magnetic projections, as well as that of the intrinsic BSW magnetic field. Importantly,

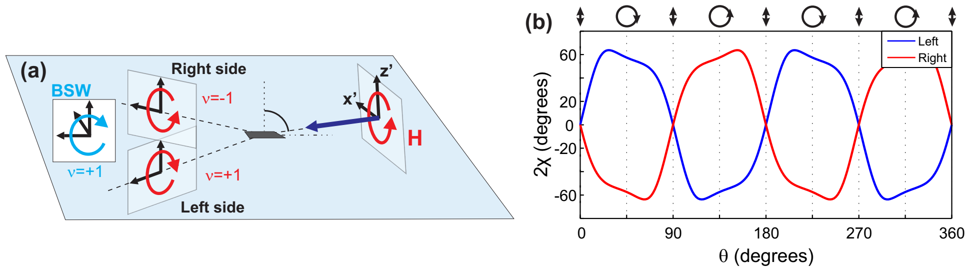

Figure 2.15: (a) Schematic diagram of the magnetic field handedness in the helicity planes of the left and right BSWs for an incident right-handed polarization. (b) Ellipticity 2χ of the incident magnetic field in the helicity planes (y^L, z^L) and (y^R, z^R) of the left and right TE-polarized BSWs.

the incident magnetic field shows opposite handedness when projected onto the helicity planes of the right and left BSWs. For instance, a right-handed incident polarization leads to a magnetic field rotating clockwise ($\nu = +1$) and anticlockwise ($\nu = -1$) in the helicity planes of the left and right BSWs, respectively. Such a configuration is favorable for spin-controlled unidirectional excitation of the BSWs, whose magnetic field is described by handedness $\nu_{BSW} = +1$. A right-handed (left-handed, respectively) incident polarization would thus steer TE-polarized BSWs to the left side (to the right side, respectively) of the groove. Such a spin-controlled coupling process leads to a 2θ-dependent power distribution between the two BSWs excited on both sides of the groove.

To conclude, intrinsic properties of the BSWs and the near-field coupler define the roles of the optical electric and magnetic fields in the BSW excitation process. The former mediates the energy coupling from light to BSWs, which is helicity independent. The latter, however, controls the directionality of phenomenon, by means of its helicity. By rotating the QWP with respect to the fixed LP, we introduce to the incident light a 2θ- and 4θ-modulation of its intensity and helicity, respectively. This polarization manipulation thus makes it possible to distinguish the mixed electric and magnetic contributions to light-BSW coupling.

2.3.3/ NUMERICAL SIMULATION OF THE EXPERIMENTAL SETUP

We also numerically simulate the experimental configuration with Fullwave software from Synopsis. Figure 2.16 shows the model built in Fullwave. As shown in Fig. 2.16, the groove is in the top layer of a 1D PC, and along the y-axis. A Gaussian laser beam with a waist diameter of $1.5\ \mu$m is projected onto the groove at a grazing angle of $80°$ degree. It radiates in continuous wave regime at a wavelength of $1.55\ \mu$m. The position of the launch source is set to let its center coincide with that of the groove. The groove has the same cross-section sizes as these used in our experiments ($400\ nm \times 400\ nm$). The 3D mesh grid near the groove and the photonic crystal layers has a size of 10 nm. In the circumference regions, a larger mesh grid of 30 nm is used to save simulation time. A two-dimensional monitor parallel to the $x0y$ plane is placed 100 nm above the photonic crystal surface to gather field data of the excited BSW modes on the two sides of the groove.

In order to simulate the BSW excitation including a rotating QWP and a fixed LP, we carry

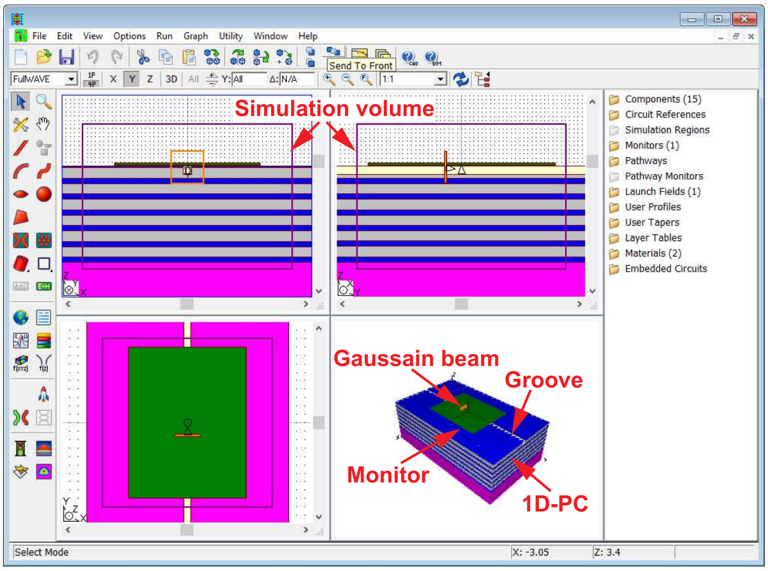
File Edit View Options Run Graph Utility Window Help
Send To Front
FullWAVE
Simulation volume
Gaussain beam
Groove
Monitor
1D-PC
Components (15)
Circuit References
Simulation Regions
Monitors (1)
Pathways
Pathway Monitors
Launch Fields (1)
User Profiles
User Tapers
Layer Tables
Materials (2)
Embedded Circuits
Select Mode
X: -3.05
Z: 3.4

Figure 2.16: Screen print of the 3D FDTD model built with Fullwave software to simulate the scenario of a BSW excitation with the configuration depicted in Figs. 2.10.

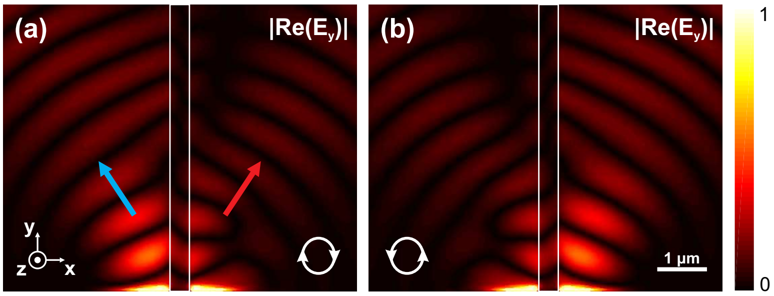

Figure 2.17: Simulation snapshots of the TE-polarized BSWs excited by a groove under the illumination with (a) left circular polarization and (b) right circular polarization. The two results show, in false colors, the absolute value of the real part of the electric field ($|Re(Ey)|$). The white lines show the profile of the subwavelength groove, which has a cross-section of $400\ nm \times 400\ nm$. The blue and red arrows in (a), which have a angle of $33.8°$ with respect to the groove, indicate the BSW propagation directions on the left and right sides, respectively.

out two simulations where the incident light is linearly polarized along x'- and z'- axis, respectively (cf Fig. 2.13). The results at an arbitrary QWP orientation are then constructed by linearly combining those obtained with these two simulations. The according combination coefficients read $-(1-j)\sin\theta\cos\theta$ and $cos^2\theta + j\sin^2\theta$, which are derived by projecting the vectors denoted by Eq. 2.5 back to the local coordinate frame of the incident wave (x', y', z'). Figure 2.17 shows the results corresponding to the cases of a groove illumination with right and left circularly polarized light. As indicated by the red and blue arrows, the excited BSWs propagate at an angle around $33°$ with respect to the groove, which is consistent with our experimental results. Besides, we can also see from Fig. 2.17 an imbalanced excitation of the BSW on the two sides of the groove. Such a symmetry breaking shows the same helicity dependence as the experimental results. A full set of simulation results will be shown later to compare with the experimental ones.

2.3.4/ Results and discussions

We then study the distribution of the incoupled power between the two surface waves as a function of the incident polarization. We experimentally acquire images of the structure while varying the polarization of the incident beam, following the procedure described in Sec. 2.3.1. For each image recorded at a specific polarization state, we integrate the signal detected over two square areas located symmetrically with respect to the groove (shown in light red and blue colors in Fig. 2.11 (a)). Finally, the resulting values S_r and S_l measured on the right and left BSWs, respectively, are plotted as a function of the angle θ between the LP and QWP (Fig. 2.18 (a)). The experimental plots are represented with circles together with the simulation results (solid lines) obtained with the 3D FDTD method (see details in Sec. 2.3.3).

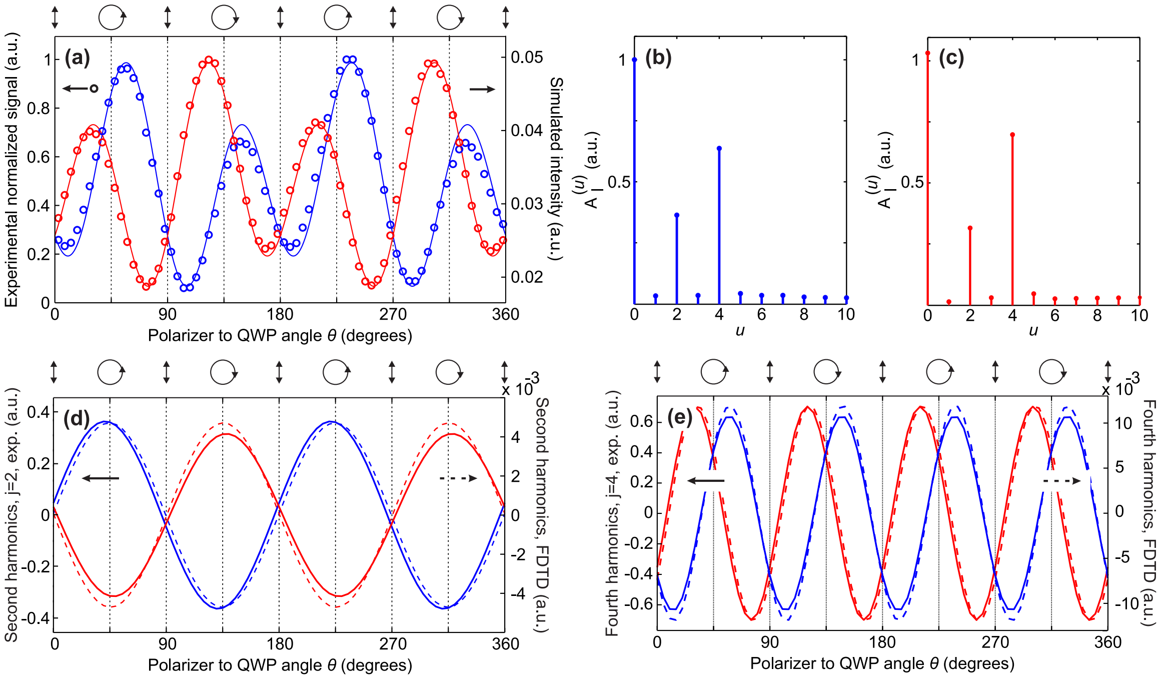

Figure 2.18: Magnetic spin-orbit interaction steers Bloch surface waves. (a) detected signals (circles) and simulated intensities by FDTD (solid lines), on the right and left BSWs, as a function of the angle θ between the QWP and the LP. The curves related to the right and left BSWs are represented in red and blue, respectively. (b) and (c) Fourier spectra (amplitude) of the experimental blue and red curves of (a), obtained by Fourier transformation. Coefficient u defines the harmonic orders for the Fourier series. (d) and (e) Representation, in the real space, of the non-null harmonics for the two Fourier series shown in (b) and (c): (d) second harmonics and (e) fourth harmonics. Experimental and numerical curves are shown by solid and dash lines, respectively. [74]

S_r and S_l are described by sinusoidal functions, shifted by approximately $30°$ from each other. Their amplitudes are modulated by a sinusoidal function. The experimental results and simulation predictions are in good agreement. As expected, the coupling process is asymmetric excepted from linear incident polarizations (when $\theta = k90°, k = 0, 1, 2, 3$). In this case, the optical system is fully symmetric with respect to the groove and the two curves for S_r and S_l merge. As discussed above, the electric and magnetic contributions to the BSW excitation process show a 4θ- and 2θ-dependence, respectively. Therefore, a Fourier analysis for S_r and S_l may assist the identification of these electric and magnetic optical effects. By Fourier transforming these two functions (cf. Figs. 2.18 (b) and (c)), we see that they can be simply expressed analytically as:

$$S_i(\theta) = A_i^{(0)} + A_i^{(2)} \sin\left(2\theta + \phi_i^{(2)}\right) + A_i^{(4)} \sin\left(4\theta + \phi_i^{(4)}\right) \tag{2.14}$$

where $i = r, l$, and the coefficients $A_i^{(0)}$, $A_i^{(u)}$ and $\phi_i^{(u)}$ $(u = 0, 2, 4)$ are constant. Coefficients $A_i^{(0)}$ and $\phi_i^{(u)}$ $(u = 2, 4)$ are given by the Fourier transform of S_r and S_l.

We see in Fig. 2.18 (d) that the second harmonic components relative to the left and right BSWs are almost in opposition, i.e., shifted by $180°$. The fourth harmonics (cf. Fig. 2.18 (e)) undergo a shift of approximately $30°$, initially evidenced in Fig. 2.18 (a). Importantly, the local maxima and minima of the second harmonic component closely coincide with the right and left-handed circular polarization states of the incident wave. Moreover, changing the incident polarization handedness inverts the distribution for the incoupled light in the right and left BSWs. The second harmonic contribution to the BSW coupling is, therefore, helicity dependent. In contrast, the fourth harmonics of the Fourier series stay unchanged when the input polarization handedness is reversed (See Figs. 2.18 (e)). Therefore, the fourth harmonic contribution to the BSW coupling is independent of the helicity of the incident light.

The subwavelength groove on top of a 1D PC, as discussed before, are optically governed by an electric dipole moment (per unit length). It interacts with the electric field of an incoming wave to transfer energy to the BSWs. Following a pure electric model, and assuming an incident plane wave, the previously defined coefficients S_r and S_l become proportional to the coupling rates R_i $(i = r, l)$ obtained in Sec. 2.3.2. By comparing Fig. 2.14 and Fig. 2.18 (e), we see that R_r and R_l closely match the fourth harmonic component of Eq. 2.14. The unbalanced electric coupling is due to the asymmetric projections of the incident electric field with respect to those of the BSWs (see Sec. 2.3.2). The larger angular shift observed between the couple of experimental curves ($8°$ versus $10°$ with our model) may be explained by the scattering properties of our 600-nm large (i.e., $\lambda/2.5$) groove coupler which slightly deviate from the point-like dipole emission.

The modulation of the electric coupling by a helicity dependent optical process (Fig. 2.18 (a) and (d)) is not predicted by our analytical model. As noted above, only the magnetic field of the TE-polarized BSW is rotating, the electric field shows zero helicity. A helicity dependent process for such waves, may thus solely involve the magnetic field of light. We plot, as a function of θ, the ellipticity factor of the magnetic field (plane-wave illumination) projected onto the helicity planes of the right and left BSWs (i.e., the planes perpendicular to the transverse spin momentum of the surface waves). The ellipticity curves show a periodicity of 2θ and opposite values when the polarization handedness is changed (Fig. 2.15). These curves closely resemble the second harmonic functions of Eq. 2.14 (Fig. 2.18 (d)). Therefore, the second harmonic contribution to the optical coupling is solely controlled by the magnetic field of light.

Remarkably, the magnetic effect is clearly visible using a dielectric scatterer described by an electric dipole moment (per unit length). Fig. 2.18 (b) and (c) show that its contribution is larger than 45% of the electric contribution to the coupling. Despite the extremely low response of the scatterer to the magnetic field of the impinging wave, the rotating magnetic field incident at an electric scatterer provides initial conditions favorable for steering a large portion of the incoupled energy to the right or to the left BSW, depending on the polarization handedness. The second harmonic curves shown in Fig. 2.18 (d) thus describe a magnetic spin-directional coupling, as shown in Fig. 2.7. In the experimental case, however, the phase matching between the incident light and the BSW is mediated by the electric optical field, given the electric dipole nature of the scatterer. The rotating incident magnetic field incident at the groove, which is less affected by the scatterer, controls the directionality of the launched surface waves. This specific electric-magnetic coupling explains the 4θ dependence of the experimental coupling process (Fig. 2.18) that is comparatively not observed for MD excitation. Fig. 2.7 (d) shows a directionality curve with only a 180° periodicity. A subwavelength resonant particle or antenna, whose resonance is described by a MD moment, would cancel the electric component of the coupling. Such a configuration is, however, beyond the scope of this thesis.

2.4/ CONCLUSIONS

We describe a new magnetic effect in a light-matter interaction called the magnetic SOI of light. On the basis of this magnetic SOI, we show that an elliptically polarized MD develops a tunable unidirectional coupling of light into TE-polarized BSWs: depending on the helicity of the MD, the surface waves propagate upstream or downstream. The underlying phenomenon is a transverse spin-directional coupling in BSWs, with the spin momentum solely described by a rotating magnetic light field. This phenomenon has been demonstrated using a simple subwavelength groove used as a light-to-BSW converter. Despite the electric dipole nature of this coupler, the magnetic effect is of the same order of magnitude as the electric effect in the coupling process. In this particular case, the magnetic field is not involved in the transfer of energy to the BSW, but instead, it controls the directionality of the incoupled energy. By using couplers that can develop magnetic resonances [162, 163], a pure magnetic tunable unidirectional coupling is experimentally possible, in accordance with our theoretical predictions. In addition to the fundamental questions raised regarding magnetic optical control of light-matter interaction, our results open possibilities for controlling optical flows in ultra-compact architectures. The results can also be generalized to all TE-polarized guided modes. Reciprocally, BSWs can also be used as probes to locally investigate the magnetic polarization properties of light. Compared to the (plasmonic) nanoprobes that are currently used, which are limited to measuring the electric spin density only, such BSW probes would enable measurement of the optical magnetic spin density [65, 94].

3

TRAVELING-WAVE HELICAL PLASMONIC ANTENNA: CONCEPT AND DESIGN

A characteristic of surface plasmons (SPs) guided along curved trajectories is their ability to acquire extrinsic orbital angular momentum (EOAM) [55, 112] and to induce, by leakage, free-space light emission [83]. For sharp curvatures, the EOAM of the SP mode can match the spin angular momentum (SAM) of free space propagating photons, thus opening a route towards localized light emissions of controlled helicity, owing to optical spin-orbit interaction (SOI) [55]. On the basis of this EOAM-to-SAM transfer, we investigate a helical plasmonic antenna (HPA) to produce circularly polarized light on the subwavelength scale by swirling subdiffraction SPs. Our optical antenna differs from existing helical plasmonic structures [45, 164, 165, 166] by its non-resonant traveling-wave nature, thus extending to optics the concept of helical antenna operating in the “axial-mode" mode [83, 167].

It is noted that, a similar swirling-plasmon involved light beaming has been demonstrated previously with conically tapered metallic structures. Originally, these structures can adiabatically compress radially polarized surface plasmon mode to the very end of the tip [168]. However, if the surface plasmons takes a vortex form, say launched by spiral slits engraved around the bottom of the tip, they will scatter into free space as a vortex or circularly polarized beam, depending on the topology of the plasmonic vortex mode [169, 170]. Such an operation is different from our case as circularly polarized light is mandatory to initiate the plasmonic vortex and thus the structure itself can not generate circular polarization. Besides, the spiral slits extend the overall structure size to be much larger than the operation wavelength, which may limit its application in subwavelength photonic systems.

This chapter will start with a brief introduction to optical antennas. Then, we will focus on the working principles of helical antennas in low-frequency regime and introduce its two modes: (1) the resonant normal mode working with standing waves and (2) the non-resonant axial mode working with traveling waves. The two working mechanisms are used to examine present researches on helical metamaterials and to develop the concept of traveling-wave helical plasmonic antennas (TW-HPA). The underlying EOAM-to-SAM transfer process will also be discussed. Then, we will detail the design process of the TW-HPA for obtaining perfect circular polarization in the far-field. In this part, both the influence of helix geometries and the nanoscale feed elements will be discussed. This chapter will finish with an optimal design and a short conclusion.

3.1/ BASICS AND STATE OF THE ART FOR OPTICAL ANTENNAS

Since Hertz's first invention in 1886, antennas soon sprouted out and developed into a huge family in the past century. Nowadays, they are pervasive in most technical fields, ranging from deep space exploration to smart phone WIFI connection. It is noted that, though those antennas have distinct differences in both size and configurations, the underlying working mechanisms are similar. They all bridge the dimension gap between subdiffraction oscillators and diffraction-limited propagating electromagnetic waves. Besides the basic working principle, these antennas also share some common points in terms of functions:

- they can play either as emitters or as receivers of electromagnetic waves.
- their feature dimension scales with respect to the working wavelength (free space).
- they can efficiently direct the radiation and strongly interact with the wave polarization.

Classical antennas work at radiowave and microwave frequencies [83], say in the low-frequency regime as compared with optical frequencies. Recently, their concepts have been transferred into the optical regime, giving the name of “optical antennas" [1, 29, 30, 31, 32]. As defined by Novotny and Van Hulst [30], “Optical antennas are devices that convert freely propagating optical radiation into localized energy, and vice versa." This definition is thus the direct translation to optics of the definition of low-frequency antennas. We can see that the role of optical antennas is to play as an efficient interface between near and far fields. The early history of optical antennas is bound to near-field imaging where metallic particles and nano apertures were used to efficiently delivery/collect energy to/from optical near-fields [29, 30]. Nowadays, their applications have been diversely extended to enhance and direct spontaneous emission from quantum light sources, to boost light–matter interactions and optical non-linearities at the nanoscale, as well as to impedance-match plasmonic nano-circuits to vacuum. [29, 30, 32].

So far, various optical antennas have been proposed and demonstrated, enabling full control over light-matter interaction at the subwavelength scale [30]. In general, they can be either dielectric or metallic, or combine these elements as the constituent material [30]. Akin to their low-frequency counterparts, plasmonic optical antennas (POAs) can also be separated in two families: the standing-wave (resonant) antennas and the traveling-wave (non-resonant) antennas.

Optical monopole [49, 50, 174, 175] or dipole antennas [50, 171, 176, 177] are typical resonant POAs. Figure 3.1 (a) shows the dipole nanoantenna that is formed by a pair of nanowires with a gap in-between. Such an antenna can efficiently couple free-space light into the nanocurcuit, and vice versa. Figure 3.1 (b) shows a monopole nanoantennas fabricated at the apex of a fiber tip. Fed by a nanoaperture placed in contact, it enables a background-free fluorescent sensing [49, 50, 174, 175]. Figure 3.1 (c) shows a gold nanobead attached to a fiber tip, allowing the probing of a single fluorescent molecule. Figure 3.1 (d) shows the cross-resonant antenna. It consists of two identical dipolar antennas placed in perpendicular. Such an antenna can control the polarization of near-field [31]. For example, a circularly polarized near field can be realized at the gap region under the illumination of circularly polarized light [173, 178].

Bow-tie nano antennas consist of two tip-to-tip triangular nanoparticles (Fig. 3.2 (a)) [179]. They can produce a strongly enhanced electric field in the gap region, enabling a fluorescence enhancement more than 1000-fold. Figure 3.2 (b) shows the so-called bowtie nano aperture (BNA) where two triangle apertures are perforated through a metal layer with a square gap connecting them at the center. Illuminated with proper polarization, a strongly enhanced electric field is created in the gap zone, which has been used to enhance various optical processes such as molecular fluorescence[181] and harmonic generation [182], etc. BNAs can be integrated on a fiber tip, leading to an integrated plug-and-play operation free of bulky optics. BNA-on-tip can then be used as optical tweezers [183] or efficient near-field sources/detectors [175, 181]. A recent work from our group integrated a doubly-resonant BNA on a fiber tip, realizing the first characterization of single infrared quantum dots at telecommunication wavelength [180]. A Babinet-complementary design of the BNA (diabolo nano antenna) is shown in Fig. 3.2 (c), which has shown the unique ability to create a strong nanoscale magnetic hot spot at optical frequencies [184].

The second family of POA are the traveling-wave antennas. Figure 3.3(a) shows an example of the optical Yagi-Uda antenna coupled to a single quantum dot placed in contact to the plasmonic feed element. Figure 3.3(b) shows both the theoretical and measured emission patterns of such a hybrid radiator. The light emitted from the quantum dot is mainly directed into a single light cone, showing an excellent directionality. Besides, the optical Yagi-Uda antenna can also be extended to include electro-luminescent devices [186]. A recent work uses multi-step electron beam lithography to fabricate an array of 3D

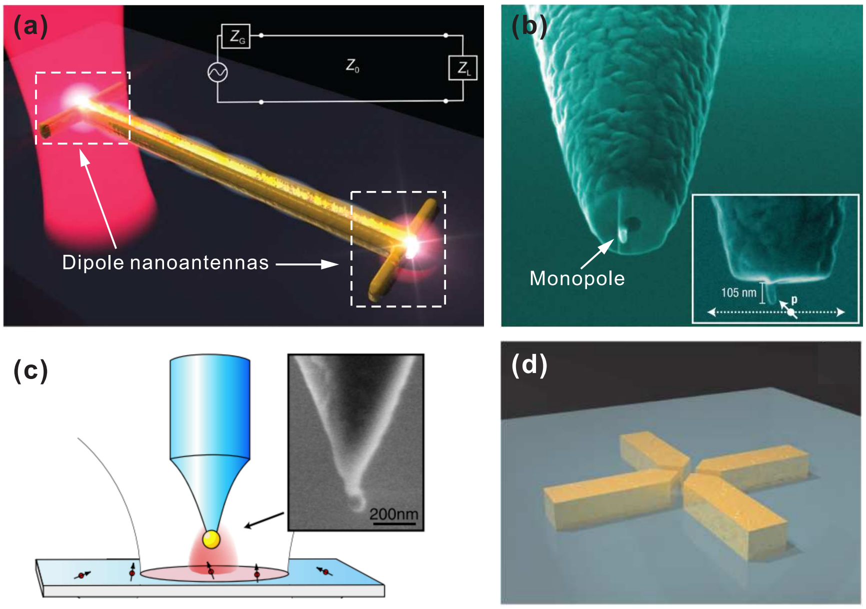

Figure 3.1: (a) Schematic of dipolar antennas connected at the two ends of a plasmonic waveguide [171]. (b) Scanning electron microscope (SEM) images of a monopole antenna mounted at a fiber tip [50]. (c) Schematic and SEM image of a gold particle antenna attached at a fiber tip [172]. (d) Schematic of a cross resonant antenna [173].

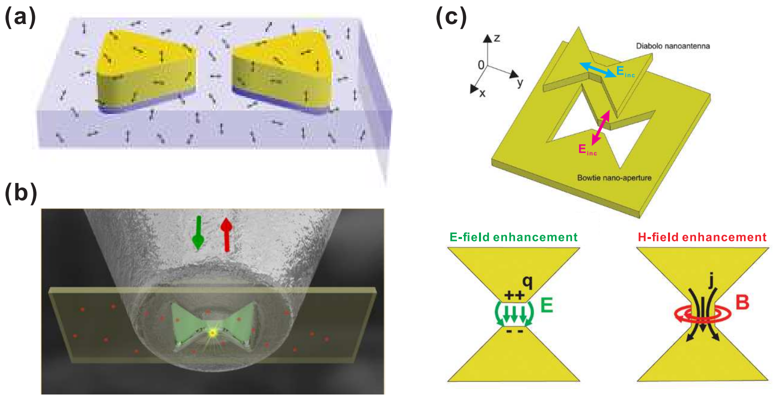

Figure 3.2: Schematics of (a) bowtie nanoantenna [179] (b) bowtie nanoaperture antenna fabricated at a fiber tip [180] (c) diabolo nanoantenna.[173]

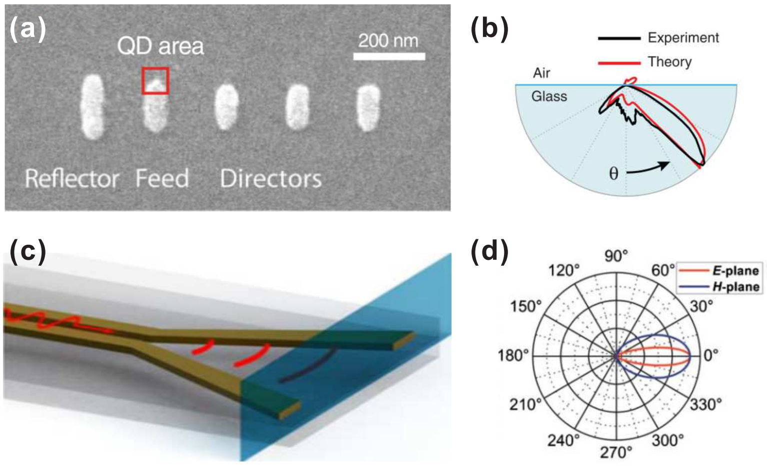

Figure 3.3: (a,b) Optical Yagi-Uda antenna[51] with (a) SEM image and (b) theoretical and measured emission patterns. (c,d) Plasmonic horn antenna [185] with (c) a schematic and (d) emission patterns on two principle planes.

Yagi-Uda antenna [187]. A phase array operation has been demonstrated with such an antenna network. Yagi-Uda antennas can be seen as a mixture between resonant and non-resonant antennas as they rely on a series of resonant optical nano-rods.

Figure 3.3 (c) shows a schematic of the plasmonic horn antenna, which is form by gradually flared metallic waveguide. Horn antenna is a true traveling-wave antenna as no resonant elements are presented. Its directional emission characteristics can be seen in Fig. 3.3 (d). Such an antenna has been proposed to build the optical link for on-chip communication [185][188]. A numerical work from Klemm shows that a similar directional emission can be realized with a rhombic POA [189], whose shape is quite close to the horn antenna. Very recently, a plasmonic V-shaped antenna has been demonstrated by Ding et al [190]. They build the antenna by bending a silver nanowire with a proper angle. Fed from one end, this antenna radiates at the bending point, with a tunable directivity.

Resonant and traveling-wave POAs have different characteristics. Resonance mechanisms allow to realize antenna functions at a smaller antenna size, which however impose a narrow-band operation. Traveling-wave antennas are usually bigger than their resonant counterparts and known for their high directivity and operation bandwidth. It is noted that, existing POAs, no matter resonant or non-resonant, are not able to generate background-free circularly polarized emission. For example, though cross-resonant antennas can produce a circularly polarized near-field hot spot under the illumination of circularly polarized light [173][178], they do not create these circular polarization states by themselves.

Looking back to the low-frequency regime, traveling-wave helical antennas offer a paradigm solution to defining circular polarizations (CP). Fed in end-fire geometry, even a single such antenna is capable of radiating directional circularly polarized beam, over a broad wavelength band [83, 167]. Recently, inspired by low-frequency helical antennas, arrayed plasmonic helices have bee demonstrated to play as a broadband circular polarizer [45]. However, these plasmonic helices work with standing wave, which is different from classical traveling-wave helical antennas. This point will be discussed in details later. Moreover, they are excited through far-field scattering. This excitation configuration introduces a background and thus is not suitable for developing a single circularly polarized antenna. Optically, background-free antenna feeding has been demonstrated by feeding the targeted antenna in the near-field with dipole-like sources, such as circular [49, 50, 174] or bowtie nanoapertures [175]. However, so far, such a near-field feeding configuration has not been investigated with a single plasmonic helix.

Here, we will work on new POA by translating into optical regime, the concept of traveling-wave helical antenna. This new POA features a traveling-wave working principle, near-field feeding configuration, and circularly polarized radiation with an individual antenna.

3.2/ THE CONCEPT OF HELICAL ANTENNA FOR LIGHT

3.2.1/ HELICAL ANTENNAS IN LOW-FREQUENCY REGIME

Helical antennas have the unique capability of generating circularly polarized (CP) radiations. They are widely employed in global positioning, ground stations for tracking satellites and data relay system [167]. The basic element of helical antennas is a conductor wire wound into a corkscrew shape. Depending on the handedness of the constituent helical wire(s), the output radiation can be either left- or right-handed. Helical antennas can work alone or in arrays to gain higher directivity [167]. Helical antennas can operate in different modes, depending on its dimensions with respect to the free-space wavelength [83, 167].

3.2.1.1/ DESCRIPTION OF THE HELICAL ANTENNAS

Figure 3.4 shows a schematic of a helical antenna with its geometrical parameters. Other useful geometric parameters of the helix can be expressed out of these parameters, including the diameter D_h ($D_h = 2R_h$), the circumference C ($C = 2\pi R_h$), the length of a single turn L_0 ($L = \sqrt{C^2 + S^2}$), the pitch angle α_h ($\alpha_h = tan^{-1}(S/C)$) and the total length of the wire L_t ($L_t = NL$), of the helix.

The above geometrical parameters can also be measured in the unit of free-space wave-

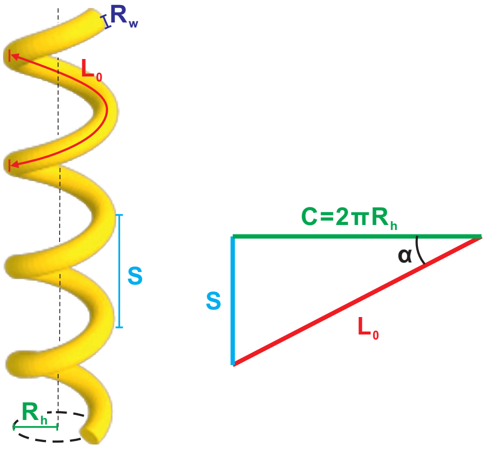

Figure 3.4: Schematic showing a single helix, whose geometrical parameters include the core radius R_h, the vertical pitch S, the total turn number N of the helix and the radius of the helix wire R_w.

length (λ). In that case, they will be represented with a subscription λ. For example, C_λ and S_λ mean C/λ and S/λ, respectively.

3.2.1.2/ OPERATION MODES OF LOW-FREQUENCY HELICAL ANTENNAS

Helical antennas can work in two principal operation modes: the normal mode and the axial mode. Figure 3.5 shows the far-field emission patterns and corresponding charge distribution along the helix of these two modes. Normal mode occurs when the total length (L_t) and the diameter (D_h) of the helix are far smaller than the working wavelength. As shown in Fig. 3.5 (a), the normal-mode radiation pattern has a doughnut shape with its maximum perpendicular to the helix axis. It is omnidirectional in the azimuth plane, resembling that of an electric dipole or a magnetic dipole orientated along the helix axis. Figure 3.5 (c) shows the corresponding transmission mode, where we can see the charges are separated by several turns. When the helix geometries are comparable to the working wavelength, eg., $C \sim \lambda_0$, the axial mode comes into play. As shown in Fig. 3.5 (b), the axial-mode radiation pattern contains a main lobe along the helix axis, witnessing a directional emission. Figure 3.5 (d) shows the corresponding transmission mode, where we can see the charges are separated by only one turn. Through careful design of the helix geometry, both the normal and axial modes can generate circularly polarized (CP) radiations.

For normal mode, the CP condition can be derived by treating the helix as a combination of tiny rod and loop arrays. Since the helix size is far less than the working wavelength, these rods and loops function as parallel electric and magnetic dipoles, whose far fields read:

$$E_\theta = j\eta \frac{k_0 I_0 S\, e^{-jk_0 r}}{4\pi r} \sin\theta \tag{3.1}$$

and

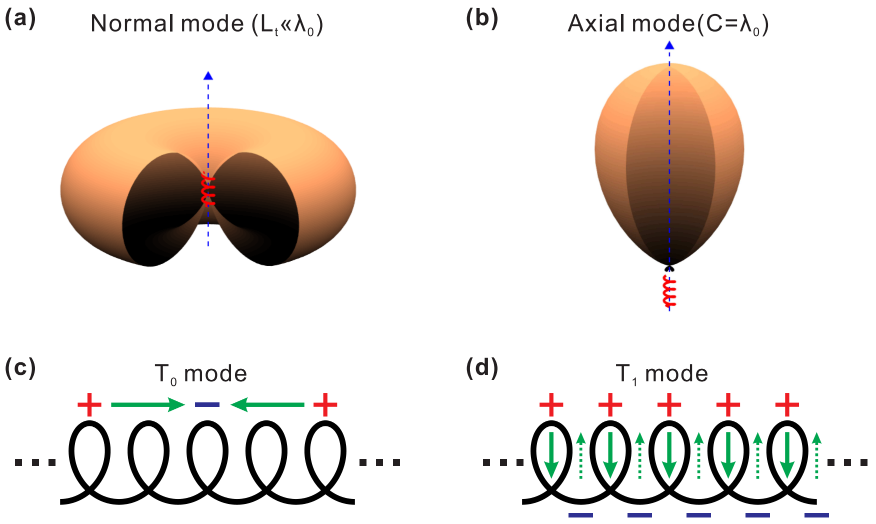

Figure 3.5: Helical antenna modes: (a) normal radiation mode and (b) axial radiation mode, (c) and (d) show the fundamental and high order transmission modes along an infinite helix wire, which correspond to the radiation modes shown in (a) and (b) respectively.

$$E_\phi = \eta \frac{(k_0 R_h)^2 I_0 e^{-jk_0 r}}{4r} \sin\theta \tag{3.2}$$

Equations 3.2 and 3.1 mean that the electric fields generated by the equivalent electric and magnetic dipoles are orthogonal and in time-phase quadrature. The CP condition can thus be satisfied when the axial ratio (AR) equals to 1, namely $|E_\theta|/|E_\phi| = 1$, which finally gives:

$$C = \sqrt{2S\lambda_0} \tag{3.3}$$

The CP condition shown in Eq. 3.3 is quite restrictive. Thus, the normal-mode helical antenna is narrow-banded and critical to antenna geometry. This mode is not widely used in practice in low-frequency regime antenna communication.

In opposition to the case of normal mode, the axial mode is far less demanding on antenna geometries. Besides, it is also advantageous in terms of directionality. Due to these merits, axial mode has much wider application than the normal mode. For axial mode, CP radiation can be reached by satisfying the following empirical rules:

$$\frac{3\lambda_0}{4} < C < \frac{4\lambda_0}{3} \tag{3.4}$$

$$12^\circ < \alpha_h < 14^\circ \tag{3.5}$$

Given the above two conditions, N will not affect much the spectral position of the circular polarization band. However, it can affect the maximum AR according to:

$$AR = \frac{2N}{2N+1} \tag{3.6}$$

As implied in 3.6, AR increases as N increases. Practically, N takes a value no less than 4 to ensure a high degree of circular polarization (DOCP). N can also affect the directivity (D) of helical antennas:

$$D = 12C_\lambda^2 S_\lambda N \tag{3.7}$$

As shown in 3.7, one can increase total helix turns to improve the antenna directivity. Other geometrical parameters of the helix are less demanding for circular polarization. For example, the wire thickness R_w can have a wide range from 0.005λ or less to 0.05λ or more. It has however to remain much smaller than the helix diameter.

3.2.1.3/ DIFFERENT MECHANISMS UNDERPINNING THE NORMAL AND AXIAL MODES

The transmission modes shown in Figs.3.5 (c) and (d) describe wave propagation behaviors along infinitely long helical wires. Real antennas are finite in length, which modifies these transmission modes.

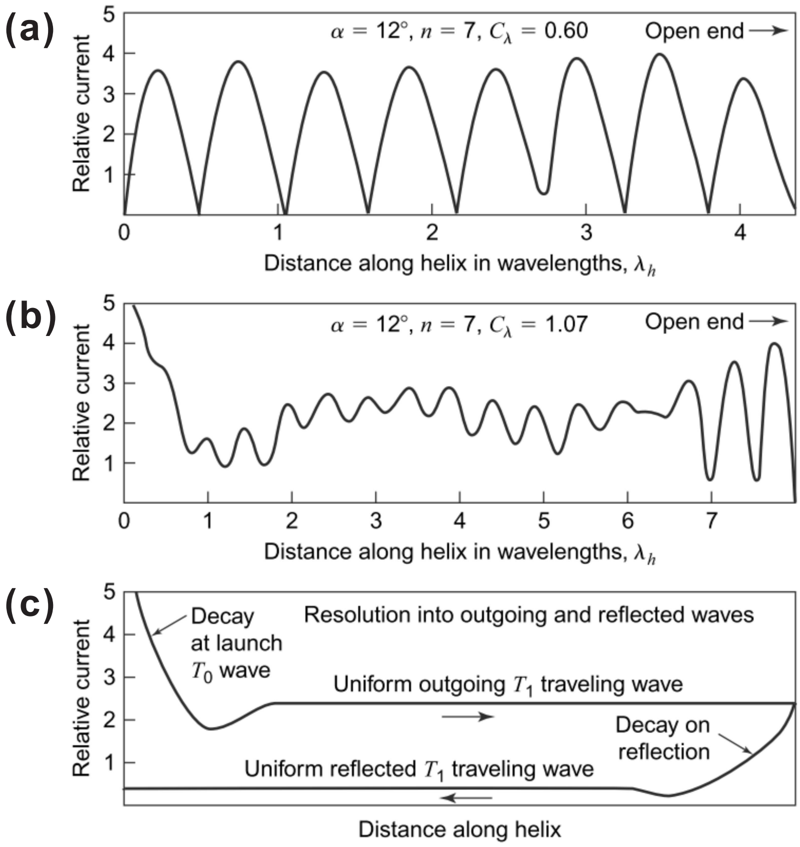

Figure 3.6: Typical current distributions measured along a helical antenna working at a wavelength (a) beyond the axial-mode operation region and (b) near the spectral center of the axial-mode region. (c) Analysis of the antenna current shown in (b) in terms of outgoing and reflected waves. [167]

Figure 3.6 shows the typical current distributions for the normal- and axial-mode helical antennas of finite lengths. As shown in Fig. 3.6 (a), at a larger wavelength ($\lambda_0 \sim 2C$, normal mode), the induced currents have almost a pure standing-wave distribution. When it comes to the axial-mode wavelength ($\lambda_0 \sim C$), current distribution shows a different behavior. As shown in Fig. 3.6 (b), the current amplitude decays exponentially near the launching end and oscillates near the open end. Notably, the current amplitude is almost uniform over a long distance in between these two regions. Such a current distribution is caused by the superposition of an outgoing wave and a reflected wave, at the open-end of the helix. Notably, the former has a overwhelmingly larger amplitude (see Fig. 3.6 (c)). Therefore, axial-mode and normal-mode helical antennas are dominated by standing-waves and traveling waves, respectively.

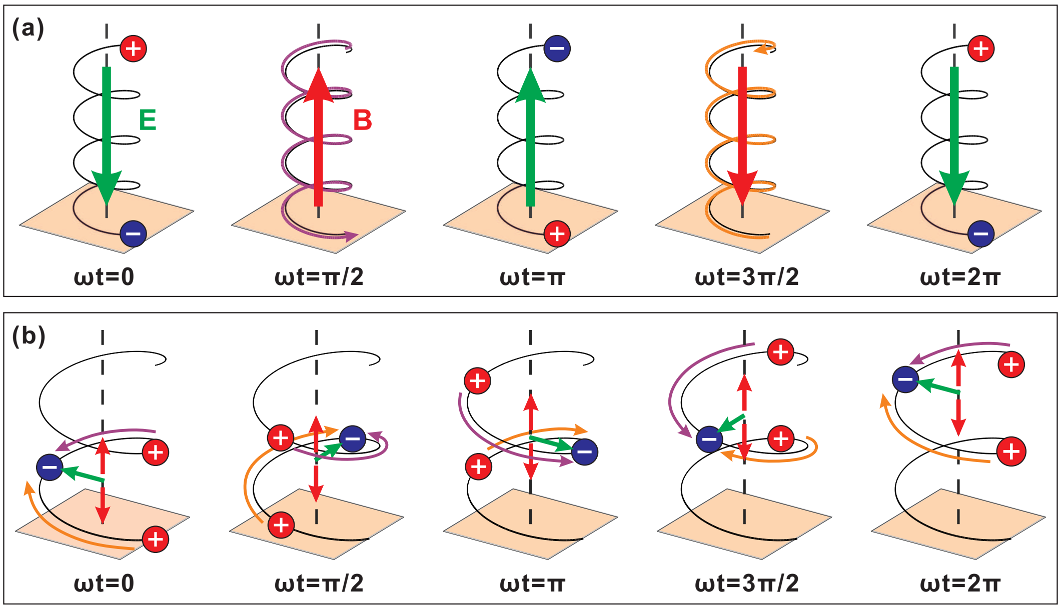

Figure 3.7: schematics of the time-evolution of induced currents and charges for a (a) normal mode and (b) axial mode, respectively. For clarity, only the very first current node is shown in (b) to represent the traveling wave. The red and blue disks with "+" and "-" sign represent positive and negative charges, respectively. The purple and orange curves with an arrow show the orbiting direction of the induced currents. Green and red straight arrows show the corresponding electric and magnetic fields, respectively. Notably, in (a) the electric and magnetic fields are parallel and have a relative phase shift of $\pi/2$, thus evidencing a signature of optical chirality. In (b), the electric and magnetic fields are always perpendicular.

Working with standing wave or traveling wave leads to a fundamental difference in the way to generating CP. Figures 3.7 (a) and (d) schematically show the time-evolution of the electric and magnetic fields in normal and axial mode helical antennas, respectively. As shown in Fig. 3.7 (a), normal mode causes maximum accumulation of electric charges at the two ends of the helix at a certain time. After that, due to discharging effect, circulating electric current will be induced, whose intensity peaks after a quarter period. The electric field caused by the accumulated charges is thus parallel to the magnetic field induced by the circulating currents. What is more, the two fields are phase-shifted by $\pi/2$. According to the definition of optical chirality (OC) [164, 191], this means the near-field of norm-mode antenna is chiral.

The near-field of an axial-mode helical antenna is completely different. As shown in Fig. 3.7 (b), electric charges travel along the helical wire, rather than oscillate between two fixed positions. The movements of the positive and negative charges lead to two electric currents circulating toward opposite directions. Magnetic fields induced by these two currents are thus all along the helix axis but opposite in direction. Meanwhile, as the positive and negative charges are separated by only a half turn, the corresponding electric fields are almost transverse to the helix axis. Therefore, the electric and magnetic fields are always perpendicular.

3.2.2/ HELICAL ANTENNAS IN OPTICAL REGIME

Helix is a chiral structure, namely it can not superpose with is mirror image. Recently, arrays of helices have been used as metamaterials for achieving broadband circular dichroism.

3.2.2.1/ HELICES IN METAMATERIALS

In 2009, Wegener's group first demonstrated an infrared broadband circular polarizer built with an array of gold helices, initiating the study of helical metamaterials [45]. Following that, intensive theoretical and experimental studies have been carried out to further improving the working bandwidth and circular filtering efficiency. These approaches take advantage of helices with tapered geometries [192, 193], intertwined helices [194, 195, 196, 197], helices composed of different materials [198], etc.

Figure 3.8 shows the work from Gansel et al [45], with helices characterized by $N = 2$, $R_h = 0.6$ μm, $S = 2$ μm. When packed in a square lattice of 2-μm period, these helices block circularly polarized light with the same handedness and transmit the opposite handedness, over a wide wavelength range near to one octave. This broadband operation was attributed to the combination of three resonant modes. Figure 3.8(b) shows the helix current distributions corresponding to these three modes, where we can see a standing-wave signature.

Other research groups used glancing angle deposition or focused ion/electron beam based technology to fabricate helical metamaterials [200, 201, 202, 203, 204, 205, 206, 207]. As these techniques enable a smaller helix dimension, chiro-optical responses have been reported in visible regime. Figures 3.9 (a) and (b) show triply-intertwined platinum and carbon helices fabricated with focused ion beam induced deposition (FIBID). The helix geometry reads: $R_h = 150$ nm, $R_w = 50$ nm, $N = 1$, and $S = 700$ nm. Figures 3.9 (c) and (d) show the chiral responses obtained with the two helical metamaterials.

Recently, it has been numerically shown that resonant plasmonic helices, which are much smaller than the wavelength, possess chiral eigenmodes (see Fig. 3.10 (a)) featuring parallel electric and magnetic fields. Such a chiral eigenmode can be excited by linearly-polarized light propagating perpendicularly to the helical axis. By twisting four single-turn helices together, one can obtain a near field with strongly enhanced optical chirality. In Fig. 3.10 (b), an optical chirality enhancement up to 200-fold occurs inside the helices, showing the perspective of resonant plasmonic helices in optical chiral sensing [164].

Axial-mode helical antenna is a traveling-wave antenna, which however is not the case with helical metamaterials. For example, in Gansel's case the induced currents in the

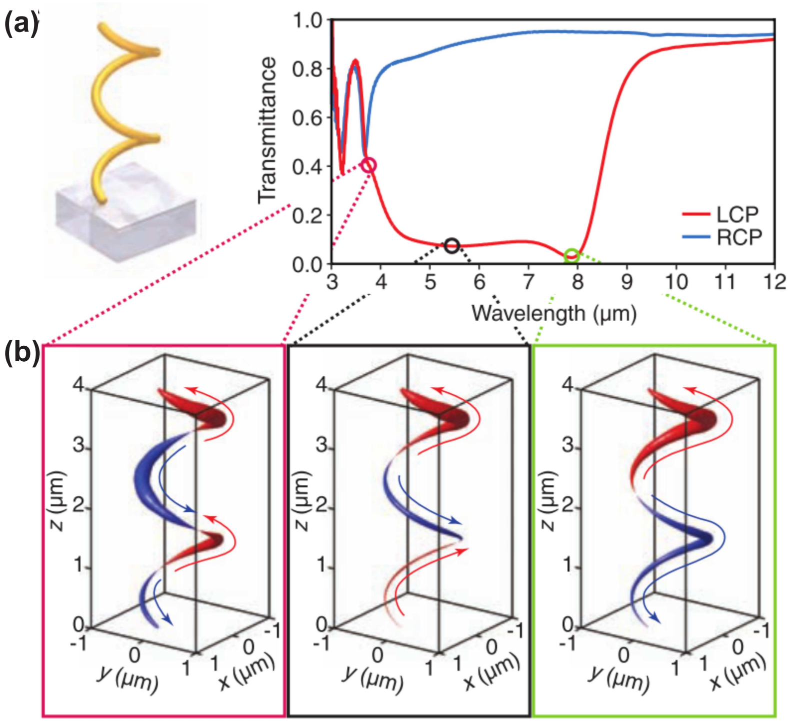

Figure 3.8: Helical metamaterial works as circular polarizer: (a) broadband chiral response (b) snapshots of the induced current along the helix, showing standing-wave characteristics along the structure. [45]

helical metamaterial show a standing-wave characteristic (Fig. 3.8). In the case shown in Fig. 3.9, chiral responses have been found with dielectric helical metamaterials. However, considering their deep subwavelength dimension, those dielectric helices are not likely to support traveling waves. The two examples hint that helices in metamaterials may not rely on axial-mode operation to attain the demonstrated functionalities. In another case shown in Fig. 3.10, it is obvious that the helices work on normal mode. Therefore, the helices used in metamaterials basically work out of the traveling-wave regime.

3.2.2.2/ TRAVELING-WAVE HELICAL PLASMONIC ANTENNA

Hereafter, we will introduce a new optical antenna concept, namely the traveling-wave helical plasmonic antenna (TW-HPA). Figure 3.11(a) shows a simple prototype, consisting of a 4-turn gold helix and a straight rod connected at one of its ends. The helix shows a core radius (R_h) and a vertical pitch (S) of 50 nm and 200 nm, respectively. The straight rod is used to control the electromagnetic components of the wire mode. In order to reduce reflections at the rod-helix junction, a round sphere is inserted to join the two elements. [31].

For simplicity, we consider the nano-wire as solid and has a circular cross-section. The fundamental mode of such a nano-wire is rotation-symmetric around the wire axis and radially polarized [208]. Given this field symmetry, we simply use an electric dipole orientated parallel to the straight rod to excite the helix. The dipole source is set 14 nm away from the rod end to ensure a good coupling efficiency while avoiding quenching effects

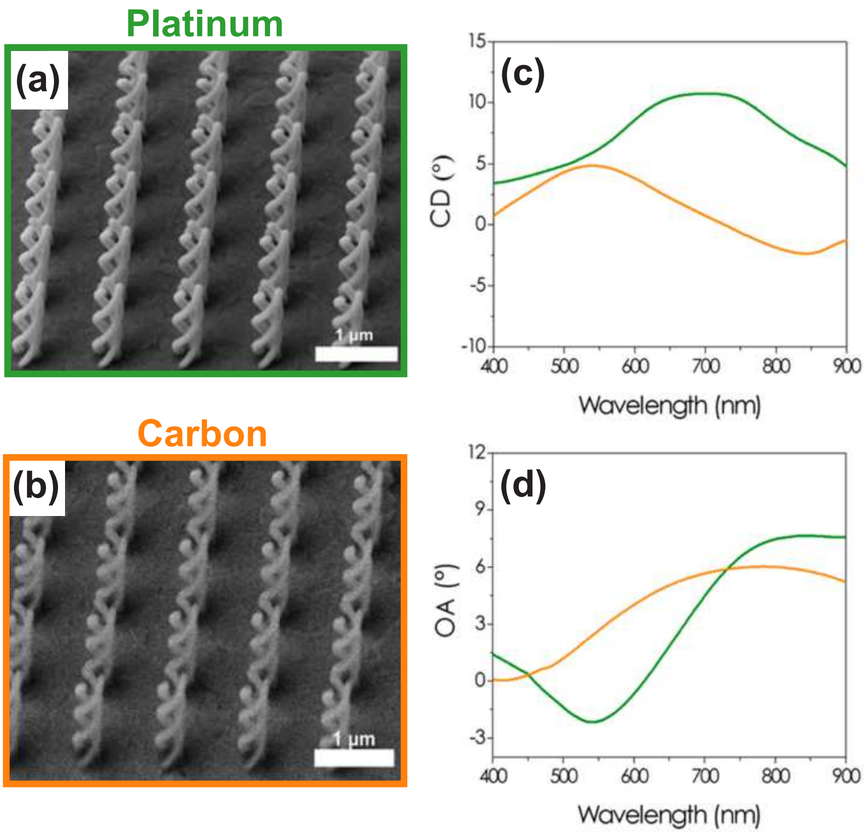

Figure 3.9: (a) and (b) SEM images of carbon and platinum helical metamaterials fabricated with FIBID, respectively. Those helices featuring a triply-intertwined configuration and ultra-small dimensions. (c) and (d): measured circular dichroism and optical activity spectra for the two metamaterials, respectively.[199]

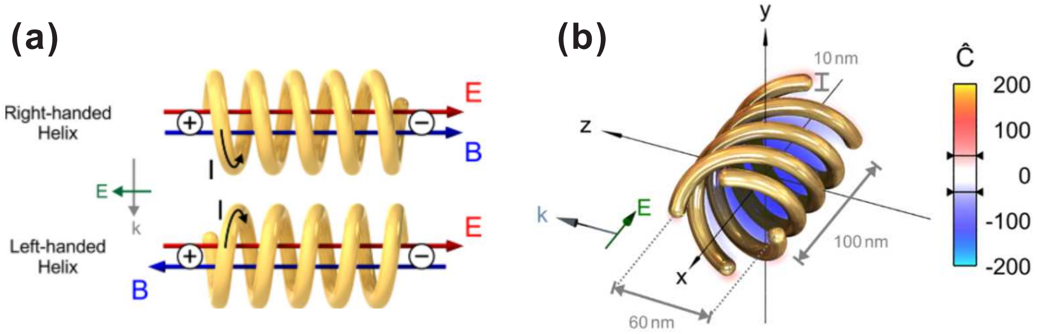

Figure 3.10: Chiro-optical near-fields produced by resonant plasmonic helices. (a) Schematics for the chiral eigenmodes of a single plasmonic helix with opposite handedness (b) False color plot of the optical chirality enhancement factor, in the near-field of an intertwined 4-helix structure. [164]

(see Fig. 3.11 (a)). We numerically study the spectra and electric field distributions of such a HPA prototype to identify its traveling-mode of interest. More simulation details will be specified in Section 3.3.1.

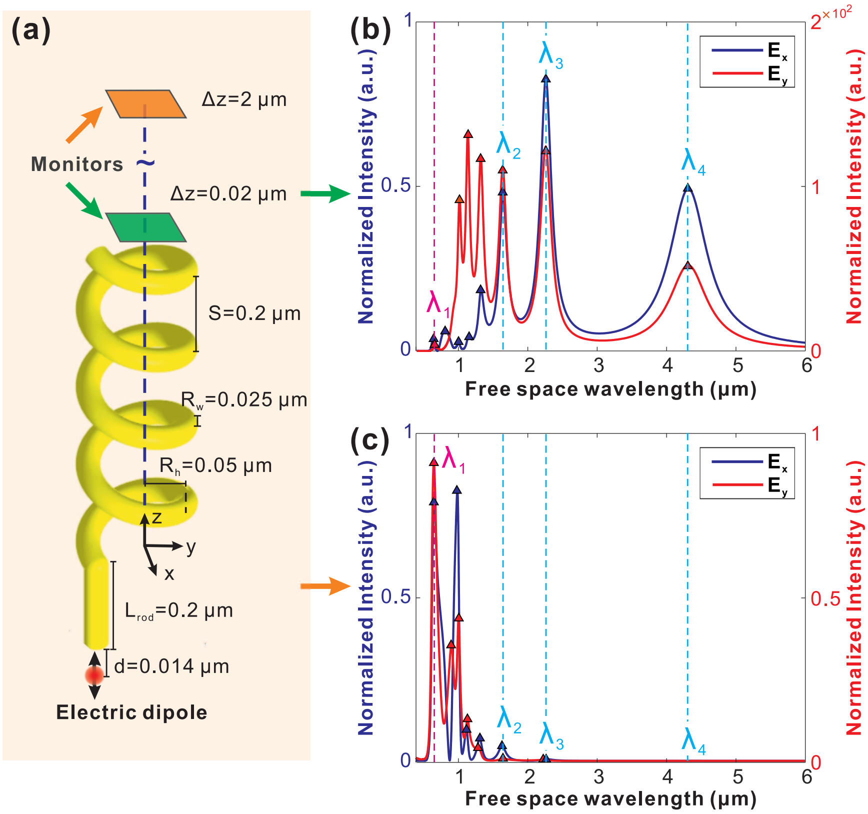

Figure 3.11: (a) A schematic of the prototype HPA, consisting of a 4-turn helical nano-wire (along z–axis), a straight rod and a round sphere to join the two parts. The HPA is fed by a z–oriented electric dipole source in end-fire configuration. FDTD simulation is used to study the spectral response of the TW-HPA. The green and orange planes represent the monitors used to collect the electric field data of the TW-HPA. They are placed 20 nm and 2 μm far away from the open end of the helix, with their centers on the helix axis. (b) and (c) show the intensity spectra (normalized by the dipole source) of the two transverse electric components (E_x and E_y, which are responsible for the CP polarization) obtained with the two monitors. Dash vertical lines in magenta and light blue show positions of the spectrum peaks at free-space wavelengths $\lambda_1 = 658$ nm, $\lambda_2 = 1641$ nm, $\lambda_3 = 2259$ nm and $\lambda_4 = 4310$ nm.

Figures 3.11 (b) and (c) show the intensity spectra of the transverse electric components (E_x and E_y), obtained in the near- and far-fields at a distance of 20 nm and 2 μm from the helix end, respectively. The two sets of spectra show distinct peak behaviors. Particularly, the ones obtained in the near-field have notable peaks at longer wavelengths λ_4, λ_3 and λ_2, which however are far less prominent in the far-field spectra. Opposed to that, the peak at a shorter wavelength (λ_1) has been dramatically enhanced as the monitor distance increases, which is in favor of an axial mode operation.

In order to clarify the two working modes of the HPA, we study the near- and far-field intensity profiles at λ_1 and λ_4. Figures 3.12 (a) and (d) show the corresponding intensity distributions in the $x0z$ cross-section plane of the helix. In Fig. 3.12 (d), the helix optical mode has two maxima at the two ends of the HPA and a minimum in the middle, showing a clear standing-wave signature. However, in Fig. 3.12 (a), though the intensity decays fast at the first turn, it remains almost constant among the rest of the helix. The absence of well-defined intensity node indicates the traveling-wave nature of the helix wire mode at this wavelength. The two modes can also be confirmed by checking the radiation patterns. As can be seen from Fig. 3.12 (e), intensity on the helix axis exhibits the maximum value in the near field, which however turns to the minimum as it transits to the far field. The maximum radiation directions, marked by the two red arrows, are normal to the helical axis. The final far-field emission pattern develops a doughnut shape as shown in Fig. 3.12 (f), showing clearly that the HPA works on normal mode at a wavelength of 4310 nm. In contrast, one can identify in Fig. 3.12 (b) a significant radiation along the helical axis, as indicated by the red arrow. This axial radiation lobe can also be seen in the far-field emission pattern shown in Fig. 3.12 (c). Therefore, the HPA works in the axial mode at a wavelength of 658 nm.

We further extract the intensity and axial ratio (AR, see Section 1.1.2) spectra of the prototype HPA from the further monitor ($\Delta z = 2\ \mu$m). These results are shown in Fig. 3.13 with the blue and red curves, respectively. Notably, the peak of the red curve represents an AR value as high as 0.99 at the wavelength of 701 nm, indicating that an almost per-

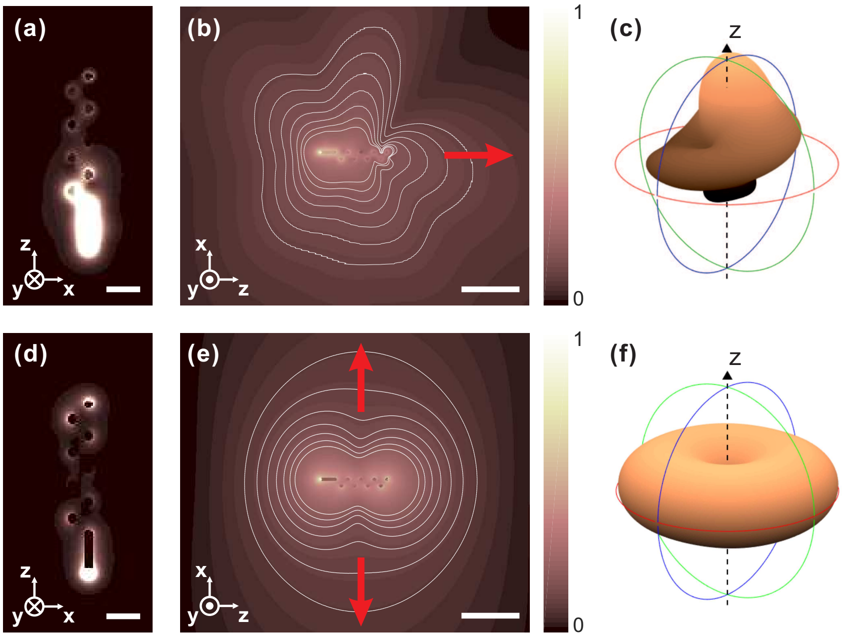

Figure 3.12: Near-field and far-field properties of the helical plasmonic antenna (HPA) working on axial and normal modes. The HPA has the same geometries as shown in 3.11 but working at different wavelengths, which are 658 nm (λ_1) for (a~c) and 4310 nm (λ_4) for (d~e). (a,d) pseudo-color plots for the normalized electric field intensity closely around the HPA, where regions around the dipole source have been saturated for a better view of the helix wire modes. (b,e) pseudo-color plots for the electric field intensity in a larger area around the HPA. In (b) and (e), the intensities have been taken logarithm before normalization, for showing the transition from near-field to far-field. Red arrows in (b) and (e) mark the directions with the maximum far-field radiation. (c,f) intensity radiation patterns of the HPA constructed via near-field to far-field projections. The near field data are recorded with box monitors enclosing the HPA, which are finally projected to a far-field sphere with a radius of 100 m.

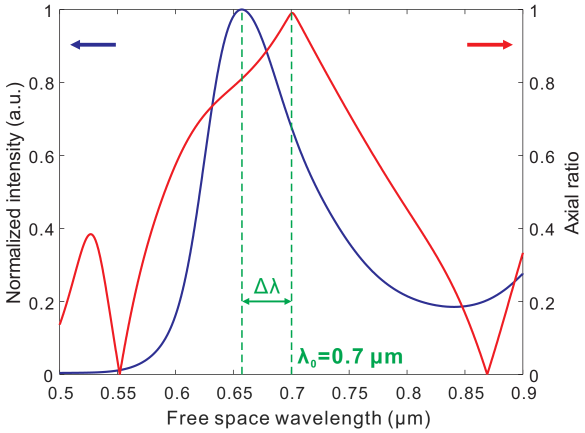

Figure 3.13: Far-field spectra of the prototype HPA, where the blue and red curves represent the intensity and AR spectrum, respectively. To obtain the blue curve, the raw far-field intensity spectrum has been normalized twice: first with the intensity spectrum of the dipole source and then with its own maximum value to offer a clear view. The AR spectrum is constructed with the spectra data of the two transverse electric components (E_x and E_y).

fect on-axis CP far-field has been reached at this wavelength. Interestingly, the intensity peaks at a different wavelength ($\lambda = 658$ nm). This spectral shift between the AR and intensity peaks confirm that the axial-mode HPA is non-resonant. This phenomenon originates from the directional emission of the antenna (Fig. 3.12 (c)). It is noted that, the CP conditions for the HPA are far from those predicted by classical antenna theory. According to Eq. 3.4, our HPA with a radius of 50 nm should gain a maximum AR around a wavelength of 314 nm, which is far from the actual value 701 nm. Besides, the HPA has a pitch angle of $32.48°$, which is out of the classical pitch angle range $12° \sim 14°$. Those differences signify that our HPA follows a different scaling law from the classical helical antennas, which is a common phenomenon existing between the low-frequency and plasmonic optical antennas [209].

3.2.3/ TRAVELING-WAVE HPA (TW-HPA): GENERATING CP LIGHT VIA SPIN-ORBIT INTERACTION

As discussed in former sections, the axial-mode TW-HPA relies on traveling waves. In this section, we will introduce the spin-orbit interaction (SOI) on these traveling waves, at the origin of the emission of CP light. More rigorously, this SOI is an orbit-to-spin transfer process. The TW-HPA relies on the propagation of surface plasmons (SPs) along the helical wire. Because the plasmonic helix plays as a chiral waveguide operating near cutoff, the propagation length of the SPs is dramatically reduced and its energy is efficiently transfered to free-space photons.

In a quantum view, propagating SPs carry linear momentum:

$$\boldsymbol{p}_{sp} = \hbar \boldsymbol{k}_{sp} = \hbar k_{sp} \hat{k}_{sp} \tag{3.8}$$

per plasmons (in $\hbar$ units). Here, k_{sp} and $\hat{k}_{sp}$ denote the magnitude and unit directional vector of $\boldsymbol{k}_{sp}$, respectively. k_{sp} has the following form:

$$k_{sp} = \frac{2\pi}{\lambda_{eff}} \tag{3.9}$$

In Eq. 3.9, λ_{eff} represents the effective wavelength of the SPs. Propagating along the helical wire, SPs gain an extrinsic orbital angular momentum ($\boldsymbol{J}_{sp}$), which can be expressed as:

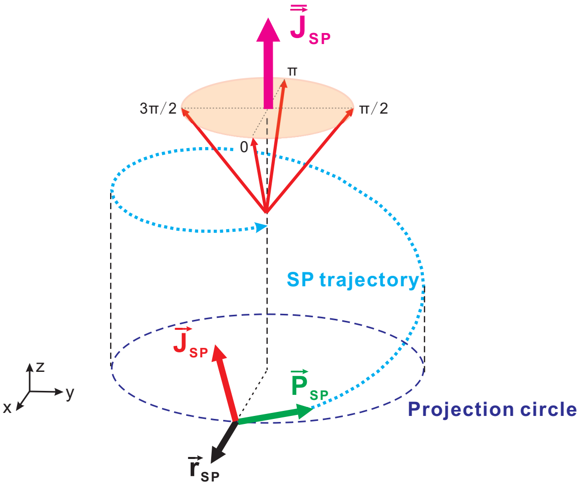

Figure 3.14: Schematic showing the optical angular momenta associated with the helical SPs.

$$\boldsymbol{J}_{sp} = \boldsymbol{r}_{sp} \times \boldsymbol{p}_{sp}, \tag{3.10}$$

where $\boldsymbol{r}_{sp}$ is the position vector. We have:

$$\boldsymbol{r}_{sp} = R_h \hat{r}, \tag{3.11}$$

where R_h and $\hat{r}$ denote the magnitude and the unit directional vector of $\boldsymbol{r}_{sp}$. Considering the rotational symmetry of the problem and $\boldsymbol{r}_{sp}$ perpendicular to $\boldsymbol{p}_{sp}$, we have:

$$\bar{\boldsymbol{J}}_{sp} = K\hat{\boldsymbol{z}}, \tag{3.12}$$

with:

$$K = \frac{2\pi R_h}{\lambda_{eff}} \cos\alpha \tag{3.13}$$

Helical antenna radiates a directional beam with the major power flow along its axis (z-axis). Considering an emission described by a spin angular momentum (SAM) orientated along $(0z)$ ($\boldsymbol{s} = \sigma\hat{\boldsymbol{z}}$ with $\sigma = \pm 1$), SOI imposes: $\bar{\boldsymbol{J}}_{sp} = \boldsymbol{s}$. Note that the transverse SAM of the wire mode is equal to zero, owing to the mode symmetry along the wire axis. Mode dissymmetry around cutoff of the overall structure could make transverse SAM appear. Then, connection of momentum matching could be realized. However, we think that near cutoff, the electric field of the wire may become purely transverse, i.e., linearly polarized. This should then imply a null transverse SAM.

According to SOI ($\bar{\boldsymbol{J}}_{sp} = \boldsymbol{s}$), we find that CP is generated by the TW-HPA when:

$$\lambda_{eff} = 2\pi R_h \cos\alpha \tag{3.14}$$

If the antenna operates at cutoff, we have linear momentum matching between the SPs and the free-space propagating wave ($\boldsymbol{k}_{sp} = k_0$). Operation in this ideal case thus implies:

$$\lambda_0 = 2\pi R_h \cos\alpha \tag{3.15}$$

to reach a CP emission.

SOI analysis within the TW-HPA thus leads to a geometrical dynamic condition to reach CP that is closer to that provided for the low-frequency helical antennas.

In a general case, the far-field radiation is elliptically polarized. Assuming the angular momentum conservation still holds between the EOAM of SPs and the SAM of far-field emissions, we have:

$$\bar{\sigma} = \sigma_{SP}\frac{2\pi R_h}{\lambda_{eff}}\cos\alpha_h, \tag{3.16}$$

where $\bar{\sigma}$ $(1 \leq \bar{\sigma} \leq 1)$ is the average SAM factor of the far-field emission and σ_{SP} $(\sigma_{SP} = \pm 1)$ denotes the handedness of EOAM carried by the traveling SPs. R_h, α_h is the radius and pitch angle of the helix, respectively. Equation 3.16 signifies that the helix handedness defines the helicity of TW-HPA emission. It also implies a scaling relation between the helix dimension and spectral behavior of the TW-HPA.

3.3/ Design of TW-HPAs as subwavelength circular polarizer

In this section, we will detail the design of TW-HPA for reaching CP at telecommunication wavelengths. We will start from the design of a single gold helix and end up with the final TW-HPA, which consists of the configuration of a gold helix and a nano aperture as a dipolar feed element. In these studies, the dielectric functions of considered materials excepted from carbon are obtained from the library of Fullwave software (FDTD method [161]). The carbon material, which will be used later to build a realistic TW-HPA, is assumed to be amorphous. Its dielectric function is interpolated from the published experimental data [210].

3.3.1/ Design of the helix

We start from the prototype TW-HPA shown in Section 3.2.2.2 but with a larger helix radius ($R_h = 180$ nm) to red-shift the axial ratio peak.

Figure 3.15 specifies the simulation configuration. As shown, the simulation volume (blue dash rectangle) is defined regarding the overall helix dimensions (green dash rectangle)

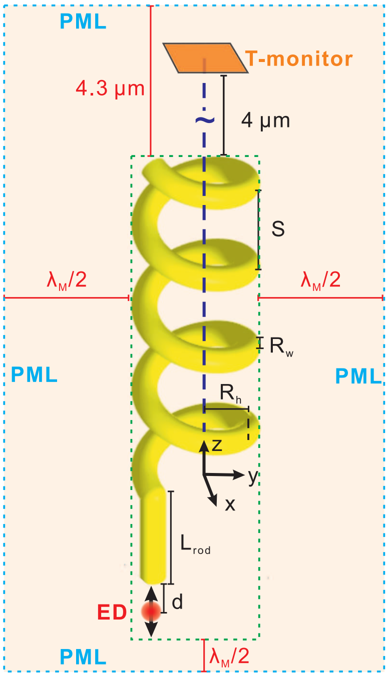

Figure 3.15: Schematic of the FDTD simulation model for studying the effects of the helix geometries on the AR spectrum.

and the longest wavelength (λ_M) involved in the simulations. The upper boundary ($+z$) of the simulation volume is 4.3 μm far from the open end of the helix (the one not connected to the straight rod). The other five boundaries ($\pm x$, $\pm y$ and $-z$) extend $\lambda_M/2$ far from the helix. The simulation volume is surrounded by perfect matching layers (PML) at all six boundaries to avoid parasitic physical reflections. A fine meshgrid of 5 nm is adopted in the portion enclosing the helix while a larger meshgrid of 30 nm is applied to the periphery. A z-orientated electric dipole (ED) is placed right under the end of the straight rod, 14 nm away from the nanostructures.

The spectral response of the TW-HPA is obtained with a gaussian excitation described by a single temporal pulse. The wavelength center and total duration (T) are set as 1.5 μm and 0.75 μm (cT with c the vacuum light speed), respectively. The time-varying electric field is calculated at a single cell located on the helix axis, 4.3 μm away from the end of the helix, along (0z). Given $\lambda_M < 2.5$ μm, such a monitor/helix spacing allows to reliably study the far-field properties of the helix over the full wavelength range of interest. The spectra of the vector components E_x and E_y are calculated by Fourier-transforming this result. From these results, the axial ratio (AR) is deduced as a function of the wavelength. To simulate the electromagnetic field distributions, the electric dipole emission is set to work in continuous-wave regime at desired wavelengths.

We tune each helix geometric parameters to see their influences on the AR spectrum. Those parameters include the helix radius (R_h), the wire radius (R_w), vertical pitch (S), total turn number (N) and helix handedness (see Fig. 3.15). We mainly use two criteria to evaluate our antennas: 1) maximum AR value, which shows the perfectness of CP and 2) CP band, where we follow the criterion for low-frequency antennas that an antenna with $AR > 0.5$ can be seen as circularly polarized [211]. Our study ends up with an optimum design, which gives perfect CP far-field at a wavelength of $\lambda_0 = 1550$ nm. All the design and optimization processes are carried out with Fullwave (a commercial FDTD software).

3.3.1.1/ EFFECT OF THE HELIX VERTICAL PITCH

We first tune the vertical pitch from 240 nm to 840 nm while keeping other geometries unchanged: $R_h = 180$ nm, $R_w = 25$, $N = 4$. The corresponding pitch angle (α_h) ranges from $12.0°$ to $36.6°$. As shown in Fig. 3.16, the AR spectrum at $S = 240$ nm contains strong oscillations from 1.11 μm and 1.32 μm, as well as a dull AR peak ($AR \sim 0.6$) at a wavelength of 1630 nm. Given the small distance between adjacent helix turns (190 nm), this may be caused by the SP mode coupling between them. When S increases to 340 nm ($\alpha_h = 16.7°$), the strong oscillations greatly cease while the dull peak becomes prominent at a wavelength of 1.65 μm. Notably, this meaningful AR peak gradually reaches the highest value as S increases from 340 nm ($\alpha_h = 16.7°$) to 740 nm ($\alpha_h = 33.2°$), which however drops slightly as S further enlarges. $S = 740$ nm ($\alpha_h = 33.2°$) is optimal, which gives an AR value as high as 0.99. In the previous TW-HPA case ($R_h = 50$ nm, $R_w = 25$, $N = 4$, see Section 3.2.2.2), where $\alpha_h = 32.48°$ gives the best AR peak, we can see the optimal pitch angle condition has been respected even when the helix radius has been enlarged by more than three times.

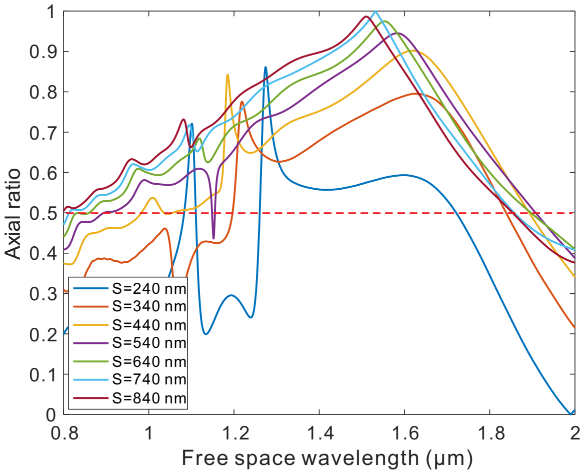

Figure 3.16: AR spectra of an TW-HPA with various S values ranging from 240 nm to 840 nm. Other geometric parameters are the same for all helices: $R_h = 180$ nm, $R_w = 25$ nm, $N = 4$.

In addition, we can see a trend in the spectral position of the AR peak: it steadily shifts to a shorter wavelength as S increases from 340 nm to 740 nm. Considering the fact that neither the helix circumference (C) nor the length of a single turn (L) decreases in this process, the blue shift of the AR peak is quite counter-intuitive. However, we find this could be explained by the scaling relation derived from EOAM-to-SAM transfer, namely Eq. 3.16. When S approaches the optimal value from 340 nm, one can expect the spin factor α on the right side of Eq. 3.16 increase as well. Meanwhile, the increasing S lowers the $\cos\alpha_h$ factor on the left side. Thus, to equal the two sides of Eq. 3.16, the effective wavelength of the wire mode λ_{eff} has to decrease, which leads to a blue shift of the AR spectra peak. This blue-shift remains when S further increases. We think it could be because AR and thus emission helicity ($\bar{\sigma}$) decreases slower than $\cos\alpha_h$ (cf. Eq. 3.16).

3.3.1.2/ EFFECT OF THE WIRE THICKNESS

First, we fix R_h (180 nm) and S (740 nm) and tune R_w to see whether the optimal CP condition holds or not. Figure 3.17 shows the AR spectra obtained with R_w varying from 25 nm to 65 nm. We can see that the perfect AR peak degrades when R_w differs from 25 nm. That means, R_w can affect the optimal α_h significantly, which is opposite to low-frequency helical antennas.

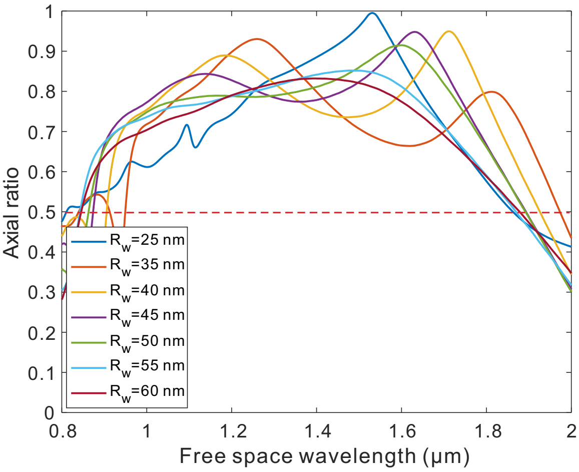

Figure 3.17: Influence of the helix wire radius (R_w) on the far-field polarization property of TW-HPA. Solid lines with different colors show the AR spectra of HPAs with various R_w values ranging from 25 nm to 60 nm. Other geometric parameters are the same for all helices: $R_h = 180$ nm, $S = 740$ nm, $N = 4$. The red dash line shows an axial ratio of 0.5.

Then, we tune S at each R_w value to investigate the optimal CP condition. Interestingly, we find two optimal S values for thick wires (R_w between 40 nm to 60 nm) while only one for thin wires (R_w: 25 nm and 35 nm). The AR spectra corresponding to those optimal S values are shown in Fig. 3.18 (a) and (b), where we divide them into two groups according to their similarity.

For thick wires, the two optimal S values give different AR spectra. Take $R_w = 60$ nm for example, a S value of 540 nm gives a CP band (900 nm, see Fig. 3.18 (b)) much broader than a lower S value of 195 nm (320 nm, see Fig. 3.18 (a)). The former case is highly desired here for realizing a broadband operation. We think that the lower optimal S value could be related to the interaction of SPs between adjacent helix turns. Such an interaction is common in coupled plasmonic systems, which leads to SP mode hybridization and thus a spectral splitting [212, 213]. Indeed, the AR peaks given by the two optimal S values are at different positions: one is around 1.68 μm while the other is about 1.50 μm. Besides, there exists only one optimal S value for helices with thinner wires, which might be because the coupling between different turns is lower in these cases.

Another phenomenon we can see from Fig. 3.18 is that the CP band enlarges as the wire thickness decreases. This can be explained by the dispersion of SP wire mode in those wires, as shown in Fig. 3.19. We calculated those curves by following Novotny [208] and using the dielectric function of gold built in Fullwave (a commercial FDTD software).

As shown in Fig. 3.19, these dispersion curves show a good linearity when the free space wavelength is larger than 0.8 μm. Significantly, the slope of the dispersion curve decreases as R_w decreases. Recalling Eq. 3.16, this means that a larger range of free space wavelengths can approach the CP condition, which causes a broadening CP band.

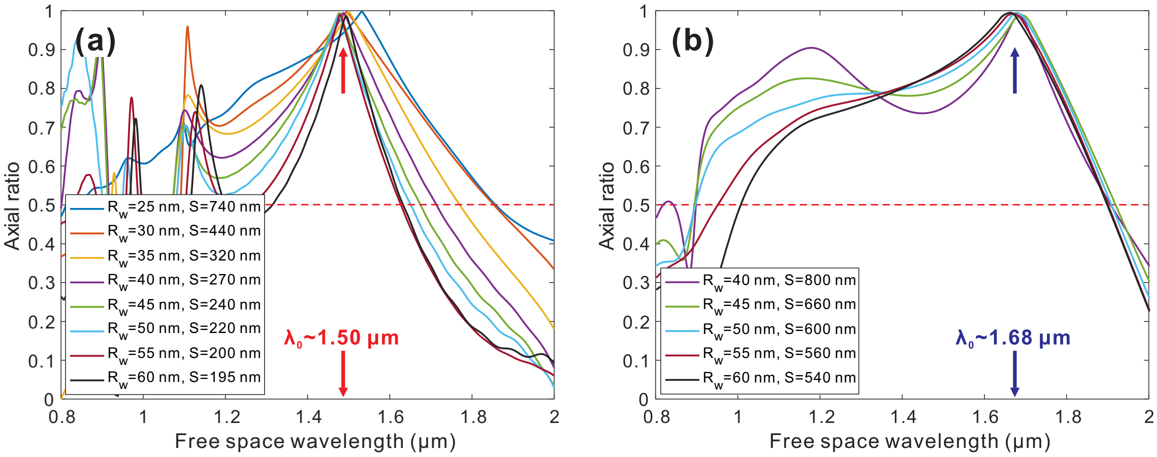

Figure 3.18: Axial ratio spectra of HPAs with various wire radii (R_w ranging from 25 nm to 60 nm) and optimal vertical pitches (S) that enable an AR peak. Note for helices with different wire radius, the total number of such optimal α_h values are different, which is one when R_w ranges from 25 nm to 35 nm and two when R_w ranges from 40 nm to 60 nm. According to their similar shapes, those AR spectra have been divided in two groups, i.e. (a) and (b) for a better view. All helices have the same radius($R_h = 180$ nm) and total turn number ($N = 4$). The red dash line shows an axial ratio of 0.5.

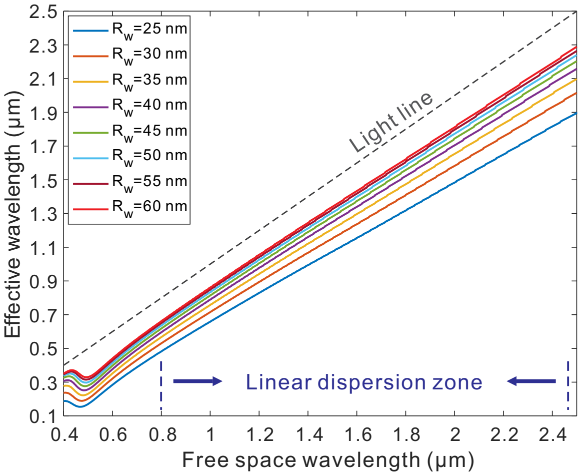

Figure 3.19: Dispersion relations of gold nano-wires with various radii ranging from 25 nm to 60 nm.

Above, we have discussed the influence of R_w on the polarization properties of the TW-HPA. An almost perfect AR peak and a broad CP band can be reached with thick gold wires (R_w:$50 \sim 60$ nm). This is very encouraging as helices with such wire thicknesses are experimentally achievable.

3.3.1.3/ EFFECT OF THE HELIX RADIUS

According to Eq. 3.16 and the linear dispersion relation of the SP wire mode (see Fig. 3.19), one can expect that the spectral position of AR peak scales linearly regarding the circumference or radius of the helix. In order to validate this assumption, we study the AR spectrum by tuning the helix radius (R_h) while fixing the other parameters, i.e. α_h as the optimal values obtained before.

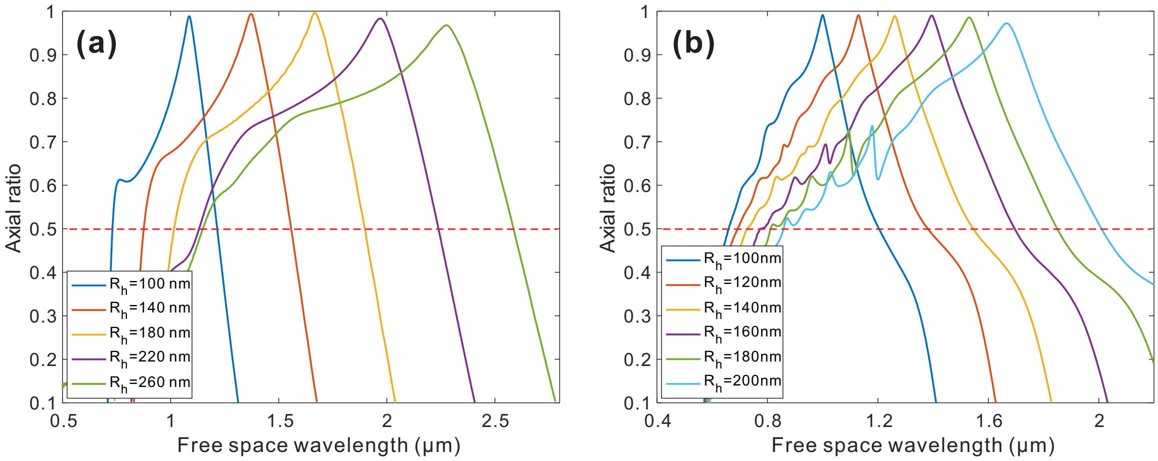

Figure 3.20: (a) and (b) show the AR spectra for two sets of helices, whose wire thickness is fixed as 60 nm and 25 nm and pitch angle is 14° and 39°, respectively. Here, we only plot the axial ratio spectra around its peak to have a better view.

We basically try with two representative wire thicknesses, namely 60 nm and 25 nm. R_h is tuned from 100 to 260 nm for $R_w = 60$ nm, while from 100 to 200 nm for $R_w = 25$ nm. We consider a narrower R_h range in the latter case to save simulation time. The results of the two cases are shown in Fig. 3.20 (a) and (b), respectively. In both cases, the AR peak undergoes a spectral red-shift as we increase R_h with a fixed increment. Meanwhile, the AR peak basically maintains a high value that is larger than 0.96. It means that one can simply tailor the helix radius to shift the AR peak from one to another.

Further, we can see the CP spectral bandwidth enlarges considerably as R_h increases. Interestingly, the spectral shift of its upper boundary roughly keeps a fixed ratio to that of the lower boundary, which takes an average value of 1.82 and 3.95 in Fig. 3.20 (a) and (b), respectively. Similar phenomenon can be found in low-frequency helical antennas, where the CP band reads $3C/4 < \lambda < 4C/3$ (C: helix circumference). If one tunes the helix radius, the spectral shift of the upper and lower CP boundaries remains at a fixed ratio of 1.78.

3.3.1.4/ EFFECT OF THE NUMBER OF TURN

Figure 3.21 shows the AR spectra of helices with the turn number N ranging from 1 to 4. The peak of AR spectrum reaches a high value of 0.99 as N increases from 1 to 4, which coincides with the case in low-frequency helical antennas. For the latter, N needs to be no less than 3 to ensure a high axial ratio. Recalling Fig. 3.6, we can see that the helix current distribution does not take a typical traveling-wave form at the first and last

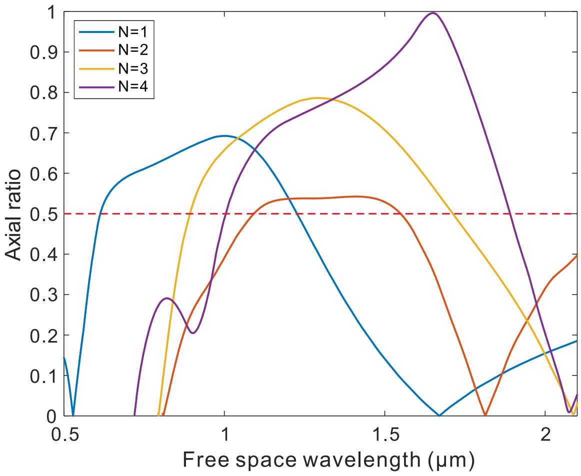

Figure 3.21: Axial ratio spectra of HPAs with various N values ranging from 1 to 4. Other geometric parameters remain identical for all helices: $R_h = 180$ nm, $R_w = 60$ nm, $S = 540$ nm. The red dash line shows an axial ratio of 0.5, above which an antenna can be thought as circularly polarized antenna.

turn. This means that only with a large N value, say 4, we are able to reach a traveling-wave antenna. A single TW-HPA thus needs a sufficient turn number ($N \geq 4$) to generate circularly polarized light.

3.3.1.5/ EFFECT OF THE HELIX HANDEDNESS

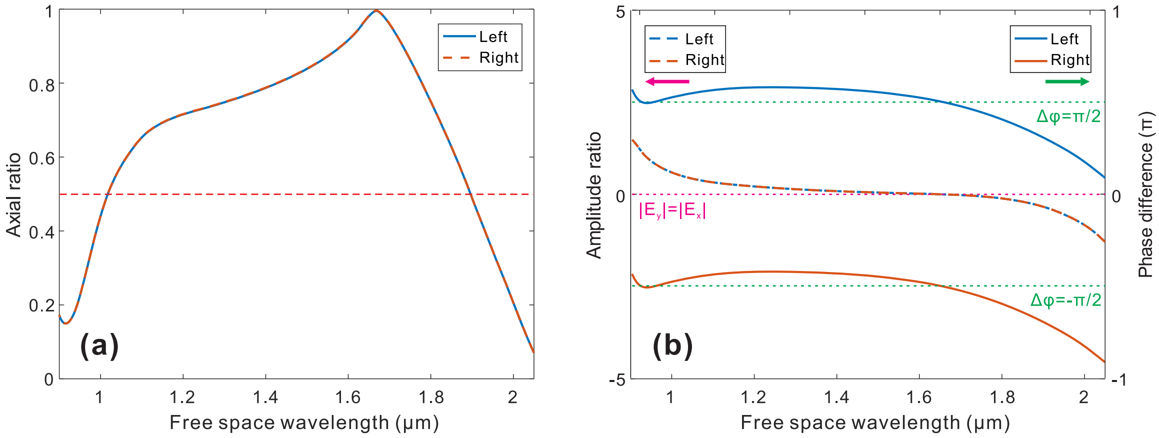

Figure 3.22: (a) Axial ratio spectra (on-axis calculations) of left and right-handed helices (b) Corresponding amplitude ratio ($\ln\left(|E_y|/|E_x|\right)$) and phase difference ($\varphi(E_x) - \varphi(E_y)$) spectra of the two transverse electric components of the far-field emission. The helices have geometric parameters: $R_h = 180$ nm, $R_w = 60$ nm, $S = 540$ nm, $N = 4$.

Figure 3.22(a) shows the AR spectra of two identical TW-HPAs except the handedness, which are opposite. The two spectra perfectly overlap. We can see from Fig. 3.22 (b) that the helicities of their emissions are opposite. They undergo the handedness of the helix.

This means that the antenna gives angular momentum to light through the SP swirling effect.

3.3.1.6/ CONCLUSIONS

Figure 3.23 shows the final design of a single TW-HPA for operation at 1550 nm. The turn number N is fixed to 4 and the helix wire radius R_w is set as 60 nm considering the capability of existing fabrication techniques. An axial ratio peak with a value as high as 0.98 has been reached at $\lambda = 1550$ nm. The CP wavelength band ($AR \geq 0.5$) ranges from 963 nm to 1769 nm, roughly one octave.

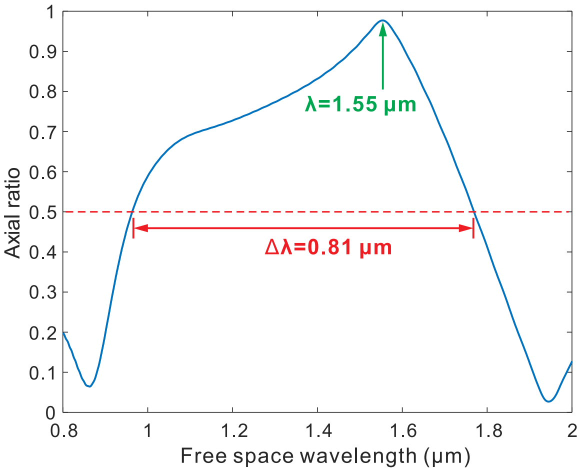

Figure 3.23: Aspect ratio spectra of a helix optimized for working at optical telecommunication wavelengths. The helix dimensions are: $R_h = 160$ nm, $R_w = 60$ nm, $S = 495$ nm, $N = 4$.

3.3.2/ NEAR-FIELD FEED ELEMENT

Previously, we have studied the helix coupled to a dipolar point-like source. Practically, this point-like source will be replaced by a dipolar aperture nanoantenna, which offers a background-free excitation of the plasmonic helix. We here explore different potential feed elements for the TW-HPA. We basically try three types of feed elements: the bowtie nanoaperture (BNA) [175, 180, 214, 215], the circular nanoaperture (CNA) [49, 50, 174, 216] and the rectangular nanoaperture (RNA) [47, 217, 216, 218]. Tuned on resonance, all of them can produce more or less intense electric fields as shown in Figs. 3.24 (a-c). We have shown that the plasmonic helix can be non-radiatively fed with a dipolar emitter put in close proximity (cf. Fig. 3.11). Likewise, we put these nanoapertures beside the TW-HPA pedestal for antenna feeding.

Due to the presence of the nanoapertures, the polarization property of the plasmonic helix can be detuned. These nanoapertures can also dramatically modify the intrinsic properties of the chiral structure, in terms of polarization and emission properties. We will see that with proper design, circularly polarized emission can be obtained in a final realistic TW-HPA. Moreover, as for its low-frequency counterpart, the presence of a ground plane will dramatically enhance the emission directionality. Well-defined axial lobe can be realized thanks to the ground plane.

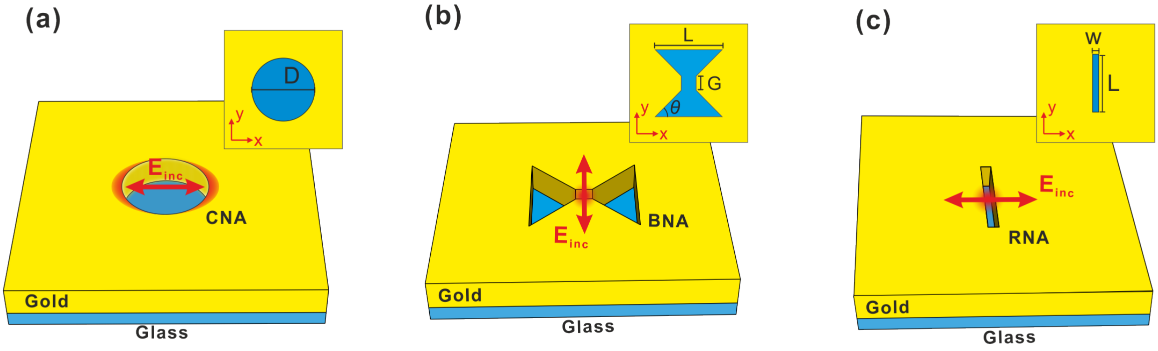

Figure 3.24: Schematics of (a) circular nano aperture (b) bowtie nano aperture and (c) rectangular nano aperture. The red arrows show the linear polarization of the excitation light (E_{inc}), which leads to enhanced electric fields in the regions marked by the red halos.

Given the axial-symmetrical radial polarization state of the plasmon wire mode (Fig. 3.27 (b)). We focus on compact apertures that develop a electric dipole moment upon illumination. The goal is to set the aperture in contact to the helix pedestal so that its dipole moment is parallel to the local electric field of the wire mode sustained by the nano-rod. We choose between three types of apertures: the bowtie nano aperture (BNA), the circular nano aperture (CNA) and the rectangular nano aperture (RNA) (Fig. 3.24). The circular aperture has modest field enhancement upon illumination, which has been rejected first. The BNA and RNA overcome cutoff problems of the CNA and thus lead to higher intensity enhancement. We finally retained the RNA which is easier to fabricate than the BNA. Moreover, the RNA is more adapted to be coupled to the helix, whose pedestal diameter is larger than 150 nm. Such a dimension is 3-fold larger than the typical gap size of the BNA. Therefore, mounting the helix pedestal in contact to the gap of the BNA is impossible due to the size compatibility. We avoid such problem with the RNA.

The initial TW-HPA geometry used to build the hybrid antenna (feed and helix) is defined with: $R_h = 160$ nm, $R_w = 60$ nm, $S = 533$ nm, $N = 4$, $L_{rod} = 200$ nm (L_{rod} is the length of the straight rod connected at the end of the helix). As shown before, it has an AR peak around 1.55 μm (see Fig. 3.23). The design process starts with tailoring the geometric parameters of the nanoaperture antennas to obtain resonances at the helix operation wavelength. Then, we combine the two components and optimize TW-HPA design to reach circularly polarized radiation.

All design processes are conducted with the FDTD method by using “Fullwave", a commercial software, which are schematically shown in Fig. 3.25. The simulation volume has been adapted with respect to the overall hybrid TW-HPA structure volume (indicated by orange squares) that includes the plasmonic helix and the aperture. The simulation boundaries along $\pm x$ and $\pm y$ axis have a fixed distance of 2 μm from the outermost rims of the overall antenna structure; the $-z$ boundary extends in glass and 2 μm below the lower surface of the aperture. The $+z$ boundary extends in air, which is 4.5 μm away from the helix end. A 5-nm meshgrid has been adopted within and closely around the antennas while a coarser meshgrid of 0.03 μm is applied in the periphery. The optical source is a Gaussian beam whose waist size is fixed to 1.5 μm (i.e., almost one wavelength). The

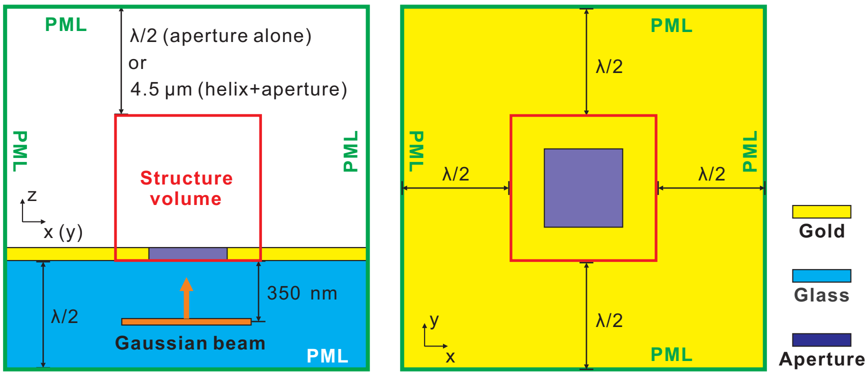

Figure 3.25: Schematics showing the FDTD model built for studying the optical properties of a helix with a feed element. PML:perfect match layer, λ: largest wavelength involved in the simulation.

.

beam waist is placed 350 nm far from the lower boundary of the aperture in the substrate. For spectral studies, the structure is excited in pulse regime, with the central wavelength and pulse duration set as 1.55 μm and 0.775 μm, respectively. To study the electromagnetic field distributions of the TW-HPA, the optical source works in the continuous-wave regime at a specific wavelength.

3.3.2.1/ HELIX FED WITH A RECTANGULAR NANOAPERTURE

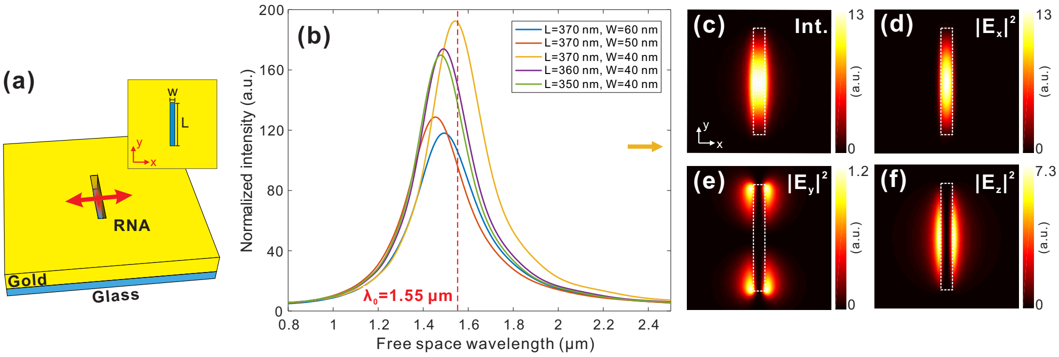

Figure 3.26: Design of the rectangular nano aperture (RNA) for working at optical telecommunication wavelength ($\lambda_0 = 1.55$ μm). (a) Schematic of the RNA. (b) Normalized intensity spectra of RNAs with various side lengths (L) and widths (W). The gold layer in which the RNA resides has a fixed thickness of 100 nm. (d) Electric field intensity distribution of the RNA in the ($x0y$) plane.

RNA milled in a thin metal layer operates as a linear electric dipole source [217]. Akin to BNA, the fundamental mode of RNA is also confined at the aperture center. Illuminated by light with a linear polarization perpendicular to the long side, the RNA fundamental mode can be excited on resonance. The resonance behavior of RNA is determined by its side lengths and the thickness of the metal layer, which has been well-studied in literature ([217]).

Figure 3.26 (a) shows a schematic diagram of a RNA. In the following, it will be considered to be perforated in a 100-nm-thick gold layer coating a glass substrate. Its resonance properties are thus determined by the length (L) and width (W) of the aperture. We tune the two geometrical parameters to reach a resonance peak around 1.55 μm. Figure 3.26 (b) shows the intensity spectra of the RNA with various L and W values, these spectra are calculated at a single grid cell positioned 10 nm above the top of the RNA, at its center. If we fix W as 40 nm and increase L from 350 nm to 370, the peak strength is enhanced accompanying with a redshift of its spectral position. As we fix L at 370 nm and increase W from 40 nm to 60 nm, we lower the resonance peak. The peak spectral position undergoes a blue shift first (W from 40 nm to 50 nm) and then a red shift (W from 50 nm to 60 nm).

Figure 3.26 (b) shows a resonance peak (enhance factor ~ 190) at the wavelength 1556 nm, when L and W take the values 370 nm and 40 nm, respectively. Fig. 3.26 (c) shows the electric field distribution of such a RNA at the resonance wavelength. The mode is mainly confined within the RNA gap with some residual fields extending slightly outside, along x axis. Fig. 3.26 (d~f) show the intensity of the E_x, E_y and E_z components, respectively. The E_x component, which is well-confined at the gap zone, is the main contributor of the RNA mode. The secondary E_z component contributes to the residual field out of the RNA. The E_y component is negligible as compared to the other two electric components. Such a near-field polarization structure is that of an electric dipole oriented along $(0x)$. Near-field coupling between the aperture and the helix thus occurs when the long side of the aperture is set in contact to the helix pedestal. In that case, the dipole moment of the aperture mode is aligned in the radial direction of the pedestal, ensuring field overlap between the two coupled modes of the two structures.

We consider a realistic helix configuration in our simulations (see Fig. 3.27 (a)). We assume a 105-nm-wide carbon core and a 25-nm-thick gold cover, which is within our fabrication capability (see Section 4.2.2). Such a gold wire sustains a cutoff-free axially symmetric traveling SP, known as the TM_0 mode, whose electric field is radially distributed all around the wire [208] (Fig. 3.27 (b)). It is locally fed with the dipolar mode of the RNA. An incident wave projected on the back of the aperture is transmitted as a sub-diffraction guided SP, which is non-radiatively converted into the swirling plasmon wire mode of the helix (see Fig. 3.28). The contact between the aperture and the helix's pedestal ensures a good near-field coupling between the two plasmonic structures. We also decrease the length of the helix pedestal to 100 nm to reduce the energy dissipation of the mode on the pedestal.

For operation at λ=1.5 μm, the helix geometry is defined by: $R_h = 175$ nm, $S = 415$ nm, $N = 4$. Fig. 3.27 (c) shows the degree of circular polarization (DOCP, see Section 1.1.2) and AR spectra of such a TW-HPA. TW-HPA emits light with AR and DOCP peaking at 0.97 and 0.999, respectively, at a wavelength of 1493 nm (Fig. 3.27 (c)).

To identify the traveling-wave nature of the antenna, we calculate the distribution of current amplitude within the helix. To this end, we integrate the simulated optical current density across the gold-coated helical wire, at each curvilinear coordinate along the wire. The final result is shown in Fig. 3.27 (d). The so-depicted mode closely resembles a traveling wave (cf. Fig. 3.6), as no clearly marked current nodes are evidenced. Figure 3.28 shows the time-evolution of the traveling SP within the helix. The SP in the helix is generated by the rectangular nano-aperture. It swirls over the first turn and leaks as free space propagating waves along z, which explains the remarkable current amplitude decay

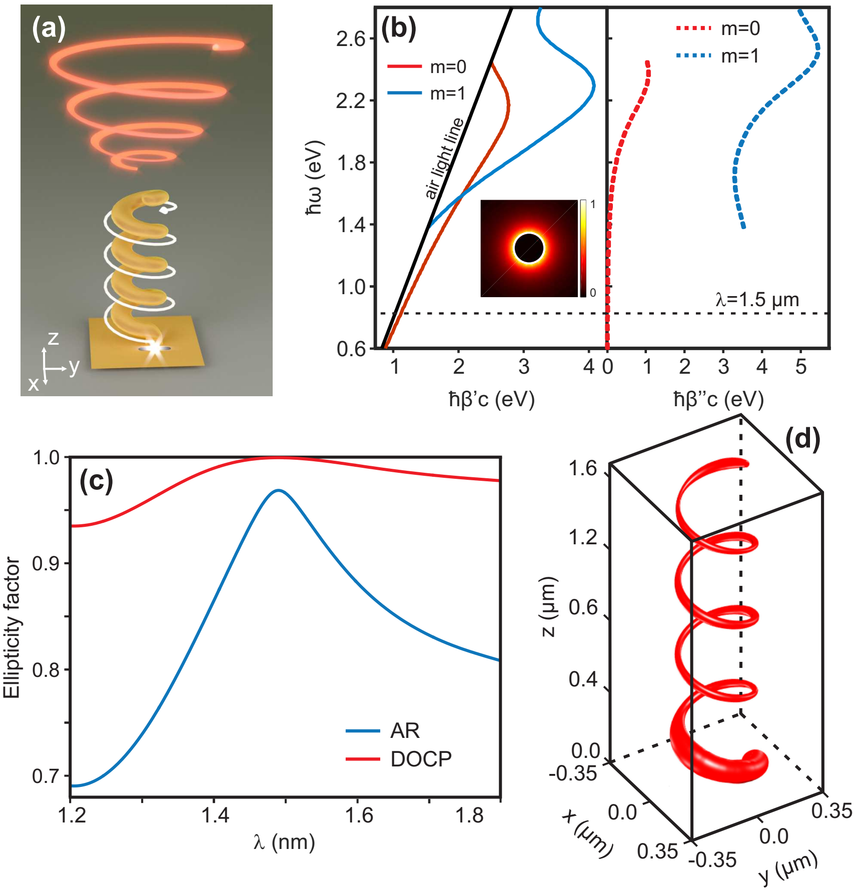

Figure 3.27: Helical plasmonic antenna as circularly polarized subwavelength source: (a) Schematics of the final TW-HPA and operation principle. End-fire excitation is represented with a white spike. Under curved trajectory along the helix, SPs acquire EOAM and are simultaneously released as freely propagating waves (white arrow). Part of the mode leakage re-excites the plasmon wire mode, thus participating in the plasmon swirling effect. (b) dispersion relations of the $m = 0$ and $m = 1$ modes of a gold-coated carbon wire (105-nm diameter carbon wire, 25-nm thick gold coating). Energy is plotted versus $\hbar c\beta'$ and $\hbar c\beta$". At λ=1.5 μm, only the $m = 0$ mode is guided. Figure inset: intensity plot of the $m = 0$ mode at λ=1.5 µm. (c) Spectra of the AR and DOCP of the TW-HPA emission. (d) Amplitude of the electric current distribution along the gold-coated carbon wire for λ=1.5 μm.

.

within the first turn (cf. Fig. 3.27 (d)). Part of these released free-space waves re-excite the SP in real time due to operation near cut-off, which optimizes the interplay between the guided mode and free space propagating photons. As a consequence, the current maintains almost uniform along the rest turns of the helix (cf. Fig. 3.27 (d)). This ensures a well-defined SP swirling effect which contributes to the high DOCP of the far-field emissions.

Figure 3.29 shows the emission diagram of the TW-HPA in its two principle planes ($x0z$ and $y0z$). It reveals a directional emission along the helix axis ($0z$), thus confirming the axial operation mode of our TW-HPA.

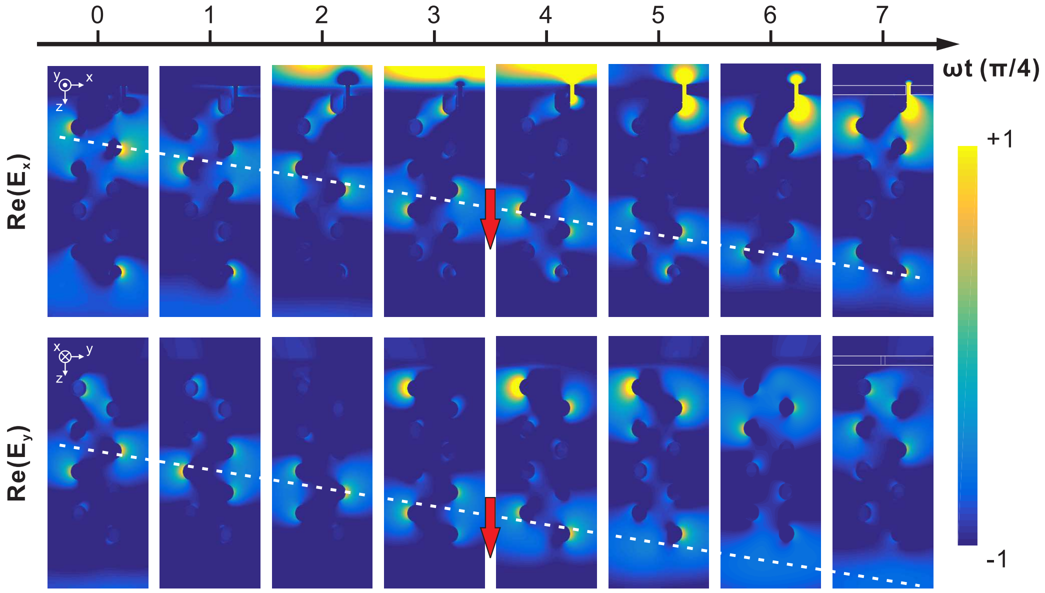

Figure 3.28: Traveling SP mode in a TW-HPA (see more information in Section 3.3.2.1). The pseudo-color field maps show the simulation snapshots of the instantaneous electric field distribution at $\omega t = i\frac{\pi}{4}$ ($i = 0, 1, 2...7$) and on two planes that cross the helix axis. The $x0z$ and $y0z$ plane field maps are shown on the upper and lower sides, respectively. These field maps are normalized with the same maximum amplitude value. The white dash line and red arrow indicate the axial advance of SP modes. The white thin solid lines show the gold layer and the nanoaperture on the substrate.

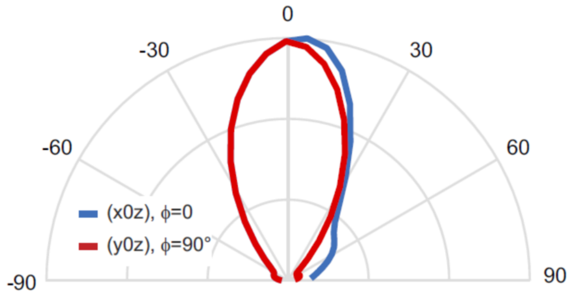

Figure 3.29: TW-HPA emission diagram. The TW-HPA shows a directional emission perpendicularly to the (x0y) ground plane of the antenna, thus confirming its axial operation mode.

.

3.4/ CONCLUSIONS

In this chapter, we first give a brief introduction to optical antennas, we then introduce the concept of optical helical antenna. We discuss the normal and axial modes of low-frequency helical antennas and show that they rely on different mechanisms to produce CP radiations. Then, by reviewing preceding works focused on metamaterial research, we evidence that, so far, plasmonic helices work in the normal mode, which involves plasmon resonances. Then, we introduce the concept of non-resonant traveling-wave helical plasmonic antenna. This antenna features a near-field excitation configuration and takes advantage of swirling SPs to radiate CP light. We specify the underlying EOAM-to-SAM transfer process. Finally, we address the TW-HPA design. We evidence the effect of the geometrical parameters of the plasmonic helix onto its ability to radiate CP light. We discuss our choice of a feed element and optimize the plasmonic nanoantennas to operate at $1.5\ \mu$m. We end up with a final hybrid antenna by coupling the helix and the feed antenna, thus obtain a realistic design for fabrication.

4

TRAVELING-WAVE HELICAL PLASMONIC ANTENNA: FABRICATION AND EXPERIMENTAL DEMONSTRATION

In the last chapter, we numerically investigate a single traveling-wave helical plasmonic antenna (TW-HPA) that radiates circularly polarized (CP) beam at optical wavelengths. The 4-turn helix structure has a typical core radius and vertical pitch of 175 nm and 415 nm, respectively. The fabrication of such a 3D architecture is challenging. We finally succeed by combining existing fabrication techniques. We have experimentally observed a circular polarization property with the fabricated TW-HPAs. In this chapter, we will detail the fabrication process and experimental demonstration of single TW-HPAs. Besides, we will also provide experimental evidences for the working mechanism of the TW-HPA.

4.1/ OVERVIEW OF THE FABRICATION TECHNIQUES

A wide variety of techniques have been proposed and demonstrated for realizing helical structures at small scale [44, 219, 220, 221, 222]. Limited to plasmonic helices, the most popular fabrication methods include [44]: 1) Direct laser writing (DLW) [44, 45, 196], 2) Focused ion or electron beam induced deposition (FIBID/FEBID) [199, 223, 224] and 3) Glancing angle deposition (GLAD) [204, 205, 206, 207]. In this section, we will show the capabilities and drawbacks of those methods, which helps us establish our own way to fabricate the TW-HPA.

Direct laser writing (DLW) utilizes tightly-focused laser spot to locally induce chemical reactions in photosensitive polymers. By scanning the laser spot, it enables the fabrication of arbitrary three-dimensional architectures in photopolymer [225]. Figure 4.1 (a) shows the DLW-based fabrication process of a gold helix array. As a first step, positive-tone photoresist is deposited on an ITO-covered substrate. Next, DLW together with chemical development is used to create helix-shape voids in the photoresist layer, which are then filled by gold material by electro-plating (see Fig. 4.1 (b)). After removal of the polymer by plasma etching, one can realize a monofilar gold helical array (Fig. 4.1 (c)). This method can be further extended for the fabrication of more complex triply-intertwined helices [196], by utilizing stimulated-emission depletion and negative-tone photoresist to improve the pattern resolution [225]. Figures 4.1 (e) and (f) show the molds and final helices fabricated by the DLW-based method. Those helices are well-defined with smooth

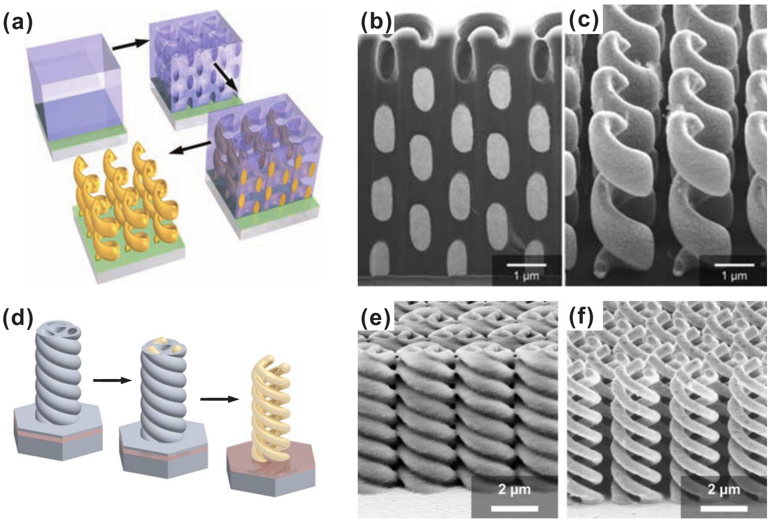

Figure 4.1: DLW for the fabrication of gold helix arrays. (a) Schematic for the original DLW process where a positive-tone photoresist is used to form the mould with helical voids. (b) Cross-sectional SEM image of the polymer mould filled by electro-plated gold. (c) Side-view SEM image of the resulting monofilar gold helix array after mould removal. (d) Schematics of the modified DLW process where a negative-tone photoresist is patterned by stimulated-emission-depletion-DLW to form the mould. (b) SEM image of the written polymer mould after chemical development and (c) Side-view SEM image of the final triply-intertwined gold helix array. (a)~(c) and (d)~(f) are snapped from the Refs. [45] and [196], respectively.

surfaces. Besides, electro-plating of pure gold also ensures a good plasmonic property of the structure.

In general, DLW offers a versatile tool for the fabrication of gold helices. However, limited by both the focal size [225] and the photoresist chemistry [196], the resulting helices normally have a radius above 1 μm. The working wavelength band of those helices is thus limited to mid-infrared [45] or longer wavelengths [226]. Therefore, this method is not suitable for fabricating our smaller TW-HPA, which operates at near infrared wavelengths.

Focused ion beam or electron beam induced depositions (FIBID or FEBID, respectively) enables bottom-up fabrication of structures with nanometer accuracy [227, 228, 229, 230]. Recently, these techniques have been employed for the fabrication of nano-helices for optics [200, 203, 223]. The working principles of both methods are quite similar and here we take FIBID for example. The fabrication is normally conducted in a high vacuum environment. Gaseous precursors containing desired chemical elements are applied through a needle-like gas injection system. Using a focused ion beam, these precursors decompose with the nonvolatile products deposited locally. By sweeping the ion focal spot properly, successive nucleations are induced, which finally develops into a helical wire shape. Together with tomographic rotation, this method also enables the fabrication of triply-intertwined helices [202, 203].

Figures 4.2 (b-d) show SEM images of helices fabricated with FIBID and FEBID techniques. Those images show great flexibility (of both methods) in tuning the helix geometry accurately. Moreover, helices of sub-micrometer radius can be reached, which is

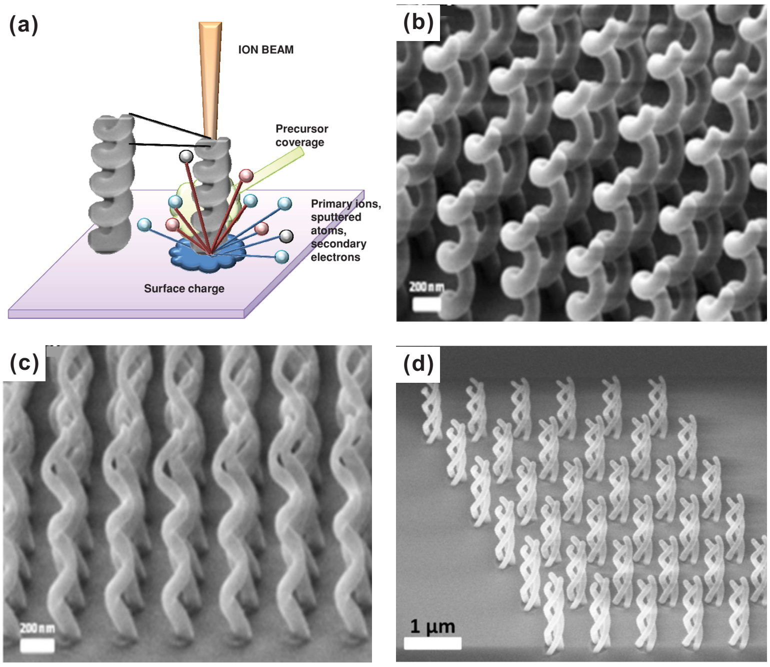

Figure 4.2: FIBID/FEBID fabrication of nano-helix structures: (a) Schematic depicting the FIBID fabrication process. [200] (b) and (c) : SEM images of the platinum helices fabricated by FIBID and FEBID, respectively. The helix geometry shown in (b) is: $R_h = 200$nm, $R_w = 65$ nm, $S = 300$ nm and in (c) are $R_h = 100$nm, $R_w = 30$ nm, $S = 350$ nm, respectively. (d) Triply inter-winded Pt helix array fabricated by tomographic rotatory FIBID growth. Dimensions of a single helix are: $R_h = 187.5$nm, $R_w = 55$ nm, $S = 705$ nm. [203]

mandatory to operate at near infrared and visible frequencies [203, 199, 224]. In addition, FIBID and FEBID enable the fabrication of helices with total turn number larger than 4. As previously discussed, this is highly desirable for obtaining a good circular polarization performance of the TW-HPA.

It is noted that, FIBID and FEBID also have some critical downsides concerning material qualities. For example, structures fabricated by FIBID suffer from Ga+ implantation and atomic mixing during deposition [231]. The ion implementation problem can be solved by using FEBID. In order to deposit gold, carbon-based precursors like $\mathrm{AuMe_2}$(tfac) are normally used during FEBID. However, carbon element in those precursors will cause a substantial carbon content in deposited structures, which severely degrades the optical properties of gold [231]. Though a few tentative approaches have been proposed to purify the deposit material [231, 232], we can not expect a pure gold helix deposition with FIBID or FEBID at this stage.

GLAD is another bottom-up tool for fabricating nano-sculptured films with various elements such as arrays of slanted columns, zig-zags and helices, etc. [219, 220]. Historically, GLAD has been mainly used for the deposition of dielectric materials. Plasmonic materials, which are normally noble metals, are not suitable for GLAD patterning due to their high surface mobility [205, 233]. Recently, a few groups have made it possible by adapting the conventional GLAD method, producing plasmonic helical metamaterials working at visible wavelengths [204, 205, 206, 207].

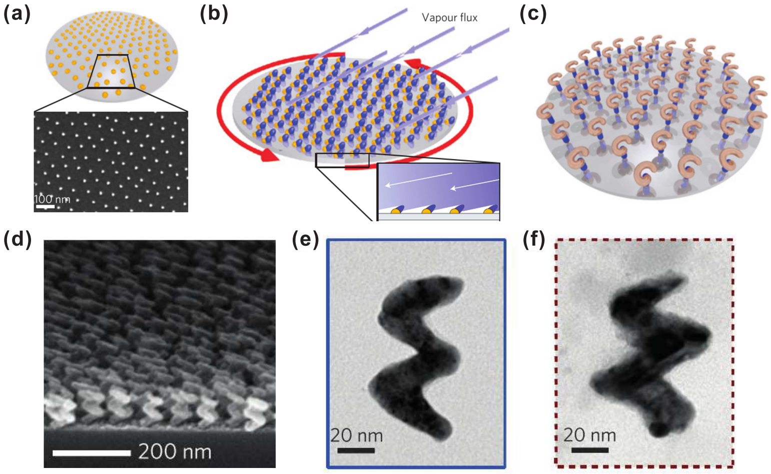

Figure 4.3: GLAD fabrication of nano-helix structures [205]. (a-c): Schematics of the GLAD fabrication process with (a) seeded substrate with grain sites prepared by nanolithography, (b) structure growth under grazing-incidence particle flux and (c) resulting nano-helix arrays. (d-f): SEM images of the GLAD-fabricated nano-helices with (d) a nano-helix array attached on the substrate (e) and (f) a single left- and right-handed helix picked out from the nano-helix array, respectively.

Figures 4.3 (a~c) show a modified GLAD method that enables the fabrication of sparse nano-helix arrays [205]. A seeded substrate is used to enable the growth of structures on the predefined nucleation sites. During the deposition process, the substrate is tilted at a glancing angle with respect to the incoming atom vapor flux to initiate a slant island growth (see Fig. 4.2 (b)). Due to extreme atomic shadowing and limited adatom diffusion, the island growth will be confined at the pre-defined nucleation sites [219]. Further, by rotating the substrate at a proper speed, each slanted island will evolve into a helical shape as shown in Figure 4.3 (c).

GLAD can massively produce ultra-small helices, as shown in Figs. 4.3 (d-f). The helix diameter and wire thickness is merely around 50 nm and 20 nm, respectively. In addition, GLAD also has advantages in high material purity [205, 206, 207]. However, compared to the aforementioned two methods, GLAD is less flexible in tailoring helix geometrical parameters.

4.2/ FABRICATION OF THE TW-HPA

4.2.1/ GLAD-BASED FABRICATION

The principle of GLAD has been introduced in the last section. We adopt this method as a first attempt to fabricate helical structures. Figures 4.4 (a) and (b) show the scheme and picture of our home-made GLAD machine. The machine contains a 40-L vacuum chamber, a 51-mm wide circular target and a substrate holder that can be tilted and rotated at will around the target. A turbo-molecular pump backed by a primary pump ensures a high vacuum background close to 10^{-6} Pa. During the fabrication, argon is injected at a steady flow rate (2.3 cm^3/min) to keep the pressure constant at 3.0×10^{-1} Pa.

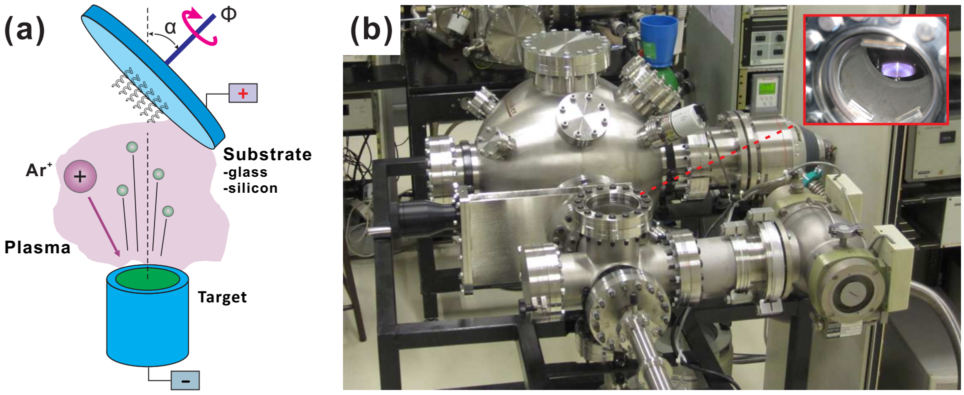

Figure 4.4: Glancing angle deposition (GLAD) equipment used in my thesis: (a) Schematic diagram and (b) a photo of the running machine. Inset of (b) shows the glowing plasma in the fabrication chamber.

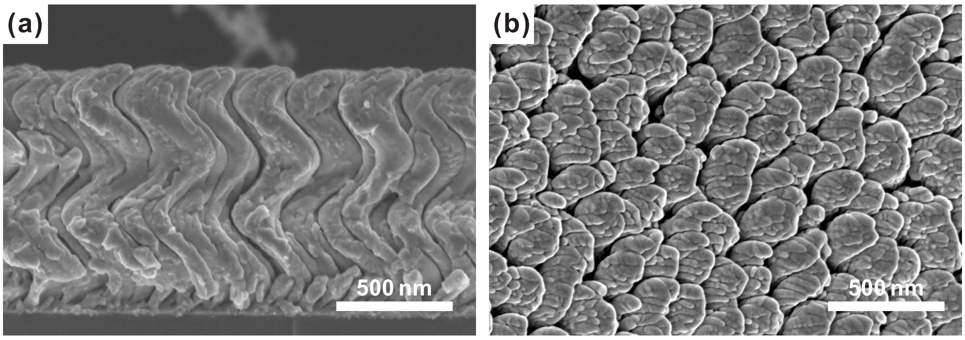

Figure 4.5: SEM images of the nano-helix structure fabricated by GLAD: (a) cross-section and (b) top view.

By applying a voltage between the substrate and target, argon plasma is ignited, which sputters materials out of the target. To form the helix structures, the substrate is tilted at a angle of 80° and rotated at a steady angular speed (ϕ = a few rev/h). No external heating is applied during the growth stage and the deposition is performed at room temperature. The total thickness of the film is monitored with a crystal oscillator. The GLAD deposition is conducted at FEMTO-ST Institute by Prof. Nicolas Martin.

Figures 4.5 (a) and (b) show the SEM images of TiCu nano-helices fabricated by GLAD. As shown in Figures 4.5 (a), the total helix turn number is around 2. The helix radius and vertical pitch are around 250 nm and 500 nm, respectively. The helix wire thickness is inhomogeneous, which increases from ~ 100 nm to ~ 200 nm from the bottom to the top. As shown here, those helix geometrical parameters differ from that of our designed TW-HPA. Besides, as shown in Figs. 4.5 (a) and (b), these helices are so densely packed that it would be a challenging task to pick a single one out for our usage. We thus turn to another approach.

4.2.2/ FIBID-BASED FABRICATION

As discussed in section 4.1, FIBID and FEBID technologies show great advantages in precisely defining helix geometries. Here, we take advantage of FIB and FEM technologies, including deposition, milling and imaging to fabricate and characterize our helical antennas.

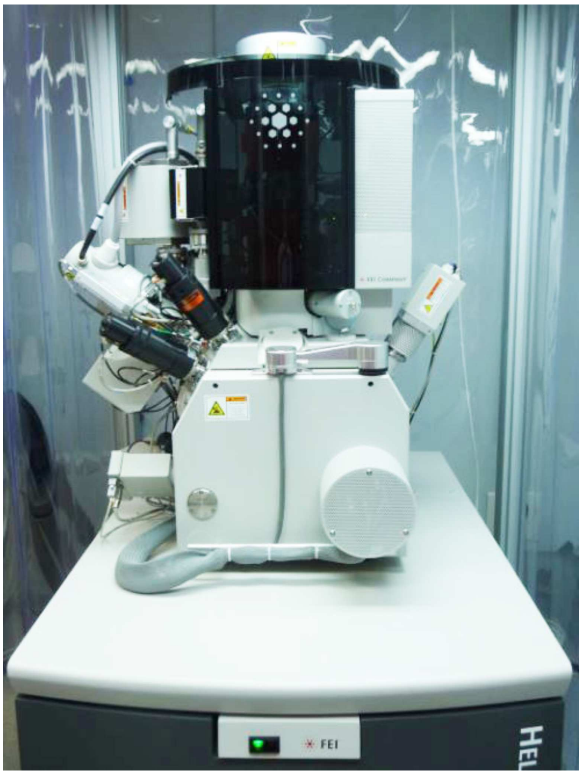

Figure 4.6: Photograph of the SEM/FIB dual-beam system (Helios Nanolab 600i, FEI) available at FEMTO-ST Institute. It is the workhorse for both structuring and characterizing HPAs.

Figure 4.6 shows the Helios Nanolab 600i SEM/FIB dual beam system available at FEMTO-ST Institute. This system consists of an electron column and an ion column that have an angle of 52° from each other. The FIB column is capable of milling, depositing and coarse imaging while the FEM column offers finer imaging quality. The sample stage is aligned with respect to the two columns. It can move to let the sample orthogonal to one or the other column to maximize the imaging or fabrication precision, respectively. At the same time, high-precision 5-axis motorized stage endows this system with a high flexibility in fabrication. The gas injection systems can supply various precursors, enabling the deposition of carbon, platinum, silicon oxide, etc. In addition, the tomography function of this machine allows us to build 3D maps for our helices, which is very helpful for analyzing in details the fabrication process and performances and for understanding their optical properties of the resulting structures.

Based on FIBID and GLAD technologies, we develop a nano-fabrication process for realizing our TW-HPA. It contains three steps as shown in Fig. 4.7. As a first step, FIBID is used to fabricate the carbon helices. We can accurately define helix geometries including

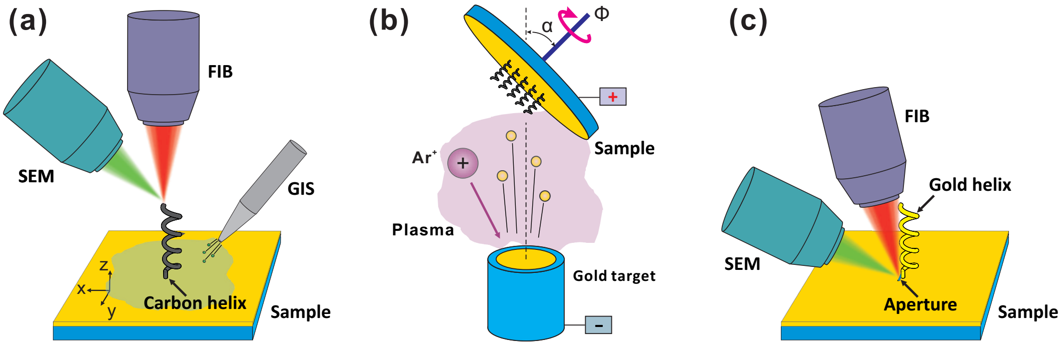

Figure 4.7: Schematic diagrams of the fabrication process we develop for realizing the TW-HPA structures. (a) Fabrication of the carbon helices on a gold coated glass substrate by FIBID. The FIB is used to induce the carbon wire deposition and the SEM is used to monitor the deposition process. (b) Metalization of carbon helices with gold by GLAD involving plasma sputtering approach. Direct current is applied between the substrate and gold target to generate argon plasma. (c) Fabrication of the rectangular aperture by FIB milling. The small angle is kept between ion flux and the helix to avoid side-cutting effect.

handedness, helix radius, vertical pitch, total turn number and wire diameter. We are also able to assemble a few helices in a group, for obtaining various optical functionalities. Then, in order to metalize the carbon helix, we adopt plasma sputtering to deposit a thin gold layer on its surface. Remarkably, material purity as high as 99.9% can be reached by this method. Such a high gold purity ensures a good plasmonic property, which is critical to our antennas. Considering the complex 3D shape of the helix, the GLAD technique described before (see Section 4.2.1) has been adopted to limit the shadowing effect and to homogenize the gold cover onto the helix surface. Finally, FIB is used again to mill the aperture feed element in contact to the helix pedestal. To avoid side-cutting of the fabricated helix structure during milling the aperture, the substrate has been adapted with a small angle ($\sim 10°$) regarding the focused ion beam.

Generally speaking, our fabrication method combines the merits of FIBID and GLAD together. The according technical details and fabrication results will be shown in the following subsections.

4.2.2.1/ CARBON HELIX

The carbon helix deposition is conducted with the Helios Nanolab 600i dual beam system in a high vacuum background about 10^{-5} mbar. Gaseous carbon-based precursor (Naphthalene) is supplied by the gas injection system with a constant temperature of 35 °C applied to the precursor reservoir. The Ga^{+} ion energy and beam current is set at 16 KeV and 1 pA, respectively. During fabrication, the FIB focal spot scans in steps around a circle to define the helix profile. The according step size and dwell time are controlled simultaneously to ensure a continuous carbon deposition to form the helix wire. A detailed discussion on the two parameters can be found in the literature [203]. In our fabrication, the step size is fixed at 10 nm while the dwell time needs to be adjusted to avoid inhomogeneous vertical pitch. This challenging fabrication is carried out by Dr. Roland

Salut.

Figure 4.8 (a) shows a 4-turn carbon helix fabricated by FIBID without vertical pitch correction. This helix has excellent surface quality and homogeneous radius, which is ~ 175 nm for all turns. However, its vertical pitch decreases notably from bottom to top, as indicated by the white arrow. For example, the vertical pitches of the second and forth turn is 428 nm and 278 nm, respectively. Such a pitch variation results from the concentration gradient and decomposition rate of the precursor, which decrease from the substrate to air [200, 203]. For compensation, we continuously increase the dwell time by about 30% from the first turn to the last turn during fabrication. Fig. 4.8 (b) shows an helix fabricated with pitch correction. We can see that the pitch variation is reduced below 36 nm.

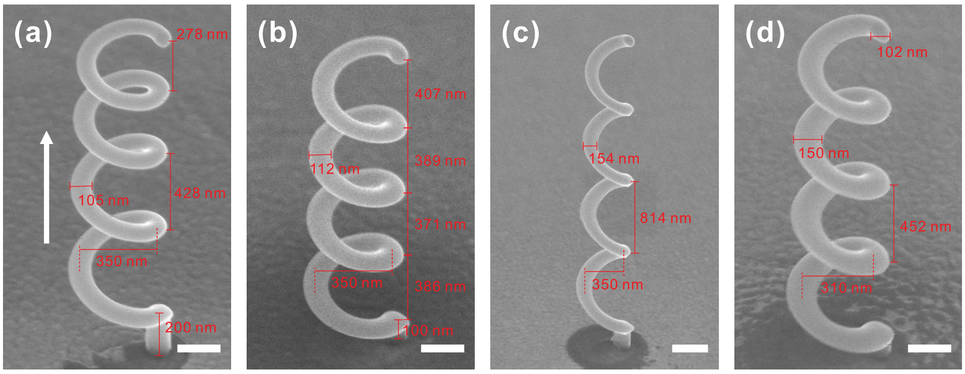

Figure 4.8: SEM images of various 4-turn carbon helices fabricated by FIBID: (a) without pitch correction (b-d) with pitch correction. Scale bars: 200 nm.

Figures 4.8 (c) and (d) show two other corrected helices, which feature an enlarged vertical pitch (~ 845 nm) and a shrinked core radius (~ 155 nm), respectively. As to the wire diameter, we can see from Figs. 4.8 (a-d) that it falls in the ranges from 105 nm to 154 nm. The carbon wire shown in 4.8 (d) has an elliptical cross-section, whose major and minor axes are of 102 nm and 150 nm, respectively. Such a wire shape may cause spectral shifts of the TW-HPA, which however, can be compensated by tailoring the helix radius. Therefore, we save our effort for further optimizing the wire cross-section. Figure 4.9 shows the carbon helices with the turn number ranging from 1 to 4. Remarkably, they share high uniformity in all other parameters, allowing us to study the effect of helix turns on TW-HPA performances.

Figures 4.8 and 4.9 show a high flexibility of the FIBID technique for tailoring helix geometry. Besides, FIBID also enables to manipulate at will the handedness and arrangement of multiple helices. As shown in Fig. 4.10 (a), left and right helices are placed at a center-to-center distance of 5 μm. Figure 4.10(b) shows a more closely-packed four-helix structure where the center-to-center distance between the two helices of the same handedness is approximately 800 nm.

Therefore, FIBID satisfies well our demand for accurately defining the helix geometry.

4.2.2.2/ METAL COATING

We metalize the carbon helix by depositing a thin gold layer on its surface with our GLAD machine (see Fig. 4.4). The fabrication is conducted under a high background vacuum

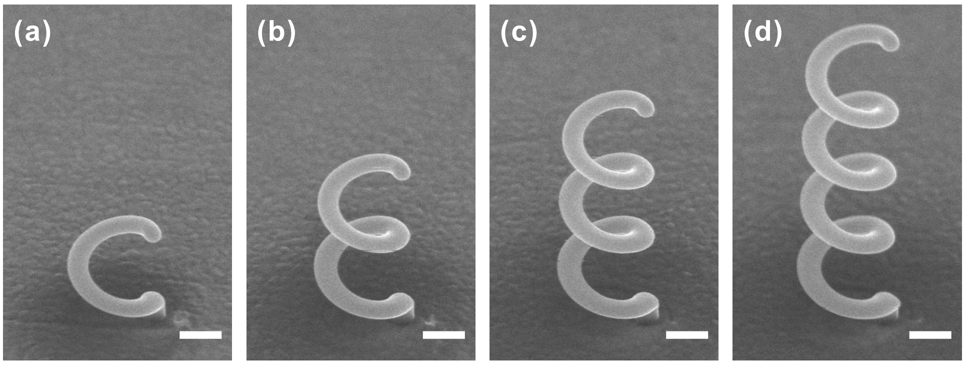

Figure 4.9: SEM images of carbon helices with total turn number varying from 1 to 4. Scale bars: 200 nm.

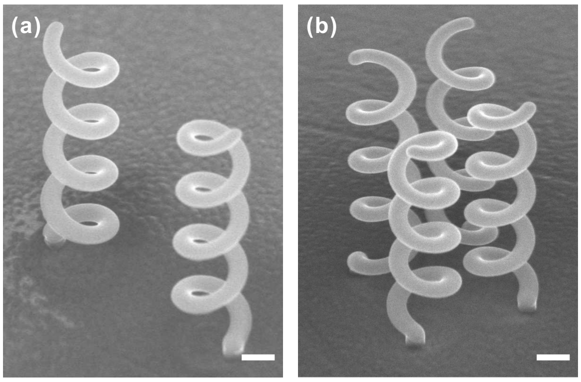

Figure 4.10: SEM images of grouped carbon helices with opposite handedness. (a) Paired left and right helices. (b) Closely-packed four-helix system where helices with the same handedness are placed at the diagonal positions of a subwavelength square. Scale bars: 200 nm.

($\sim 10^{-6}$ Pa). During the fabrication process, gold target (51 mm in diameter and 99.9% in purity) is sputtered by argon plasma under constant direct current (20 mA) and argon pressure (3.0×10^{-1} Pa). No external heating is applied during the growth stage and deposition is performed at room temperature. To optimize the gold coverage on the carbon helix, the sample is tilted by an angle of $\alpha \sim 80^\circ$ with respect to the sputtered particle flux and rotated at a steady angular speed $\phi = 10$ rev/h. The total deposition time is adjusted to obtain an overall coating thickness around 25 nm.

Figure 4.11 (a) shows the SEM images of a single helix after gold coating. We can see a high surface smoothness of the gold layer. The roughness of the gold layer on the helix is even smaller than that on the plane substrate. It is estimated to be approximately 1 nm. We further characterize the coating uniformity all around the carbon wire. To this end, platinum is first deposited about the HPA to form an HPA-embedded platinum block. We then slice such a structure in series with FIB milling to obtain the cross-section micrograph and to construct the 3D tomography of the HPA. Figure 4.11 (b) shows a cross-sectional SEM image of the gold-coated carbon helix. The gold coating thickness is inhomogeneous around the carbon wire, which is around 25 nm and almost zero on the upper and lower part of the carbon wire, respectively. Such an inhomogeneity can

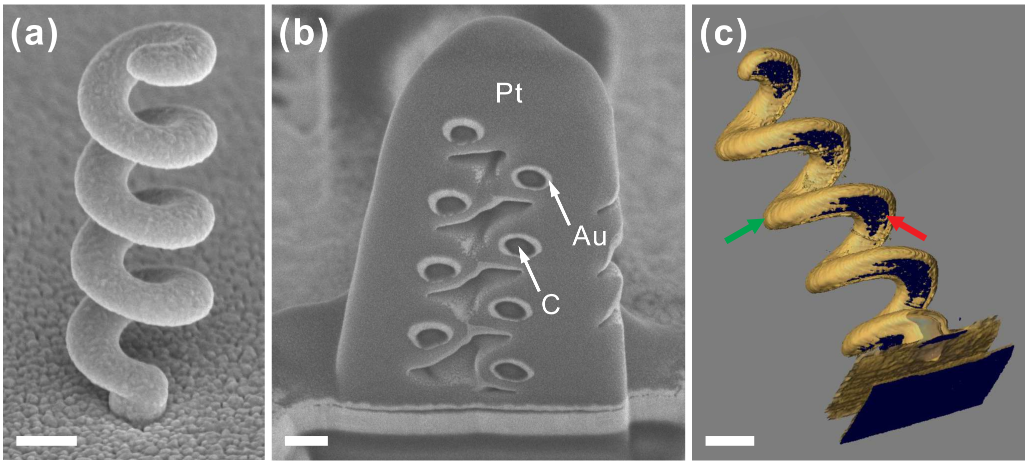

Figure 4.11: Metal coating results of a carbon helix with $R_h \sim 155$ nm, $S \sim 350$ nm. (a) Bird-view SEM image of the gold-coated carbon helix. (b) Cross-section SEM image of the helix, embedded in a FIBID-deposited platinum (Pt) block. The bright gray areas show the gold coating (Au) and the dark gray areas show the carbon core (C). (c) 3D tomographic image of the gold-coated carbon helix, which is reconstructed from a series of sliced SEM images of the HPA. The gold and carbon materials are represented in yellow and black, respectively. Scale bars: 200 nm. The green and red arrows in (c) show two representative regions with a thick and thin gold coating, respectively.

also be seen from the 3D tomographic view of the structure in Fig. 4.11 (c). Since the gold coating thickness around the carbon wire is less than the skin depth of gold, surface plasmons can interact with the carbon core. This may cause a spectral red shift of the TW-HPA response, which will be shown later.

4.2.2.3/ FEED ELEMENTS

The aperture feed element of the TW-HPA is milled by FIB. Thanks to the simple shape of the RNA, the side-cutting effect can be completely eliminated by adopting a small milling angle of $10°$. Figure 4.12(a) shows the side-view SEM image of the fabricated helix-RNA structure. The helix wire keeps intact after RNA milling even when they contact. Figure 4.12(b) shows the top view of a single RNA. The lengths of its long and short side are around 366.5 nm and 39.7 nm, matching well the design values 370 nm and 40 nm, respectively. FIB milling allows to freely combine the helix and RNA in various ways, as shown in Figure 4.12 (c~e).

Figure 4.13 summarizes the fabrication process divided into three steps. It shows the antenna after each fabrication step, namely, (a) carbon helix growth on a thin gold film, (b) metal coating and (c) aperture nanoantenna milling. The fabricated TW-HPA have well-defined geometry, as well as high surface qualities.

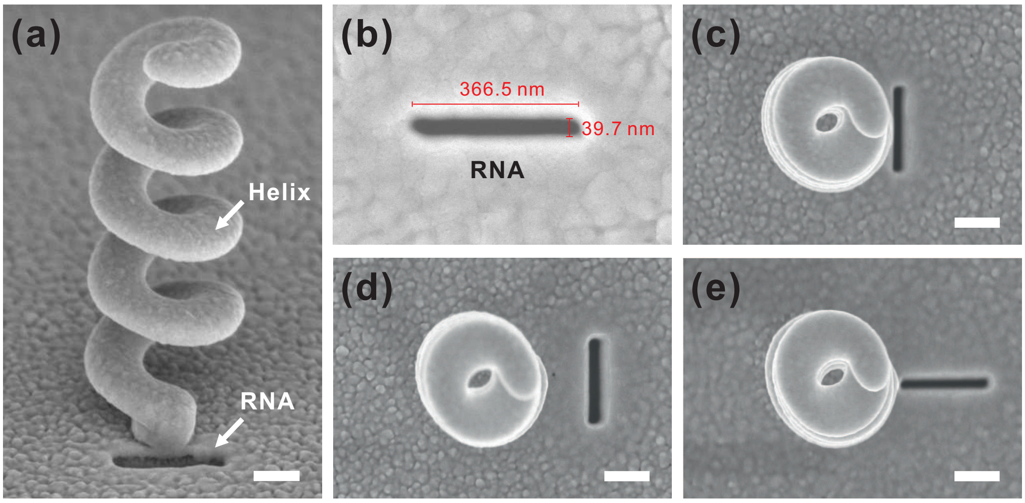

Figure 4.12: Fabrication results of the helix-RNA nano-structure. (a) SEM images of a resulting structure. (b) Top view of a single RNA and (c~e) its combination with a gold-coated helix in different configurations. Here, the aperture is milled outside the winding area of the helix.

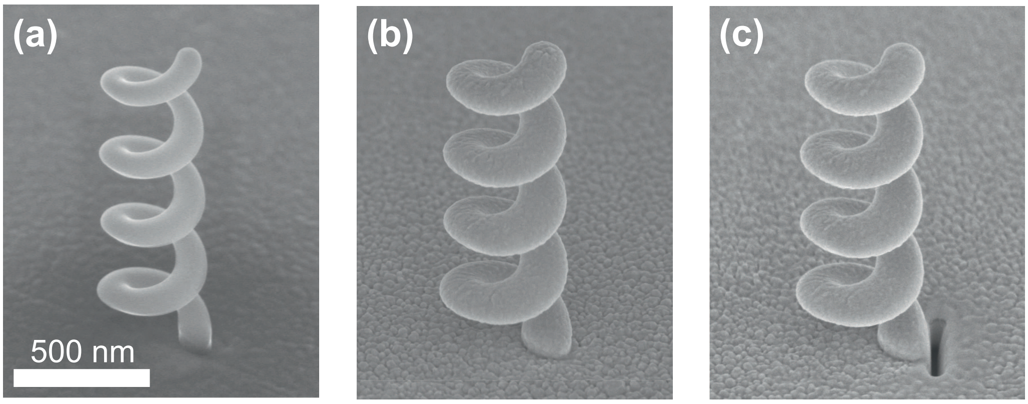

Figure 4.13: Fabrication of the TW-HPA: three steps. Scanning electron micrographs of the subwavelength structure after (a) fabrication of the carbon helix skeleton by FIBID, (b) metal deposition onto the helix skeleton, and (c) fabrication of rectangular nano-aperture antenna by FIB milling.

4.3/ EXPERIMENTAL DEMONSTRATION OF TW-HPA

4.3.1/ EXPERIMENTAL SET-UP

Figures 4.14 (a) and (b) show a schematic and a photograph of our experimental bench, respectively. It is mounted onto a Nikon TE2000 inverted microscope. As shown in Fig. 4.14 (a), infrared light emitted from a tunable laser (Yanista Tunics-T100S: $1470 \sim 1650$ nm) passes through a polarization maintaining fiber (P3-1500PM-FC-2, Thorlabs). The fiber output beam is then collimated by a reflective collimator (RC08APC-P01, Thorlabs). In order to control the polarization state of the input light, a linear polarizer (LPNIR100-

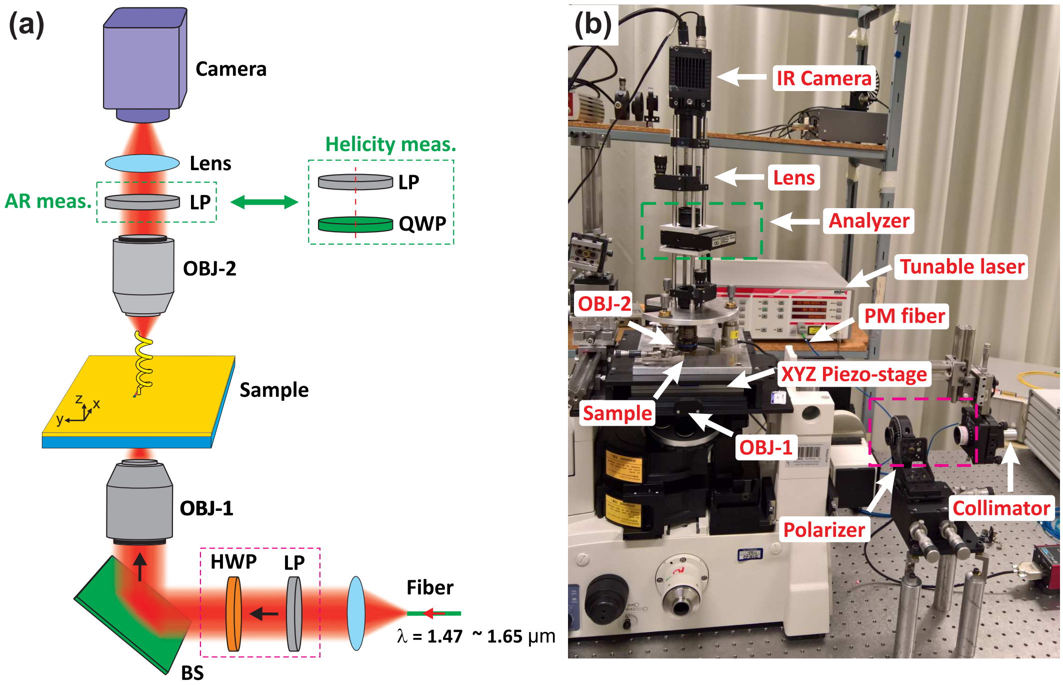

Figure 4.14: Experimental setup for measuring the polarization property of the antenna emission: (a) Schematic diagram and (b) photograph of the experimental bench. LP: linear polarizer, QWP: quarter wave plate, HWP: half wave plate, OBJ: objective, BS: beam splitter. The fiber used here is a polarization maintaining fiber, which transmits infrared light produced by a tunable laser ($1470 \sim 1650$ nm). The magenta dash rectangle in the illumination bench indicates the polarizer system, which contains a LP and a HWP. The green dash rectangles in the detection bench indicate the analyzer system, which can be switched between i) a rotating LP for acquiring the polarization diagram, and ii) a rotating QWP followed by a linear polarizer for analyzing the helicity of light. Both the polarizer and analyzer systems are driven by a motorized stages. The sample holder is mounted on a 3D piezoelectric translation stage, which enables the precise focusing of the excitation light onto the antenna.

MP2, Thorlabs) and a half wave plate (AHWP05M-1600, Thorlabs) are inserted in the illumination path. The linear polarizer is fixed while the HWP can be rotated at will with a brushed motor (PRM1Z8, Thorlabs). The ensemble produces linear polarization at desired orientation in the $(x0y)$ plane. Refracted by a beam splitter, the collimated laser beam is focused onto the backside of the sample with an objective $(25\times/0.4)$ to excite the TW-HPA. To ensure a fine superposition of the laser spot to the antenna feed element, a XYZ piezoelectric transition stage (Mad city lab, Model S02080) is employed. In the collection bench, a high numerical aperture infrared objective (Olympus LCPlanN, $50\times/0.65$) collects the emission from our antennas. The collected light is then coupled by a field lens $(f = 50$ mm) to the infrared camera (Gold eye G-033,SWIR TEC1, Allied vision) for image acquisition.

The polarization state of the antenna emission is measured by inserting an analyzer system in front of the camera, either for measuring polarization diagrams or for ellipticity and helicity analysis, respectively. The former is realized with a rotating linear analyzer (LPNIR100-MP, Thorlabs), while the latter is accomplished with a rotating quarter wave plate (AQWP05M-1600, Thorlabs) and a fixed linear polarizer (LPNIR100-MP, Thorlabs). By recording the transmission intensity with respect to the orientation of those mobile elements, we extract all information of the polarization ellipse including its ellipticity (AR), orientation and handedness of the polarization. Degree of circular polarization (DOCP), which is also widely used for evaluating CP systems [46], can be derived from the measured AR value from:

$$DOCP = \frac{2AR}{1 + AR^2}, \tag{4.1}$$

which has been described in the first chapter (Eqs. 1.45 and 1.49).

4.3.2/ Optical response of the feed element

We first characterize the polarization response of the feed element, i.e. a single RNA. Such an antenna, as predicted in the last chapter, has a linearly polarized emission. We validate this point by examining both its response to the input polarization and its far-field polarization property. The experimental schemes and results are shown in Figs. 4.15 (a) and (b), respectively.

As shown in Fig. 4.15 (a), the excitation rate of the RNA, presented in polar plot, follows well the two-lobe pattern described by Malus' law ($I = \cos^2\theta$), showing that the RNA behaves as a linear polarizer regarding the incident beam. Such a response is highly favorable for achieving a well-defined polarization-controlled tunability of the TW-HPA emission intensity. The linear response of the RNA is also confirmed by measuring the polarization state of its far-field emission. As shown in Fig 4.15(b), the zero and maximum transmissions occur when $\theta = k90°,\ (k = 1,\ 3)$ and $\theta = k90°,\ (k = 0,\ 2)$. The other immediate analyzer orientations again lead to a transmission intensity curve that follows the Malus' law.

The RNA response shown in Figs. 4.15 (a) and (b) demonstrates the linear polarization response of the RNA. We can thus conclude that the RNA, by itself, can not produce circular polarization. Therefore, any CP polarization light component obtained in the far-field with the final TW-HPA should solely originates from the helix, rather than the feed element. Since the RNA plays as a linear polarizer, the polarization properties of a TW-HPA are not sensitive to the polarization of input light. This point will be confirmed later.

4.3.3/ Polarization properties of the TW-HPA

Figure 4.16 (a) shows a simplified schematics of the experimental setup used for measuring the polarization response of a single TW-HPA. We first characterize the response of the TW-HPA to different input polarizations. To this end, the linear analyzer (LP2), as shown in green dash square is removed. We rotate the linear polarizer (LP1) and record the intensity of TW-HPA emission. Fig. 4.16 (b) shows the corresponding result, where we can see that the presence of TW-HPA does not change the polarization filtering property of the feeding RNA. Thus, the optimal excitation of the TW-HPA occurs when the input light is linearly polarized perpendicular to the long side of the RNA.

The inset of Fig. 4.16 (a) shows an optical image of the TW-HPA under the optimal excitation condition. We can see that the emission from our TW-HPA has a well-defined

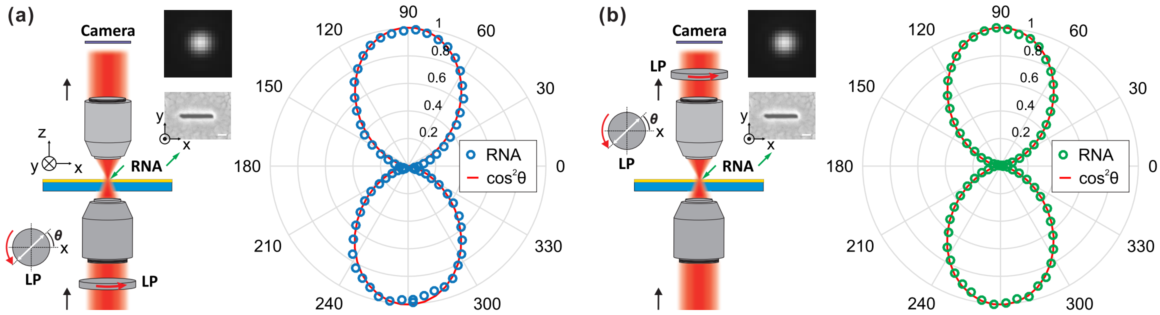

Figure 4.15: RNA response measurements. (a) Measurement of RNA's response to the input polarization: simplified experimental scheme (left panel) and measured RNA emission intensity regarding the input polarization orientation (right panel). Experimental results (blue circles) are compared with Malus law (red curve). Measurement of RNA's radiation property: simplified experimental set-up (left panel) and measured RNA polarization diagram (intensity), compared with the typical response of a dipole Malus's curve (right panel). Those measurements in (a) and (b) are enabled by rotating a linear polarizer inserted either in the input or output benches, respectively. The two insets, in both (a) and (b), show the optical and SEM images of the RNA. In all cases, θ denotes the orientation of the polarizer's transmission axis, counted from x-axis).

spot shape without noticeable side lobes. Such an intensity profile basically keeps unchanged as we scan the excitation wavelengths from 1470 nm to 1650 nm. We analyze the polarization state of TW-HPA emission with a rotating linear polarizer (LP2) inserted in front of the camera. The obtained polarization states of the TW-HPA is shown in Fig. 4.16 (c). Notably, we can see that the polarization ellipse at $\lambda = 1640$ nm is almost a circle ($AR = 0.97$, $DOCP = 0.99$). This indicates a near perfect circular polarization state of our TW-HPA. At $\lambda = 1470$ nm, the TW-HPA keeps fairly well circular polarization with however a little decrease of the ellipticity factors ($AR = 0.86$, $DOCP = 0.98$).

A more comprehensive ellipticity measurement can be seen in Fig. 4.16 (d), within the wavelength range from 1470 nm to 1650 nm (spectra of the AR and DOCP). We can see that the ARs at the lower and higher wavelengths are around 0.70 and 0.94, respectively. In low frequency regime, the operation bandwidth of an antenna used as a circular polarizer is defined by the spectral bandwidth over which $AR > 0.5$ [211]. According to our simulation result (Fig. 3.27 (c)), we can assume that the CP operation bandwidth of our TW-HPA extends much larger than 180 nm. However, due to the limited available wavelength range of our laser, a direct experimental demonstration of such bandwidth is not possible. The point here is that we have achieved a fully functional subwavelength optical antenna, which enables the generation of CP light.

Here, the helix radius (R_h) is 155 nm and the vertical pitch (S) is around 350 nm, giving an experimental AR peak at 1640 nm. One may notice that such a TW-HPA geometry is different from that showed in the design part (see Section 3.3.2.1). In that case, the TW-HPA geometry is $R_h = 175$ nm and $S = 415$ nm, which leads to a simulated AR peak at 1493 nm (cf. Fig. 3.27 (c)). Considering their difference in helix radius, there exists a spectral redshift about ~ 200 nm between the simulation and experimental AR spectra (for HPAs of the same R_h value). Such a shift results from the inhomogeneous gold layer around the carbon wire, caused by the shadowing effect during metal coating. Indeed, the gold thickness on the back side of the carbon is about 5 nm, which significantly differs

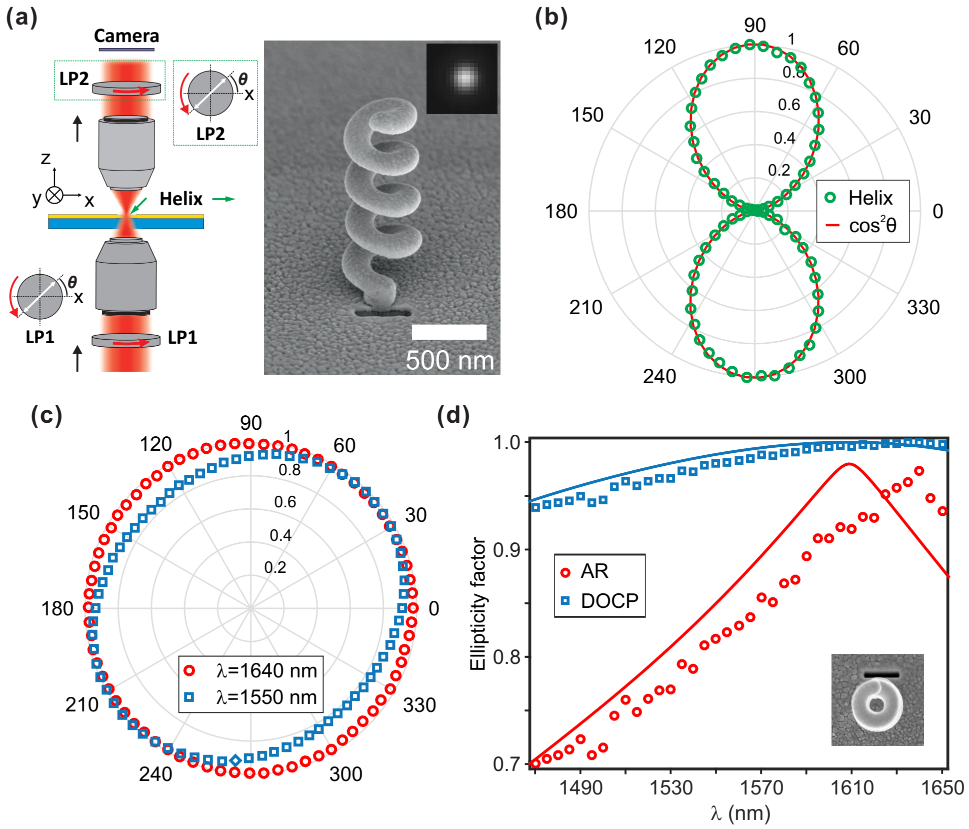

Figure 4.16: Circularly polarized optical emission from a single TW-HPA. (a) The left panel shows a simplified schematic depicting the experimental bench for characterizing the polarization properties of the helical antenna (inset shows a typical far-field optical image of the TW-HPA emission). The right panel shows a side-view SEM micrograph of the TW-HPA, whose central radius and vertical pitch are $R_h \sim 155$ nm and $S \sim 350$ nm, respectively. (b) Measured antenna emission intensity with respect to the input linear polarization. (c) State-of-polarization analysis at $\lambda = 1.55$ μm and $\lambda = 1.64$ μm. (d) Experimental spectra of the AR and DOCP, compared with the simulation results considering a 10-nm thick homogeneous metal coating onto the carbon skeleton.

from the 25-nm design value. In this case, the SP wire mode interacts with the carbon skeleton and leads to the spectral red-shift of TW-HPA. We thus adopt in our simulations an effective homogeneous coating thickness of 10 nm for the helix ($R_h = 155$ nm, $S = 350$ nm). In doing so, the numerical predictions fit better the experimental results (solid curves in Fig. 4.16 (a)).

We investigate the emission helicity of two HPAs of opposite handedness (see Fig. 4.17 (a)). The geometry and polarized emission of the left-handed TW-HPA are shown in Fig. 4.16). Here, we focus on the helicity. Fig. 4.17 (a) schematically shows our experimental bench. In front of the camera. a quarter-wave plate (QWP) is rotated with respect to a fixed linear (LP2) to analyze the emission helicity. The transmission intensity (at $\lambda = 1640$ nm, normalized) of the two HPAs are shown in Fig. 4.17 (b), regarding a full QWP turn. Assigning θ as the angle between the fast axis of the QWP and the transmission axis of the LP, the two polarization elements form a circular analyzer of left and right handedness when $\theta = 45°$ or $\theta = 135°$, respectively. As shown in Fig. 4.17 (b), the emissions from the

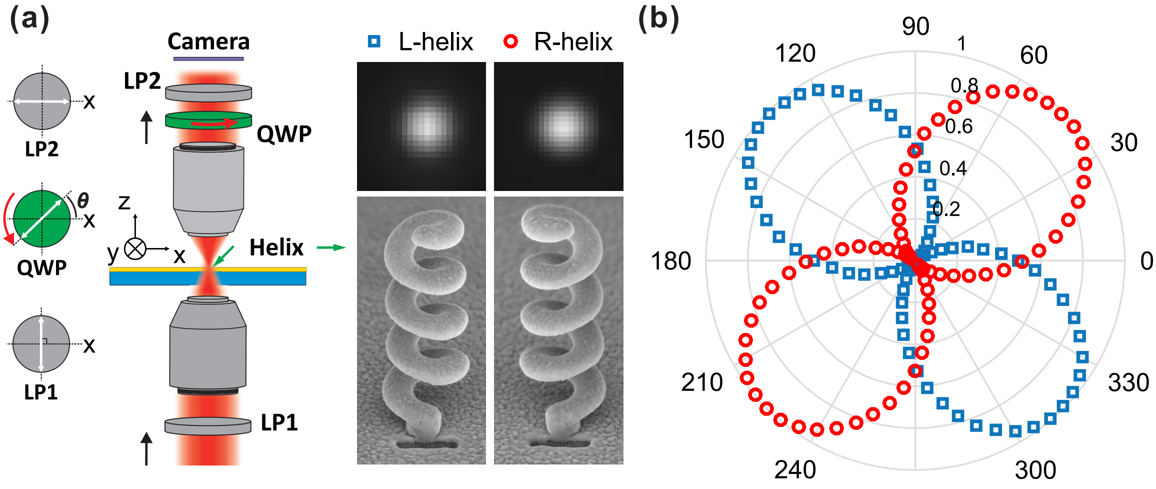

Figure 4.17: (a) Left panel: simplified schematic of the experimental set-up, where a rotating quarter wave plate (QWP) and a fixed linear polarizer (LP2) are put in front of the camera to analyze the helicity of the antenna emission. Right panel: optical and SEM images of two HPAs of opposite handedness. (b) Measured transmission intensity for the two HPAs through the circular analyzer. Maximum helicities are obtained for angles between the QWP and LP of 45° and 135°. This resembles two circular polarizers of opposite handedness. We have $\sigma = \pm 1$ for the two HPAs, where σ stands for the helicity of light.

left and right HPAs are canceled at a θ value of 45° and 135°, respectively. Therefore, the handedness of the TW-HPA emission is identical to that of the helix.

4.3.4/ DEMONSTRATION OF THE PLASMON SWIRLING EFFECT IN CIRCULAR POLARIZATION GENERATION

As discussed in the last chapter, our TW-HPA relies on spin-orbit interaction (SOI) to generate circularly polarized emission (see Section 3.2.3). Specifically, excited at one end by a nanoscale coupling feed element, the plasmonic helix develops surface plasmons (SPs) swirling along the curved path defined by the helix. Due to the helical trajectory, these traveling SPs acquire an extrinsic orbital angular momentum (EOAM) and induce, by leakage, free-space light emission. For sharp curvatures, the EOAM of the SPs can match the spin angular momentum (SAM) of free space propagating photons. The helicity of the far-field emission is thus dictated by the handedness of the near-field swirling SP mode. The swirling SPs play a critical role in the SOI driving of our TW-HPA. For generating such SPs, the helix should be locally end-fired and long enough ($N \geq 4$) to maintain well their traveling-wave characteristic. Therefore, demonstrating the near-field feeding mechanism and the helix turn number effect might offer us indirect proofs for the SOI working principle of the TW-HPA.

4.3.4.1/ DEMONSTRATION OF THE END-FIRE EXCITATION PROCESS OF THE PLASMONIC HELIX

The SOI, as discussed in the last chapter, relies on the swirling movement of surface plasmons along the helical nanowire. A critical prerequisite is that these SPs should be excited in an end-fire configuration. That is to say, the rectangular aperture transfers energy to SPs directly via near-field coupling, rather than through far-field scattering. Therefore, demonstrating the near-field coupling mechanism might offer a proof for the swirling-plasmon effect and thereby the SOI principle within the plasmonic antenna.

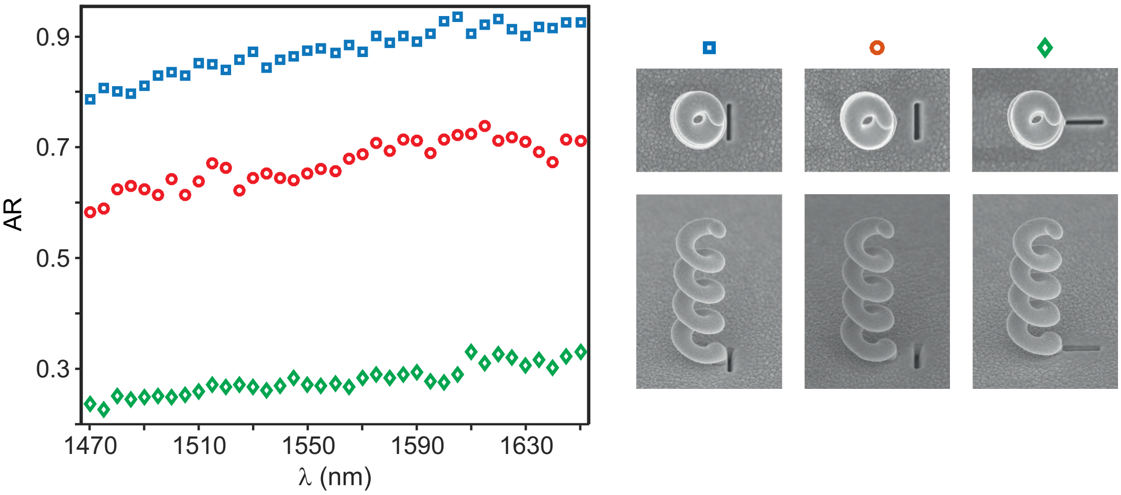

Figure 4.18: Circularly polarized emission originates from the excitation of a subdiffraction surface plasmon within the helix. AR spectrum of the TW-HPA emission for the RNA in contact to the helix pedestal (blues squares), 185 nm away from the helix pedestal (red circles), and turned by $90°$ regarding the two first cases (green diamonds), respectively.

To demonstrate the near-field interaction between the helix and the feed element, we consider their combination under three different configurations, as shown in SEM images in Fig. 4.18. The two SEM images marked by a blue square show a common Helix-RNA configuration where the RNA contacts the helix pedestal (Case-1). In the other two cases, the RNA is put with its center 185-nm far away from the helix pedestal, either parallel (Case-2, red circles) or perpendicular (Case-3, green diamonds) to the RNA in the first case. The AR spectra of the overall plasmonic structures obtained in the three cases are shown on the left side in Fig. 4.18.

The AR spectra of Case-2 shows the same trend as that of Case-1, with only a slight decrease in the overall AR level (~ 0.22). Case-3, however, gives an AR spectrum well below 0.32, distinct from the former two cases and more close to linear polarization. The similarity between Case-1 and Case-2 lies in the fact that the near-field coupling between the RNA and helix works in both cases. Placing the two elements slightly further (185 nm) just decreases their coupling efficiency. A small portion of energy leaking directly from the RNA will not harm much the polarization property of the TW-HPA. However, Case-3 is completely different. Due to its special RNA orientation, the direct RNA-to-helix energy transfer is very weak. A large portion of energy leaks from the RNA, which thus imparts the far-field a linear polarization characteristic. Therefore, our results clearly demonstrate that circular polarization at the antenna output arises from a near-field coupling between the RNA and the helix.

4.3.4.2/ DEMONSTRATION OF A HIGHER AR WHEN THE HELIX TURN NUMBER INCREASES

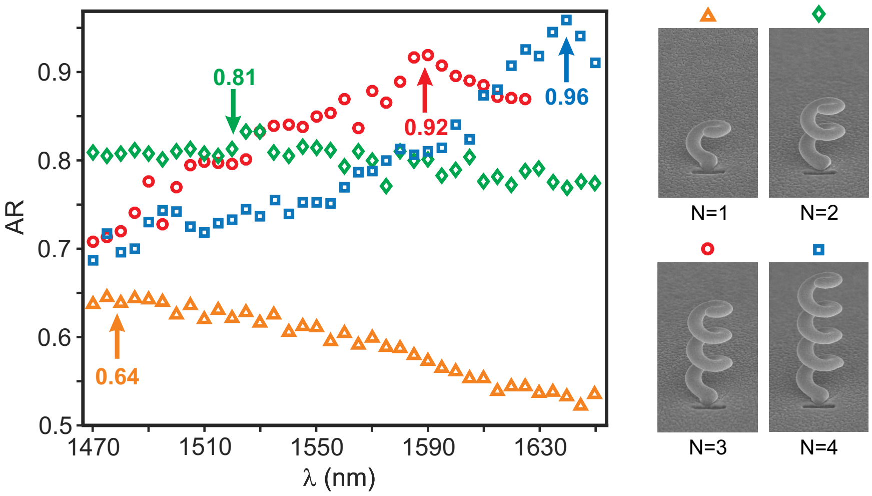

Figure 4.19: Spectrum of the AR of the TW-HPA emission for a single structure with one turn (orange triangles), two turns (green diamonds), three turns (red circles), and four turns (blue squares).

We also test helices with a growing turn number ($N = 1 \sim 4$) to finalize the demonstration of the plasmonic swirling phenomenon. The principle is that the AR peak converges to a high value close to 1 as the helix turn number increases. Figure 4.19 shows the AR spectra obtained with helices whose turn number increases from 1 to 4. A single-turn helix has an AR maximum at 1480 nm, which equals to 0.64. Then for $N = 2$, we have a flatten AR spectrum, showing a maximum AR of 0.81 at a wavelength around 1520 nm. For HPAs with $N = 3$ and 4, we can see that the AR is further enhanced to 0.92 and 0.96 at $\lambda = 1590$ nm and $\lambda = 1640$ nm, respectively. The convergence of the maximum AR is accompanied by a redshift of the AR peak of about $40 \sim 60$ nm as N increases from 1 to 4. Such a spectral redshift is much smaller than the increment of vertical pitch, which is 360 nm.

The above-shown phenomenon tend to confirm that the swirling-plasmon effect is intrinsic to traveling-wave TW-HPA. The observed helix turn effect is consistent with the low-frequency traveling-wave helical antennas whose AR performance also improves with an increasing turn number [83].

4.4/ CONCLUSIONS

By combining FIBID and GLAD techniques, we have successfully fabricated HPAs with well-defined geometries and material properties. We demonstrate that even a single TW-HPA is capable of radiating almost perfect circularly polarized light at optical telecommunication wavelengths. Fed by a linear-dipole-like nanoaperture in the near-field, such an antenna allows to control the polarization of light to produce highly localized circularly polarized light sources. The TW-HPA may find various applications in integrated optical communication and polarization-encoded optics. Finally, by experimentally examining the traveling-wave and near-field coupling mechanisms, we validate that it is the underlying swirling-plasmon effect that originates the SOI within the plasmonic antenna (EOAM-to-SAM transfer).

5

TW-HPA-BASED PLATFORM FOR DETECTING AND CONTROLLING LIGHT POLARIZATION

In the last chapter, we have shown that a single traveling-wave helical plasmonic antenna (TW-HPA) can generate circularly polarized light at subwavelength scale, with emission helicity defined by the handedness of the structure. Besides, the TW-HPA is fed with a rectangular nanoaperture, which has a dipolar response to input excitation. Taking advantage of these properties, here we develop new optical functionalities based on TW-HPA. We will first show that the TW-HPA, working in detection mode, can discriminate circular polarizations of opposite handedness. Then, we will show strongly integrated arrays of point-light emissions of opposite handedness and tunable intensities, as well as a 3D device of subwavelength volume that enables polarization manipulation unreachable with conventional materials.

5.1/ TRAVELING-WAVE HELICAL PLASMONIC ANTENNA AND CIRCULAR DICHROISM

The helix is a 3D chiral object, which has different responses to circularly polarized light of opposite handedness. For example, helical plasmonic metamaterial (arrayed helices) can transmit CP light of certain handedness and reject the opposite, with a transmission ratio for the two CP components around 10:1 [45]. Such a circular dichroism response, if transferred to a single plasmonic helix, can be used for locally probing light polarization, which however has not been demonstrated yet. In this section, we will show the circular dichroism of a single TW-HPA.

5.1.1/ CONCEPT AND SIMULATION

The TW-HPA can work on two reciprocal operation modes, which involve optical propagation in two opposite directions within the HPAs. In the emission mode, we consider the illumination of the rectangular nano-aperture antenna from the backside and the emission of circularly polarized light by the helix. The collection mode corresponds to an illumination of the helix from the front and emission of linearly polarized light from the

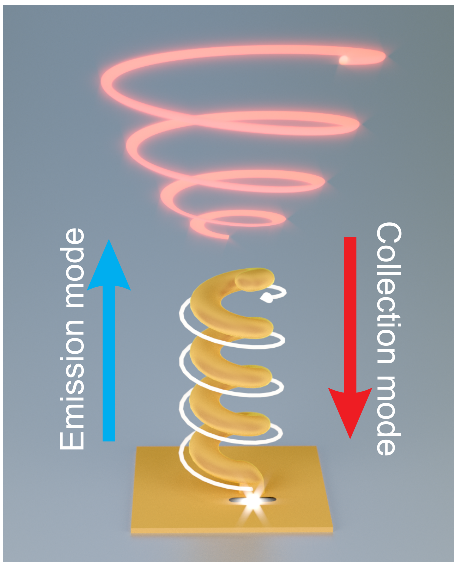

Figure 5.1: Schematics of the two operation modes of the TW-HPA, involving light wave propagation in two opposite directions along the antenna axis, respectively.

rectangular nano-aperture antenna in the substrate. Previously, we have shown that the TW-HPA, working in the emission mode, radiates CP light whose handedness follows that of the helical structure. According to the reciprocity principle, we expect that the TW-HPA, operating in detection mode, has a differential response to left and right CP illuminations.

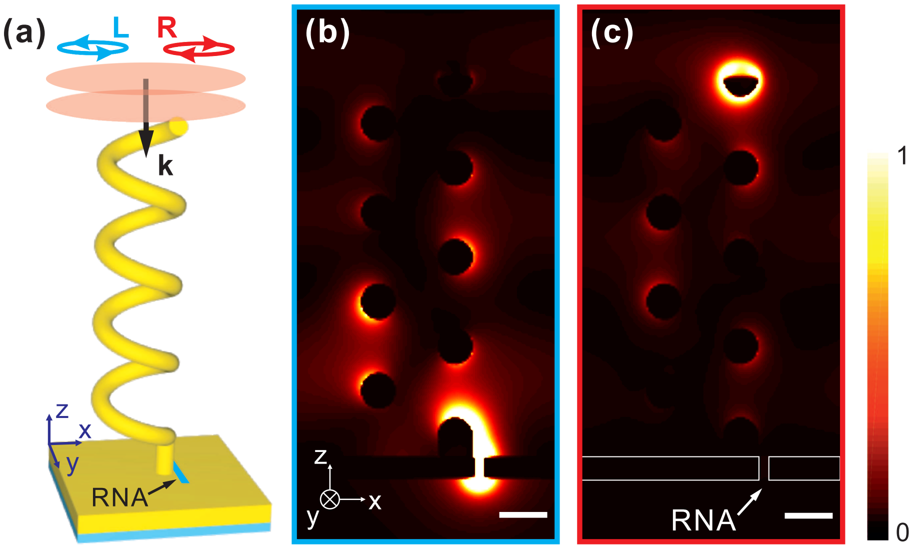

Figure 5.2: Simulation of the TW-HPA in detection mode: (a) Schematics of the simulation model. (b,c) Simulated intensity distribution ($x0z$ plane) of the TW-HPA under illumination with (b) left and (c) right-handed circularly polarized light, respectively. The intensity plots have been saturated equally for a better view of the TW-HPA wire mode. RNA: rectangular nanoaperture.

We first conduct numerical simulations with Fullwave (a commercial FDTD software) to verify our concept. Figure 5.2 (a) shows a scheme of the simulation model. The left-hand helix has a core radius of 175 nm, a vertical pitch of 415 nm and a turn number of 4. Its

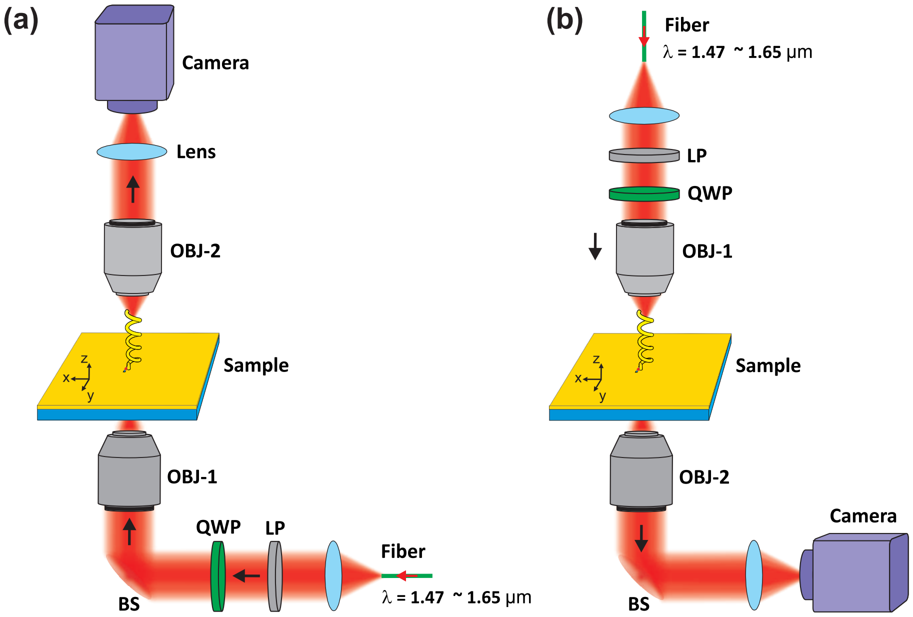

Figure 5.3: Schematic diagrams of the experimental setups for measuring the circular dichroism of the TW-HPA (a) in emission mode, and (b) in collection mode. LP: Linear Polarizer, OBJ: Objective, QWP: Quarter-wave plate, BS: beam splitter.

wire is considered to have a carbon core of a 105-nm diameter and a homogeneous gold coating of 25 nm. It lies onto a 100-nm long pedestal. A rectangular nano-aperture (RNA) with a length and width of 370 nm and 40 nm, respectively, is perforated in contact to the pedestal into a 100-nm thick gold layers covering a glass substrate. The TW-HPA is illuminated with LCP or RCP plane waves from the front side, at a wavelength of 1493 nm. The launch plane is placed in air, 300 nm away from the helix end. The overall simulation volume extends in air, 800 nm from the utmost boundaries of the TW-HPA structure along the $\pm x$, $\pm y$ and $+z$. Along the $-z$ direction, it extends in the glass substrate, 800 nm below the lower surface of the RNA. The simulation volume is terminated by perfect match layers at all six boundaries to avoid unphysical parasitic reflections. A fine meshgrid of 5 nm is used in the portion enclosing the TW-HPA while a larger meshgrid of 30 nm is applied to the periphery.

Figures 5.2 (b) and (c) show the electric intensity distribution in the $(x0z)$ plane obtained with LCP and RCP illuminations, respectively. Under LCP illumination, the RNA shows the maximum transmission intensity, which turns to almost zero with a RCP illumination. Such a response evidences the circular dichroism of the TW-HPA in detection mode. The intensities within the RNA in the two cases have a ratio as high as 1000:1.

5.1.2/ EXPERIMENTAL DEMONSTRATION

Figures 5.3 (a) and (b) show the schematics of the measurement setups in emission and collection modes, respectively. Characterizations in emission and collection modes involve an inverse of the illumination and detection benches. Light of tunable wavelength, ranging from 1.47 μm to 1.65 μm, emerges from a tunable laser source (Yanista Tunics-T100S) and is coupled to a single mode polarization maintaining fiber (P3-1500PM-FC-2, Thorlabs). It is collimated by an achromatic reflective fiber collimator (RC08APC-P01, Thorlabs), and focused onto the plasmonic structures with a (25X, 0.4) microscope objective. The polarization of the incident collimated wave is manipulated using a fixed polarizer (LPNIR100-MP2) and a quarter-wave plate (AHWP05M-1600, Thorlabs) positioned in between the collimator and the objective. The quarter-wave plate is mounted onto a motorized stage (KDC-101, Thorlabs) to be accurately rotated with respect to the polarizer. The plasmonic structures are imaged with a (50X, 0.65) infrared objective from Olympus (LCPlanN) coupled to an infrared camera (GoldEye model G-033, Allied Vision Technologies GmbH) through a proper field lens.

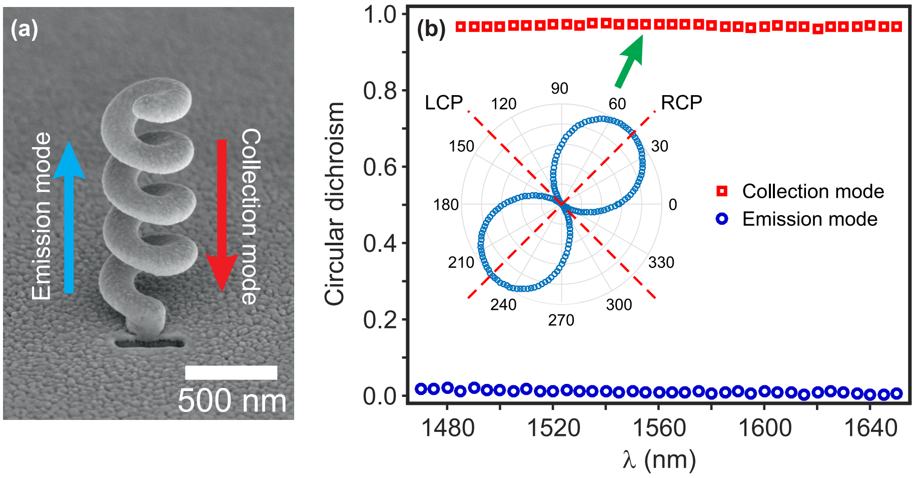

Figure 5.4: (a) Schematics of the two operation modes of the TW-HPA, involving light wave propagation in two opposite directions along the antenna axis, respectively. (b) Circular dichroism spectra measured with a left-handed TW-HPA operating in emission and collection modes. Circular dichroism is defined as $(I_{RCP} - I_{LCP})/(I_{RCP} + I_{LCP})$, where I_{RCP} and I_{LCP} stand for the emission intensity of the TW-HPA, with an illumination by right and left circularly polarized light, respectively. Emission intensity is measured either from the helix, in air (in emission mode), or from the rectangular nano-aperture antenna, through the substrate (in collection mode). Figure inset: helicity analysis in emission mode, at λ=1.55 μm. The measurement is realized by placing a circular analyzer, consisting of a rotating quarter-wave plate followed by a fixed polarizer, in front of a detector and measuring the transmitted power. RCP and LCP refer to right and left-handed circular polarization of the emitted light, respectively.

Figure 5.4 (a) shows a SEM image of the TW-HPA used for measuring the circular dichroism. In emission, such an antenna radiates almost perfect circularly polarized light at a wavelength of 1630 nm (cf Section 4.3.3). Figure 5.4 (b) shows the measured circular dichroism spectra, both in emission and collection modes. Circular dichroism occurs only in collection mode. Measured circular dichroism larger than 0.96 in the wavelength range of interest witnesses a transmission process mainly governed by a near-field coupling between the helix and the RNA, which has been shown previously in Section 4.3.4.1. The inset of Figure 5.4 (b) shows the helicity analysis in collection mode, at λ=1.55 μm. The maximum and minimum intensities occur when the input light is circular left and circular right. As a contrast, in emission mode, the circular dichroism is almost zero. That is because the feed element of TW-HPA has a dipolar response to input excitation and thus is insensitive to helicity.

To conclude, the TW-HPA working in collection mode shows a high degree of circular dichroism. The HPAs are thus appealing tools to discriminate right and left circular polarizations at the subwavelength scale, for instance, to locally measure the degree of circular polarization.

5.2/ CLOSELY PACKED SUBWAVELENGTH LIGHT SOURCES WITH OPPOSITE HELICITY

In the last chapter, we have demonstrated that a single TW-HPA is capable of radiating almost perfectly polarized light. When such HPAs of opposite handedness are arranged with a spacing of a few microns, the overall structure transmits light under the form of a small array of right and left-handed circularly polarized sources. Moreover, by using HPAs with various orientations of the feed apertures, the relative intensities of these point-like sources become controllable by the polarization of the incident light. In the following, such a device will be referred to as “circularly polarized light source array" (CP-LSA).

5.2.1/ CONCEPT AND ANALYTICAL MODEL

Figure 5.5 schematically shows the concept of CP-LSA. In this architecture, two right and left-handed HPAs are placed at the apexes A/C and B/D of a square ABCD, respectively. At the same time, the feed elements of each two adjacent HPAs on the same side of the square are set perpendicular, as shown in Fig. 5.5. The diagonal length of the square (2ρ) is set to be a few microns to fully separate the emissions from these HPAs.

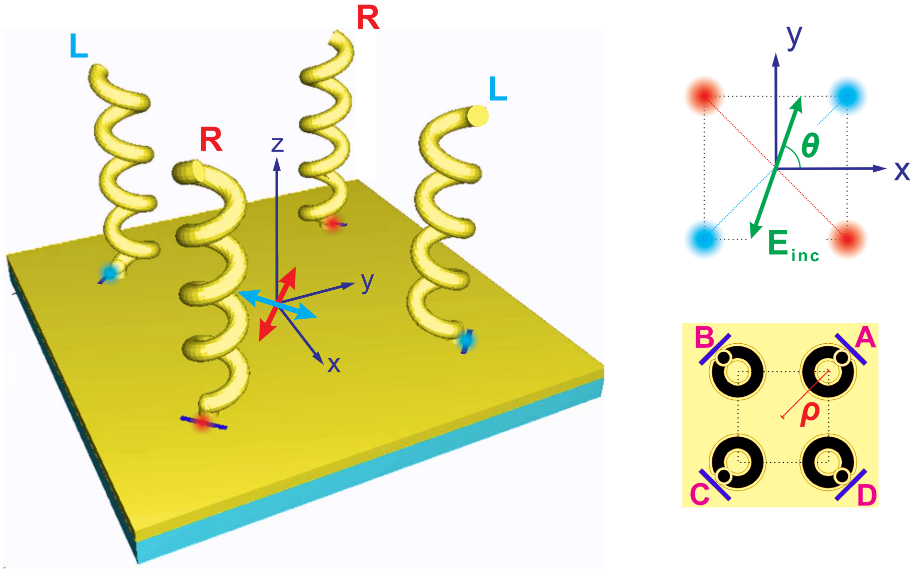

Figure 5.5: Schematics of the CP-LSA, consisting of two couples of HPAs of opposite handedness and orthogonal aperture nano-antennas. The right and left handed HPAs are identified with the letters R and L, respectively. Red and blue arrows indicate the linear polarization states of the incident light, at which only the two right and left-handed HPAs are respectively switched on emission.

The rectangular nano-aperture has a linear dipole response with the emission axis perpendicular to its long side (cf. Fig. 5.5). We thus have the following analytical model to describe the emission from the CP-LSA:

$$I = \begin{bmatrix} I_A & I_B \\ I_C & I_D \end{bmatrix} \propto \begin{bmatrix} \cos^2(\theta - \pi/4)\,|\Psi_L\rangle & \sin^2(\theta - \pi/4)\,|\Psi_R\rangle \\ \cos^2(\theta - \pi/4)\,|\Psi_L\rangle & \sin^2(\theta - \pi/4)\,|\Psi_R\rangle \end{bmatrix}, \tag{5.1}$$

where θ denotes the angle between the input linear polarization (E_{inc}) and the x axis, $|\Psi_L\rangle$ and $|\Psi_R\rangle$ represent the spin state of the emitted photons.

Equation 5.1 shows that the relative intensities of the four point-like emissions is controllable by tuning the polarization of excitation light. Especially, when $\theta = m\pi + \pi/4$ and $\theta = m\pi + 3\pi/4$ ($m = 0, 1$), only the two left-handed HPAs (A and C) and the two right-handed HPAs (B and D) are switched on, respectively. When $\theta = m\pi/2$ ($m = 0, 1, 2, 3$), all HPAs emit with the same intensity.

5.2.2/ EXPERIMENTAL DEMONSTRATION

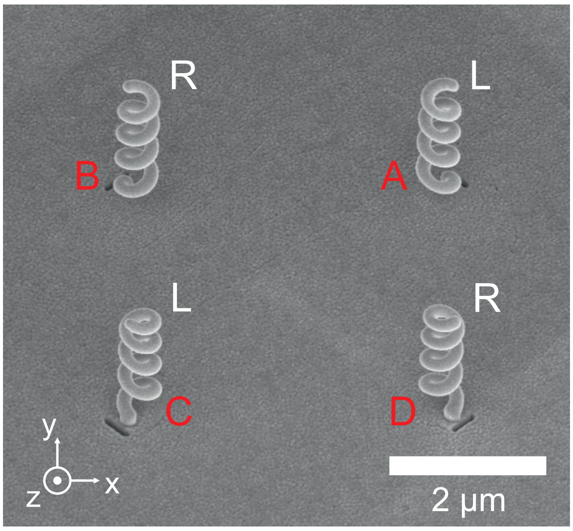

Figure 5.6: Scanning electron micrograph of the CP-LSA, which consists of two couples of HPAs of opposite handedness and orthogonal aperture nano-antennas. The right and left-handed HPAs are identified with the letters R and L, respectively. The letters A, B, C and D show the arrangement configuration of these HPAs (cf. Fig. 5.5).

Figure 5.6 shows the SEM picture of a CP-LSA with $2\rho = 5\ \mu$m. In order to characterize its emission properties, we basically follow the experimental set-up depicted in Fig. 4.14. However, in the input bench, we use a low magnification objective (OBJ-1: $4\times/0.1$) to obtain a large laser spot (around $20\ \mu$m) to cover the whole area of the CP-LSA.

The left panel of Fig. 5.7 (a) shows a simplified scheme of the experimental setup used to examine the tunability of the CP-LSA. The input polarization is linear and has an tunable angle θ with respect to the x-axis. The right panel of Fig. 5.7 (a) shows the optical images of the structure obtained with three different linear polarizations, at a wavelength of 1640 nm. As indicated by the bright spots, the SLA is switched from the status “L-helices on/R-helices off" ($\theta = 0°$) to “L-helices on/R-helices on" ($\theta = 90°$) and then “L-helices off/R-helices on" ($\theta = 135°$). Figure 5.7 (b) shows the emission intensities of the two left- (red circles) and right-handed HPAs (blue squares) corresponding to a full turn of the input polarization. They follow the two-lobe Malus' patterns that are perpendicular in orientation, which shows orthogonal polarization responses of HPAs with opposite handedness. Such a property is predicted by Eq. 5.1.

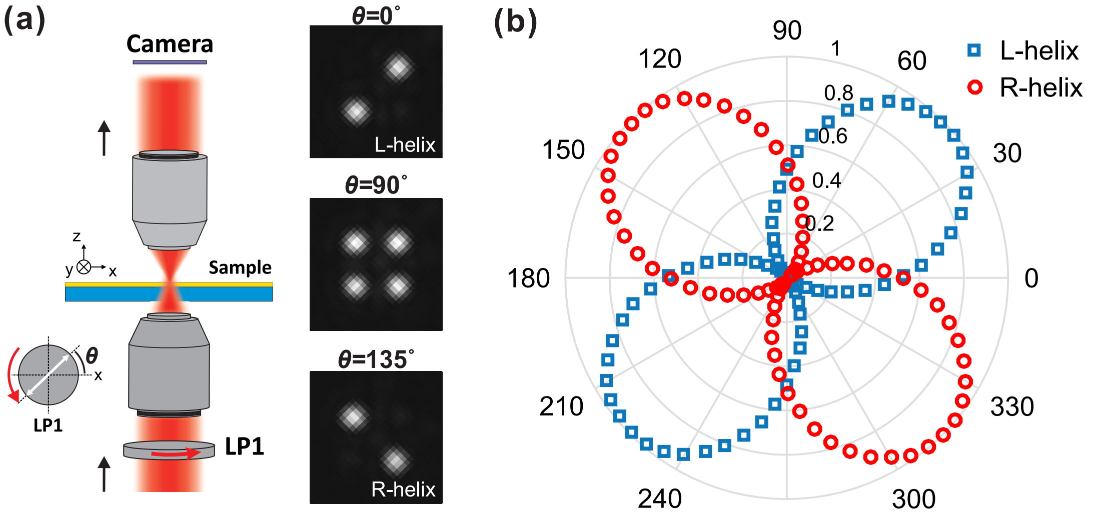

Figure 5.7: Measurement on the tuning property of the spin-light array (cf. Fig. 5.6) with linearly polarized excitation light. (a) Left panel: schematic diagram of the experimental setup and right panel: far-field optical images of the four-HPA device at three input polarizations. (b) Emission intensities of the two HPAs of opposite handedness at various input polarization states.

The helicity of the emissions is also investigated. To this end, the input polarization is fixed along $(0y)$ so that all HPAs are switched on simultaneously. We insert a fixed linear polarizer and a rotating quarter-wave plate in the collection bench before the camera to analyze the transmitted power (see Figure 5.8 (a), left panel). The right panel of Figure 5.8 (a) shows the optical images of the emissions as a function of the angle θ between the fast axis of the quarter wave plate and the transmission axis of the linear polarizer. Especially, θ values of $45°$ and $135°$ correspond to right- and left-handed circular analyzers, respectively. The emission helicity of each TW-HPA is identical to the handedness of the helix, which can also be confirmed by the measured transmitted power of left and right-handed HPAs at a full turn of the quarter-wave plate (Figure 5.8 (b)).

We can therefore create ultracompact optical architectures made of tiny circularly-polarized directional light sources with arbitrary handedness and tunable intensities, thus achieving unprecedented integrated devices for manipulating light polarization at small scale.

5.3/ SUBWAVELENGTH-SCALE WAVE-PLATE BY COUPLING FOUR TW-HPAS

In a traditional way, one can manipulate light polarization with a linear polarizer and a quarter-wave plate. In this process, two orthogonal linearly polarized waves that are phase-retarded by $\pi/2$ and with proper amplitudes are combined. Similar polarization

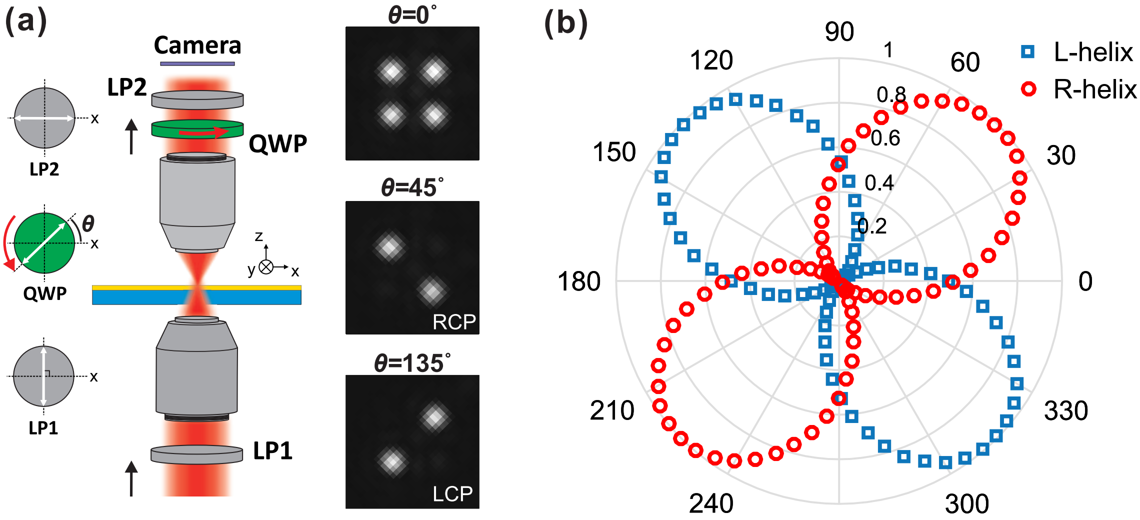

Figure 5.8: Helicity characterization of the emissions from the spin-light array (cf. Fig. 5.6). (a) left panel: schematic diagram of the experimental setup, right panel: far-field optical images of the four-TW-HPA device with a (middle) right-handed and (bottom) a left-handed circular analyzer in front of the camera. (b) Helicity analysis of two HPAs of opposite handedness. The measurement is realized by placing a rotating quarter wave-plate and a fixed linear polarizer in front of a detector and measuring the transmitted power.

manipulation can be realized by composing two elliptical polarizations of opposite helicities. In the CP-LSA shown previously, HPAs of the opposite handedness are placed at a distance larger than one wavelength to produce decoupled far-field emissions. The emission intensities of the left and right handed HPAs can be controlled by tuning the polarization of incident light. In this section, we will introduce a more complex polarization response by reducing the spacing between the HPAs to a value smaller than one wavelength, resulting in the coupling of the light emissions created by individual plasmonic antennas.

5.3.1/ CONCEPT AND ANALYTICAL MODEL

Figures 5.9 (a) and (b) schematically show the concept of four-coupled TW-HPA-platform. Two couples of HPAs of opposite handedness (as marked by “L" and “R") are arranged with the helices centered at the apexes of a subwavelength square. The polarization manipulation of such a device relies on the combination of two elliptically polarized waves described by parallel polarization ellipses of opposite handedness, and the control of their respective amplitudes. Such a configuration can be simply modeled by the interference of two co-propagating plane waves described by parallel polarization ellipses of opposite handedness and tunable amplitudes.

Owing to the field projection rules defined by the two involved pairs of orthogonal aperture nano-antennas, the electric fields $\boldsymbol{E}_1$ and $\boldsymbol{E}_2$ of these two plane waves take the form:

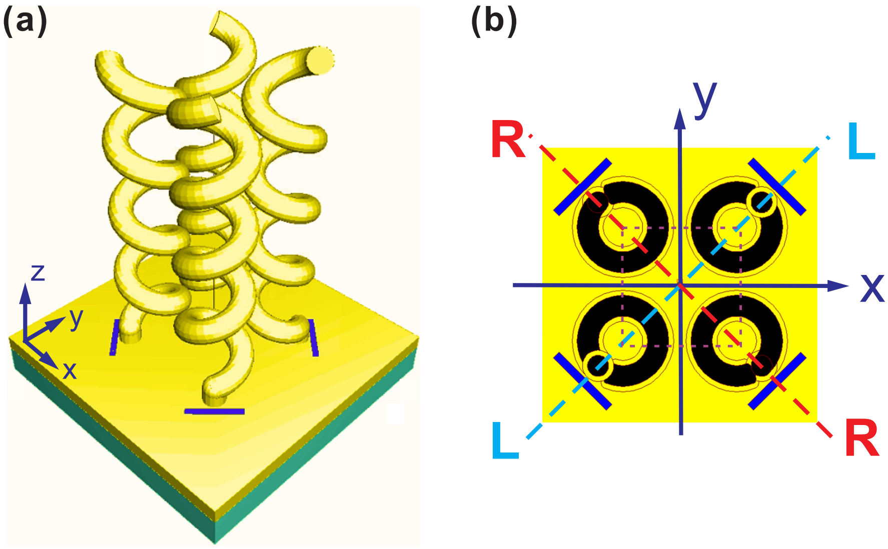

Figure 5.9: (a) 3D and (b) 2D top-view schematics of the four-coupled HPAs. It consists of two couples of HPAs of opposite handedness and orthogonal aperture nano-antennas. The right- and left-handed HPAs are identified with the letters R and L, respectively.

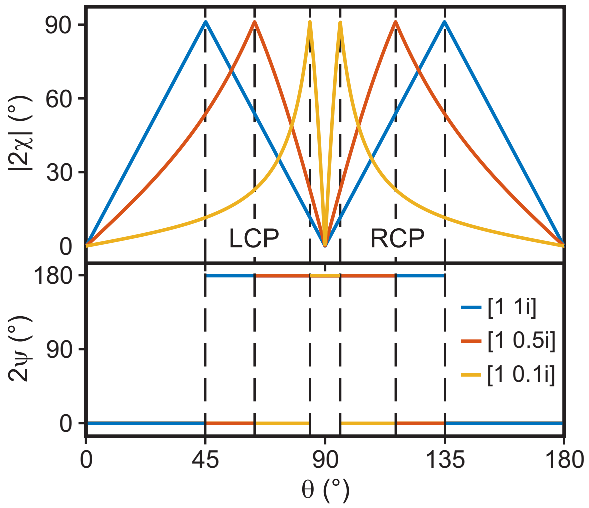

Figure 5.10: Theoretical prediction of the polarization state of the four-coupled TW-HPA structure (i.e., the polarization angles $|2\chi|$ and 2ψ on the Poincaré sphere), as a function of the polarization direction (angle θ) of an incident linearly polarized wave. Three ellipticity factors are considered: $b_1 = b_2 = 1$ (blue curves), $b_1 = b_2 = 0.5$ (orange curves) and $b_1 = b_2 = 0.1$ (yellow curves).

$$\boldsymbol{E}_1 = \sin\left(\theta - \frac{\pi}{4}\right)(1, ib_1, 0)\exp\left[-i(\omega t - wz)\right], \tag{5.2}$$

$$\boldsymbol{E}_2 = \cos\left(\theta - \frac{\pi}{4}\right)(-1, ib_2, 0)\exp\left[-i(\omega t - wz)\right]. \tag{5.3}$$

The two plane waves show the same wave vector $(0, 0, w)$. (x, y, z) are the space coordinates, ω is the angular frequency, and t refers to time. b_1 and b_2 are two positive constants smaller than 1, called axial ratios.

According to this configuration, circular polarization arises when:

$$\boldsymbol{E}_1 + \boldsymbol{E}_2 = K\,(\pm 1, i, 0)\exp\left[-i(\omega t - wz)\right], \tag{5.4}$$

where K is a constant, thus imposing:

$$\tan(\theta) = \left|\frac{1 \pm b_2}{1 \mp b_1}\right| + \frac{\pi}{4}, \tag{5.5}$$

Right and left circular polarizations are then obtained with two specific values of θ that are dependent on the axial ratios b_1 and b_2 of the two initial waves.

More generally the electric field resulting from the wave combination can be written:

$$(E_x, E_y, 0) = \sin\!\left(\theta - \frac{\pi}{4}\right)(1, ib_1, 0) + \cos\!\left(\theta - \frac{\pi}{4}\right)(-1, ib_2, 0). \tag{5.6}$$

We can consider this total field as an elliptically polarized wave whose major and minor radii take respectively the form :

$$OA = \frac{1}{\sqrt{2}}\left[|E_x|^2 + |E_y|^2 + \sqrt{|E_x|^4 + |E_y|^4 + 2|E_x|^2|E_y|^2\cos(2\Delta\phi)}\right]^{\frac{1}{2}}, \tag{5.7}$$

$$OB = \frac{1}{\sqrt{2}}\left[|E_x|^2 + |E_y|^2 - \sqrt{|E_x|^4 + |E_y|^4 + 2|E_x|^2|E_y|^2\cos(2\Delta\phi)}\right]^{\frac{1}{2}}, \tag{5.8}$$

where $\Delta\phi$ refers to the phase difference between E_x and E_y [83]. From Eqs. 5.7 and 5.8, we anticipate the polarization state of the four-TW-HPA emission, as a function of the projection angle θ related to incident polarization (Fig. 5.10). We consider the particular case where $b_1 = b_2$, i.e., two plane waves of identical ellipticities and opposite handedness. When these two waves are circularly polarized, the angular spacing $\Delta\theta$ between right and left polarizations is 90°. The resulting polarization manipulation is similar to that of a rotating polarizer in front of quarter-wave plate. In that case, θ refers to the projection angle of an incident linearly polarized wave onto the crystalline axes of the retardation plate.

Polarization control deviates from this well-known conventional configuration when we consider two elliptically polarized waves (b_1 and b_2 become smaller than 1). Depending on the axial ratio of the two initial waves, the angular spacing $\Delta\theta$ between the right and left circular polarizations decreases down to 53° when $b_1 = b_2 = 0.5$ and 11.5° when $b_1 = b_2 = 0.1$. The four-coupled TW-HPA structure would thus possibly lead to a near-switching effect of circular polarization handedness while rotating linear polarization of an incoming light.

5.3.2/ EXPERIMENTAL DEMONSTRATION

Figure 5.11 shows the SEM images of a nanofabricated four-coupled TW-HPA structure. The antennas of opposite handedness are spaced a distance of 560 nm apart and are

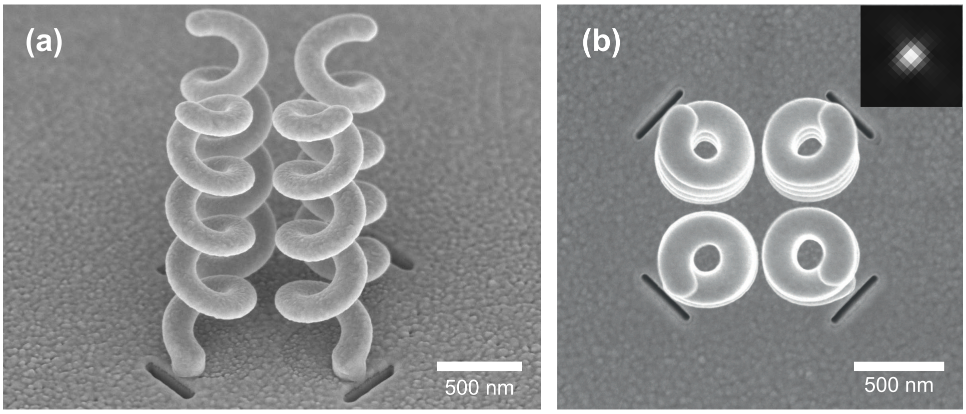

Figure 5.11: Scanning electron micrographs of the four-coupled TW-HPA structure: (a) Angled view, (b) Top view. Figure inset shows the optical image of the structure on emission, exhibiting a single light spot (regardless of the input polarization).

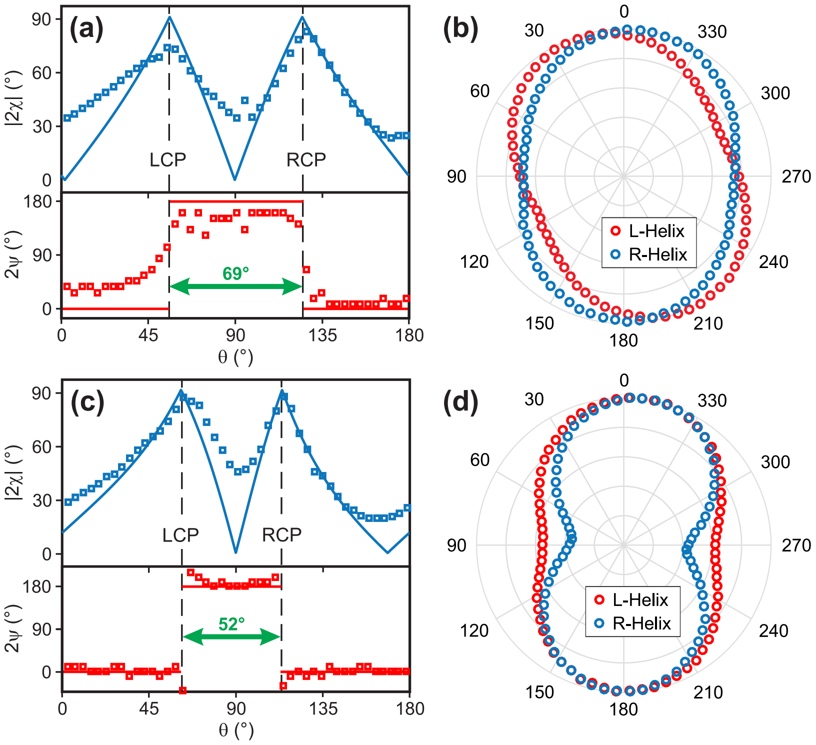

Figure 5.12: Subwavelength scale manipulation of light polarization by four coupled HPAs. (a,c) Polarization angles 2χ and 2ψ of the emitted field versus the polarization direction of an incident linearly polarized light (Poincaré sphere approach of polarization). The optical waves are impinging from the substrate at normal incidence, with (a) λ=1615 nm and (c) λ=1470 nm. (b,d) Polarization diagram of the antenna emission for incident polarization corresponding to θ equal to 45° and 135°, leading to the selective excitation of the two couples of HPAs of opposite handedness: (b) λ=1615 nm. (d) λ=1470 nm. Near-field coupling between the HPAs of opposite handedness ensures parallel outcoming polarization ellipses for orthogonal incident linear polarizations.

made up of orthogonal apertures (Fig. 5.11 (a) and (b)). Each TW-HPA has a radius of 175 nm and a vertical pitch around 380 nm. The wire has a carbon core of 100-nm diameter and a gold coating of around 25 nm. The rectangular aperture is 370-nm long and 40-nm wide. We use the experimental setup shown in Fig. 4.14 (a) to characterize the optical property of the four-coupled HPAs. Inset of Fig. 5.11 (b) shows the far-field emission of the four-TW-HPA device. It exhibits a single spot whatever the incident polarization, which confirms a coupling between the four antennas.

We further analyze the polarization transformation functionality of the four-coupled HPAs. We rotate a half-wave plate to tune the incident polarization angle (θ), by rotating a half-wave plate. Owing to the oscillatory nature of light fields, the full set of incident linear polarizations is covered with a polarization angle θ ranging from 0 to 180 ° (see theoretical predictions in Fig. 5.10). At each $4°$ increment of θ, we analyze the polarization state of the emitted light. To this end, we insert a rotating polarizer in front of the camera and analyze the transmission power to measure the polarization ellipticity. The emission helicity is analyzed with a rotating quarter wave plate and a fixed linear polarizer inserted in front of the camera.

Figures 5.12 (a) and (c) compare measured and calculated tilt angle 2ψ and ellipticity angle 2χ of the outcoming polarization (Poincaré sphere approach), as a function of the direction angle θ of the incident linear polarization, at two different wavelengths 1615 nm and 1470 nm, respectively. The measurements reveal the theoretically anticipated tuning of the angular spacing $\Delta\theta$ between the two right- and left-handed outcoming circular polarizations. Whereas $\Delta\theta$ is fixed at 90° with conventional phase retardation plates, it is here equal to 69° at λ= 1615 nm and decreases down to 51° at λ=1470 nm. Such a tunability in polarization manipulation is not standard at all. It arises from the ability

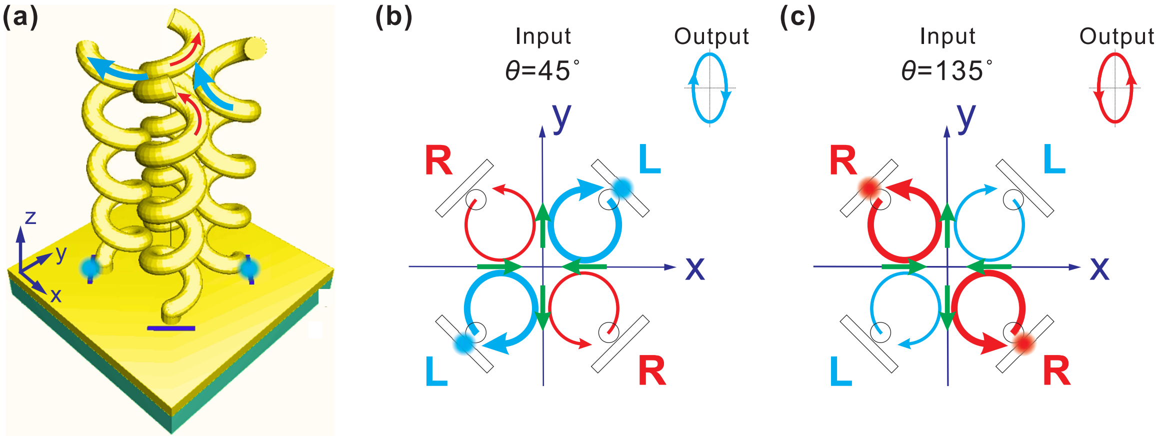

Figure 5.13: Schematics illustrating the generation of parallel elliptical polarizations of opposite helicity at $\theta = 45°$ and $135°$, due to the near-field coupling of SPs in the four-coupled TW-HPA device. (a) 3D schematic showing the near-field coupling of surface plasmons (SPs) in the four TW-HPAs at $\theta = 45°$. (b,c) Top-view schematics showing the coupling between SPs in such a system with (b) $\theta = 45°$ and (c) $\theta = 135°$. The blue and red open circles with an arrow indicate the swirling SPs in the left- and right-handed TW-HPAs, respectively. The green arrows indicate the parallel propagation directions of those SPs. The corresponding output polarization states are represented by the blue and red ellipses in the insets of (a) and (b).

of our structure to generate circular polarizations from the combination of the two elliptically polarized waves of parallel ellipticities (as shown experimentally in Figs. 5.12 (b) and (d)), opposite handedness and tunable intensities. By spectrally detuning the HPAs, the outcoming polarization ellipticities are modified, thus resulting in a controlled angular spacing $\Delta\theta$.

The two experimental polarization ellipses with $\theta = 45°$ and $\theta = 135°$ are basically parallel at the two wavelengths ($\lambda = 1615$ nm and $\lambda = 1470$ nm), as shown both in Figs. 5.13 (b) and (d). We think this is imposed by the near-field coupling between the four TW-HPAs, as shown in Fig. 5.13. Take $\theta = 45°$ for example (see Fig. 5.13 (a,b)), the two left-handed TW-HPAs are excited by the rectangular nanoapertures (marked by blue halos). The resulting SPs (blue curved arrows) evoke, by near-field coupling, the SPs in the two right handed TW-HPAs (red curved arrows). Such a coupling is rendered possible because the adjacent rims of the TW-HPAs of opposite handedness are in close proximity (distance: ~ 100 nm) and the allowed local wave vectors for the two HPAs are parallel (favorable of phase matching). The above-described coupling process imposes on the four TW-HPAs system an optical response of mirror-symmetry about the y axis, leading to the emission polarization shown by the ellipse in Fig. 5.13 (a). As the SPs in the left-handed HPAs has a stronger amplitude than those in the opposite, the emission is left-handed. Similar coupling process happens when $\theta = 135°$ (see Fig. 5.13 (b)), which produces an emission polarization parallel but in opposite helicity to the case when $\theta = 45°$.

5.4/ CONCLUSIONS

In this chapter, we first show the circular dichroism of TW-HPA in collection mode. Then, we show a circularly polarized light source array by assembling four TW-HPAs of opposite handedness with a distance of a few microns. We show that the emission intensity from those TW-HPAs is tunable regarding the input linear polarizations. Finally, we introduce and demonstrate the concept of a subwavelength-scale wave-plate by coupling the four TW-HPAs. We show an unconventional polarization transformation of such a device that the output polarization can be switched between the two circular polarization states with the input polarizations rotated by an angle much smaller than $90°$.

6

SUMMARY AND PERSPECTIVES

My thesis is devoted to novel nano-optical phenomena and devices based on spin-orbit interaction (SOI) of light. Two major works have been accomplished under this frame: 1) magnetic spin-locking, i.e., an SOI solely driven by the magnetic field of light, which provides a new manifestation of the magnetic light field. 2) traveling-wave helical plasmonic antenna (TW-HPA), which offers an unconventional approach to flexibly and tunably define light polarizations on subwavelength scale.

First, we showed a magnetic spin-orbit interaction of light (magnetic spin-locking), where the magnetic field of light tunably steers Bloch surface waves. We experimentally demonstrate that the helicity of optical magnetic field defines a directional excitation phenomenon, with a single subwavelength groove as the light-to-BSW coupler. Despite the electric dipole nature of this coupler, we found this new magnetic optical effect is of the same order of magnitude as the electric effect in play in the coupling process. As a perspective, we could use couplers that can develop magnetic resonances to realize a pure magnetic tunable unidirectional coupling. In addition, we could use BSWs as probes to locally investigate the magnetic polarization properties of light. They may enable measurement of the optical magnetic spin density of light [66].

We also introduced the concept of traveling-wave helical plasmonic antenna (TW-HPA). We assumed an EOAM-to-SAM transfer process underlying the TW-HPA to link near-field swirling plasmons and far-field circular polarized emissions. It is noted that, this is far from enough to fully understand the behavior of the TW-HPA. For example, the current distribution along the helix wire has almost uniform amplitude over a long distance. Considering the field damping caused by ohmic and radiation losses, this is pretty unusual. Theoretical understanding is currently carried out by our group.

We fabricated and characterized the TW-HPA. We experimentally showed that the fabricated TW-HPA radiates almost perfect circularly polarized light at infrared wavelengths. Such an antenna can be used to define the polarization properties of nano-emitters such as quantum dots, which might be interesting for developing circularly polarized single-photon sources. Besides, one can geometrically scale the TW-HPA for working in other optical regimes, e.g., in the visible wavelength band. We could also taper the helix geometry to further broaden the operation bandwidth.

We developed new optical functionalities by combining two couples of HPAs of opposite handedness, including a compact circularly polarized light source array with programmable helicity and a four-coupled TW-HPA device whose volume is smaller than one cubic wavelength. The former offers an approach to unprecedented integrated devices for manipulating light polarization and intensity at small scale. The latter enables, at subwavelength scale, a background-free polarization transformation featuring a faster switching between the two CP states. It would be interesting to integrate these components with active polarization-control components, say a liquid crystal device, to gain more advanced polarization tunability. It might be also interesting to optimize the helix dimension for a faster switching between the two CP states.

The detection of light polarizations is important for many applications. We show that the TW-HPA, operating in detection mode, exhibit circular dichroism. We can thus use the TW-HPA to resolve and characterize light polarizations at the subwavelength scale. Local measurement of the DOCP or even polarimetry could be foreseen with our TW-HPAs. In addition, the TW-HPA may also enable new polarization-based optical functionalities for sensing or communications, which could include the unique electrical and mechanical properties of our 3D metal-coated helical wires.

BIBLIOGRAPHY

[1] NOVOTNY, L., AND HECHT, B. **Principles of nano-optics**. Cambridge university press, 2012.

[2] LIEBERMAN, K., HARUSH, S., LEWIS, A., AND KOPELMAN, R. **A light source smaller than the optical wavelength**. *Science 247*, 4938 (1990), 59.

[3] POHL, D. W., AND COURJON, D. **Near field optics**. Springer Science & Business Media, 2012.

[4] COURJON, D., AND BAINIER, C. **Near field microscopy and near field optics**. *Rep. Prog. Phys. 57*, 10 (1994), 989.

[5] OHTSU, M. **Near-field nano/atom optics and technology**. Springer Science & Business Media, 2012.

[6] HECHT, B., SICK, B., WILD, U. P., DECKERT, V., ZENOBI, R., MARTIN, O. J., AND POHL, D. W. **Scanning near-field optical microscopy with aperture probes: Fundamentals and applications**. *J. Chem. Phys. 112*, 18 (2000), 7761.

[7] KAWATA, S. **Near-field microscope probes utilizing surface plasmon polaritons**. In *Near-Field Optics and Surface Plasmon Polaritons*. Springer, 2001, p. 15.

[8] COURJON, D. **Near-field microscopy and near-field optics**. World Scientific Publishing Company, 2003.

[9] NOVOTNY, L., AND STRANICK, S. J. **Near-field optical microscopy and spectroscopy with pointed probes**. *Annu. Rev. Phys. Chem. 57* (2006), 303.

[10] LAL, S., LINK, S., AND HALAS, N. J. **Nano-optics from sensing to waveguiding**. *Nat. Photonics 1*, 11 (2007), 641.

[11] TAO, A., KIM, F., HESS, C., GOLDBERGER, J., HE, R., SUN, Y., XIA, Y., AND YANG, P. **Langmuir-blodgett silver nanowire monolayers for molecular sensing using surface-enhanced raman spectroscopy**. *Nano Lett. 3*, 9 (2003), 1229.

[12] SCHATZ, G., YOUNG, M., AND VAN DUYNE, R. **Surface enhanced raman scattering: physics and applications**, 2006.

[13] STILES, P. L., DIERINGER, J. A., SHAH, N. C., AND VAN DUYNE, R. P. **Surface-enhanced raman spectroscopy**. *Annu. Rev. Anal. Chem. 1* (2008), 601.

[14] LE RU, E., AND ETCHEGOIN, P. **Principles of surface-enhanced Raman spectroscopy: and related plasmonic effects**. Elsevier, 2008.

[15] OZAKI, Y., KNEIPP, K., AND AROCA, R. **Frontiers of surface-enhanced Raman scattering: single nanoparticles and single cells**. John Wiley & Sons, 2014.

[16] Raether, H. **Surface plasmons on gratings**. In *Surface plasmons on smooth and rough surfaces and on gratings*. Springer, 1988, p. 91.

[17] Barnes, W. L., Dereux, A., and Ebbesen, T. W. **Surface plasmon subwavelength optics**. *nature 424*, 6950 (2003), 824.

[18] Maier, S. A. **Plasmonics: fundamentals and applications**. Springer Science & Business Media, 2007.

[19] Zayats, A. V., Smolyaninov, I. I., and Maradudin, A. A. **Nano-optics of surface plasmon polaritons**. *Phys. Rep. 408*, 3-4 (2005), 131.

[20] Ozbay, E. **Plasmonics: merging photonics and electronics at nanoscale dimensions**. *science 311*, 5758 (2006), 189.

[21] Brongersma, M. L., and Kik, P. G. **Surface plasmon nanophotonics**, vol. 131. Springer, 2007.

[22] Kawata, S., Inouye, Y., and Verma, P. **Plasmonics for near-field nano-imaging and superlensing**. *Nat. Photonics 3*, 7 (2009), 388.

[23] Schuller, J. A., Barnard, E. S., Cai, W., Jun, Y. C., White, J. S., and Brongersma, M. L. **Plasmonics for extreme light concentration and manipulation**. *Nat. Mater 9*, 3 (2010), 193.

[24] Juan, M. L., Righini, M., and Quidant, R. **Plasmon nano-optical tweezers**. *Nat. Photonics 5*, 6 (2011), 349.

[25] Zhang, J., and Zhang, L. **Nanostructures for surface plasmons**. *Adv. Opt. Photonics 4*, 2 (2012), 157.

[26] Kauranen, M., and Zayats, A. V. **Nonlinear plasmonics**. *Nat. Photonics 6*, 11 (2012), 737.

[27] Novotny, L. **Nano-optics: Optical antennas tuned to pitch**. *Nature 455*, 7215 (2008), 887.

[28] Bharadwaj, P., Deutsch, B., and Novotny, L. **Optical antennas**. *Adv. Opt. Photonics 1*, 3 (2009), 438.

[29] Novotny, L. **From near-field optics to optical antennas**. *Phys. Today 64*, 7 (2011), 47.

[30] Novotny, L., and Van Hulst, N. **Antennas for light**. *Nat. Photonics 5*, 2 (2011), 83.

[31] Biagioni, P., Huang, J.-S., and Hecht, B. **Nanoantennas for visible and infrared radiation**. *Rep. Prog. Phys. 75*, 2 (2012), 024402.

[32] Agio, M., and Alù, A. **Optical antennas**. Cambridge University Press, 2013.

[33] Engheta, N., and Ziolkowski, R. W. **Metamaterials: physics and engineering explorations**. John Wiley & Sons, 2006.

[34] Shalaev, V. M. **Optical negative-index metamaterials**. *Nat. Photonics 1*, 1 (2007), 41.

[35] Liu, N., Guo, H., Fu, L., Kaiser, S., Schweizer, H., and Giessen, H. **Three-dimensional photonic metamaterials at optical frequencies**. *Nat. Mater 7*, 1 (2008), 31.

[36] Cai, W., and Shalaev, V. **Optical metamaterials: fundamentals and applications**. Springer Science & Business Media, 2009.

[37] Capolino, F. **Theory and phenomena of metamaterials**. CRC press, 2009.

[38] Cui, T. J., Smith, D. R., and Liu, R. **Metamaterials**. Springer, 2010.

[39] Boltasseva, A., and Atwater, H. A. **Low-loss plasmonic metamaterials**. *Science 331*, 6015 (2011), 290.

[40] Noginov, M. A., and Podolskiy, V. A. **Tutorials in metamaterials**. CRC press, 2011.

[41] Yu, N., and Capasso, F. **Flat optics with designer metasurfaces**. *Nat. Mater 13*, 2 (2014), 139.

[42] Yao, K., and Liu, Y. **Plasmonic metamaterials**. *Nanotechnol. Rev. 3*, 2 (2014), 177.

[43] Genevet, P., and Capasso, F. **Holographic optical metasurfaces: a review of current progress**. *Rep. Prog. Phys. 78*, 2 (2015), 024401.

[44] Kaschke, J., and Wegener, M. **Optical and infrared helical metamaterials**. *Nanophotonics 5*, 4 (2016), 510.

[45] Gansel, J. K., Thiel, M., Rill, M. S., Decker, M., Bade, K., Saile, V., von Freymann, G., Linden, S., and Wegener, M. **Gold helix photonic metamaterial as broadband circular polarizer**. *Science 325*, 5947 (2009), 1513.

[46] Yu, N., Aieta, F., Genevet, P., Kats, M. A., Gaburro, Z., and Capasso, F. **A broadband, background-free quarter-wave plate based on plasmonic metasurfaces**. *Nano Lett. 12*, 12 (2012), 6328.

[47] Lin, J., Mueller, J. B., Wang, Q., Yuan, G., Antoniou, N., Yuan, X.-C., and Capasso, F. **Polarization-controlled tunable directional coupling of surface plasmon polaritons**. *Science 340*, 6130 (2013), 331.

[48] Du, L., Kou, S. S., Balaur, E., Cadusch, J. J., Roberts, A., Abbey, B., Yuan, X.-C., Tang, D., and Lin, J. **Broadband chirality-coded meta-aperture for photon-spin resolving**. *Nature Commun. 6* (2015), 10051.

[49] Taminiau, T. H., Moerland, R. J., Segerink, F. B., Kuipers, L., and van Hulst, N. F. **λ/4 resonance of an optical monopole antenna probed by single molecule fluorescence**. *Nano Lett. 7*, 1 (2007), 28.

[50] Taminiau, T., Stefani, F., Segerink, F. B., and Van Hulst, N. **Optical antennas direct single-molecule emission**. *Nat. Photonics 2*, 4 (2008), 234.

[51] Curto, A. G., Volpe, G., Taminiau, T. H., Kreuzer, M. P., Quidant, R., and van Hulst, N. F. **Unidirectional emission of a quantum dot coupled to a nanoantenna**. *Science 329*, 5994 (2010), 930.

[52] Farahani, J. N., Pohl, D. W., Eisler, H.-J., and Hecht, B. **Single quantum dot coupled to a scanning optical antenna: a tunable superemitter**. *Phys. Rev. Lett. 95*, 1 (2005), 017402.

[53] Yao, A. M., and Padgett, M. J. **Orbital angular momentum: origins, behavior and applications**. *Adv. Opt. Photonics 3*, 2 (2011), 161.

[54] Bliokh, K. Y., and Aiello, A. **Goos–hänchen and imbert–fedorov beam shifts: an overview**. *J. Opt. 15*, 1 (2013), 014001.

[55] Bliokh, K. Y., Rodríguez-Fortuño, F., Nori, F., and Zayats, A. V. **Spin–orbit interactions of light**. *Nat. Photonics 9*, 12 (2015), 796.

[56] Aiello, A., Banzer, P., Neugebauer, M., and Leuchs, G. **From transverse angular momentum to photonic wheels**. *Nat. Photonics 9*, 12 (2015), 789.

[57] Cardano, F., and Marrucci, L. **Spin–orbit photonics**. *Nat. Photonics 9*, 12 (2015), 776.

[58] Zhao, Y., Edgar, J. S., Jeffries, G. D., McGloin, D., and Chiu, D. T. **Spin-to-orbital angular momentum conversion in a strongly focused optical beam**. *Phys. Rev. Lett. 99*, 7 (2007), 073901.

[59] Zhao, Y., Shapiro, D., Mcgloin, D., Chiu, D. T., and Marchesini, S. **Direct observation of the transfer of orbital angular momentum to metal particles from a focused circularly polarized gaussian beam**. *Opt. Express 17*, 25 (2009), 23316.

[60] Biener, G., Niv, A., Kleiner, V., and Hasman, E. **Formation of helical beams by use of pancharatnam–berry phase optical elements**. *Opt. Lett. 27*, 21 (2002), 1875.

[61] Brasselet, E., Murazawa, N., Misawa, H., and Juodkazis, S. **Optical vortices from liquid crystal droplets**. *Phys. Rev. Lett. 103*, 10 (2009), 103903.

[62] Shitrit, N., Bretner, I., Gorodetski, Y., Kleiner, V., and Hasman, E. **Optical spin hall effects in plasmonic chains**. *Nano Lett. 11*, 5 (2011), 2038.

[63] Brasselet, E., Gervinskas, G., Seniutinas, G., and Juodkazis, S. **Topological shaping of light by closed-path nanoslits**. *Phys. Rev. Lett. 111*, 19 (2013), 193901.

[64] Neugebauer, M., Bauer, T., Banzer, P., and Leuchs, G. **Polarization tailored light driven directional optical nanobeacon**. *Nano Lett. 14*, 5 (2014), 2546.

[65] Neugebauer, M., Bauer, T., Aiello, A., and Banzer, P. **Measuring the transverse spin density of light**. *Phys. Rev. Lett. 114*, 6 (2015), 063901.

[66] Neugebauer, M., Eismann, J. S., Bauer, T., and Banzer, P. **Magnetic and electric transverse spin density of spatially confined light**. *Phys. Rev. X 8*, 2 (2018), 021042.

[67] Yang, A., Du, L., Meng, F., and Yuan, X. **Optical transverse spin coupling through a plasmonic nanoparticle for particle-identification and field-mapping**. *Nanoscale 10*, 19 (2018), 9286.

[68] Rodríguez-Fortuño, F. J., Marino, G., Ginzburg, P., O'Connor, D., Martínez, A., Wurtz, G. A., and Zayats, A. V. **Near-field interference for the unidirectional excitation of electromagnetic guided modes**. *Science 340*, 6130 (2013), 328.

[69] O'connor, D., Ginzburg, P., Rodríguez-Fortuño, F., Wurtz, G., and Zayats, A. **Spin–orbit coupling in surface plasmon scattering by nanostructures**. *Nature Commun. 5* (2014), 5327.

[70] Mitsch, R., Sayrin, C., Albrecht, B., Schneeweiss, P., and Rauschenbeutel, A. **Quantum state-controlled directional spontaneous emission of photons into a nanophotonic waveguide**. *Nature Commun. 5* (2014), 5713.

[71] Petersen, J., Volz, J., and Rauschenbeutel, A. **Chiral nanophotonic waveguide interface based on spin-orbit interaction of light**. *Science 346*, 6205 (2014), 67.

[72] Söllner, I., Mahmoodian, S., Hansen, S. L., Midolo, L., Javadi, A., Kiršanskė, G., Pregnolato, T., El-Ella, H., Lee, E. H., Song, J. D., and others. **Deterministic photon–emitter coupling in chiral photonic circuits**. *Nat. Nanotechnol. 10*, 9 (2015), 775.

[73] Le Feber, B., Rotenberg, N., and Kuipers, L. **Nanophotonic control of circular dipole emission**. *Nature Commun. 6* (2015), 6695.

[74] Wang, M., Zhang, H., Kovalevich, T., Salut, R., Kim, M.-S., Suarez, M. A., Bernal, M.-P., Herzig, H.-P., Lu, H., and Grosjean, T. **Magnetic spin–orbit interaction of light**. *Light Sci. Appl. 7*, 1 (2018), 24.

[75] Arnold, V. I. **Mathematical methods of classical mechanics**, vol. 60. Springer Science & Business Media, 2013.

[76] Feynman, R. P., Leighton, R. B., and Sands, M. **The Feynman lectures on physics**. Addison-Wesley, 1963.

[77] L. Allen, S. B., and Padgett, M. **Optical angular momentum**. Taylor & Francis, London, 2003.

[78] Allen, L., Beijersbergen, M. W., Spreeuw, R., and Woerdman, J. **Orbital angular momentum of light and the transformation of laguerre-gaussian laser modes**. *Phys. Rev. A 45*, 11 (1992), 8185.

[79] Ling, X., Zhou, X., Huang, K., Liu, Y., Qiu, C.-W., Luo, H., and Wen, S. **Recent advances in the spin hall effect of light**. *Rep. Prog. Phys. 80*, 6 (2017), 066401.

[80] Jackson, J. D. **Classical electrodynamics**. John Wiley & Sons, 1999.

[81] Van Enk, S., and Nienhuis, G. **Eigenfunction description of laser beams and orbital angular momentum of light**. *Opt. Commun. 94*, 1 (1992), 147.

[82] Huard, S. **Polarization of light**. Wiley-Blackwell, 1997.

[83] Constantine, A. B. **Antenna theory: analysis and design**. John wiley & sons, 2005.

[84] Grosjean, T., Ibrahim, I., Suarez, M., Burr, G., Mivelle, M., and Charraut, D. **Full vectorial imaging of electromagnetic light at subwavelength scale**. *Opt. Express 18*, 6 (2010), 5809.

[85] Bekshaev, A. Y., Bliokh, K. Y., and Nori, F. **Transverse spin and momentum in two-wave interference**. *Phys. Rev. X 5*, 1 (2015), 011039.

[86] Bliokh, K. Y., Bekshaev, A. Y., and Nori, F. **Extraordinary momentum and spin in evanescent waves**. *Nature Commun. 5* (2014), 3300.

[87] Bliokh, K. Y., Smirnova, D., and Nori, F. **Quantum spin hall effect of light**. *Science 348*, 6242 (2015), 1448.

[88] Bliokh, K. Y., and Nori, F. **Transverse and longitudinal angular momenta of light**. *Phys. Rep. 592* (2015), 1.

[89] Kalhor, F., Thundat, T., and Jacob, Z. **Universal spin-momentum locked optical forces**. *Appl. Phys. Lett. 108*, 6 (2016), 061102.

[90] Van Mechelen, T., and Jacob, Z. **Universal spin-momentum locking of evanescent waves**. *Optica 3*, 2 (2016), 118.

[91] Padgett, M. **Light's twist**. *Proc. R. Soc. A 470*, 2172 (2014).

[92] Padgett, M., Courtial, J., and Allen, L. **Light's orbital angular momentum**. *Phys. Today 57*, 5 (2004), 35.

[93] Allen, L., Padgett, M., and Babiker, M. **The orbital angular momentum of light**. In *Progress in optics:IV*, vol. 39. Elsevier, 1999, p. 291.

[94] Bliokh, K. Y., Dressel, J., and Nori, F. **Conservation of the spin and orbital angular momenta in electromagnetism**. *New J. Phys. 16*, 9 (2014), 093037.

[95] Berry, M. V. **The adiabatic phase and pancharatnam's phase for polarized light**. *J. Mod. Opt. 34*, 11 (1987), 1401.

[96] Berry, M. **Classical adiabatic angles and quantal adiabatic phase**. *J. Phys. A 18*, 1 (1985), 15.

[97] Bliokh, K. Y., Gorodetski, Y., Kleiner, V., and Hasman, E. **Coriolis effect in optics: unified geometric phase and spin-hall effect**. *Phys. Rev. Lett. 101*, 3 (2008), 030404.

[98] Bliokh, K. Y., Niv, A., Kleiner, V., and Hasman, E. **Geometrodynamics of spinning light**. *Nat. Photonics 2*, 12 (2008), 748.

[99] Bekshaev, A. Y. **Spin–orbit interaction of light and diffraction of polarized beams**. *J. Opt. 19*, 8 (2017), 085602.

[100] Chiao, R., and Wu, Y. **Manifestations of berry's topological phase for the photon.** *Phys. Rev. Lett. 57*, 8 (1986), 933.

[101] Tomita, A., and Chiao, R. Y. **Observation of berry's topological phase by use of an optical fiber**. *Phys. Rev. Lett. 57*, 8 (1986), 937.

[102] Bliokh, K. Y., and Bliokh, Y. P. **Topological spin transport of photons: the optical magnus effect and berry phase**. *Phys. Lett. A 333*, 3-4 (2004), 181.

[103] Bliokh, K. Y. **Geometrodynamics of polarized light: Berry phase and spin hall effect in a gradient-index medium**. *J. Opt. A: Pure Appl. Opt. 11*, 9 (2009), 094009.

[104] Hosten, O., and Kwiat, P. **Observation of the spin hall effect of light via weak measurements**. *Science 319*, 5864 (2008), 787.

[105] Gorodetski, Y., Bliokh, K., Stein, B., Genet, C., Shitrit, N., Kleiner, V., Hasman, E., and Ebbesen, T. **Weak measurements of light chirality with a plasmonic slit**. *Phys. Rev. Lett. 109*, 1 (2012), 013901.

[106] Aiello, A., and Woerdman, J. **Role of beam propagation in goos–hänchen and imbert–fedorov shifts**. *Opt. Lett. 33*, 13 (2008), 1437.

[107] Bliokh, K. Y., and Bliokh, Y. P. **Conservation of angular momentum, transverse shift, and spin hall effect in reflection and refraction of an electromagnetic wave packet**. *Phys. Rev. Lett. 96*, 7 (2006), 073903.

[108] Bliokh, K. Y., Ostrovskaya, E. A., Alonso, M. A., Rodríguez-Herrera, O. G., Lara, D., and Dainty, C. **Spin-to-orbital angular momentum conversion in focusing, scattering, and imaging systems**. *Opt. Express 19*, 27 (2011), 26132.

[109] Mansuripur, M., Zakharian, A. R., and Wright, E. M. **Spin and orbital angular momenta of light reflected from a cone**. *Phys. Rev. A 84*, 3 (2011), 033813.

[110] Bomzon, Z., Biener, G., Kleiner, V., and Hasman, E. **Space-variant pancharatnam–berry phase optical elements with computer-generated subwavelength gratings**. *Opt. Lett. 27*, 13 (2002), 1141.

[111] Lin, D., Fan, P., Hasman, E., and Brongersma, M. L. **Dielectric gradient metasurface optical elements**. *Science 345*, 6194 (2014), 298.

[112] Lefier, Y., Salut, R., Suarez, M., and Grosjean, T. **Directing nanoscale optical flows by coupling photon spin to plasmon extrinsic angular momentum.** *Nano Lett. 18*, 1 (2018), 38.

[113] Marrucci, L., Manzo, C., and Paparo, D. **Optical spin-to-orbital angular momentum conversion in inhomogeneous anisotropic media**. *Phys. Rev. Lett. 96*, 16 (2006), 163905.

[114] Shitrit, N., Yulevich, I., Maguid, E., Ozeri, D., Veksler, D., Kleiner, V., and Hasman, E. **Spin-optical metamaterial route to spin-controlled photonics**. *Science 340*, 6133 (2013), 724.

[115] Ling, X., Zhou, X., Yi, X., Shu, W., Liu, Y., Chen, S., Luo, H., Wen, S., and Fan, D. **Giant photonic spin hall effect in momentum space in a structured metamaterial with spatially varying birefringence**. *Light Sci. Appl. 4*, 5 (2015), e290.

[116] Liu, Y., Ling, X., Yi, X., Zhou, X., Chen, S., Ke, Y., Luo, H., and Wen, S. **Photonic spin hall effect in dielectric metasurfaces with rotational symmetry breaking**. *Opt. Lett. 40*, 5 (2015), 756.

[117] Lefier, Y., and Grosjean, T. **Unidirectional sub-diffraction waveguiding based on optical spin–orbit coupling in subwavelength plasmonic waveguides**. *Opt. Lett. 40*, 12 (2015), 2890.

[118] Rodríguez-Fortuño, F. J., Marino, G., Ginzburg, P., O'Connor, D., Martínez, A., Wurtz, G. A., and Zayats, A. V. **Near-field interference for the unidirectional excitation of electromagnetic guided modes**. *Science 340*, 6130 (2013), 328.

[119] Marrucci, L. **Quantum optics: Spin gives direction**. *Nat. Phys. 11*, 1 (2015), 9.

[120] Petersen, J., Volz, J., and Rauschenbeutel, A. **Chiral nanophotonic waveguide interface based on spin-orbit interaction of light**. *Science 346*, 6205 (2014), 67.

[121] Coles, R., Price, D., Dixon, J., Royall, B., Clarke, E., Kok, P., Skolnick, M., Fox, A., and Makhonin, M. **Chirality of nanophotonic waveguide with embedded quantum emitter for unidirectional spin transfer**. *Nature Commun. 7* (2016), 11183.

[122] Lee, S.-Y., Lee, I.-M., Park, J., Oh, S., Lee, W., Kim, K.-Y., and Lee, B. **Role of magnetic induction currents in nanoslit excitation of surface plasmon polaritons**. *Phys. Rev. Lett. 108*, 21 (2012), 213907.

[123] Rodríguez-Fortuño, F. J., Barber-Sanz, I., Puerto, D., Griol, A., and Martínez, A. **Resolving light handedness with an on-chip silicon microdisk**. *ACS Photonics 1*, 9 (2014), 762.

[124] Mueller, J. B., and Capasso, F. **Asymmetric surface plasmon polariton emission by a dipole emitter near a metal surface**. *Phys. Rev. B 88*, 12 (2013), 121410.

[125] Wang, S., and Chan, C. **Lateral optical force on chiral particles near a surface**. *Nature Commun. 5* (2014), ncomms4307.

[126] Rodríguez-Fortuño, F. J., Engheta, N., Martínez, A., and Zayats, A. V. **Lateral forces on circularly polarizable particles near a surface**. *Nature Commun. 6* (2015), 8799.

[127] Liu, L., Kheifets, S., Ginis, V., Di Donato, A., Amirzhan, A., and Capasso, F. **Measuring the spin-dependent lateral force in evanescent fields**. In *CLEO: QELS_Fundamental Science* (2018), Optical Society of America, pp. FF3E–6.

[128] Hayat, A., Mueller, J. B., and Capasso, F. **Lateral chirality-sorting optical forces**. *Proceedings of the National Academy of Sciences 112*, 43 (2015), 13190.

[129] Pendry, J. B., and Smith, D. R. **The quest for the superlens**. *Scientific American 295*, 1 (2006), 60.

[130] Pendry, J. B. **Negative refraction makes a perfect lens**. *Phys. Rev. Lett. 85*, 18 (2000), 3966.

[131] Dolling, G., Enkrich, C., Wegener, M., Soukoulis, C. M., and Linden, S. **Simultaneous negative phase and group velocity of light in a metamaterial**. *Science 312*, 5775 (2006), 892.

[132] Shalaev, V. M. **Optical negative-index metamaterials**. *Nat. Photonics 1*, 1 (2007), 41.

[133] Mivelle, M., Grosjean, T., Burr, G. W., Fischer, U. C., and Garcia-Parajo, M. F. **Strong modification of magnetic dipole emission through diabolo nanoantennas**. *ACS Photonics 2*, 8 (2015), 1071.

[134] Rolly, B., Bebey, B., Bidault, S., Stout, B., and Bonod, N. **Promoting magnetic dipolar transition in trivalent lanthanide ions with lossless mie resonances**. *Phys. Rev. B 85*, 24 (2012), 245432.

[135] Hein, S. M., and Giessen, H. **Tailoring magnetic dipole emission with plasmonic split-ring resonators**. *Phys. Rev. Lett. 111*, 2 (2013), 026803.

[136] Devaux, E., Dereux, A., Bourillot, E., Weeber, J.-C., Lacroute, Y., Goudonnet, J.-P., and Girard, C. **Local detection of the optical magnetic field in the near zone of dielectric samples**. *Phys. Rev. B 62*, 15 (2000), 10504.

[137] Burresi, M., van Oosten, D., Kampfrath, T., Schoenmaker, H., Heideman, R., Leinse, A., and Kuipers, L. **Probing the magnetic field of light at optical frequencies**. *Science 326*, 5952 (2009), 550.

[138] Suarez, M., Grosjean, T., Charraut, D., and Courjon, D. **Nanoring as a magnetic or electric field sensitive nano-antenna for near-field optics applications**. *Opt. Commun. 270*, 2 (2007), 447.

[139] Grosjean, T., Fahys, A., Suarez, M., Charraut, D., Salut, R., and Courjon, D. **Annular nanoantenna on fibre micro-axicon**. *J. Microsc. 229*, 2 (2008), 354.

[140] Kihm, H., Koo, S., Kim, Q., Bao, K., Kihm, J., Bak, W., Eah, S., Lienau, C., Kim, H., Nordlander, P., and others. **Bethe-hole polarization analyser for the magnetic vector of light**. *Nature Commun. 2* (2011), 451.

[141] Le Feber, B., Rotenberg, N., Beggs, D. M., and Kuipers, L. **Simultaneous measurement of nanoscale electric and magnetic optical fields**. *Nat. Photonics 8*, 1 (2014), 43.

[142] Burresi, M., Kampfrath, T., van Oosten, D., Prangsma, J., Song, B., Noda, S., and Kuipers, L. **Magnetic light-matter interactions in a photonic crystal nanocavity**. *Phys. Rev. Lett. 105*, 12 (2010), 123901.

[143] Vignolini, S., Intonti, F., Riboli, F., Balet, L., Li, L. H., Francardi, M., Gerardino, A., Fiore, A., Wiersma, D. S., and Gurioli, M. **Magnetic imaging in photonic crystal microcavities**. *Phys. Rev. Lett. 105*, 12 (2010), 123902.

[144] Baida, F. I., and Grosjean, T. **Double-way spectral tunability for the control of optical nanocavity resonance**. *Sci. Rep. 5* (2015), 17907.

[145] Xi, Z., Lu, Y., Yu, W., Wang, P., and Ming, H. **Unidirectional surface plasmon launcher: rotating dipole mimicked by optical antennas**. *J. Opt. 16*, 10 (2014), 105002.

[146] Mueller, J. B., Leosson, K., and Capasso, F. **Polarization-selective coupling to long-range surface plasmon polariton waveguides**. *Nano Lett. 14*, 10 (2014), 5524.

[147] Bliokh, K. Y., and Nori, F. **Transverse spin of a surface polariton**. *Phys. Rev. A 85*, 6 (2012), 061801.

[148] Kim, K.-Y., Lee, I.-M., Kim, J., Jung, J., and Lee, B. **Time reversal and the spin angular momentum of transverse-electric and transverse-magnetic surface modes**. *Phys. Rev. A 86*, 6 (2012), 063805.

[149] Kim, J., Naik, G. V., Gavrilenko, A. V., Dondapati, K., Gavrilenko, V. I., Prokes, S., Glembocki, O. J., Shalaev, V. M., and Boltasseva, A. **Optical properties of gallium-doped zinc oxide—a low-loss plasmonic material: first-principles theory and experiment**. *Phys. Rev. X 3*, 4 (2013), 041037.

[150] Picardi, M. F., Manjavacas, A., Zayats, A. V., and Rodríguez-Fortuño, F. J. **Unidirectional evanescent-wave coupling from circularly polarized electric and magnetic dipoles: An angular spectrum approach**. *Phys. Rev. B 95*, 24 (2017), 245416.

[151] Yeh, P., Yariv, A., and Cho, A. Y. **Optical surface waves in periodic layered media**. *Appl. Phys. Lett. 32*, 2 (1978), 104.

[152] Descrovi, E., Sfez, T., Dominici, L., Nakagawa, W., Michelotti, F., Giorgis, F., and Herzig, H.-P. **Near-field imaging of bloch surface waves on silicon nitride one-dimensional photonic crystals**. *Opt. Express 16*, 8 (2008), 5453.

[153] Kovalevich, T., Boyer, P., Suarez, M., Salut, R., Kim, M.-S., Herzig, H. P., Bernal, M.-P., and Grosjean, T. **Polarization controlled directional propagation of bloch surface wave**. *Opt. Express 25*, 5 (2017), 5710.

[154] Dubey, R., Lahijani, B. V., Häyrinen, M., Roussey, M., Kuittinen, M., and Herzig, H. P. **Ultra-thin bloch-surface-wave-based reflector at telecommunication wavelength**. *Photonics Res. 5*, 5 (2017), 494.

[155] Descrovi, E., Sfez, T., Quaglio, M., Brunazzo, D., Dominici, L., Michelotti, F., Herzig, H. P., Martin, O. J., and Giorgis, F. **Guided bloch surface waves on ultrathin polymeric ridges**. *Nano Lett. 10*, 6 (2010), 2087.

[156] Munzert, P., Danz, N., Sinibaldi, A., and Michelotti, F. **Multilayer coatings for bloch surface wave optical biosensors**. *Surf. Coatings Technol. 314* (2017), 79.

[157] Shilkin, D. A., Lyubin, E. V., Soboleva, I. V., and Fedyanin, A. A. **Direct measurements of forces induced by bloch surface waves in a one-dimensional photonic crystal**. *Opt. Lett. 40*, 21 (2015), 4883.

[158] KOVALEVICH, T. **Tunable Bloch surface waves devices**. PhD thesis, University of Bourgogne-Franche-Comté, 2017.

[159] KONOPSKY, V. N. **Plasmon-polariton waves in nanofilms on one-dimensional photonic crystal surfaces**. *New J. Phys. 12*, 9 (2010), 093006.

[160] WANG, J., CHEN, J., CHEN, K., YI, W., AND ZHANG, W. **Harmonically trapped quasi-two-dimensional fermi gases with synthetic spin-orbit coupling**. *Sci. China Physics, Mech. Astron. 59*, 9 (2016), 693011.

[161] TAFLOVE, A., AND HAGNESS, S. C. **Computational electrodynamics: the finite-difference time-domain method**. Artech house, 2005.

[162] KUZNETSOV, A. I., MIROSHNICHENKO, A. E., FU, Y. H., ZHANG, J., AND LUKANCHUK, B. **Magnetic light**. *Sci. Rep. 2* (2012), 492.

[163] EVLYUKHIN, A. B., NOVIKOV, S. M., ZYWIETZ, U., ERIKSEN, R. L., REINHARDT, C., BOZHEVOLNYI, S. I., AND CHICHKOV, B. N. **Demonstration of magnetic dipole resonances of dielectric nanospheres in the visible region**. *Nano Lett. 12*, 7 (2012), 3749.

[164] SCHÄFERLING, M., YIN, X., ENGHETA, N., AND GIESSEN, H. **Helical plasmonic nanostructures as prototypical chiral near-field sources**. *Acs Photonics 1*, 6 (2014), 530.

[165] WOZNIAK, P., DE LEON, I., HOEFLICH, K., HAVERKAMP, C., CHRISTIANSEN, S., LEUCHS, G., AND BANZER, P. **Chiroptical response of a single plasmonic nanohelix**. *Opt. Express 26*, 15 (2018), 19275.

[166] PASSASEO, A., ESPOSITO, M., CUSCUNÀ, M., AND TASCO, V. **Materials and 3d designs of helix nanostructures for chirality at optical frequencies**. *Adv. Opt. Mater. 5*, 16 (2017), 1601079.

[167] KRAUS, J. D., MARHEFKA, R. J., AND KHAN, A. S. **Antennas and wave propagation**. Tata McGraw-Hill Education, 2006.

[168] STOCKMAN, M. I. **Nanofocusing of optical energy in tapered plasmonic waveguides**. *Phys. Rev. Lett. 93*, 13 (2004), 137404.

[169] GAROLI, D., ZILIO, P., GORODETSKI, Y., TANTUSSI, F., AND DE ANGELIS, F. **Beaming of helical light from plasmonic vortices via adiabatically tapered nanotip**. *Nano Lett. 16*, 10 (2016), 6636.

[170] GAROLI, D., ZILIO, P., DE ANGELIS, F., AND GORODETSKI, Y. **Helicity locking of chiral light emitted from a plasmonic nanotaper**. *Nanoscale 9*, 21 (2017), 6965.

[171] HUANG, J.-S., FEICHTNER, T., BIAGIONI, P., AND HECHT, B. **Impedance matching and emission properties of nanoantennas in an optical nanocircuit**. *Nano Lett. 9*, 5 (2009), 1897.

[172] ANGER, P., BHARADWAJ, P., AND NOVOTNY, L. **Enhancement and quenching of single-molecule fluorescence**. *Phys. Rev. Lett. 96*, 11 (2006), 113002.

[173] BIAGIONI, P., HUANG, J., DUÒ, L., FINAZZI, M., AND HECHT, B. **Cross resonant optical antenna**. *Phys. Rev. Lett. 102*, 25 (2009), 256801.

[174] Taminiau, T. H., Segerink, F. B., Moerland, R. J., Kuipers, L. K., and van Hulst, N. F. **Near-field driving of a optical monopole antenna**. *J. Opt. A: Pure Appl. Opt. 9*, 9 (2007), S315.

[175] Mivelle, M., van Zanten, T. S., and Garcia-Parajo, M. F. **Hybrid photonic antennas for subnanometer multicolor localization and nanoimaging of single molecules**. *Nano Lett. 14*, 8 (2014), 4895.

[176] Alu, A., and Engheta, N. **Tuning the scattering response of optical nanoantennas with nanocircuit loads**. *Nat. Photonics 2*, 5 (2008), 307.

[177] Alù, A., and Engheta, N. **Wireless at the nanoscale: optical interconnects using matched nanoantennas**. *Phys. Rev. Lett. 104*, 21 (2010), 213902.

[178] Biagioni, P., Savoini, M., Huang, J.-S., Duò, L., Finazzi, M., and Hecht, B. **Near-field polarization shaping by a near-resonant plasmonic cross antenna**. *Phys. Rev. B 80*, 15 (2009), 153409.

[179] Kinkhabwala, A., Yu, Z., Fan, S., Avlasevich, Y., Müllen, K., and Moerner, W. **Large single-molecule fluorescence enhancements produced by a bowtie nanoantenna**. *Nat. Photonics 3*, 11 (2009), 654.

[180] Xie, Z., Lefier, Y., Suarez, M. A., Mivelle, M., Salut, R., Merolla, J.-M., and Grosjean, T. **Doubly resonant photonic antenna for single infrared quantum dot imaging at telecommunication wavelengths**. *Nano Lett. 17*, 4 (2017), 2152.

[181] Mivelle, M., van Zanten, T. S., Neumann, L., van Hulst, N. F., and Garcia-Parajo, M. F. **Ultrabright bowtie nanoaperture antenna probes studied by single molecule fluorescence**. *Nano Lett. 12*, 11 (2012), 5972.

[182] Flauraud, V., van Zanten, T. S., Mivelle, M., Manzo, C., Garcia Parajo, M. F., and Brugger, J. **Large-scale arrays of bowtie nanoaperture antennas for nanoscale dynamics in living cell membranes**. *Nano Lett. 15*, 6 (2015), 4176.

[183] El Eter, A., Hameed, N. M., Baida, F. I., Salut, R., Filiatre, C., Nedeljkovic, D., Atie, E., Bole, S., and Grosjean, T. **Fiber-integrated optical nano-tweezer based on a bowtie-aperture nano-antenna at the apex of a snom tip**. *Opt. Express 22*, 8 (2014), 10072.

[184] Grosjean, T., Mivelle, M., Baida, F., Burr, G., and Fischer, U. **Diabolo nanoantenna for enhancing and confining the magnetic optical field**. *Nano Lett. 11*, 3 (2011), 1009.

[185] Yang, Y., Zhao, D., Gong, H., Li, Q., and Qiu, M. **Plasmonic sectoral horn nanoantennas**. *Opt. Lett. 39*, 11 (2014), 3204.

[186] Kern, J., Kullock, R., Prangsma, J., Emmerling, M., Kamp, M., and Hecht, B. **Electrically driven optical antennas**. *Nat. Photonics 9*, 9 (2015), 582.

[187] Dregely, D., Taubert, R., Dorfmüller, J., Vogelgesang, R., Kern, K., and Giessen, H. **3d optical yagi–uda nanoantenna array**. *Nature Commun. 2* (2011), 267.

[188] Yang, Y., Li, Q., and Qiu, M. **Broadband nanophotonic wireless links and networks using on-chip integrated plasmonic antennas**. *Sci. Rep. 6* (2016), 19490.

[189] Klemm, M. **Novel directional nanoantennas for single-emitter sources and wireless nano-links**. *Int. J. Opt. 2012* (2012), 1.

[190] Ding, Y., Song, X., Jiang, P., Jiao, R., Wang, L., Yu, L., and Zhang, J. **Directional optical travelling wave antenna based on surface plasmon transmission line**. *Laser & Photon. Rev. 12*, 4 (2018), 1700073.

[191] Tang, Y., and Cohen, A. E. **Optical chirality and its interaction with matter**. *Phys. Rev. Lett. 104*, 16 (2010), 163901.

[192] Sobhkhiz, N., and Moshaii, A. **Silver conical helix broadband plasmonic nanoantenna**. *Journal of Nanophotonics 8*, 1 (2014), 083078.

[193] Gansel, J. K., Latzel, M., Frölich, A., Kaschke, J., Thiel, M., and Wegener, M. **Tapered gold-helix metamaterials as improved circular polarizers**. *Appl. Phys. Lett. 100*, 10 (2012), 101109.

[194] Yang, Z., Zhao, M., Lu, P., and Lu, Y. **Ultrabroadband optical circular polarizers consisting of double-helical nanowire structures**. *Opt. Lett. 35*, 15 (2010), 2588.

[195] Kaschke, J., Gansel, J. K., and Wegener, M. **On metamaterial circular polarizers based on metal n-helices**. *Opt. Express 20*, 23 (2012), 26012.

[196] Kaschke, J., and Wegener, M. **Gold triple-helix mid-infrared metamaterial by sted-inspired laser lithography**. *Opt. Lett. 40*, 17 (2015), 3986.

[197] Kaschke, J., Blome, M., Burger, S., and Wegener, M. **Tapered n-helical metamaterials with three-fold rotational symmetry as improved circular polarizers**. *Opt. Express 22*, 17 (2014), 19936.

[198] Yang, Z., Zhao, M., and Lu, P. **A numerical study on helix nanowire metamaterials as optical circular polarizers in the visible region**. *IEEE Photonics Technol. Lett. 22*, 17 (2010), 1303.

[199] Esposito, M., Tasco, V., Todisco, F., Cuscunà, M., Benedetti, A., Scuderi, M., Nicotra, G., and Passaseo, A. **Programmable extreme chirality in the visible by helix-shaped metamaterial platform**. *Nano Lett. 16*, 9 (2016), 5823.

[200] Esposito, M., Tasco, V., Todisco, F., Benedetti, A., Sanvitto, D., and Passaseo, A. **Three dimensional chiral metamaterial nanospirals in the visible range by vertically compensated focused ion beam induced-deposition**. *Adv. Opt. Mater. 2*, 2 (2014), 154.

[201] Esposito, M., Tasco, V., Cuscunà, M., Todisco, F., Benedetti, A., Tarantini, I., Giorgi, M. D., Sanvitto, D., and Passaseo, A. **Nanoscale 3d chiral plasmonic helices with circular dichroism at visible frequencies**. *ACS Photonics 2*, 1 (2014), 105.

[202] Esposito, M., Tasco, V., Todisco, F., Cuscunà, M., Benedetti, A., Sanvitto, D., and Passaseo, A. **Triple-helical nanowires by tomographic rotatory growth for chiral photonics**. *Nature Commun. 6* (2015), 6484.

[203] Tasco, V., Esposito, M., Todisco, F., Benedetti, A., Cuscunà, M., Sanvitto, D., and Passaseo, A. **Three-dimensional nanohelices for chiral photonics**. *Appl. Phys. A 122*, 4 (2016), 280.

[204] Singh, J. H., Nair, G., Ghosh, A., and Ghosh, A. **Wafer scale fabrication of porous three-dimensional plasmonic metamaterials for the visible region: chiral and beyond**. *Nanoscale 5*, 16 (2013), 7224.

[205] Mark, A. G., Gibbs, J. G., Lee, T.-C., and Fischer, P. **Hybrid nanocolloids with programmed three-dimensional shape and material composition**. *Nat. Mater 12*, 9 (2013), 802.

[206] Caridad, J. M., McCloskey, D., Donegan, J. F., and Krstić, V. **Controllable growth of metallic nano-helices at room temperature conditions**. *Appl. Phys. Lett. 105*, 23 (2014), 233114.

[207] Caridad, J. M., McCloskey, D., Rossella, F., Bellani, V., Donegan, J. F., and Krstić, V. **Effective wavelength scaling of and damping in plasmonic helical antennae**. *ACS Photonics 2*, 6 (2015), 675.

[208] Novotny, L., and Hafner, C. **Light propagation in a cylindrical waveguide with a complex, metallic, dielectric function**. *Phys. Rev. E 50*, 5 (1994), 4094.

[209] Novotny, L. **Effective wavelength scaling for optical antennas**. *Phys. Rev. Lett. 98*, 26 (2007), 266802.

[210] Hagemann, H.-J., Gudat, W., and Kunz, C. **Optical constants from the far infrared to the x-ray region: Mg, al, cu, ag, au, bi, c, and al 2 o 3**. *J. Opt. Soc. Am. 65*, 6 (1975), 742.

[211] Gao, S. S., Luo, Q., and Zhu, F. **Circularly polarized antennas**. John Wiley & Sons, 2013.

[212] Prodan, E., Radloff, C., Halas, N. J., and Nordlander, P. **A hybridization model for the plasmon response of complex nanostructures**. *science 302*, 5644 (2003), 419.

[213] Li, Y.-R., Ho, R.-M., and Hung, Y.-C. **Plasmon hybridization and dipolar interaction on the resonances of helix metamaterials**. *IEEE Photonics J. 5*, 2 (2013), 2700510.

[214] Ibrahim, I. A., Mivelle, M., Grosjean, T., Allegre, J.-T., Burr, G., and Baida, F. **Bowtie-shaped nanoaperture: a modal study**. *Opt. Lett. 35*, 14 (2010), 2448.

[215] Jin, E. X., and Xu, X. **Enhanced optical near field from a bowtie aperture**. *Appl. Phys. Lett. 88*, 15 (2006), 153110.

[216] Baida, F. I., Belkhir, A., Van Labeke, D., and Lamrous, O. **Subwavelength metallic coaxial waveguides in the optical range: Role of the plasmonic modes**. *Phys. Rev. B 74*, 20 (2006), 205419.

[217] Chen, Y., Yu, L., Zhang, J., and Gordon, R. **Effective wavelength scaling of rectangular aperture antennas**. *Opt. Express 23*, 8 (2015), 10385.

[218] Wenger, J., Lenne, P.-F., Popov, E., Rigneault, H., Dintinger, J., and Ebbesen, T. W. **Single molecule fluorescence in rectangular nano-apertures**. *Opt. Express 13*, 18 (2005), 7035.

[219] Robbie, K., and Brett, M. **Sculptured thin films and glancing angle deposition: Growth mechanics and applications**. *J. Vac. Sci. Technol. A 15*, 3 (1997), 1460.

[220] Robbie, K., Beydaghyan, G., Brown, T., Dean, C., Adams, J., and Buzea, C. **Ultrahigh vacuum glancing angle deposition system for thin films with controlled three-dimensional nanoscale structure**. *Rev. Sci. Instrum. 75*, 4 (2004), 1089.

[221] Ren, Z., and Gao, P.-X. **A review of helical nanostructures: growth theories, synthesis strategies and properties**. *Nanoscale 6*, 16 (2014), 9366.

[222] Liu, L., Zhang, L., Kim, S. M., and Park, S. **Helical metallic micro-and nanostructures: fabrication and application**. *Nanoscale 6*, 16 (2014), 9355.

[223] Höflich, K., Yang, R. B., Berger, A., Leuchs, G., and Christiansen, S. **The direct writing of plasmonic gold nanostructures by electron-beam-induced deposition**. *Adv. Mater. 23*, 22-23 (2011), 2657.

[224] Esposito, M., Tasco, V., Cuscunà, M., Todisco, F., Benedetti, A., Tarantini, I., Giorgi, M. D., Sanvitto, D., and Passaseo, A. **Nanoscale 3d chiral plasmonic helices with circular dichroism at visible frequencies**. *ACS Photonics 2*, 1 (2014), 105.

[225] Fischer, J., and Wegener, M. **Three-dimensional direct laser writing inspired by stimulated-emission-depletion microscopy**. *Opt. Mater. Express 1*, 4 (2011), 614.

[226] Kaschke, J., Blume, L., Wu, L., Thiel, M., Bade, K., Yang, Z., and Wegener, M. **A helical metamaterial for broadband circular polarization conversion**. *Adv. Opt. Mater. 3*, 10 (2015), 1411.

[227] Reyntjens, S., and Puers, R. **A review of focused ion beam applications in microsystem technology**. *J. Micromech. Microeng. 11*, 4 (2001), 287.

[228] Matsui, S. **Three-dimensional nanostructure fabrication by focused ion beam chemical vapor deposition**. In *Springer Handbook of Nanotechnology*. Springer, 2007, p. 179.

[229] Randolph, S., Fowlkes, J., and Rack, P. **Focused, nanoscale electron-beam-induced deposition and etching**. *Crit. Rev. Solid State Mater. Sci. 31*, 3 (2006), 55.

[230] Van Dorp, W., and Hagen, C. W. **A critical literature review of focused electron beam induced deposition**. *J. Appl. Phys. 104*, 8 (2008), 10.

[231] Shawrav, M. M., Taus, P., Wanzenboeck, H. D., Schinnerl, M., Stöger-Pollach, M., Schwarz, S., Steiger-Thirsfeld, A., and Bertagnolli, E. **Highly conductive and pure gold nanostructures grown by electron beam induced deposition**. *Sci. Rep. 6* (2016), 34003.

[232] Haverkamp, C., Höflich, K., Jäckle, S., Manzoni, A., and Christiansen, S. **Plasmonic gold helices for the visible range fabricated by oxygen plasma purification of electron beam induced deposits**. *Nanotechnology 28*, 5 (2016), 055303.

[233] Larsen, G. K., He, Y., Wang, J., and Zhao, Y. **Scalable fabrication of composite ti/ag plasmonic helices: controlling morphology and optical activity by tailoring material properties**. *Adv. Opt. Mater. 2*, 3 (2014), 245.

LIST OF FIGURES

1.1 Schematics of the electric fields of circularly polarized light with: (a) right and (b) left handedness, respectively. The green curved arrows indicate the rotation sense of the electric field in a single transverse plane. σ denotes the helicity of SAM ($\boldsymbol{s}$), which is parallel or anti-parallel to the wave vector $\boldsymbol{k}$. 8

1.2 Schematic diagrams of (a) polarization ellipse and (b) Poincaré sphere. Note the north and south poles of the Poincaré sphere stand for RCP and LCP, respectively. On the equator of the Poincaré sphere, the corresponding polarization states are linear with the orientation varying with the azimuthal position. 9

1.3 Schematic diagram depicting the rotating electric and magnetic fields of a circularly polarized light. 10

1.4 Transverse spin angular momentum and optical evanescent fields. (a) Schematic showing the field damping and the corresponding spin angular momentum ($s_\perp$). k_x and k_z are the wave vector projections along the x and z axis, respectively. (b) Polarization structure of a TM-polarized evanescent wave. 11

1.5 Coupling between the helicity of transverse SAM to the propagation direction of evanescent waves: (a) and (b) schematically show TM-polarized evanescent waves propagating to the left (a) and right (b), respectively. This spin-locking phenomenon is akin to that with a rolling wheel, which thus gives optical transverse SAM the name "photonic wheel" [56]. 12

1.6 Phase and intensity properties of light beams with a vortex charge number $\ell = -1, 0, 1, 2, 3$ (from right to left): (a) Schematic snapshots of the instantaneous phase. Helical phase fronts occurs when $\ell \neq 0$. The blue dash lines indicate the wave propagation. (b) Phase profiles in a transverse plane [91]. (c) Intensity distributions in a transverse plane. Annual intensity patterns can be seen when $\ell \neq 0$. 13

1.7 Two examples for extrinsic orbital angular momentum (EOAM) of light. (a) Light gains a transverse EOAM when its centroid has a distance with respect to an external reference (z-axis). (b) Light propagates along a helical trajectory, developing an EOAM parallel to z-axis. 15

1.8 Schematic illustrating the geometric phase induced by the rotation of coordinate frames. 16

1.9 Schematics illustrating the optical geometric phases induced by (a) the redirection of wave vectors [55] and (b) the transformation of polarization state on the Poincaré sphere. (a,b) are reproduced from literature [98]. . . . 17

1.10 Spin-orbit interactions in paraxial regime. Spin-Hall effect occurs when light travels along a helical pathway in a glass cylinder [55, 98]: (a) schematic showing the helicity-dependent trajectories for LCP and RCP lights, and (b) measured transverse splitting of LCP and RCP lights with respect to the propagation distance. Helicity-dependent lateral shift of a paraxial beam occurs while deflecting at optical interfaces [104]: (c) schematic showing the transverse shift attached to a RCP light during reflection. (d) Measured Spin-Hall splitting of the LCP and RCP components when a linearly polarized Gaussian beam refracts at air-glass interface. Angstrom accuracy can be reached with "quantum weak measurement" techniques [104, 105]. (a-d) are grabbed from the literature [55]. 19

1.11 Spin-orbit interactions in nonparaxial regime: (a) Schematic showing the optical vortex generated by tightly focusing circularly polarized light [55] (b) Tightly focused LG modes with $\ell = 1$ and $\sigma = \pm 1$. An optical vortex appears in the longitudinal electric component when σ and ℓ have the same sign (top panel), evidenced by a faster orbiting speed of the trapped nanoparticles (middle panel) than that with σ and ℓ of opposite sign (bottom panel) [58]. 20

1.12 Spin-orbit interactions due to Pancharatnam-Berry (PB) phase. Space-variant wave plates induce (a) linear [110] and (b) azimuthal PB phase gradients, leading to a helicity-dependent light splitting and optical vortices with charge numbers $\ell' = 2q$, respectively. (c) Polychromatic optical vortex generation with a single nematic liquid crystal droplet whose anisotropy directs radially in three dimensions. The numbered photos show the intensity profile of the polychromatic vortex and its RGB components, respectively. [61] (d) A 100-nm thick silicon metamaterial splits lights of opposite handedness [111]. (e) Closed-path nano-slits convert CP light into optical vortices, with the charge number defined by the number of slit loops. [63] (f) Chains of plasmonic nano-structures generate vortex beams of various orders [62]. (g) A simple subwavelength arch leads to tunable helicity-controlled directional excitation of nanoscale surface plasmons. The orange, blue and pink halos indicate the positions of incident light and those from the right and left nanoantenna out-couplers, respectively. [112] 22

1.13 Spin-locked unidirectional excitation of surface plasmons (SPs). (a,b) Simulation snapshots of the transverse magnetic component of a spinning electric dipole (a) in air and (b) coupled to surface plasmons [118]. (c,d) Experimental demonstration of the spin-locked directional launching of surface plasmons with a subwavelength groove: (c) schematic of the experimental setup and (d) measured coupling ratios of the left and right SPs (solid lines), in comparison with simulation results (dash lines) [118]. (e-g) Unidirectional light-SP coupling mediated by a gold nanoparticle: (e) schematic for the light-to-SP coupling process, (f) measured left and right SP intensities with respect to the polarization state of the incident light and (g) schematic of the reciprocal SP-to-light coupling process. The scattered light shows a tunable helicity, depending on the direction at which the SP encounters the nanoparticle. [69] 23

1.14 (a) Schematics of the helicity-dependent unidirectional light coupling from a local emitter to an optical waveguide (left panel). The right two panels show that the helicity of the transverse spin depends on both the propagation direction of the waveguide mode and the azimuthal position regarding the waveguide. [119] (b) A spin-locking architecture built by attaching a scattering nanoparticle to a nano fiber. Both the polarization state of the illumination (green arrow) and the azimuthal position of the scatterer are controlled separately, which lead to a tuning ratio of energies coupled to the left and right sides of the nanofiber. [120] (c) Quantum dot zone inside a photonic crystal waveguide that is engineered to be asymmetric (glided plane-waveguide), allowing one-way propagation of helicity-opposite photons. [72] (d) QD embedded in a symmetric suspended waveguide, the directionality shows a dependence on the lateral position of the QD in the waveguide. [121] 24

2.1 Electromagnetic field induced by a circularly polarized magnetic dipole in close proximity to an interface of a material with $\mu = -1.5 + 0.2j$, $(j = \sqrt{-1})$ and $\epsilon = 1$. The color map represents amplitude, and white arrows represent the direction of instantaneous magnetic field. [150] 28

2.2 Design of the 1D photonic crystal (1D PC). (a) Schematic diagram for the 1D PC structure and corresponding field intensity distribution across the 1D PC (at a wavelength of 1.55 μm). (b) Dispersion diagram of the 1D PC with a log-scale color bar. The structure generates a photonic band gap at the middle of which a BSW dispersion curve is observed. 29

2.3 Screen print of the 3D FDTD model built in Rsoft Fullwave for simulating the scenarios of BSW mode excitation with various electric dipole sources. Here, we show the case of an electric dipole oriented along $x-$axis. 30

2.4 Simulation of the electromagnetic field of the BSW mode: (a) and (b) real part of the magnetic and electric field components H_x and E_x, respectively. (c) and (d) real part of the in-plane magnetic field components H_y and H_z, respectively. 31

2.5 Schematic diagram of the polarization of TE-polarized BSWs. (a) and (b) correspond to BSWs propagating toward the right and left directions, respectively. 31

2.6 Real part of the electric field (Ex) of the TE-polarized Bloch surface wave excited with various dipole sources. (a), (b) and (c) are obtained with an electric dipole oriented along the x, y and z axis, respectively. (d), (e) and (f) are obtained with a magnetic dipole oriented along the x, y and z axis, respectively. 32

2.7 TE-polarized Bloch surface waves excited with linear ED and spinning MD. Simulation by FDTD of the coupling of (a) an ED oriented along the x axis, and (b,c), a spinning MD, to a TE-polarized BSW. All three results show, in false colors, the absolute value of the real part of the electric field ($|Re(E_x)|$).The MD rotates either (b) anti-clockwise or (c) clockwise. (d) Directionality factor (ratio of the electric intensities for the left and right BSWs) for various MD polarizations. The MD polarization ellipticity is changed along the path shown in red in the Poincaré sphere (see inset). The MD moment is also expressed at specific values of the ellipticity angle 2χ related to the Poincaré sphere. [74] 33

2.8 (a) and (b) Snapshots (FDTD simulations) of the optical electric field produced in the (yz) plane by two MDs oriented along y and z axis, respectively. In these figures, the field around the dipoles has been saturated in order to provide a better view of the light distributions across the structure. The field distribution in (b) is multiplied by $0.53j$. By adding/subtracting the results of (a) and (b), we achieve the field distributions across the 1D photonic crystal, produced by two spinning MDs of opposite handedness, which are described by dipole moments $\boldsymbol{m}$ proportional to $(\boldsymbol{e}_y \pm 0.53j\boldsymbol{e}_z)$. (c) Electric field profiles $(Re(E_x))$ along the dashed lines of (a) and (b), respectively. Adding these field profiles leads to the total electric field produced by a spinning MD moment proportional to $\boldsymbol{e}_y + 0.53j\boldsymbol{e}_z$ (anti-clockwise rotation). (d) Electric field profiles with a spinning MD moment of $\boldsymbol{e}_y - 0.53j\boldsymbol{e}_z$ (the field plotted in (b) is inverted, leading to a clockwise rotating MD). (c) and (d) show that the BSW coupling process is unidirectional and tunable with the helicity of light. 34

2.9 Schematic diagrams of the excitation process of the BSW mode with (a) a linear ED and (b) spinning MD source, which corresponds to the scenarios shown in 2.7(a) and (b), respectively. The schematics compare the polarization states of the excitation dipole sources and the corresponding electric or magnetic components of the BSW mode. Large red arrows show the energy flow of the emerging BSW mode. In (a), the ED source(purple) is linearly polarized, which coincides with the polarization state of the BSW electric field. In (b), the MD is elliptically polarized (in purple), which is orthogonal to the polarization state of the BSW electric field on the left side. 35

2.10 A simple all-dielectric platform unveiling the magnetic spin-orbit interaction. (a) Photograph of the collection bench, (b) Schematic diagram of the experimental setup, (c) SEM images of the 1D PC (inset: top view graphs of the subwavelength groove milled in the top layer of the 1D PC), (d) photo of the illumination bench. BSW: Bloch surface wave, PC: photonic crystal, QWP: quarter wave plate, LP: linear polarizer. 36

2.11 Images of the 1D PC surface obtained by illuminating the subwavelength groove with light of various polarization states: (a) linear polarization (b) right elliptic polarization (c) left elliptic polarization. 37

2.12 Schematic diagrams for the polarization state of the incident light after passing through a LP and a QWP: (a) the QWP is fixed and the LP is rotated. (b) the LP is fixed and the QWP is rotated. The green arrow in (a) and (b) show the immediate linear polarization state after the LP. The red ellipse (with handedness indication) in (a) and (b) show the final polarization state after the QWP. 38

2.13 Schematic diagram of the electric field projection and corresponding global and local coordinate frames. e_r and e_l (in red) represent the unit vectors parallel to the electric field components of the right and left BSWs. 38

2.14 Pure electric coupling model for the excitation of BSWs from the oblique illumination of a subwavelength groove. Plot of the coupling rates R_r and R_l of the incident light into the right and left BSWs, calculated from Eqs. 2.9 and 2.10, respectively. 40

2.15 (a) Schematic diagram of the magnetic field handedness in the helicity planes of the left and right BSWs for an incident right-handed polarization. (b) Ellipticity 2χ of the incident magnetic field in the helicity planes (y^L, z^L) and (y^R, z^R) of the left and right TE-polarized BSWs. 41

2.16 Screen print of the 3D FDTD model built with Fullwave software to simulate the scenario of a BSW excitation with the configuration depicted in Figs. 2.10. 42

2.17 Simulation snapshots of the TE-polarized BSWs excited by a groove under the illumination with (a) left circular polarization and (b) right circular polarization. The two results show, in false colors, the absolute value of the real part of the electric field ($|Re(Ey)|$). The white lines show the profile of the subwavelength groove, which has a cross-section of $400\ nm \times 400\ nm$. The blue and red arrows in (a), which have a angle of $33.8°$ with respect to the groove, indicate the BSW propagation directions on the left and right sides, respectively. 42

2.18 Magnetic spin-orbit interaction steers Bloch surface waves. (a) detected signals (circles) and simulated intensities by FDTD (solid lines), on the right and left BSWs, as a function of the angle θ between the QWP and the LP. The curves related to the right and left BSWs are represented in red and blue, respectively. (b) and (c) Fourier spectra (amplitude) of the experimental blue and red curves of (a), obtained by Fourier transformation. Coefficient u defines the harmonic orders for the Fourier series. (d) and (e) Representation, in the real space, of the non-null harmonics for the two Fourier series shown in (b) and (c): (d) second harmonics and (e) fourth harmonics. Experimental and numerical curves are shown by solid and dash lines, respectively. [74] 43

3.1 (a) Schematic of dipolar antennas connected at the two ends of a plasmonic waveguide [171]. (b) Scanning electron microscope (SEM) images of a monopole antenna mounted at a fiber tip [50]. (c) Schematic and SEM image of a gold particle antenna attached at a fiber tip [172]. (d) Schematic of a cross resonant antenna [173]. 49

3.2 Schematics of (a) bowtie nanoantenna [179] (b) bowtie nanoaperture antenna fabricated at a fiber tip [180] (c) diabolo nanoantenna.[173] 50

3.3 (a,b) Optical Yagi-Uda antenna[51] with (a) SEM image and (b) theoretical and measured emission patterns. (c,d) Plasmonic horn antenna [185] with (c) a schematic and (d) emission patterns on two principle planes. 50

3.4 Schematic showing a single helix, whose geometrical parameters include the core radius R_h, the vertical pitch S, the total turn number N of the helix and the radius of the helix wire R_w. 52

3.5 Helical antenna modes: (a) normal radiation mode and (b) axial radiation mode, (c) and (d) show the fundamental and high order transmission modes along an infinite helix wire, which correspond to the radiation modes shown in (a) and (b) respectively. 53

3.6 Typical current distributions measured along a helical antenna working at a wavelength (a) beyond the axial-mode operation region and (b) near the spectral center of the axial-mode region. (c) Analysis of the antenna current shown in (b) in terms of outgoing and reflected waves. [167] 54

3.7 schematics of the time-evolution of induced currents and charges for a (a) normal mode and (b) axial mode, respectively. For clarity, only the very first current node is shown in (b) to represent the traveling wave. The red and blue disks with "+" and "-" sign represent positive and negative charges, respectively. The purple and orange curves with an arrow show the orbiting direction of the induced currents. Green and red straight arrows show the corresponding electric and magnetic fields, respectively. Notably, in (a) the electric and magnetic fields are parallel and have a relative phase shift of $\pi/2$, thus evidencing a signature of optical chirality. In (b), the electric and magnetic fields are always perpendicular. 55

3.8 Helical metamaterial works as circular polarizer: (a) broadband chiral response (b) snapshots of the induced current along the helix, showing standing-wave characteristics along the structure. [45] 57

3.9 (a) and (b) SEM images of carbon and platinum helical metamaterials fabricated with FIBID, respectively. Those helices featuring a triply-intertwined configuration and ultra-small dimensions. (c) and (d): measured circular dichroism and optical activity spectra for the two metamaterials, respectively.[199] 58

3.10 Chiro-optical near-fields produced by resonant plasmonic helices. (a) Schematics for the chiral eigenmodes of a single plasmonic helix with opposite handedness (b) False color plot of the optical chirality enhancement factor, in the near-field of an intertwined 4-helix structure. [164] 58

3.11 (a) A schematic of the prototype HPA, consisting of a 4-turn helical nanowire (along z–axis), a straight rod and a round sphere to join the two parts. The HPA is fed by a z–oriented electric dipole source in end-fire configuration. FDTD simulation is used to study the spectral response of the TW-HPA. The green and orange planes represent the monitors used to collect the electric field data of the TW-HPA. They are placed 20 nm and 2 μm far away from the open end of the helix, with their centers on the helix axis. (b) and (c) show the intensity spectra (normalized by the dipole source) of the two transverse electric components (E_x and E_y, which are responsible for the CP polarization) obtained with the two monitors. Dash vertical lines in magenta and light blue show positions of the spectrum peaks at free-space wavelengths $\lambda_1 = 658$ nm, $\lambda_2 = 1641$ nm, $\lambda_3 = 2259$ nm and $\lambda_4 = 4310$ nm. . 59

3.12 Near-field and far-field properties of the helical plasmonic antenna (HPA) working on axial and normal modes. The HPA has the same geometries as shown in 3.11 but working at different wavelengths, which are 658 nm (λ_1) for (a~c) and 4310 nm (λ_4) for (d~e). (a,d) pseudo-color plots for the normalized electric field intensity closely around the HPA, where regions around the dipole source have been saturated for a better view of the helix wire modes. (b,e) pseudo-color plots for the electric field intensity in a larger area around the HPA. In (b) and (e), the intensities have been taken logarithm before normalization, for showing the transition from near-field to far-field. Red arrows in (b) and (e) mark the directions with the maximum far-field radiation. (c,f) intensity radiation patterns of the HPA constructed via near-field to far-field projections. The near field data are recorded with box monitors enclosing the HPA, which are finally projected to a far-field sphere with a radius of 100 m. 60

3.13 Far-field spectra of the prototype HPA, where the blue and red curves represent the intensity and AR spectrum, respectively. To obtain the blue curve, the raw far-field intensity spectrum has been normalized twice: first with the intensity spectrum of the dipole source and then with its own maximum value to offer a clear view. The AR spectrum is constructed with the spectra data of the two transverse electric components (E_x and E_y). 61

3.14 Schematic showing the optical angular momenta associated with the helical SPs. 62

3.15 Schematic of the FDTD simulation model for studying the effects of the helix geometries on the AR spectrum. 64

3.16 AR spectra of an TW-HPA with various S values ranging from 240 nm to 840 nm. Other geometric parameters are the same for all helices: $R_h = 180$ nm, $R_w = 25$ nm, $N = 4$. 65

3.17 Influence of the helix wire radius (R_w) on the far-field polarization property of TW-HPA. Solid lines with different colors show the AR spectra of HPAs with various R_w values ranging from 25 nm to 60 nm. Other geometric parameters are the same for all helices: $R_h = 180$ nm, $S = 740$ nm, $N = 4$. The red dash line shows an axial ratio of 0.5. 66

3.18 Axial ratio spectra of HPAs with various wire radii (R_w ranging from 25 nm to 60 nm) and optimal vertical pitches (S) that enable an AR peak. Note for helices with different wire radius, the total number of such optimal α_h values are different, which is one when R_w ranges from 25 nm to 35 nm and two when R_w ranges from 40 nm to 60 nm. According to their similar shapes, those AR spectra have been divided in two groups, i.e. (a) and (b) for a better view. All helices have the same radius($R_h = 180$ nm) and total turn number ($N = 4$). The red dash line shows an axial ratio of 0.5. 67

3.19 Dispersion relations of gold nano-wires with various radii ranging from 25 nm to 60 nm. 67

3.20 (a) and (b) show the AR spectra for two sets of helices, whose wire thickness is fixed as 60 nm and 25 nm and pitch angle is $14°$ and $39°$, respectively. Here, we only plot the axial ratio spectra around its peak to have a better view. 68

3.21 Axial ratio spectra of HPAs with various N values ranging from 1 to 4. Other geometric parameters remain identical for all helices: $R_h = 180$ nm, $R_w = 60$ nm, $S = 540$ nm. The red dash line shows an axial ratio of 0.5, above which an antenna can be thought as circularly polarized antenna. 69

3.22 (a) Axial ratio spectra (on-axis calculations) of left and right-handed helices (b) Corresponding amplitude ratio ($\ln\left(|E_y|/|E_x|\right)$) and phase difference ($(\varphi(E_x) - \varphi(E_y))$) spectra of the two transverse electric components of the far-field emission. The helices have geometric parameters: $R_h = 180$ nm, $R_w = 60$ nm, $S = 540$ nm, $N = 4$. 69

3.23 Aspect ratio spectra of a helix optimized for working at optical telecommunication wavelengths. The helix dimensions are: $R_h = 160$ nm, $R_w = 60$ nm, $S = 495$ nm, $N = 4$. 70

3.24 Schematics of (a) circular nano aperture (b) bowtie nano aperture and (c) rectangular nano aperture. The red arrows show the linear polarization of the excitation light (E_{inc}), which leads to enhanced electric fields in the regions marked by the red halos. 71

3.25 Schematics showing the FDTD model built for studying the optical properties of a helix with a feed element. PML:perfect match layer, λ: largest wavelength involved in the simulation. 72

3.26 Design of the rectangular nano aperture (RNA) for working at optical telecommunication wavelength ($\lambda_0 = 1.55$ μm). (a) Schematic of the RNA. (b) Normalized intensity spectra of RNAs with various side lengths (L) and widths (W). The gold layer in which the RNA resides has a fixed thickness of 100 nm. (d) Electric field intensity distribution of the RNA in the ($x0y$) plane. 72

3.27 Helical plasmonic antenna as circularly polarized subwavelength source: (a) Schematics of the final TW-HPA and operation principle. End-fire excitation is represented with a white spike. Under curved trajectory along the helix, SPs acquire EOAM and are simultaneously released as freely propagating waves (white arrow). Part of the mode leakage re-excites the plasmon wire mode, thus participating in the plasmon swirling effect. (b) dispersion relations of the $m = 0$ and $m = 1$ modes of a gold-coated carbon wire (105-nm diameter carbon wire, 25-nm thick gold coating). Energy is plotted versus $\hbar c\beta'$ and $\hbar c\beta$". At λ=1.5 μm, only the $m = 0$ mode is guided. Figure inset: intensity plot of the $m = 0$ mode at λ=1.5 µm. (c) Spectra of the AR and DOCP of the TW-HPA emission. (d) Amplitude of the electric current distribution along the gold-coated carbon wire for λ=1.5 μm. 74

3.28 Traveling SP mode in a TW-HPA (see more information in Section 3.3.2.1). The pseudo-color field maps show the simulation snapshots of the instantaneous electric field distribution at $\omega t = i\frac{\pi}{4}$ ($i = 0, 1, 2...7$) and on two planes that cross the helix axis. The $x0z$ and $y0z$ plane field maps are shown on the upper and lower sides, respectively. These field maps are normalized with the same maximum amplitude value. The white dash line and red arrow indicate the axial advance of SP modes. The white thin solid lines show the gold layer and the nanoaperture on the substrate. 75

3.29 TW-HPA emission diagram. The TW-HPA shows a directional emission perpendicularly to the (x0y) ground plane of the antenna, thus confirming its axial operation mode. 75

4.1 DLW for the fabrication of gold helix arrays. (a) Schematic for the original DLW process where a positive-tone photoresist is used to form the mould with helical voids. (b) Cross-sectional SEM image of the polymer mould filled by electro-plated gold. (c) Side-view SEM image of the resulting monofilar gold helix array after mould removal. (d) Schematics of the modified DLW process where a negative-tone photoresist is patterned by stimulated-emission-depletion-DLW to form the mould. (b) SEM image of the written polymer mould after chemical development and (c) Side-view SEM image of the final triply-intertwined gold helix array. (a)~(c) and (d)~(f) are snapped from the Refs. [45] and [196], respectively. 78

4.2 FIBID/FEBID fabrication of nano-helix structures: (a) Schematic depicting the FIBID fabrication process. [200] (b) and (c) : SEM images of the platinum helices fabricated by FIBID and FEBID, respectively. The helix geometry shown in (b) is: $R_h = 200$nm, $R_w = 65$ nm, $S = 300$ nm and in (c) are $R_h = 100$nm, $R_w = 30$ nm, $S = 350$ nm, respectively. (d) Triply inter-winded Pt helix array fabricated by tomographic rotatory FIBID growth. Dimensions of a single helix are: $R_h = 187.5$nm, $R_w = 55$ nm, $S = 705$ nm. [203] 79

4.3 GLAD fabrication of nano-helix structures [205]. (a-c): Schematics of the GLAD fabrication process with (a) seeded substrate with grain sites prepared by nano-lithography, (b) structure growth under grazing-incidence particle flux and (c) resulting nano-helix arrays. (d-f): SEM images of the GLAD-fabricated nano-helices with (d) a nano-helix array attached on the substrate (e) and (f) a single left- and right-handed helix picked out from the nano-helix array, respectively. 80

4.4 Glancing angle deposition (GLAD) equipment used in my thesis: (a) Schematic diagram and (b) a photo of the running machine. Inset of (b) shows the glowing plasma in the fabrication chamber. 81

4.5 SEM images of the nano-helix structure fabricated by GLAD: (a) cross-section and (b) top view. 81

4.6 Photograph of the SEM/FIB dual-beam system (Helios Nanolab 600i, FEI) available at FEMTO-ST Institute. It is the workhorse for both structuring and characterizing HPAs. 82

4.7 Schematic diagrams of the fabrication process we develop for realizing the TW-HPA structures. (a) Fabrication of the carbon helices on a gold coated glass substrate by FIBID. The FIB is used to induce the carbon wire deposition and the SEM is used to monitor the deposition process. (b) Metalization of carbon helices with gold by GLAD involving plasma sputtering approach. Direct current is applied between the substrate and gold target to generate argon plasma. (c) Fabrication of the rectangular aperture by FIB milling. The small angle is kept between ion flux and the helix to avoid side-cutting effect. 83

4.8 SEM images of various 4-turn carbon helices fabricated by FIBID: (a) without pitch correction (b-d) with pitch correction. Scale bars: 200 nm. 84

4.9 SEM images of carbon helices with total turn number varying from 1 to 4. Scale bars: 200 nm. 85

4.10 SEM images of grouped carbon helices with opposite handedness. (a) Paired left and right helices. (b) Closely-packed four-helix system where helices with the same handedness are placed at the diagonal positions of a subwavelength square. Scale bars: 200 nm. 85

4.11 Metal coating results of a carbon helix with $R_h \sim 155$ nm, $S \sim 350$ nm. (a) Bird-view SEM image of the gold-coated carbon helix. (b) Cross-section SEM image of the helix, embedded in a FIBID-deposited platinum (Pt) block. The bright gray areas show the gold coating (Au) and the dark gray areas show the carbon core (C). (c) 3D tomographic image of the gold-coated carbon helix, which is reconstructed from a series of sliced SEM images of the HPA. The gold and carbon materials are represented in yellow and black, respectively. Scale bars: 200 nm. The green and red arrows in (c) show two representative regions with a thick and thin gold coating, respectively. 86

4.12 Fabrication results of the helix-RNA nano-structure. (a) SEM images of a resulting structure. (b) Top view of a single RNA and (c~e) its combination with a gold-coated helix in different configurations. Here, the aperture is milled outside the winding area of the helix. 87

4.13 Fabrication of the TW-HPA: three steps. Scanning electron micrographs of the subwavelength structure after (a) fabrication of the carbon helix skeleton by FIBID, (b) metal deposition onto the helix skeleton, and (c) fabrication of rectangular nano-aperture antenna by FIB milling. 87

4.14 Experimental setup for measuring the polarization property of the antenna emission: (a) Schematic diagram and (b) photograph of the experimental bench. LP: linear polarizer, QWP: quarter wave plate, HWP: half wave plate, OBJ: objective, BS: beam splitter. The fiber used here is a polarization maintaining fiber, which transmits infrared light produced by a tunable laser ($1470 \sim 1650$ nm). The magenta dash rectangle in the illumination bench indicates the polarizer system, which contains a LP and a HWP. The green dash rectangles in the detection bench indicate the analyzer system, which can be switched between i) a rotating LP for acquiring the polarization diagram, and ii) a rotating QWP followed by a linear polarizer for analyzing the helicity of light. Both the polarizer and analyzer systems are driven by a motorized stages. The sample holder is mounted on a 3D piezoelectric translation stage, which enables the precise focusing of the excitation light onto the antenna. 88

4.15 RNA response measurements. (a) Measurement of RNA's response to the input polarization: simplified experimental scheme (left panel) and measured RNA emission intensity regarding the input polarization orientation (right panel). Experimental results (blue circles) are compared with Malus law (red curve). Measurement of RNA's radiation property: simplified experimental set-up (left panel) and measured RNA polarization diagram (intensity), compared with the typical response of a dipole Malus's curve (right panel). Those measurements in (a) and (b) are enabled by rotating a linear polarizer inserted either in the input or output benches, respectively. The two insets, in both (a) and (b), show the optical and SEM images of the RNA. In all cases, θ denotes the orientation of the polarizer's transmission axis, counted from x-axis). 90

4.16 Circularly polarized optical emission from a single TW-HPA. (a) The left panel shows a simplified schematic depicting the experimental bench for characterizing the polarization properties of the helical antenna (inset shows a typical far-field optical image of the TW-HPA emission). The right panel shows a side-view SEM micrograph of the TW-HPA, whose central radius and vertical pitch are $R_h \sim 155$ nm and $S \sim 350$ nm, respectively. (b) Measured antenna emission intensity with respect to the input linear polarization. (c) State-of-polarization analysis at $\lambda = 1.55$ μm and $\lambda = 1.64$ μm. (d) Experimental spectra of the AR and DOCP, compared with the simulation results considering a 10-nm thick homogeneous metal coating onto the carbon skeleton. 91

4.17 (a) Left panel: simplified schematic of the experimental set-up, where a rotating quarter wave plate (QWP) and a fixed linear polarizer (LP2) are put in front of the camera to analyze the helicity of the antenna emission. Right panel: optical and SEM images of two HPAs of opposite handedness. (b) Measured transmission intensity for the two HPAs through the circular analyzer. Maximum helicities are obtained for angles between the QWP and LP of $45°$ and $135°$. This resembles two circular polarizers of opposite handedness. We have $\sigma = \pm 1$ for the two HPAs, where σ stands for the helicity of light. 92

4.18 Circularly polarized emission originates from the excitation of a subdiffraction surface plasmon within the helix. AR spectrum of the TW-HPA emission for the RNA in contact to the helix pedestal (blues squares), 185 nm away from the helix pedestal (red circles), and turned by $90°$ regarding the two first cases (green diamonds), respectively. 93

4.19 Spectrum of the AR of the TW-HPA emission for a single structure with one turn (orange triangles), two turns (green diamonds), three turns (red circles), and four turns (blue squares). 94

5.1 Schematics of the two operation modes of the TW-HPA, involving light wave propagation in two opposite directions along the antenna axis, respectively. 98

5.2 Simulation of the TW-HPA in detection mode: (a) Schematics of the simulation model. (b,c) Simulated intensity distribution ($x0z$ plane) of the TW-HPA under illumination with (b) left and (c) right-handed circularly polarized light, respectively. The intensity plots have been saturated equally for a better view of the TW-HPA wire mode. RNA: rectangular nanoaperture. 98

5.3 Schematic diagrams of the experimental setups for measuring the circular dichroism of the TW-HPA (a) in emission mode, and (b) in collection mode. LP: Linear Polarizer, OBJ: Objective, QWP: Quarter-wave plate, BS: beam splitter. 99

5.4 (a) Schematics of the two operation modes of the TW-HPA, involving light wave propagation in two opposite directions along the antenna axis, respectively. (b) Circular dichroism spectra measured with a left-handed TW-HPA operating in emission and collection modes. Circular dichroism is defined as $(I_{RCP} - I_{LCP})/(I_{RCP} + I_{LCP})$, where I_{RCP} and I_{LCP} stand for the emission intensity of the TW-HPA, with an illumination by right and left circularly polarized light, respectively. Emission intensity is measured either from the helix, in air (in emission mode), or from the rectangular nanoaperture antenna, through the substrate (in collection mode). Figure inset: helicity analysis in emission mode, at λ=1.55 μm. The measurement is realized by placing a circular analyzer, consisting of a rotating quarter-wave plate followed by a fixed polarizer, in front of a detector and measuring the transmitted power. RCP and LCP refer to right and left-handed circular polarization of the emitted light, respectively. 100

5.5 Schematics of the CP-LSA, consisting of two couples of HPAs of opposite handedness and orthogonal aperture nano-antennas. The right and left handed HPAs are identified with the letters R and L, respectively. Red and blue arrows indicate the linear polarization states of the incident light, at which only the two right and left-handed HPAs are respectively switched on emission. 101

5.6 Scanning electron micrograph of the CP-LSA, which consists of two couples of HPAs of opposite handedness and orthogonal aperture nano-antennas. The right and left-handed HPAs are identified with the letters R and L, respectively. The letters A, B, C and D show the arrangement configuration of these HPAs (cf. Fig. 5.5). 102

5.7 Measurement on the tuning property of the spin-light array (cf. Fig. 5.6) with linearly polarized excitation light. (a) Left panel: schematic diagram of the experimental setup and right panel: far-field optical images of the four-HPA device at three input polarizations. (b) Emission intensities of the two HPAs of opposite handedness at various input polarization states. . . . 103

5.8 Helicity characterization of the emissions from the spin-light array (cf. Fig. 5.6). (a) left panel: schematic diagram of the experimental setup, right panel: far-field optical images of the four-TW-HPA device with a (middle) right-handed and (bottom) a left-handed circular analyzer in front of the camera. (b) Helicity analysis of two HPAs of opposite handedness. The measurement is realized by placing a rotating quarter wave-plate and a fixed linear polarizer in front of a detector and measuring the transmitted power. 104

5.9 (a) 3D and (b) 2D top-view schematics of the four-coupled HPAs. It consists of two couples of HPAs of opposite handedness and orthogonal aperture nano-antennas. The right- and left-handed HPAs are identified with the letters R and L, respectively. 105

5.10 Theoretical prediction of the polarization state of the four-coupled TW-HPA structure (i.e., the polarization angles $|2\chi|$ and 2ψ on the Poincaré sphere), as a function of the polarization direction (angle θ) of an incident linearly polarized wave. Three ellipticity factors are considered: $b_1 = b_2 = 1$ (blue curves), $b_1 = b_2 = 0.5$ (orange curves) and $b_1 = b_2 = 0.1$ (yellow curves). . . 105

5.11 Scanning electron micrographs of the four-coupled TW-HPA structure: (a) Angled view, (b) Top view. Figure inset shows the optical image of the structure on emission, exhibiting a single light spot (regardless of the input polarization). 107

5.12 Subwavelength scale manipulation of light polarization by four coupled HPAs. (a,c) Polarization angles 2χ and 2ψ of the emitted field versus the polarization direction of an incident linearly polarized light (Poincaré sphere approach of polarization). The optical waves are impinging from the substrate at normal incidence, with (a) λ=1615 nm and (c) λ=1470 nm. (b,d) Polarization diagram of the antenna emission for incident polarization corresponding to θ equal to 45° and 135°, leading to the selective excitation of the two couples of HPAs of opposite handedness: (b) λ=1615 nm. (d) λ=1470 nm. Near-field coupling between the HPAs of opposite handedness ensures parallel outcoming polarization ellipses for orthogonal incident linear polarizations. 107

5.13 Schematics illustrating the generation of parallel elliptical polarizations of opposite helicity at $\theta = 45°$ and $135°$, due to the near-field coupling of SPs in the four-coupled TW-HPA device. (a) 3D schematic showing the near-field coupling of surface plasmons (SPs) in the four TW-HPAs at $\theta = 45°$. (b,c) Top-view schematics showing the coupling between SPs in such a system with (b) $\theta = 45°$ and (c) $\theta = 135°$. The blue and red open circles with an arrow indicate the swirling SPs in the left- and right-handed TW-HPAs, respectively. The green arrows indicate the parallel propagation directions of those SPs. The corresponding output polarization states are represented by the blue and red ellipses in the insets of (a) and (b). 108

PUBLICATIONS

JOURNAL PUBLICATIONS

1. **M. Wang**, H. Zhang, T. Kovalevitch, R. Salut, M-S. Kim, M. A. Suarez, M-P. Bernal, H-P. Herzig, H. Lu, and T. Grosjean, “Magnetic spin-orbit interaction of light". **Light: Science & Applications**, 7(1): 24-31, 2018.

2. **M. Wang**, R. Salut, H. Lu, M. A. Suarez, N. Martin, and T. Grosjean, “Controlling the polarization state of light by swirling surface plasmons". (Submitted)

INTERNATIONAL CONFERENCES

1. **M. Wang**, H. Zhang, T. Kovalevitch, R. Salut, M-S. Kim, M. A. Suarez, M-P. Bernal, H-P. Herzig, H. Lu, and T. Grosjean, “Magnetic spin-orbit interaction of light". **NFO-15**, Troyes, France, 26 August – 31 August 2018. (Oral)

2. **M. Wang**, H. Zhang, T. Kovalevitch, R. Salut, M-S. Kim, M. A. Suarez, M-P. Bernal, H-P. Herzig, H. Lu, and T. Grosjean, “Magnetic spin-orbit interaction of light steers Bloch surface waves". **OMN-2018**, pp: 227, Lausanne, Switzerland, 29 July – 2 August 2018. (Oral)

3. **M. Wang**, H. Zhang, T. Kovalevitch, R. Salut, M-S. Kim, M. A. Suarez, M-P. Bernal, H-P. Herzig, H. Lu, and T. Grosjean, “Magnetic spin-orbit interaction of light steers Bloch surface waves". **META-2018**, pp: 49, Marseille, France, 24 June – 1 July 2018. (Oral)

4. **M. Wang**, H. Zhang, T. Kovalevitch, R. Salut, M-S. Kim, M. A. Suarez, M-P. Bernal, H-P. Herzig, H. Lu, and T. Grosjean, “Tunable unidirectional coupling of Bloch surface waves controlled by the magnetic field of light". **Photonics West-2018**, pp: 10541-95, San Francisco, California United States, 27 January – 1 February 2018. (Poster)

OTHER PRESENTATIONS

1. **M. Wang**, H. Zhang, T. Kovalevitch, R. Salut, M-S. Kim, M. A. Suarez, M-P. Bernal, H-P. Herzig, H. Lu, and T. Grosjean, “Magnetic spin-orbit interaction directs Bloch surface waves". **GDR Ondes-2017**, pp:9 Nice, France, 23 October – 25 October 2017. (Poster)

Document generated with LaTeX and:
the LaTeX style for PhD Thesis created by S. Galland — http://www.multiagent.fr/ThesisStyle
the `tex-upmethodology` package suite — http://www.arakhne.org/tex-upmethodology/